



**A SEARCH FOR ECLIPSING  
COMPANIONS TO WHITE  
DWARF STARS**

by

**Claudia Belardi**

**Thesis**

Submitted to the University of Leicester

for the degree of

**Doctor of Philosophy**

**Department of Physics and Astronomy**

September 2019

# Declarations

I hereby declare that no part of this thesis has been previously submitted to this or any other University as part of the requirement for a higher degree. The work described herein was conducted by the undersigned except for contributions from colleagues as acknowledged in the text.

Signed: Claudia Belardi

Date: 20 September 2019

# Abstract

In this Thesis, I present a search for eclipsing companions to white dwarf stars, with the aim of studying and more accurately constraining the properties of evolved planetary systems.

I first undertake an independent, ground-based survey of metal-rich white dwarfs with similar physical properties to WD1145+017, the first discovered white dwarf hosting a disrupting planetesimal. While no transit-like features are detected in the survey, photometric variability is discovered in two objects. I investigate the nature of such variability in both objects. At the time of writing this work, I am awaiting spectroscopic data for one of the targets in order to search for evidence of an unseen companion. The second object reveals no radial velocity variations, thus the most likely source of variability is determined to be accretion events from the surrounding environment.

Moreover, I take part in analysing the white dwarf sample in Campaign 14 of the Kepler K2 mission, sampling 368 white dwarfs brighter than 20 mag. In the sample, I find a brown dwarf totally eclipsing a white dwarf with a period of  $\sim 133$  minutes. Only two other eclipsing white dwarf + brown dwarf systems were known previous to this discovery.

Finally, I present the discovery of two post common-envelope binary systems in the Next Generation Transit Survey. The first system consists of an M4 star orbiting a cool ( $\sim 7500$  K) white dwarf with a period of  $\sim 13.85$  hours. Only one other system similar to this had been previously discovered. The second binary is a younger, hotter system, in which an  $\sim 18,000$  K white dwarf is eclipsed by a late-K or early-M main sequence companion.

# Acknowledgments

I would like to dedicate this work to my parents (Cesare and Matilde), who supported me in every way possible, even when I made the mad decision of pursuing a Ph.D. Thanks to my sister Patrizia, who taught me to be brave and venture out in the world to follow my dreams, and to my brother Fausto, for reminding me that no matter how much effort I put into my research, there will still be people who believe the Earth is flat. And to my partner Adam: thank you for putting up with me and my three plague-carrying pets (Houston, Problem and Zorro), and remember I will always hate you a little for getting your Ph.D. before me.

I would like to thank my supervisors. Martin Barstow, thank you for always supporting and believing in me. Matt Burleigh, thank you for everything (including penguins, dinosaur footprints, Pinotage and well, even ‘bones in gravy’). And Sarah Casewell, thank you for always helping me keep my sanity in check.

Special thanks to my ‘tea buddy’ Simon Joyce, for following me step by step in my writing up process and for being such an amazing person and friend. To Ian Braker, I will always appreciate you for providing me with great guidance and advice, astronomy-related or not. And thanks to the amazing people in the White Dwarf and NGTS research groups: Emma, Nicolle, Simon, Alex, Liam, Rosie and Jack.

I am grateful to the University of Leicester for giving me this opportunity, which allowed me to meet great people and great life-long friends: Sarah (the most brutally honest friend one could ever hope for), Mike (great provider of coffee breaks), Giovanni and his taralli, Katie, Maria, Adam, Jordan, Jack and all the other physics Ph.D. students.

Thanks to all the great people I got to meet during my (many) observing trips at SAAO, in particular to Lee: the best person to have sushi with.

And finally, I would like mention my friends outside of the University: Luca, Chiara, Elena, Justine, Lavinia, Alessia, Martina, Valerio, Anastasia, Lorenzo, Sunniva and Lani. Thank you all for being the living proof that friendship knows no borders, no distance, and no time.

# Contents

<b>Declarations</b>	<b>i</b>
<b>Abstract</b>	<b>ii</b>
<b>Acknowledgments</b>	<b>iii</b>
<b>List of Tables</b>	<b>ix</b>
<b>List of Figures</b>	<b>xi</b>
<b>Chapter 1 Introduction</b>	<b>1</b>
1.1 Overview . . . . .	1
1.2 White Dwarfs . . . . .	2
1.2.1 Evolution of White Dwarfs . . . . .	2
1.2.2 Characterisation of White Dwarfs . . . . .	4
1.3 Metal-Rich White Dwarfs . . . . .	6
1.3.1 Sources of Metal Contamination in White Dwarfs . . . . .	6
1.4 Planetary Systems Around White Dwarfs . . . . .	8
1.4.1 Debris Disks Around White Dwarfs . . . . .	8
1.4.2 Planetary Systems Around White Dwarfs . . . . .	10
1.4.3 Transiting Planets Around White Dwarfs: Surveys . . . . .	14
1.5 Sub-stellar Companions to White Dwarfs . . . . .	18
1.6 Variability in White Dwarfs . . . . .	20
1.6.1 Pulsating White Dwarfs . . . . .	21
1.6.2 Magnetic White Dwarfs . . . . .	21
1.6.3 Metal Accretion . . . . .	23
1.6.4 Stellar and Sub-stellar Companions . . . . .	24

1.7	Purpose of This Thesis . . . . .	25
<b>Chapter 2 Methods for Reducing and Analysing Data</b>		<b>27</b>
2.1	Photometric Data Reduction . . . . .	27
2.1.1	SHOC Data Reduction . . . . .	28
2.2	Photometric Data Analysis . . . . .	28
2.2.1	Aperture Photometry . . . . .	28
2.2.2	Differential Photometry . . . . .	32
2.3	Light Curve Fitting . . . . .	36
2.3.1	JKTEBOP . . . . .	36
2.4	Spectroscopic Data Reduction and Extraction . . . . .	38
2.4.1	Bias Correction . . . . .	39
2.4.2	Flat Correction . . . . .	42
2.4.3	Spectrum Extraction . . . . .	44
2.4.4	Wavelength Calibration . . . . .	47
2.4.5	Flux Calibration . . . . .	48
2.5	Spectroscopic Data Analysis . . . . .	51
2.5.1	Normalisation and Processing . . . . .	51
2.5.2	Radial Velocity Measurement . . . . .	52
2.6	Summary . . . . .	59
<b>Chapter 3 A Ground-Based Photometric Survey of Metal Rich White Dwarfs</b>		<b>60</b>
3.1	The Discovery of WD1145+017 . . . . .	61
3.1.1	Motivation for a Metal-rich WD Survey . . . . .	62
3.2	Instrumentation . . . . .	63
3.2.1	The SAAO 1.0 m Telescope . . . . .	63
3.2.2	The Sutherland High Speed Optical Cameras . . . . .	64
3.2.3	GPS and Control Computers . . . . .	65
3.3	The Ground-Based DAZ Survey . . . . .	66
3.3.1	Survey Results . . . . .	72
3.3.2	Detection Rate . . . . .	73
3.3.3	Statistical Implications of the Survey . . . . .	75
3.3.4	SDSS J161717.04+162022.4 . . . . .	77
3.4	Summary . . . . .	82

## **Chapter 4 WD1201-049: A Variable White Dwarf in the DAZ**

<b>Survey</b>	<b>84</b>
4.1 Observations . . . . .	85
4.2 Instrumentation - SpUpNIC . . . . .	86
4.2.1 Instrument Layout . . . . .	87
4.3 Observing Strategy for WD1201-049 . . . . .	91
4.3.1 SHOC Observations . . . . .	91
4.3.2 SpUpNIC Observations . . . . .	91
4.4 Data Reduction . . . . .	93
4.4.1 Reducing and Extracting Photometric Data . . . . .	93
4.4.2 Reducing and Extracting Spectroscopic Data . . . . .	94
4.5 Results . . . . .	94
4.5.1 Preliminary Results . . . . .	94
4.5.2 Follow-up Results - Spectroscopy . . . . .	100
4.5.3 Follow-up Results: Photometry . . . . .	103
4.6 Discussion . . . . .	106
4.7 Summary . . . . .	110

## **Chapter 5 A New Eclipsing White Dwarf + Brown Dwarf System in the Kepler K2 Mission**

<b>5.1 The Kepler Mission . . . . .</b>	<b>116</b>
5.1.1 Telescope Design . . . . .	117
5.1.2 Original Mission Design . . . . .	118
5.1.3 The Kepler K2 Mission . . . . .	119
5.1.4 Kepler and K2 Light Curve Processing . . . . .	121
5.1.5 Target Selection . . . . .	122
<b>5.2 WD1032+011: A New Eclipsing WD+BD System - Discovery and Preliminary Results . . . . .</b>	<b>123</b>
5.2.1 Photometry: Kepler K2 . . . . .	124
5.2.2 Photometry: ULTRACAM . . . . .	127
5.2.3 Photometry: Brown Dwarf Spectral Type . . . . .	128
5.2.4 Spectroscopy: FORS . . . . .	129
<b>5.3 Follow-up Spectroscopy . . . . .</b>	<b>131</b>
5.3.1 GMOS: Design and Observing Strategy . . . . .	131

5.3.2	GNIRS: Design and Observing Strategy . . . . .	134
5.3.3	Data Reduction . . . . .	134
5.4	Results . . . . .	136
5.4.1	Radial Velocity . . . . .	136
5.4.2	Follow-Up on the Brown Dwarf Spectral Type . . . . .	139
5.4.3	$T_{\text{eff}}$ and $\log g$ Calculation . . . . .	141
5.4.4	Light Curve Fitting . . . . .	142
5.5	Discussion . . . . .	142
5.6	Summary . . . . .	148

**Chapter 6 NOI-101535 and NOI-103465: Two Newly Discovered Eclipsing WD+MS Systems in NGTS** **150**

6.1	The Next Generation Transit Survey . . . . .	151
6.1.1	NGTS Design . . . . .	152
6.1.2	NGTS Observing Strategy and Operations . . . . .	153
6.1.3	Data Storage and Reduction . . . . .	156
6.1.4	Transit Detection . . . . .	157
6.2	Two New Eclipsing White Dwarf + main sequence Star Systems	158
6.3	NOI-101535 . . . . .	161
6.3.1	Optical Observations . . . . .	161
6.3.2	Results: Light Curve Fitting . . . . .	172
6.3.3	Results: Radial Velocity Measurements . . . . .	175
6.3.4	Results: M-Dwarf Spectral Type . . . . .	179
6.3.5	Results: Final Parameters . . . . .	180
6.3.6	Discussion . . . . .	186
6.3.7	Summary . . . . .	187
6.4	NOI-103465 . . . . .	189
6.4.1	Optical Observations . . . . .	189
6.4.2	Results: Radial Velocity Measurements . . . . .	197
6.4.3	Results: White Dwarf Parameters . . . . .	202
6.4.4	Results: Light Curve Fitting . . . . .	204
6.4.5	Results: Final Parameters . . . . .	206
6.4.6	Discussion . . . . .	207
6.4.7	Summary . . . . .	210

<b>Chapter 7</b>	<b>Conclusions and Future Applications</b>	<b>212</b>
7.1	Chapter 3: The SAAO DAZ Survey . . . . .	213
7.1.1	Future Work . . . . .	214
7.2	Chapter 4: WD1201-049 . . . . .	214
7.2.1	Future Work . . . . .	215
7.3	Chapter 5: WD1032+011, a New WD+BD system . . . . .	216
7.3.1	Future Work . . . . .	217
7.4	Chapter 6: NOI-101535 and NOI-103465 . . . . .	217
7.4.1	NOI-101535 . . . . .	218
7.4.2	NOI-103465 . . . . .	218
7.4.3	Future Work . . . . .	219
7.5	Final Remarks . . . . .	220

# List of Tables

3.1	A list of astrometric and physical properties, as well as observation details for the surveyed metal-rich white dwarfs. . . . .	71
3.2	Minimum detectable transit depth for white dwarfs of different brightnesses in my sample. . . . .	73
3.3	Cumulative detection probability for each of the sampled observing windows. The predicted number of detected planets is also shown, as a result of applying the actual 1% chance of detecting a planet around a white dwarf to the simulated data.	75
3.4	A table showing dates and lengths of all photometric follow-up observations of SDSS J1617+1620. . . . .	81
4.1	Photometry and literature parameters for WD1201-049. . . . .	86
4.2	Parameters for the available SpUpNIC gratings (Crause et al., 2016). . . . .	90
4.3	Observing details and weather conditions for WD1201-049 spectroscopy with SpUpNIC. . . . .	92
5.1	Photometry and literature parameters for WD1032+011. . . . .	124
5.2	ULTRACAM observations of WD1032+011 . . . . .	127
5.3	WD1032+011AB parameters from fitting the mass function. . . . .	144
5.4	WD1032+011AB final parameters. . . . .	145
6.1	Stellar Properties for NOI-101535 . . . . .	163
6.2	Observations taken using KOSMOS on the 4m Mayall Telescope	173
6.3	Radial velocity fitting parameters for NOI-101535. . . . .	175
6.4	Radial velocity fitting parameters for NOI-101535. . . . .	177

6.5	Calculated masses, radii and orbital separation for the NOI-101535 system components. . . . .	185
6.6	Stellar Properties for NOI-103465 . . . . .	190
6.7	Observations taken using SpUpNIC on the 1.0 m SAAO telescope.197	
6.8	Radial velocity fitting parameters for NOI-103465. . . . .	199
6.9	Radial velocity fitting parameters for NOI-101535. . . . .	204
6.10	Calculated masses, radii and orbital separation for the NOI-101535 system components. . . . .	206

# List of Figures

1.1	Photospheric chemical abundances of metal-polluted white dwarfs from Gänsicke et al. (2012). The four panels show a range of different metal-to-Si ratios for four metal polluted white dwarfs. These are compared to the abundances of bulk-Earth (BE) and silicate-Earth (BSE) from McDonough (2000); solar abundances (S) and CI chondrites (CI) from (Lodders, 2003) and several meteorite classes from Nittler et al. (2004) (carbonaceous chondrites in grey, mesoderites in green, pallasites in blue, diogenites in red, howardites in orange and eucrites in magenta). The light blue data points show abundances for polluted white dwarfs GD362 (Zuckerman et al., 2007), GD 40 (Jura et al., 2012) and HS 2253+8023 (Klein et al., 2011). . . . .	11
1.2	The habitable zone (blue region) of a $0.6 M_{\odot}$ white dwarf as a function of the white dwarf age and the planet orbital distance. The white dwarf effective temperatures and luminosities are indicated on the right, and the planet orbital periods are shown on the top of the top of the graph. The dashed line represents the Roche limit for an Earth-density planet. The dotted line indicates the limit past which a planet would remain in the habitable zone for less than 3 Gyr (Agol, 2011). . . . .	13
1.3	A simulation of a $0.6 M_{\odot}$ white dwarf being eclipsed by a $1 M_{\oplus}$ planet (black line) and a $10 M_{\oplus}$ planet at an orbital distance of 0.1 AU (Kilic et al., 2013). . . . .	16

2.1	An example, from SHOC data, of the aperture photometry parameters. The annulus, used to measure the background counts, is represented by the inner and outer red circles, while the aperture, used to measure the source counts, is displayed as a green circle around the targeted star. . . . .	30
2.2	An example of the signal-to-noise as a function of aperture. This plot was used to determine the aperture size to be employed by the aperture photometry software. . . . .	31
2.3	An example of light curve of white dwarf EC11246-2923, after performing aperture photometry, using an aperture of 8 pixels. The plot shows several drops in brightness. . . . .	33
2.4	The same light curve of white dwarf EC11246-2923 as shown in Figure 2.3, after performing differential photometry using three comparison stars. . . . .	35
2.5	In panel [b] I fitted a second-degree polynomial function (red line) in agreement with the airmass shape (shown in panel [a]). I subsequently divided my data set by the polynomial in order to eliminate airmass effects. . . . .	37
2.6	An example of SHOC data analysed using JKTEBOP (Popper and Etzel, 1981; Etzel, 1981; Nelson and Davis, 1972; Southworth et al., 2004), which provided some of the physical parameters of the system, such as fractional radii and inclination. The top panel shows the model fit to the data (green line), while the bottom panel shows the residuals (model - data). . . . .	38
2.7	A section of one of the SpUpNIC flat frames. The overscan regions (black) can be seen on both sides of the image. These are created as part of the CCD read-out process, and do not represent actual CCD pixels. . . . .	40
2.8	A section of the SpUpNIC master bias frame used in the reduction of WD1201-049. This is the result of an average of one hundred bias frames collected during the observing run. . . . .	41

2.9	Section of the master flat frame used in the reduction of SpUpNIC data. This was the result of averaging thirty individual frames, as well as eliminating the wavelength dependent effects caused by the lamp illumination and the instrument itself. . .	43
2.10	A section of a SpUpNIC spectrum, which has been bias- and flat-calibrated, as seen on the CCD before extraction. In this image, wavelength and flux calibrations have not yet been applied. The wavelength dispersion axis runs vertically along the spectrum (top to bottom), while the spatial axis lays horizontally (left to right). . . . .	45
2.11	Example of a newly extracted spectrum, before wavelength calibration. . . . .	46
2.12	Example of an extracted arc spectrum from the SpUpNIC observation of a CuAr calibration lamp. . . . .	47
2.13	Example of a wavelength calibrated spectrum obtained using SpUpNIC. . . . .	49
2.14	Example of a flux calibrated spectrum obtained using SpUpNIC	50
2.15	Example of a reduced spectrum from SpUpNIC data, before normalisation. The red regions represent the sections masked out during the fitting. The green line represents the polynomial function used to normalise the spectra. . . . .	52
2.16	The same spectrum shown in Figure 2.15, after normalisation was applied. As expected, the continuum level is at $\sim 1$ mJy. .	53
2.17	An example of a $H\gamma$ emission line (grey) being shifted both in the red and the blue direction compared to its rest wavelength (green vertical line). The red line represents the models fit to the line to measure its radial velocity. . . . .	56
2.18	An example of fitting performed by MGFIT. Here, the $H\gamma$ Balmer line presents both emission and absorption, and the features are fitted simultaneously. The emission and absorption lines were fitted with one and two Gaussians respectively. . . .	57

2.19	An example of trailed spectrum for H $\gamma$ . Each horizontal line represents one spectrum. In the spectrum, the emission line is clearly visible in shades of green/blue. The x-axis shows the radial velocity of the line, centred at the rest wavelength of 4340.462 Å for H $\gamma$ . . . . .	58
3.1	A schematic (not to scale) of SHOC setup and mount on one of the SAAO telescopes (Coppejans et al., 2013). . . . .	63
3.2	A schematic (not to scale) diagram of the different plane inclinations in which a planetary system around a white dwarf may be found. Panel a) represents the best inclination ( $i = 90^\circ$ ) required to detect a transiting planet; at this angle, none of the infra-red excess light emitted by the disc would be detected. Panel b) shows the best inclination ( $i = 90^\circ$ ) required to maximise the detected infra-red flux from the disc; a system in such inclination would present no sign of planetary eclipses. Panel c) shows an example of inclination at which both the planet and the disc could be detected: the planet is still eclipsing the star, and some of the infra-red excess from the disc is measurable. . . . .	67
3.3	A plot of the probability of detecting a transit around a white dwarf for observing windows ranging between 1 and 7 hours, as function of the orbital period. The range of orbital periods was chosen based on the extent of the Habitable Zone of 0.6 M $_{\odot}$ white dwarf, as well as on the period of WD1145+017. . . . .	76
3.4	A light curve of the photometric data collected for SDSS J1617+1620 on 10 July 2017. A clear, $\sim 1\%$ peak-to-peak variation is noticeable in the data. The pink data points represent the unbinned data collected. The blue data points show the data binned to intervals of 10 minutes. . . . .	79
3.5	A plot of SDSS J1617+1620 discrete Fourier Transform. The red dashed line represents the $3\langle A \rangle$ limit, while the blue dotted line represents the $4\langle A \rangle$ limit. . . . .	80

4.1	A diagram for SpUpNIC. The upper and lower boxes are represented by the dark green section and the black section respectively. The optical elements of the instrument are shown in blue, the electronic parts are red, and the lamps are light green. The yellow area represents the instrument frame attached to the telescope, which is coloured in orange (Crause et al., 2016).	88
4.2	Examples of field of view (FOV) of the observations of WD1201-049 in white light (a) and I filter (b). In both panels, the target is circled in green and the comparison stars employed in differential photometry are marked with numbers from 1 to 3. . . .	93
4.3	Calibrated light curve of WD1201-049, observed in white light. The pink data points represent the unbinned data collected. The blue data points show the data binned to intervals of 10 minutes. The light curve shows a sinusoidal modulation, with peak-to-peak amplitude of $\sim 2\%$ . . . . .	95
4.4	Periodogram of WD1201-049, as seen in white light. The red dashed line represents the $3\langle A \rangle$ limit, while the blue dotted line shows the $4\langle A \rangle$ limit. . . . .	96
4.5	A plot of the calibrated and normalised light curves for WD1201-049 (black), and Comparison stars 1 (green), 2 (blue) and 3 (red).	98
4.6	Periodograms for comparison star 1, 2 and 3 (top, middle and bottom panels respectively). The red dashed lines represent the $3\langle A \rangle$ limit, while the blue dotted lines show the $4\langle A \rangle$ limit. All three stars show a significant peak at $\sim 6$ hours. . . . .	99
4.7	An example of the MGFIT model (red) applied to the $H\beta$ line (dark grey). In order to reproduce the shape of the line, three Gaussian functions were fitted simultaneously. The continuum was fitted with a first-degree polynomial pivoted at the central wavelength. . . . .	101
4.8	Trailed SpUpNIC spectra centred on the $H\beta$ absorption line. The plots show the data (left panel), the model generated from the Gaussian fitting (central panel) and the residuals to the fit (right panel). . . . .	102

4.9	Calibrated light curve of WD1201-049, observed in the I filter. The pink data points represent the unbinned data collected. The blue data points show the data binned to intervals of 10 minutes. The light curve shows no sign of sinusoidal variation.	104
4.10	Periodogram of WD1201-049, as seen in the I filter. The red dashed line represents the $3\langle A \rangle$ limit, while the blue dotted line shows the $4\langle A \rangle$ limit.	105
4.11	Model spectrum of a $T_{\text{eff}} = 57,200$ K, $\log g = 7.61$ DAO white dwarf fitted to the photometric data from <i>Galex</i> (stars), PAN-STARRS (triangles) and VISTA (circles) of WD1201-049.	107
4.12	Trailed SpUpNIC spectra centred at the C IV line ( $\lambda = 4658$ Å) discussed by Gianninas et al. (2010). The trail does not show any evidence of C IV at this wavelength.	109
5.1	A schematic of the Kepler Space Telescope (from the NASA Kepler Instrument Handbook).	118
5.2	The proposed – and ultimately observed – Kepler K2 campaigns. The Kepler mission had to be repurposed after the failure of two reaction wheels. Each K2 campaign was observed for $\sim 80 - 90$ days (Image credits: <a href="https://keplerscience.arc.nasa.gov/">https://keplerscience.arc.nasa.gov/</a> ).	120
5.3	The phase-folded K2 light curve of WD1032+011, on a period of $\sim 0.092$ days. The plot displays two periods for clarity. Eclipse-like features are clearly present, although they appear shallower and broader than they are in reality, due to K2 long cadence of 29.4 minutes.	125
5.4	The binned and phase-folded K2 light curve of WD1032+011, on a period of $\sim 0.092$ days. The plot displays two periods for clarity. The primary eclipse feature is evident. No sign of a secondary eclipse (which should appear at phase 0.5) is present.	126
5.5	SDSS spectrum of WD1032+011 matched to various white dwarf + brown dwarf template spectra. The <i>Galex</i> (stars), SDSS (triangles) and UKIDSS (diamonds) magnitudes are also shown.	130

5.6	FORS trailed spectra (sorted in order of phase) of the $H\beta$ line for WD1032+011. A clear sinusoidal movement can be seen in the trail. However, as the spectra were collected as part of a bad-weather programme, the resolution was not high enough to fit the spectra and extract a radial velocity measurement. . . .	132
5.7	A diagram representing the main structure and components of GMOS (from the GMOS fact sheet). . . . .	133
5.8	A diagram representing the main structure and components of GNIRS (from the GNIRS fact sheet). . . . .	135
5.9	An example of the ‘mgfit’ fit to the $H\alpha$ absorption line of WD1032+011. I used a combination of three Gaussian functions to produce the model, which was then fit to all the 24 GMOS spectra. . . . .	137
5.10	Trailed GMOS spectra (in order of phase) centred on the $H\alpha$ absorption line. The plots show the data (left panel), the model generated from the Gaussian fitting (central panel) and the residuals to the fit (right panel). . . . .	138
5.11	GNIRS infrared spectrum of WD1032+011 matched to various white dwarf + brown dwarf template spectra. The SDSS (triangles) and UKIDSS (diamonds) magnitudes are also shown. .	139
5.12	GNIRS infrared spectrum of WD1032+011 matched to various white dwarf + brown dwarf and white dwarf + late M-dwarf template spectra, zoomed in to the near-infrared. The SDSS (triangles) and UKIDSS (diamonds) magnitudes are also shown.	140
5.13	ULTRACAM light curve in $u'$ (top), $g'$ (middle) and $r'$ (bottom) bands, shown with their best fitting models and respective residuals. The system totally eclipses in all three bands (Casewell et al., in prep.). . . . .	143
5.14	Best fit (red line) to the combined FORS spectrum of WD1032+011. The best fitting model is $T_{\text{eff}} = 10196 \pm 235$ K and $\log g = 7.81 \pm 0.07$ . . . . .	146

5.15	The mass-radius relation for the brown dwarf in WD1032+011. In the plot, different isochrones from Baraffe et al. (2015) are shown as solid and dashed lines. The black pentagon represents WD1032+011, while the two black circles represent the only other eclipsing white dwarf + brown dwarf systems. The rest of the objects plotted represent known main sequence star + brown dwarf systems. . . . .	147
6.1	The two arrays of 20 cm telescopes used at the NGTS facility (Wheatley et al., 2014). . . . .	154
6.2	Trailed spectra of SDSS J013851.54-001621.6, centred on the Ca II line at 3934 Å. Emission is seen from both the white dwarf (stronger line with smaller amplitude) and the M-dwarf (weaker line with larger amplitude). The red lines track the motion of each component (Parsons et al., 2012a). . . . .	160
6.3	NGTS light curve for NOI-101535. The top panel shows the initial BLS fitting (green line). . . . .	162
6.4	Simultaneous observations of the primary eclipse of NOI-101535 from the SAAO 1.0 m and 1.9 m facilities in the $z'$ band (red) and $V$ band (green) respectively. . . . .	165
6.5	NITES observations of the primary eclipse of NOI-101535 in $I$ band. . . . .	166
6.6	Eulercam observations of the primary eclipse of NOI-101535 in ZG band. . . . .	167
6.7	A three-colour image from SkyMapper showing NOI-101535 (red star, marked with crosshair) and its close, K-dwarf neighbour (green star to the north). . . . .	169
6.8	The centroid position shift in the x-direction (bottom panel) during a primary eclipse of NOI-101535 observed in the NGTS data (top panel). The image is directly taken from the OPIS database. The x-axis shows the phase of the system, while the y-axis shows relative flux (top panel) and centroiding shift (bottom panel). . . . .	170

6.9	The extracted red and blue WiFeS spectra for the K-dwarf neighbour to NOI-101535 (Star A) and for the target itself (Star B). . . . .	171
6.10	Light curve fitting of SAAO data in $V$ band (top panel) and $z'$ band (bottom panel), and NITES data in $I$ band (middle panel). All three plots are maintained at the same flux scale to show the difference in eclipse depth in the different filters. Although only the eclipse is depicted in these plots, all data points in the light curve were used to determine the flux level. The residuals for each light curve represent the model fit - the data. . . . .	174
6.11	An example of MGFIT model fit to the $H\beta$ emission and absorption lines in one of the KOSMOS spectra of NOI-101535. .	177
6.12	Trailed KOSMOS spectra (in order of phase) of NOI-101535, centred on the $H\beta$ emission and absorption lines. The plots show the data (left panel), the model generated from the Gaussian fitting (central panel) and the residuals to the fit (right panel). . . . .	178
6.13	WiFeS spectrum and SkyMapper $ugriz$ photometry compared to the combined SED of a $T_{\text{eff}} = 7000$ K and $\log g = 8$ white dwarf and multiple M-dwarf type spectra. The data best fits with an M4 spectral type. . . . .	181
6.14	WiFeS spectrum and SkyMapper $ugriz$ photometry compared to the combined SED of a $T_{\text{eff}} = 7500$ K and $\log g = 8$ white dwarf and multiple M-dwarf type spectra. The data best fits with an M4 spectral type. . . . .	182
6.15	WiFeS spectrum and SkyMapper $ugriz$ photometry compared to the combined SED of a $T_{\text{eff}} = 8000$ K and $\log g = 8$ white dwarf and multiple M-dwarf type spectra. The data best fits with an M4 spectral type. . . . .	183

6.16	WiFeS spectrum and SkyMapper <i>ugriz</i> photometry compared to the combined SEDs of an M4 dwarf with white dwarfs spectra of $T_{\text{eff}} = 8000$ K (top), $T_{\text{eff}} = 7500$ K (middle) and $T_{\text{eff}} = 7000$ K (bottom). The data best fits with a $T_{\text{eff}} = 7500$ K and $\log g = 8$ white dwarf. . . . .	184
6.17	Mass-radius plot for the white dwarf component in NOI-101535. The black solid, dashed and dotted lines represent tracks from Renedo et al. (2010) for a $T_{\text{eff}} = 7500$ K, $T_{\text{eff}} = 5000$ K and $T_{\text{eff}} = 3000$ K white dwarf respectively. . . . .	187
6.18	Mass-radius plot for the M-dwarf component in NOI-101535. The black solid and dashed lines represent the 8 Gyr and 5 Gyr isochrones respectively from Baraffe et al. (2015). The blue star-shaped data point shows the M dwarf in SDSS 0138-0016 (Parsons et al., 2012a), the only WD + M-dwarf systems in which the white dwarf has a temperature cooler than 4000 K. The black error bars represent other M-dwarfs in eclipsing PCEBs from Pyrzas et al. (2012); Parsons et al. (2012c,b) and Beatty et al. (2007). Finally, the green error bars show M-dwarfs in double M-dwarf binaries from Leinert et al. (1990) and Wilson et al. (2017) . . . . .	188
6.19	NGTS light curve for NOI-103465. The top panel shows the initial BLS fitting (green line). . . . .	191
6.20	SHOC light curve for NOI-103465 in <i>I</i> band. . . . .	192
6.21	SHOC light curve for NOI-103465 in <i>V</i> band. Just before the eclipse, a flare feature is visible, indicating activity in the MS star's atmosphere. . . . .	193
6.22	Phase folded and binned NGTS light curve from the OPIS database. The plot shows relative flux for the even (blue) and odd (red) eclipses as a function of phase. A significant asymmetric reflection effect can be observed between eclipses. . . . .	194
6.23	Eulercam light curve for NOI-103465 in <i>R</i> band. Just after the eclipse, a flare feature is visible, indicating activity in the MS star's atmosphere. . . . .	196

6.24	One of the SpUpNIC spectra collected at SAAO. Prominent broad absorption features related to the white dwarf can be observed at $H\beta$ , $H\gamma$ , $H\delta$ and $H\epsilon$ , as well as narrow emission lines at the same wavelengths, related to the active main sequence companion. . . . .	198
6.25	An example of model fit performed by MGFIT to the $H\gamma$ emission and absorption lines in one of the spectra of NOI-103465 collected at SAAO. . . . .	200
6.26	Trailed SpUpNIC spectra of NOI-103465, centred on the $H\gamma$ emission and absorption lines. The plots show the data (left panel), the model generated from the Gaussian fitting (central panel) and the residuals to the fit (right panel). . . . .	201
6.27	An example of model fit performed through XSPEC to the $H\delta$ and $H\epsilon$ absorption lines in one of the spectra of NOI-103465 collected at SAAO. This fit estimated a $T_{\text{eff}}$ and $\log g$ of 18,000 K and 8.48 respectively. . . . .	203
6.28	Light curve fitting of SAAO data in $V$ band (top panel) and $I$ band (bottom panel), and Eulercam data in $R$ band (middle panel). All three plots represent the primary eclipse, and are maintained at the same flux scale to show the difference in eclipse depth in the different filters. The residuals under each light curve represent the difference between the model fit and the data. . . . .	205
6.29	Hertzsprung-Russell Diagram of stars in Gaia DR2 (Gaia Collaboration et al., 2018a) . . . . .	208

# Chapter 1

## Introduction

### 1.1 Overview

97% of the stars present in our Galaxy will end their lives as white dwarfs, making these objects the most common type of stellar remnant. It is therefore crucial to understand the processes that lead to the formation of such remnants, as well as the consequences that these processes will have on pre-existing planetary systems orbiting their progenitor stars.

Since the discovery of the first extrasolar planet (Wolszczan and Frail, 1992), thousands of planets have been discovered orbiting other stars. To date (August 2019), [www.exoplanets.org](http://www.exoplanets.org) reports 3262 confirmed planetary systems, and 2485 that appear as candidates from the Kepler mission. The vast majority of these planets are found orbiting main sequence stars, and in some cases they are observed around evolved stars (Lee et al., 2013; Ciceri et al., 2015), and even in extreme environments like in the case of pulsar PSR 1257+12 (Wolszczan and Frail, 1992).

To date, no planets have been observed around a white dwarf star. This

is most likely due to the physical characteristics of these systems, which pose limitations on their chance of being observed, as well as the precision of such observations. Nevertheless, many large-scale surveys have been undertaken in the last decade, such as the DODO (Degenerate Object around Degenerate Object) survey (Burleigh et al., 2008; Hogan et al., 2009), The SuperWASP survey (Faedi et al., 2011), the Pan-STARRS1 survey (Fulton et al., 2014) and the DECam Minute-cadence survey (Belardi et al., 2016; Dame et al., 2019). Discovering a planetary system around a white dwarf would not only provide us with precious information on the fate of planetary systems beyond the main sequence, but would also give us a better opportunity to study the characteristics of extrasolar planets, thanks to the low luminosities of these stellar remnants.

In the following sections, I will provide a brief outline to white dwarfs and their characterisation. I will also discuss the properties of metal-rich white dwarfs and debris discs found orbiting such stars. I will then discuss the characteristics of sub-stellar companions to white dwarfs (such as brown dwarfs and planets) and other sources of variability in the light curves of these stellar remnants.

## **1.2 White Dwarfs**

### **1.2.1 Evolution of White Dwarfs**

When an average,  $M < 8 M_{\odot}$  main sequence star exhausts all the hydrogen in its core by fusing it into helium, hydrostatic equilibrium is no longer maintained and the stellar core will start to cool and collapse under gravitational pressure

(Schönberg and Chandrasekhar, 1942).

At this stage, the gravitational energy driving the collapse is converted into thermal energy, which results in an increase in temperature in the core of the star. The rising temperature in and around the core then accelerates the hydrogen burning processes in the shell directly surrounding it. As the newly fused helium falls towards the core, the central mass increases, resulting in further contraction and hence even higher temperatures. As a consequence of the increased energy, the outer layers of the star will expand. The star's brightness will increase by a factor of  $\sim 100$ , while the surface temperature will decrease. This stage is known as the Red Giant Branch (RGB) of stellar evolution.

During this stage, the outer layers will be cool enough for convection to occur. The convective layers will then feed hydrogen into the burning shell surrounding the core, which will subsequently release newly created helium into the contracting core. The temperature in the centre of the star will then increase until helium can finally be fused into heavier elements. At this stage, the fusion processes will re-establish hydrostatic equilibrium and the core will slowly expand, lowering the temperature of the hydrogen-burning shell and causing the outer layers of the star to contract. The star hence enters the Horizontal Branch (HB) of its evolution and will maintain this stage until all the helium in the core is depleted.

At the end of this phase, the star will undergo a second giant-stage, in which the core will contract increasing the temperature in the surrounding shell and thus igniting helium-burning within it. The outer layers of the star will expand again, and the star will enter the Asymptotic Giant Branch (AGB) stage until all helium in the burning shell is consumed and the outer layers

contract for a second time.

A short phase of helium flashes or pulses follows, in which the contracting layers feed more helium ash to the helium shell shortly reigniting the process.

Eventually all burning will cease, and as the core continues to contract, the outer layers will continue to expand until they are no longer gravitationally bound to the core, forming a planetary nebula. Due to the lack of nuclear fusion in the core, the star will no longer generate energy, and it will therefore start to release its thermal energy over billions of years. As the core continues to collapse, the density of electron gas will rise, and the electrons will tend to occupy higher energy levels. No quantum state can be occupied by more than one electron due to the Pauli Exclusion Principle. Once all the states are filled, there will be a resistance against further contraction, known as the electron degeneracy pressure. As this pressure becomes greater than the inward gravitational pull, the star's core will cease to shrink, hydrostatic equilibrium will be once again achieved and a white dwarf will be born (Fowler, 1926).

### **1.2.2 Characterisation of White Dwarfs**

Depending on the initial mass of the progenitor main sequence star, these remnants will have temperatures ranging between  $\sim 200,000$  K (Werner and Rauch, 2015) and  $< 5,000$  K (Hodgkin et al., 2000), masses ranging between  $0.4 M_{\odot}$  and  $1.4 M_{\odot}$  (Chandrasekhar, 1931), and sizes comparable to that of Earth.

The atmospheres of most white dwarfs consist of a thin layer that makes up for  $\sim 0.01\%$  of its total mass. The rest of their mass consists of electrons,

oxygen and carbon (or helium, in some cases) ions, condensed in the core as a plasma.

The main elements present in the atmosphere of a white dwarf are detectable from their characteristic absorption features in the star's spectral profile. These enable us to classify what type of white dwarf is being observed. The two most common types are known as DA and DB white dwarfs, depending on whether their atmospheres consist of pure hydrogen or helium, respectively. Other – less frequent – categories include DZ (showing metal lines only), DQ (in which Carbon is present in atomic and/or molecular form) and DC white dwarfs (characterised by a featureless continuum).

Of course, sub-classes do exist. For example, DA and DB objects showing evidence of metal contamination are classified as DAZ and DBZ respectively. The high density of a white dwarf will result in heavier elements sinking to the centre of the star relatively quickly (from days to a few million years), as shown in multiple white dwarf models (Fontaine and Michaud, 1979; Vauclair et al., 1979; Alcock and Illarionov, 1980). It is deduced from these models that DAZ's and DBZ's are rather young and hot objects, unless metals are continually replenished from an outside source (see below). Their higher temperature also signifies higher radiative pressure from the core, which contributes to holding heavier elements on the surface of the white dwarf for longer (Chayer et al., 1995). As the average lifespan of a white dwarf is of at least a few billion years, the sinking process of elements heavier than helium takes place on much shorter timescales and we therefore expect only a minority of white dwarfs to show evidence of metals in their photospheres.

## 1.3 Metal-Rich White Dwarfs

As previously mentioned, some – a few hundred – white dwarfs show evidence of metal contamination in their atmosphere (Vauclair et al., 1979; Fontaine and Michaud, 1979; Alcock and Illarionov, 1980). Since the rate at which heavier elements sink into the core of a white dwarf is relatively quick compared to the star’s lifetime, this means that these metals must originate from a source external to the star.

### 1.3.1 Sources of Metal Contamination in White Dwarfs

A significant proportion of hot (16,000 K – 77,000 K) DA white dwarfs, about 23%, have been found to be polluted with metals (Barstow et al., 2014). For younger, hotter white dwarfs the likelihood of metal contamination due to radiative levitation is higher than for older, cooler ones. If radiative levitation were to be the sole cause for the presence of metals in the atmosphere of a white dwarf, then stars with similar parameters such as temperature and gravity should present similar atmospheric composition. However, similar white dwarfs showed varying levels of contamination, both higher and lower than expected. It was therefore concluded that white dwarfs must have different sources of metal pollution (Barstow et al., 2014).

There are two leading hypotheses to explain the source of atmospheric metals in white dwarfs. The first is accretion of material from the surrounding Interstellar Medium (ISM) (Zeidler-K. T. et al., 1986; Fontaine and Wesemael, 1987; Koester, 1989). However, this presents some issues, as the ISM mainly consists of hydrogen and helium, while metals are present in a much lower proportion. Therefore, if accretion were to originate from the ISM, we would

expect to see evidence of hydrogen being accreted onto the stellar atmosphere. However, the existence of DBZ white dwarfs – which are almost (if not completely) depleted of hydrogen (Aannestad et al., 1993; Wesemael, 1979) –, puts this hypothesis out of discussion. If accretion from the ISM were to happen over a significant amount of time, the accreted hydrogen would not sink to the core of the star over time, and should in fact build up in the star’s atmosphere (Dupuis et al., 1992, 1993a,b).

Another issue with this hypothesis arose from a later study by Farihi et al. (2010) on white dwarfs in close proximity with one another. In the event of travelling through the same ISM region, these objects should show similar levels and types of contamination. However, the study resulted in no evidence of such correlation.

In addition, due to the gravitational sinking times of heavier metals to the core of a white dwarf being of the order of days to a few million years (Paquette et al., 1986), the very existence of DAZ white dwarfs would imply a very recent and/or ongoing accretion. For such accretion rate to happen, there would have to be a very high frequency of dense, metal-abundant ISM regions. This, however, does not match with observations (Welsh et al., 1994, 1999).

Due to these reasons, a second hypothesis has been found to be the most probable explanation to the presence of metals in the atmospheres of some white dwarfs, i.e. accretion from metal-rich bodies orbiting the white dwarf (Jura, 2003; Alcock et al., 1986).

## 1.4 Planetary Systems Around White Dwarfs

As mentioned in section 1.1, there is evidence of planets orbiting stars that have evolved past the main sequence stage. This suggests that some planets may survive the death of their host star, or that they may form from the debris left behind by a supernova explosion in a second planet-formation cycle – e.g. pulsar PSR 1257+12 (Wolszczan and Frail, 1992). It is therefore required to confirm this theory by ascertaining the existence of debris around white dwarf stars.

### 1.4.1 Debris Disks Around White Dwarfs

The first evidence of a debris disc around a white dwarf was published by Zuckerman and Becklin (1987), who detected an infra-red (IR) excess in the spectral energy distribution of white dwarf G 29-38. Since then, it has been observed that at least 4.3% of white dwarfs are hosts for circumstellar gas and dust discs (Barber et al., 2012).

When G 29-38 was first discovered, the IR excess was attributed to the presence of a brown dwarf orbiting the host star. It was only later that models postulated the presence of dusty debris due to a small rocky body, such as an asteroid. It was theorised that the object was disrupted by the star's gravitational pull after being perturbed into an eccentric orbit and having crossed the Roche limit (Jura, 2003). Furthermore, Jura (2003) and Veras et al. (2013) proved that the dust would settle into a thin disk orbiting the star, and that it would accrete onto the white dwarf's atmosphere over time. The accretion explains the presence of heavier elements polluting the atmospheres of some white dwarfs, and the presence of a disc being irradiated by the hot

host star provides an explanation for the IR emission in the stellar spectral profile.

Further evidence of the existence of discs around white dwarfs was provided by Gänsicke et al. (2006b), who identified broadened emission lines of Calcium in a sample of white dwarfs observed by the Sloan Digital Sky Survey (SDSS). The broadening of these lines confirmed the presence of a rotating gaseous disc around the star. It was furthermore demonstrated that the emission was originating from within the Roche limit of the white dwarf, thus consolidating the hypothesis of the disc being formed as a consequence of a disrupting rocky body.

In order for disruption to happen, a planetesimal has to spend at least part of its orbital phase inside the Roche limit. However, rocky planets and asteroids would not naturally form at such short orbital distances from the white dwarf. Moreover, any star going through the RGB and AGB phase would destroy any planets or asteroids in such short periods. The most credible theory as to why such planetesimals approach and cross the Roche limit is the existence of unseen larger planets, brown dwarfs or stars farther out in the system that perturb the smaller rocky object into an eccentric orbit after the AGB phase of the star's evolution. To further support this theory, it has been found that the abundances of metals in white dwarf photospheres are similar to those of various rocky bodies present in our Solar System (Figure 1.1, Gänsicke et al., 2012). Figure 1.1 shows the chemical abundances of planetary debris around four metal polluted white dwarfs, compared to those of Earth, the Sun and various classes of asteroids in the Solar System. While there are many similarities, the relative abundances of rocky constituents (such as Fe, Si, O and Mg) present quite a lot of scatter among the white dwarfs. This is due

to the fact that these elements may occur in the form of different minerals and compounds (such as metal oxides or water) as well as in their pure form. The abundance of a certain element around a polluted white dwarf is strictly dependent on the processes that the system underwent during its formation and evolution (e.g. Jura and Xu, 2010), and a certain level of diversity is therefore expected (Gänsicke et al., 2012).

## 1.4.2 Planetary Systems Around White Dwarfs

### Theoretical Models

Debris discs already provide evidence for the possible existence of evolved planetary systems around white dwarf stars. It is however crucial to understand how such systems may come to be. During the Kepler Mission, most main sequence stars discovered to be the hosts of planetary systems are found to have planets in short period orbits, and therefore close to their star. If closer than  $\sim 1$  AU to their parent star, these planets will certainly be destroyed and engulfed by the star as it evolves through the RGB phase (Nordhaus et al., 2010; Villaver and Livio, 2007). Due to the transferring of a planet's orbital angular momentum to the star's rotational angular momentum, the orbital distance of the planet will decrease steadily, and the planet will spiral in towards the host star (Livio and Soker, 1984; Sackmann et al., 1993; Siess and Livio, 1999a,b).

Jovian planets that are further out may survive the RGB and AGB phases of the star's evolution. However, planets that are closer than  $\sim 5$  AU may still be partially or completely destroyed during the planetary nebula phase. Once the star's outer layers have finally blown off, the surviving stellar

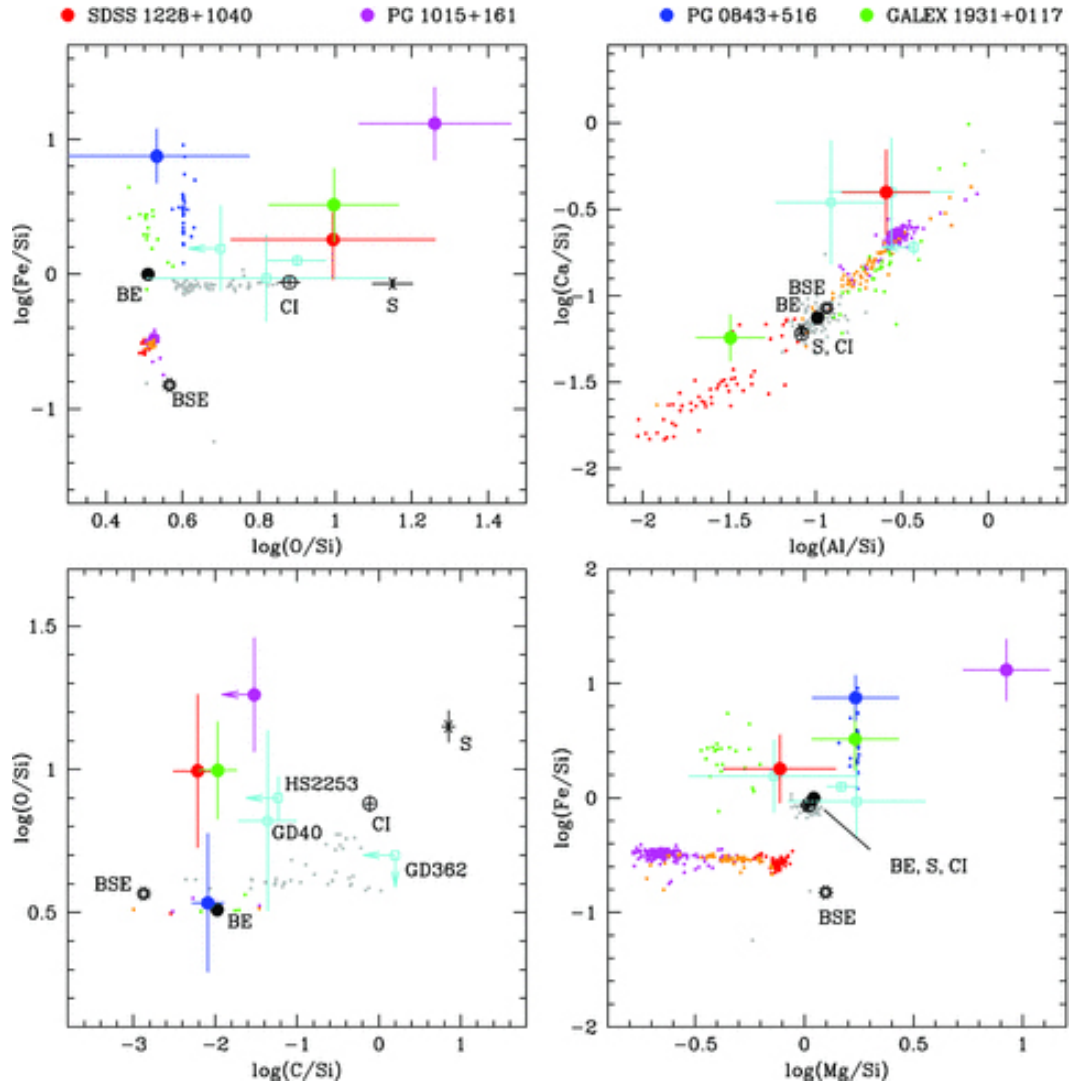


Figure 1.1: Photospheric chemical abundances of metal-polluted white dwarfs from Gänsicke et al. (2012). The four panels show a range of different metal-to-Si ratios for four metal polluted white dwarfs. These are compared to the abundances of bulk-Earth (BE) and silicate-Earth (BSE) from McDonough (2000); solar abundances (S) and CI chondrites (CI) from (Lodders, 2003) and several meteorite classes from Nittler et al. (2004) (carbonaceous chondrites in grey, mesoderites in green, pallasites in blue, diogenites in red, howardites in orange and eucrites in magenta). The light blue data points show abundances for polluted white dwarfs GD362 (Zuckerman et al., 2007), GD 40 (Jura et al., 2012) and HS 2253+8023 (Klein et al., 2011).

core will have temperatures ranging between 100,000 K and 380,000 K. Planetary atmospheres have high optical depths for shorter wavelength fluxes. The planet's atmosphere will heat up and be stripped of its outer layers due to the high-frequency stellar flux reaching it. The outer layers will be replaced by cooler gases found closer to the surface. At this point, the planetary atmosphere will start to radially expand, remaining at subsonic speeds near the surface of the planet, but reaching supersonic speeds in its outer layers, thus creating the perfect 'blow-off' conditions (Rasio et al., 1996; Villaver and Livio, 2007).

Planets at orbital distances greater than  $\sim 5$  AU from their host main sequence star will not be destroyed by the star's expansion during its giant phases (Debes and Sigurdsson, 2002). Jeans (1924) showed that, as a result of the stellar mass-loss, these planets will travel adiabatically to greater orbital distances. This expansion is proportional to the ratio of the host main sequence star mass to that of the final white dwarf. At this point, planetary systems may become unpacked and subsequently start to interact. Veras and Gänsicke (2015) demonstrated that due to these interactions, surviving planetary bodies may migrate inwards, toward short-period orbits around the newly formed white dwarf.

These planets are only shown to survive for a relatively short time, compared to the lifetime of a white dwarf. Hence, in order to find such systems, it is crucial to observe a large number of white dwarfs. Agol (2011) defines  $\eta_{\oplus}$  as the frequency at which Earth-like planets will eclipse white dwarfs. To measure this value to an accuracy of 33% it has been estimated that a minimum of 9 planets has to be detected. Using Poisson statistics, assuming  $\sqrt{N}$ , where  $N=9$ , the above level of accuracy will be reached by sampling at

least 1000 white dwarfs (Agol, 2011). Therefore, these systems are believed to be extremely rare, and the chances of detecting them are very low.

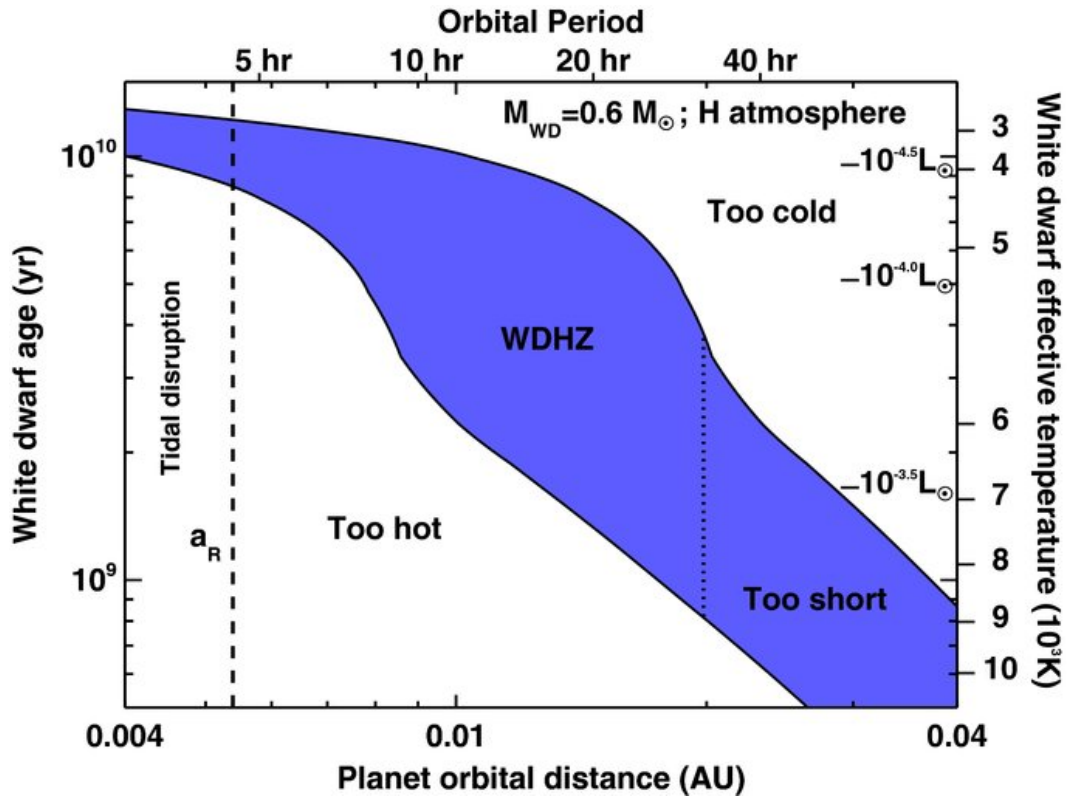


Figure 1.2: The habitable zone (blue region) of a  $0.6 M_{\odot}$  white dwarf as a function of the white dwarf age and the planet orbital distance. The white dwarf effective temperatures and luminosities are indicated on the right, and the planet orbital periods are shown on the top of the top of the graph. The dashed line represents the Roche limit for an Earth-density planet. The dotted line indicates the limit past which a planet would remain in the habitable zone for less than 3 Gyr (Agol, 2011).

### Habitable Planets

Even though planets in short orbital periods around white dwarf stars may be rare, the aforementioned theoretical models suggest that they would be terrestrial in nature. This, combined to the high surface temperature and long

cooling times of a white dwarf, opens up the possibility of these worlds being habitable.

Agol (2011) investigates the habitable zone of an average,  $0.6 M_{\odot}$  white dwarf, and finds these are significantly extended and long-lived zones, as shown in Figure 1.2. The figure shows how the white dwarf age and temperature, as well as a planet orbital distance – and therefore period – contribute to the possibility of such planets being habitable. Orbital distances of less than 0.002 AU are too close to the star to allow liquid water to survive on the surface of the planet and will also cause the planet to tidally disrupt. Conversely, at distances greater than 0.05 AU the planet will not receive enough heat from the star and water will freeze. In terms of stellar age, younger stars are too hot to allow liquid water to form and survive, while stars that are too old will not provide heat for long enough. At this point, even though water may be found on the surface of the planet, there will not be enough time for life to evolve. The habitable zone of an average white dwarf can hence generally be found for orbital periods between 2 and 30 hours, with a maximum duration of  $\sim 8$  Gyr at an orbital distance of about 0.01 AU. These shorter periods are very advantageous for ground observations, as they significantly increase the chances of detecting a planet transiting a white dwarf.

### **1.4.3 Transiting Planets Around White Dwarfs: Surveys**

One of the most successful ways of detecting planets around other stars is by looking for photometrical changes in the light curve of the host star. This has been performed in a variety of surveys, both ground- (such as WASP, Pollacco

et al., 2006) and in space-based (e.g. the Kepler missions, Borucki et al., 2010; Howell et al., 2014). The probability of finding a planet eclipsing its host star is limited, and the small size of white dwarfs decreases this probability even further, since the viewing angle for an eclipse to be observed is reduced.

For a solar type star, the expected drop in luminosity when a planetary eclipse occurs is very small, with a depth of  $\sim 1\%$  for a Jupiter-like planet. However, as the radius of an average white dwarf is only  $\sim 40\%$  greater than that of Earth, this number is due to increase significantly in the event of an eclipse. Indeed, for a standard  $0.6 M_{\odot}$  white dwarf, a  $1 M_{\oplus}$  planet orbiting at a distance of 0.1 AU would produce eclipses of  $\sim 40\%$ , while a  $10 M_{\oplus}$  planet at the same distance would completely eclipse the star, as shown in Figure 1.3 (Kilic et al., 2013).

Furthermore, Figure 1.3 shows an eclipse duration of  $\sim 2.5$  minutes, which is to be expected due to the size of the star being comparable to that of a planetary body. In comparison, a transit around a main sequence star will last a few hours. Therefore, in order to detect transiting planets around white dwarfs, exposures at short cadences over a large number of objects are required.

Large-scale transit surveys, mainly aimed at finding planets around main sequence stars, have been used in the past in order to constrain the frequency of planets around white dwarfs.

The survey conducted by Faedi et al. (2011) was the first aimed at detecting transiting planets around white dwarfs, using existing data from SuperWASP. A sample of 194 white dwarfs were observed in this survey, with an aim to search for planetary objects orbiting at distances between 0.003 and 0.1 AU (which correspond to orbital periods between 2 hours and 15 days,

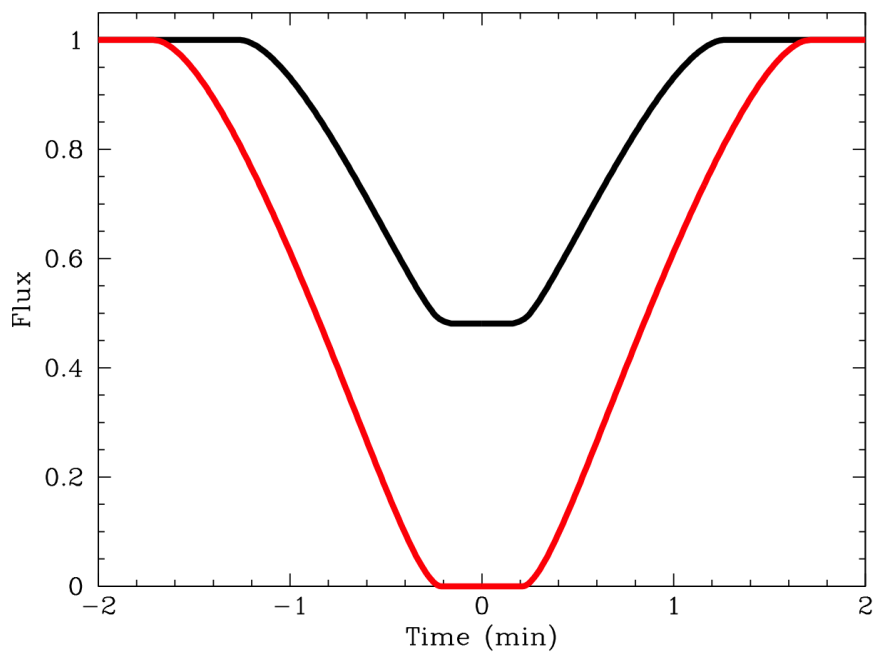


Figure 1.3: A simulation of a  $0.6 M_{\odot}$  white dwarf being eclipsed by a  $1 M_{\oplus}$  planet (black line) and a  $10 M_{\oplus}$  planet at an orbital distance of 0.1 AU (Kilic et al., 2013).

respectively). No planets were detected, most likely due to limitations related to the SuperWASP survey. The survey had a photometric precision of 1-10%, which is low for dim objects such as white dwarfs. Moreover, the observing cadence was not optimal, with one 30s exposure every 8-10 minutes.

However, this survey allowed for constraints to be placed on the occurrence of planetary eclipses in the surveyed periods. Although the detection limit for planets smaller than 1 Jovian radius was poorly constrained due to the aforementioned limitations, it was found that the frequency of gas giants and brown dwarfs in orbits of less than 0.2 days was  $<10\%$  (Faedi et al., 2011).

A second, larger survey was conducted by Fulton et al. (2014). In this instance, 3179 white dwarfs candidates (i.e. not spectroscopically confirmed) present in the Pan-STARRS medium deep fields were monitored in search for eclipsing planets. Although the sample of white dwarfs was much larger, the cadence was even worse than SuperWASP, with only 4-8 exposures per night, with an integration time of 240s each. Similarly to Faedi et al. (2011), no planetary or substellar companions were discovered. However, new constraints on the frequencies of Super-Earths, hot Super-Earths and hot Jupiters in the habitable zone of a white dwarf were placed at less than 3.4%, 1.5% and 0.5% respectively.

Although these two studies helped setting upper limits on the frequency of planets orbiting white dwarfs, they were unable to set accurate constraints due to the observing strategy of the surveys not being optimal for white dwarf planetary systems. However, more recent, short-cadence surveys aimed at finding exoplanets may provide us with better information.

As mentioned before, the optimal strategy to detect a planet around a white dwarf is to observe a large number of stars with short cadences. For

this reason, Belardi et al. (2016), followed by Dame et al. (2019), initiated a short cadence survey using the Dark Energy Camera (DECam), an instrument composed of 62 CCDs with a field of view of 3 square degrees. The survey consisted of three separate fields (previously observed in the CFHT Legacy Survey Wide 2<sup>1</sup> field between 2003 and 2008), each observed over 8 half-nights with 70-90 s exposures with overall cadences of 90-110 s, due to the instrument having a  $\sim 20$  s readout time. Belardi et al. (2016) identified 111 white dwarf candidates (using reduced proper motion and colour as proxies for luminosity and temperature respectively) in the first observed field, while Dame et al. (2019) surveyed all 31,732 point sources in the same field. This survey should statistically contain  $\sim 370$  white dwarfs as predicted by the Besançon Galaxy Model (Robin et al., 2003). In both instances, no planetary transit events were observed. When the ongoing analysis on the remaining fields is completed, the number of surveyed white dwarfs will approach  $\sim 1000$ . This will be the largest short-cadence survey aimed at white dwarfs to date, and will provide newer, more accurate constraints on the frequency of planetary and sub-stellar companions to white dwarfs.

## 1.5 Sub-stellar Companions to White Dwarfs

Although no fully formed planet has been discovered to date, a number of sub-stellar objects, known as brown dwarfs, have been identified in close systems with their host white dwarfs. Brown dwarfs are a unique category of objects that are too massive to be classified as planets, but not massive enough to fuse hydrogen into helium in their cores. They are however massive enough

---

<sup>1</sup><https://www.cfht.hawaii.edu/Science/CFHTLS/cfhtlsdeepwidefields.html>

for deuterium burning, which occurs in all objects with masses of at least 11-16.3  $M_{Jup}$  (Spiegel et al., 2011), and hence emit some infra-red radiation. Surveys such as Farihi et al. (2005); Girven et al. (2011); Steele et al. (2011) and Debes et al. (2011) have shown that less than 0.4%-2% of white dwarfs have an excess in the infra-red consistent with the presence of a brown dwarf companion.

To date, a total of nine such systems are known and published (Dobbie et al., 2005; Burleigh et al., 2006; Casewell et al., 2012; Steele et al., 2013; Beuermann et al., 2013; Littlefair et al., 2014; Parsons et al., 2017; ?; Casewell et al., 2018), with only two eclipsing. A new, eclipsing system has been discovered as part of this work, and will be discussed in Chapter 5.

A subset of these systems are known to be part the post common envelope stage, proving that even sub-stellar objects with relatively low masses can survive this stage of binary evolution. These systems will eventually evolve into cataclysmic variables, such as the  $\sim 72$  minute system identified by Parsons et al. (2017) and Rappaport et al. (2017), expected to reach a period of  $\sim 52$  minutes within 250 Myr, thus evolving into the aforementioned stage.

In these systems, the hot white dwarf irradiates the orbiting brown dwarf companion with UV radiation. At such close proximity, the brown dwarf will be tidally locked to its host star, resulting in a significant temperature difference between its star-facing and its dark sides. Casewell et al. (2014) showed that this difference in temperature leads to effects such as H<sub>2</sub> fluorescence and the transfer of heat to the “dark” side by means of strong winds and jet streams.

## 1.6 Variability in White Dwarfs

It has often been assumed that the vast majority of white dwarf stars are photometrically stable. However, photometric surveys such as SuperWASP (Pollacco et al., 2006) helped reveal variability in a significant percentage of white dwarfs, and provided an opportunity to further study these events. In some cases (as it will be discussed below), variability in the light curve of a white dwarf may indicate the presence of a sub-stellar companion, allowing the discovery of planetary systems even though they do not eclipse.

The study of variable white dwarfs may provide us with crucial information about rotation rates of these stars. Some Type Ia supernova models require white dwarfs rotating at fast rates and accreting surrounding material (Hachisu et al., 2012). Furthermore, studying the rate at which white dwarfs rotate provides us with significant information about the transfer of angular momentum between the core and the surface of these objects as they transition off the main sequence.

However, it is difficult to measure these rotation rates. Usually, stellar rotation can be measured from the broadening of the absorption lines in the stellar spectrum. Unfortunately, due to the strong gravitational fields that dominate white dwarfs, their lines are already broadened, and effects of rotation cannot be observed unless the star had been previously characterised.

Other, more effective ways of measuring rotation rates can be extracted by splitting the eigenmodes of pulsating white dwarfs, or by observing photometric variations that are attributable to the white dwarf itself.

### 1.6.1 Pulsating White Dwarfs

HL Tau 76 was the first pulsating white dwarf to be discovered (Landolt, 1968), displaying  $\sim 0.2$  mag variations in a multitude of periods – from a few hundreds to thousands of seconds. Today, hydrogen rich white dwarfs (DA) presenting such variability are known as ZZ Ceti or DAV white dwarfs. Since the discovery of HL Tau 76, pulsations of a similar nature have also been observed in helium white dwarfs (V777 Her or DBV stars) and even in C/O-rich white dwarfs (GW Vir stars). These pulsations are the result of the formation of partial ionisation zones on the photosphere of the star. Internal gravitational and buoyancy forces give rise to non-radial oscillations known as g-modes (Winget et al., 1981). These modes resonate within the surface layers of the white dwarf, causing periodic variations in surface temperature which consequently lead to luminosity variations. This phenomenon occurs at a specific set of temperatures, depending on the composition of the white dwarf. ZZ Ceti stars have temperatures of  $\sim 12,000\text{K}$ ; V777 Her type stars pulsate at  $\sim 25,000\text{ K}$ ; lastly, a temperature of  $\sim 140,000\text{ K}$  is required for GW Vir type stars to pulsate (Fontaine and Brassard, 2008).

### 1.6.2 Magnetic White Dwarfs

Another cause for variability in white dwarfs can be magnetic activity. Holberg et al. (2008) found that  $\sim 5\%$  of white dwarfs have fields stronger than 1 MG (Kawka et al., 2007; Holberg et al., 2008; Kepler et al., 2013), while 10-20% present fields of at least 10 kG. As a result of these magnetic fields, up to 40% of white dwarfs show photometric variability of 0.5% or greater (Lawrie et al., 2013a). This variability allows us to better determine rotation periods of these

stars (Brinkworth et al., 2013; Lawrie et al., 2013a).

Photometric variability in magnetic white dwarfs can have different causes. In high magnetic field environments, it is due to a phenomenon known as magnetic dichroism (Ferrario et al., 1997). In this case, changes in the continuum opacity are detected due to changes in field strength across the surface of the star. In particular, the variability is due to the magnetic field parallel to the direction of a certain ray of light having different opacities for different polarisations, where these polarisations are due to a variable field strength across the surface. These variations across the white dwarf's atmosphere result in photometric modulations, observed as the star rotates. These modulations can be of significant strength, reaching in some cases amplitudes greater than 10% (e.g. Barstow et al., 1995).

On the other hand, for white dwarfs with a weak magnetic field, variability is due to the differential temperature gradient in the atmospheres of these stars. These are older, cooler white dwarfs, and therefore dominated by convection as a source of energy transportation between the stellar core and surface. In DA white dwarfs, this happens at temperatures cooler than 12,000K, while in DB white dwarfs, convection will dominate for temperatures lower than 28,000K (Brinkworth et al., 2005; Maoz et al., 2015). The resulting convective atmosphere allows the existence of stellar spots, which will affect the brightness of the white dwarf as it rotates.

Rotation periods for these objects usually span between a few hours and a few days, with the exception of RE J0317-853, a highly magnetic white dwarf with a period of only 725 seconds (Barstow et al., 1995). However, the cause of this fast rotation period was later attributed to the star being the result of the merger of two low-mass white dwarfs (Ferrario et al., 1997).

Lawrie et al. (2013a) individually analysed a sample of 77 magnetic white dwarfs and noticed a correlation between the intensity of the magnetic field, the rotational speed and the temperature of the star. This evidence helped reinforce the hypothesis that highly magnetic white dwarfs are the result of the merger of two stars in a close binary system, and will therefore be hotter and faster rotating. As the newly formed object ages, the magnetic field will then act as a brake and slow the rotation speed down.

However, some of the objects in the sample analysed by Lawrie et al. (2013a) presented a variability that could not be explained by the aforementioned theories. These were a set of objects that were too hot for spots to form on the surface, but at the same time too cool for magnetic dichroism to occur.

### 1.6.3 Metal Accretion

In the field observed by the original Kepler mission, Holberg and Howell (2011) discovered BOKS53856: a hot ( $\sim 32,500$  K), weakly magnetic ( $\sim 350$  kG) white dwarf showing a photometric variability with  $\sim 5\%$  peak-to-peak amplitude and a period of  $\sim 6.1$  hours. In this case, the variability was not sinusoidal in nature. The hypothesis of a close companion was promptly ruled out, as a very eccentric orbit would be required to achieve the peculiar shape of the light curve, and this would not be expected for objects in such short orbital periods. Moreover, a further investigation of the star revealed no evidence of an infra-red excess in its spectral energy distribution, thus ruling out the presence of a companion.

In the end, Holberg and Howell (2011) concluded that the source of the variability could be due to the white dwarf accreting material onto its atmo-

sphere along the magnetic field lines. Previous evidence of this phenomenon had been given by the first single, metal-rich hot white dwarf to be observed, GD 394 (Holberg et al., 1999; Dupuis et al., 2001; Wilson et al., 2017). This star showed a quasi-sinusoidal photometric variation in the extreme ultraviolet (EUV) which was interpreted as the result of inhomogeneous accretion of metals onto the surface of the white dwarf, resulting in changes in opacity. Ultimately, this located the source of these metals in a reservoir orbiting the star.

#### **1.6.4 Stellar and Sub-stellar Companions**

A study conducted by Maoz et al. (2015) provided additional information on the source of variability in white dwarfs. Their sample consisted of fourteen white dwarfs observed by the Kepler mission, and half of these resulted in showing low-level variability. They concluded that the rotational effects seen in the light curves of these stars were indeed caused by the effects mentioned in sections 1.6.1, 1.6.2 and 1.6.3.

However, similar sinusoidal modulations could be expected in the event of the white dwarf having a companion (Maoz et al., 2015). The variability could in this case be attributed to a number of factors. Firstly, the variations could arise from observing the various orbital phases of the companion as it orbits the white dwarf. A cool companion would in fact reflect some of the radiation incoming from the much hotter white dwarf and produce sinusoidal variations with amplitudes dependent on the companion's albedo. Alternatively, the variability could be due to the absorption and subsequent thermal emission from a close, cool companion. When the period is short, the com-

panion will be tidally locked to its host star, resulting in one half of its surface being constantly irradiated by the white dwarf. This thermal energy is consequently re-emitted, and creates sinusoidal variations as different phases of the companion's orbit are seen. Even though it is similar to the reflection effect mentioned above, the amplitude of these modulations is observed to increase for redder wavelengths. Finally, a stellar-mass companion would induce an orbital motion of the white dwarf and cause a detectable Doppler boosting which will affect the white dwarf's emission. This effect (first observed by Maxted et al. (2000)) is due to the orbital motion of the stars, which causes a shift in their radial velocities. The photon emission is hence modulated and beamed towards the direction of motion (e.g. Bloemen et al., 2011).

After considering all these possible scenarios, it was concluded that the variability of five of the white dwarfs in the sample could have been caused by the presence of a companion (Maoz et al., 2015). However, the observed variations in their light curves could have also been caused by rotational effects, and therefore it was not possible to determine an absolute solution for the variability of these objects.

## 1.7 Purpose of This Thesis

The evolution of planetary systems past the main sequence stage of their host stars is largely unknown.  $\sim 97\%$  of stars will end their lives as white dwarfs, and an increasing fraction of these objects show evidence for planetary system remnants. While hundreds of thousands of main sequence stars have been surveyed in search for planetary systems, only a few thousands of white dwarfs have been sampled in surveys such as the Kepler K2 mission, WASP and PAN-

STARRS.

In this work, I present a search for eclipsing companions to white dwarfs, in search for surviving planetary systems. Following the discovery of the planetary remnants around white dwarf WD1145+017, I undertook a ground-based photometric survey of metal rich white dwarfs, half of which are known hosts to debris discs (Chapter 3), in search for evidence planetary transits. The survey reveals an interesting variability in a hot metal-polluted white dwarf (WD1201-049), and details on this systems are described in Chapter 4. In addition to this ground-based survey, I took part in the analysis of the white dwarf stars present in the 14<sup>th</sup> campaign of the Kepler K2 mission. In this sample, I discovered a new system in which a brown dwarf fully eclipses the white dwarf (Chapter 5 and Casewell et al., in prep.). Finally, in Chapter 7 I present the discovery of two eclipsing post common-envelope binary systems, each involving a white dwarf and a main sequence star, in the Next Generation Transit Survey (Belardi et al, in prep.).

# Chapter 2

## Methods for Reducing and Analysing Data

In this chapter, I will describe the main two methods used to reduce and analyse the data discussed in this work. These techniques will be discussed in a general matter, and specific details about observations (such as dates, cadences, etc.) will be further mentioned in the relevant science chapters.

### 2.1 Photometric Data Reduction

Most of the photometric data presented in this thesis was observed using the Sutherland High-Speed Optical Camera (SHOC), mounted on the 1.0 m telescope at the South African Astronomical Observatory (SAAO). Although other facilities were used in this work – such as the Next Generation Transit Survey (NGTS, Wheatley et al., 2014, 2018) and the Kepler K2 mission (Borucki et al., 2010; Howell et al., 2014) data –, the reduction of the data was not a part of this thesis and therefore will not be discussed in detail.

### 2.1.1 SHOC Data Reduction

Upon collecting data, the SHOC software allows the observer to select the number of exposures one wishes to acquire in series. SHOC then stores individual FITS (Flexible Image Transport System) images from a kinetic series – i.e. from a series of exposures – into a single FITS cube with multiple extensions. Each extension contains one image; however, the single FITS header is applicable to the whole cube.

In order to reduce the data into raw frames, a reduction pipeline was developed by Marissa Kotze<sup>1</sup> at SAAO. This pipeline splits the cube into individual FITS files and updates their headers to include both telescope and GPS timing information. These include pointing, airmass, filters, time of observation (both in UTC and HJD). The pipeline then uses bias and flat field images to create a master bias and a master flat frame, which will then be subtracted from the raw image files to correct them.

## 2.2 Photometric Data Analysis

### 2.2.1 Aperture Photometry

To proceed with analysis after reducing the data, I used a series of packages included in the *Starlink* software (Currie et al., 2014) to perform aperture photometry on the targets.

Aperture photometry is a method employed to extract the brightness (or flux) of a star by measuring the pixel count in an area known as the *aperture*, i.e. a circular region centred on the object. The pixel count from the region

---

<sup>1</sup><https://shoc.sao.ac.za/Pipeline/>

of sky surrounding the object is subsequently averaged and subtracted, to account for the background count rate. To determine its value, the software employs a region of sky contained in the annulus, a ring concentric to the aperture (Figure 2.1).

In order to determine the sizes of both the annulus and the aperture, the software runs an automatic photometry script on the first image of the brightest object in the imaged field using a range of different apertures. The script then extracts the flux, the associated error, the maximum pixel count and the signal-to-noise ratio associated with each of the apertures sampled. The aperture associated with the highest signal-to-noise (see Figure 2.2) is then employed to perform photometry on the rest of the images.

Once the aperture size is determined, the inner and outer limits for the annulus are calculated as the following:

$$Annulus_{inner} = R_{aper} * 2.0 \tag{2.1}$$

$$Annulus_{outer} = R_{aper} * 3.0 \tag{2.2}$$

where  $R_{aper}$  is the radius (in pixels) of the aperture. The outer and inner limits of the annulus are chosen so to minimise the chances of variation in the background level, such as contamination from nearby objects or non-uniform sky brightness.

The last step towards creating a raw light curve of a star consists of extracting the time-stamps for each of the images. This is achieved by extracting the Heliocentric Julian Date (HJD) value from the header of each FITS image.

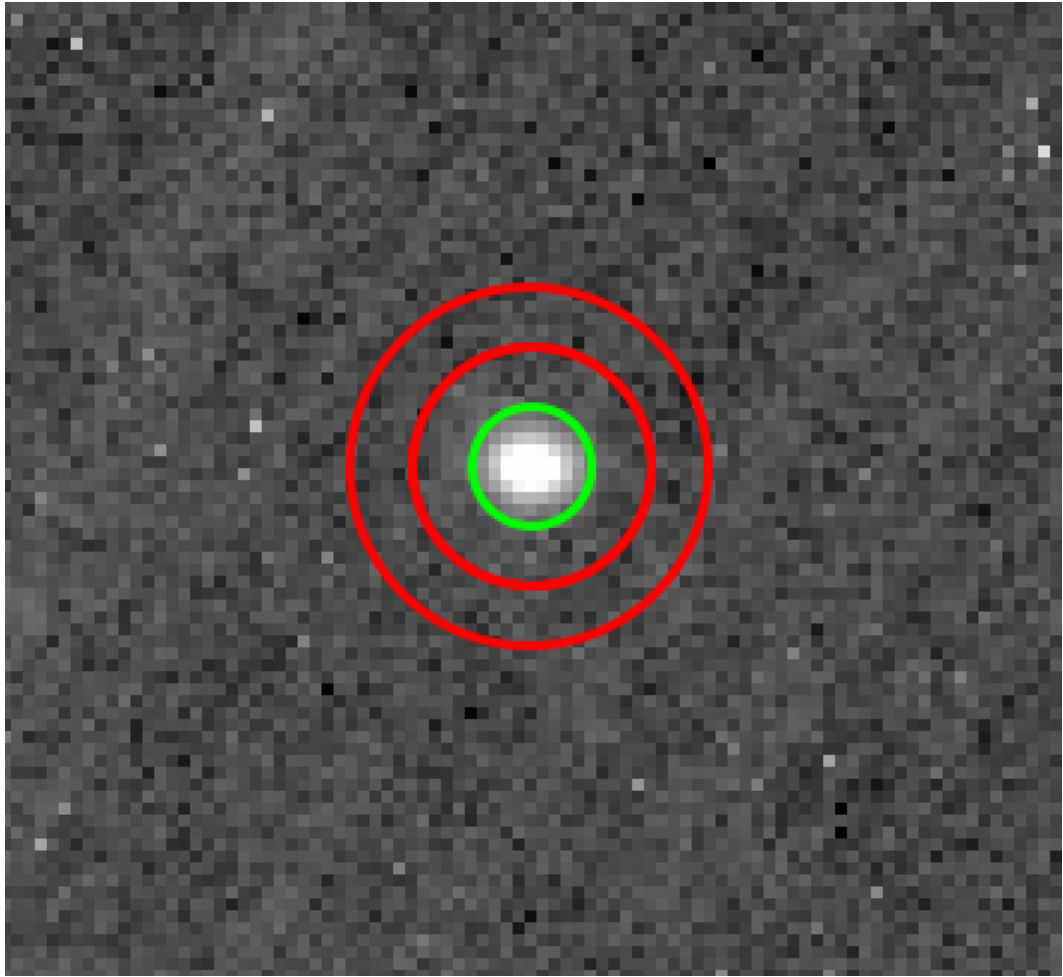


Figure 2.1: An example, from SHOC data, of the aperture photometry parameters. The annulus, used to measure the background counts, is represented by the inner and outer red circles, while the aperture, used to measure the source counts, is displayed as a green circle around the targeted star.

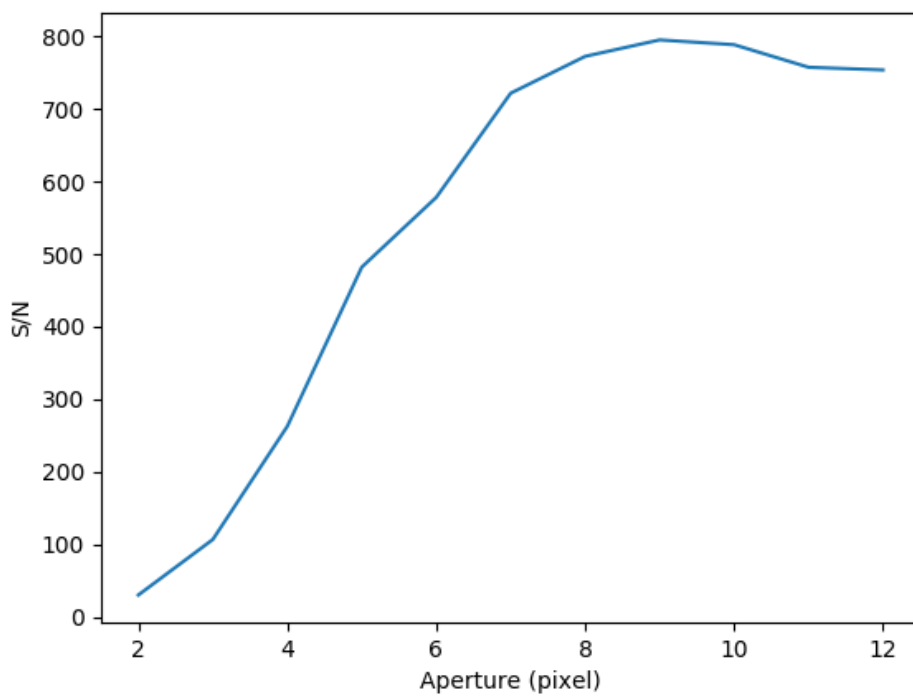


Figure 2.2: An example of the signal-to-noise as a function of aperture. This plot was used to determine the aperture size to be employed by the aperture photometry software.

## 2.2.2 Differential Photometry

Aperture photometry is the first step towards producing an accurate representation of the brightness of a star over time. A number of external factors can cause short-term variability which may be falsely attributed to the star.

When an equatorial star rises above the horizon, it will travel to its highest point in the sky before setting again. The point at which the optical path length of a celestial object through Earth's atmosphere is at its thinnest is defined as the zenith. At this point, the airmass of the object is defined as equal to 1. However, as the object rises or sets in the sky, its incoming flux must travel through a thicker portion of the atmosphere. Consequently, some of its light is scattered or absorbed by the molecules present in the atmosphere, resulting in a decreased detected flux.

Short-term effects can be caused by weather and other uncontrolled factors. High and medium clouds can temporarily decrease the amount of light detected from the star, as well as other atmospheric changes, such as humidity. Moon illumination or smaller Solar System bodies travelling in the field of view of the object may also decrease or even increase the amount of light measured in the image.

Figure 2.3. shows an example of both airmass and weather effects on a light curve. In the figure, there is an increase in flux towards the end of the observation, which can be associated to the decrease in airmass as the object travels towards its zenith. Moreover, several dips in brightness are noticeable throughout the light curve. While some of these could be real, they are most likely due to temporary atmospheric changes.

Due to SHOC's small field of view of  $2.85 \times 2.85$  arcmin, any of these

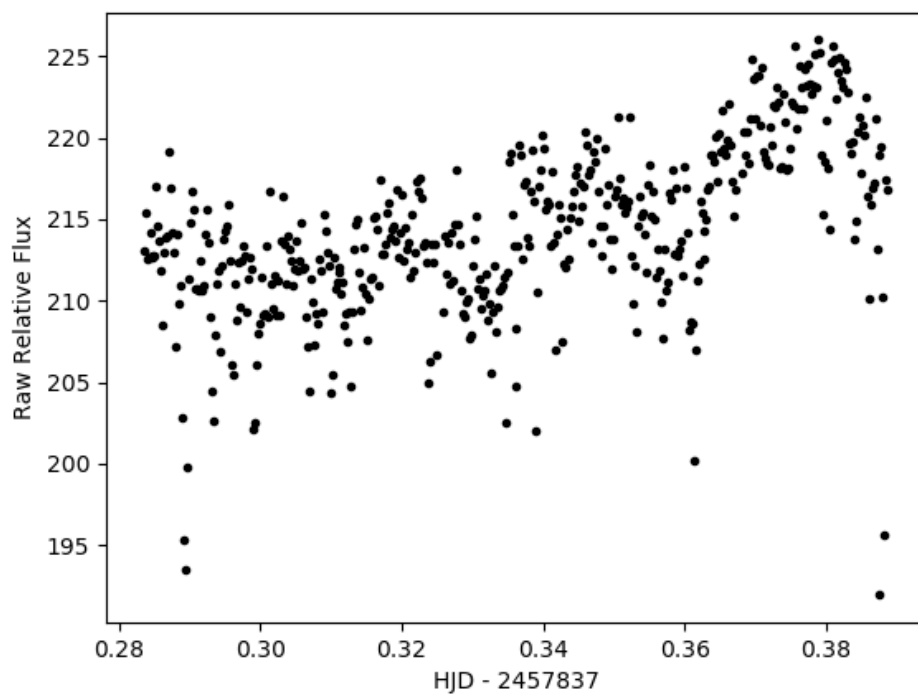


Figure 2.3: An example of light curve of white dwarf EC11246-2923, after performing aperture photometry, using an aperture of 8 pixels. The plot shows several drops in brightness.

factors will almost certainly affect all the objects in the image, due to their proximity to one another. This can therefore be exploited to eliminate the temporary changes in the target's light curve.

The method known as differential photometry consists of extracting light curves for bright stars in the vicinity of the target. The fluxes of these stars can consequently be averaged together and used to calibrate the target's flux. By dividing the target's light curve by the average light curve generated using the comparison stars in the field, all the temporary weather-related effects can be effectively eliminated, thus minimising the chances of a false detection. A calibrated light curve for the same object as the one in Figure 2.3 is shown in Figure 2.4.

While the newly calibrated light curve no longer shows signs of atmospheric disturbances, the airmass effects are still visible. This is common when performing differential photometry on white dwarfs and other blue stars. Due to their large mass, blue stars move off the main sequence at a much faster rate compared to smaller dwarfs. Statistically, there is therefore a much larger fraction of redder stars in the Galaxy, and therefore a higher chance for the comparison stars used in a certain field to be much redder than the observed white dwarf. Atmospheric particles will absorb and scatter different wavelengths in different ways. Therefore, stars of different colour may be affected differently to changes in airmass, and the differential photometry calibration may fail to work completely, leaving a false variability similar in trend to that of the change in airmass in the field.

To account for this, a further correction is applied. A star's airmass changes parabolically during an observation, as shown in Figure 2.5(a). Therefore, the target's light curve can be fitted and divided by a second-degree

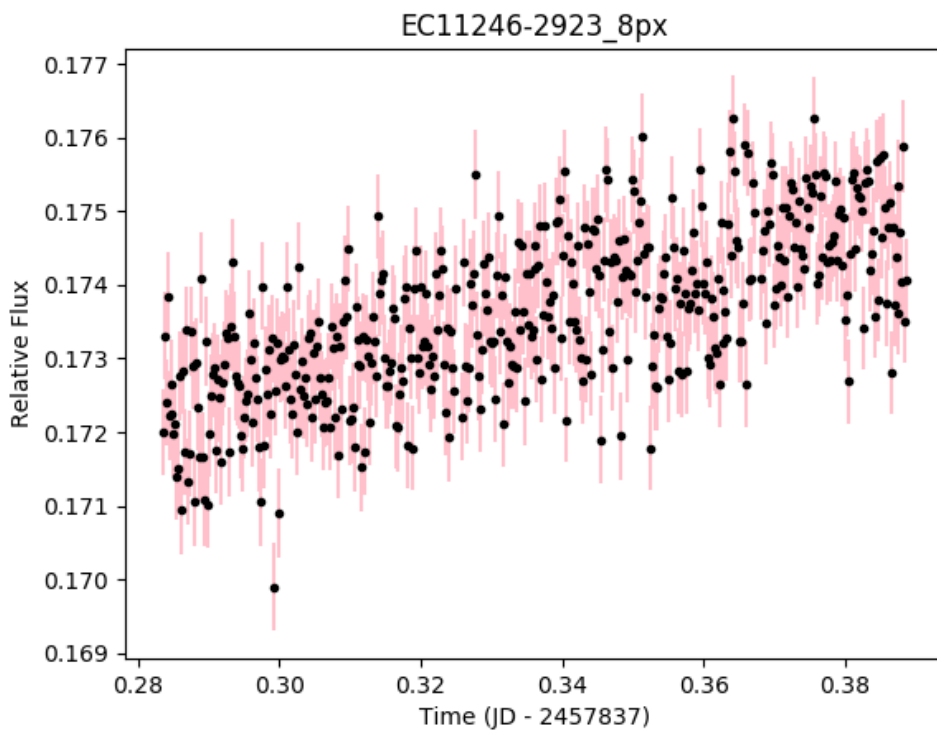


Figure 2.4: The same light curve of white dwarf EC11246-2923 as shown in Figure 2.3, after performing differential photometry using three comparison stars.

polynomial function that follows the same trend as the object's airmass, as shown in Figure 2.5(b). Once this last correction is applied, the calibration is complete, and the target will be devoid of any false periodicity.

## 2.3 Light Curve Fitting

Chapter 5 and 6 will be dedicated to the discovery of three new eclipsing systems involving white dwarfs. Photometric data of these systems can provide important information on some of the physical properties of the components as well as of the system itself. The shape, duration and depth of a transit provide insight on the sizes of both the star and the companion, as well as on the inclination of the orbit. Moreover, observations over multiple eclipses provides accurate estimates on the orbital period of the system.

### 2.3.1 JKTEBOP

In order to measure the parameters of an eclipsing system from its light curve, a light curve fitting software is required. For the analysis of this work, I used JKTEBOP (Popper and Etzel, 1981; Etzel, 1981; Nelson and Davis, 1972; Southworth et al., 2004).

JKTEBOP reads the initial parameters given by the user, and then allows them to vary to find the best fit to the entered light curve, through the Levenberg-Marquardt optimisation algorithm. In this work, the mass ratio of the system was fixed after being calculated from the radial velocity data, as explained in section 2.5.2. I then allowed the radii of the components, the surface brightness ratio, inclination and orbital period to vary, in order to obtain the best fit to the data.

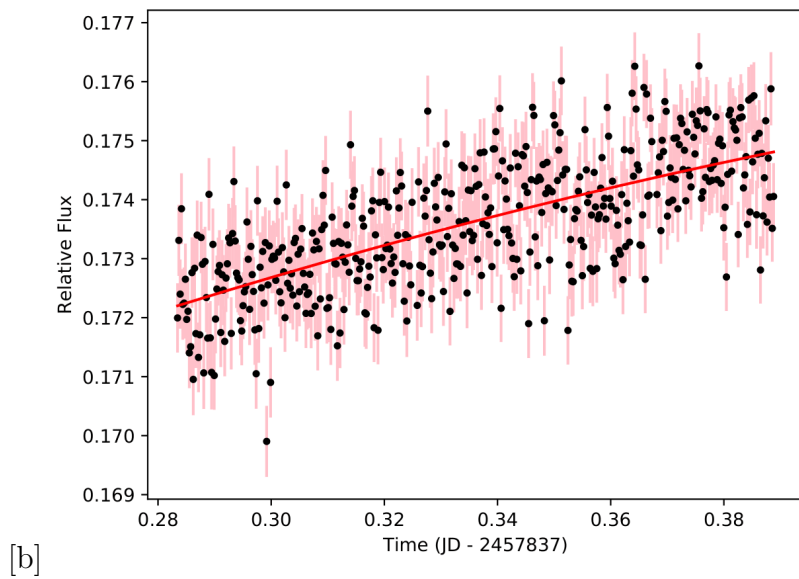
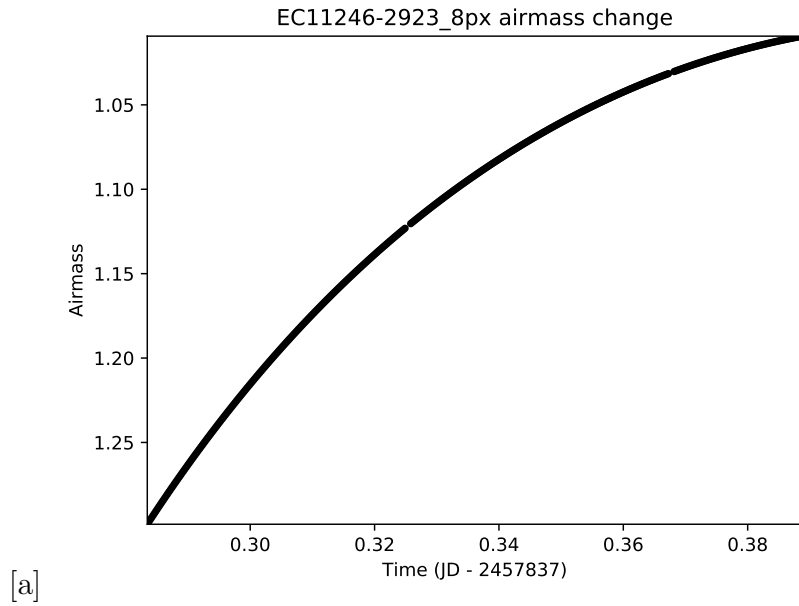


Figure 2.5: In panel [b] I fitted a second-degree polynomial function (red line) in agreement with the airmass shape (shown in panel [a]). I subsequently divided my data set by the polynomial in order to eliminate airmass effects.

In order to calculate the errors, JKTEBOP runs a Monte-Carlo algorithm once the parameters of the system are finalised. An example of light curve fit performed by JKTEBOP on collected data is shown in Figure 2.6.

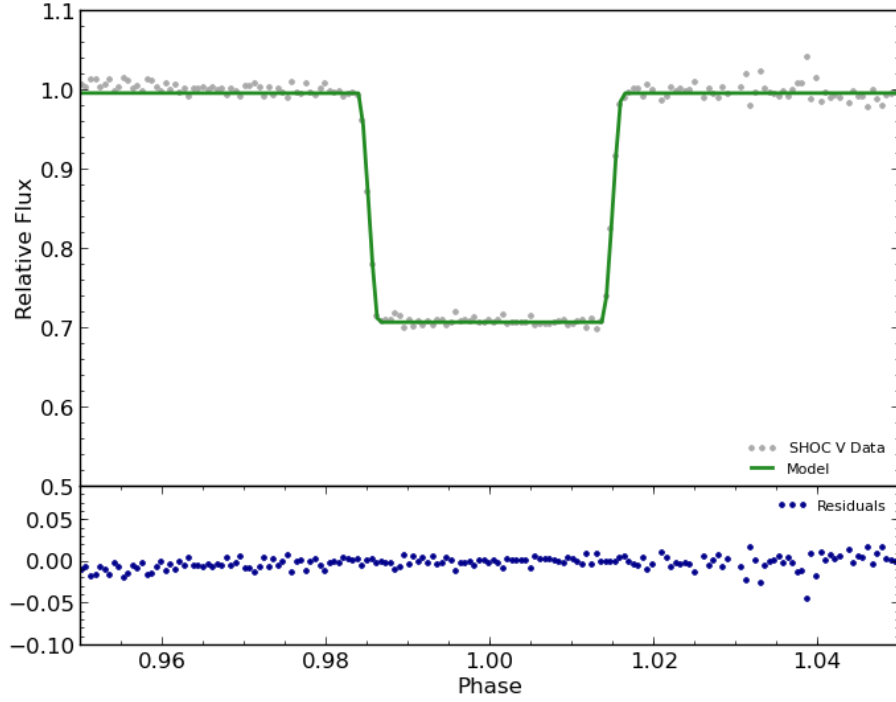


Figure 2.6: An example of SHOC data analysed using JKTEBOP (Popper and Etzel, 1981; Etzel, 1981; Nelson and Davis, 1972; Southworth et al., 2004), which provided some of the physical parameters of the system, such as fractional radii and inclination. The top panel shows the model fit to the data (green line), while the bottom panel shows the residuals (model - data).

## 2.4 Spectroscopic Data Reduction and Extraction

The measurement of the incident flux of a star as a function of wavelength is referred to as spectroscopy. In this thesis, spectroscopic data from different

facilities was analysed in order to assess properties such as the spectral type of a target and changes in radial velocities. Data from a range of instruments were employed in the upcoming science chapters of this thesis. However, I was only directly involved in the reduction of the data I collected using the Spectrograph Upgrade: Newly Improved Cassegrain (SpUpNIC, Crause et al., 2016), mounted on the 1.9 m telescope at SAAO.

The reduction and calibration of these data were performed using processing techniques outlined by Massey et al. (1992) and Massey (1997). This involved using various IRAF packages, described in the sections below.

### **2.4.1 Bias Correction**

Upon collecting an exposure on a CCD, each pixel will carry a small intrinsic value due to their individual structure. This value slightly varies from pixel to pixel, and will introduce a small amount of noise to the final science image. Obtaining bias frames, or zero time exposures, will provide information on the value of this intrinsic pixel noise. Another source of small varying noise can be also introduced by an additional column bias across the chip. This is due to the overscan region of the image, an artificial region of pixels that is created in the read-out process of the CCD. The overscan region can be visually identified upon inspecting a flat frame, as shown in Figure 2.7. This can then be trimmed out of the zero exposure frames.

Using the 'zerocombine' package on the PyRAF software, a combined average bias frame was created. The package performs a  $3\sigma$  cut on every pixel, to account for and remove any bad pixels hit by cosmic rays, that would affect the final combined master bias frame. Once the overscan region is manually

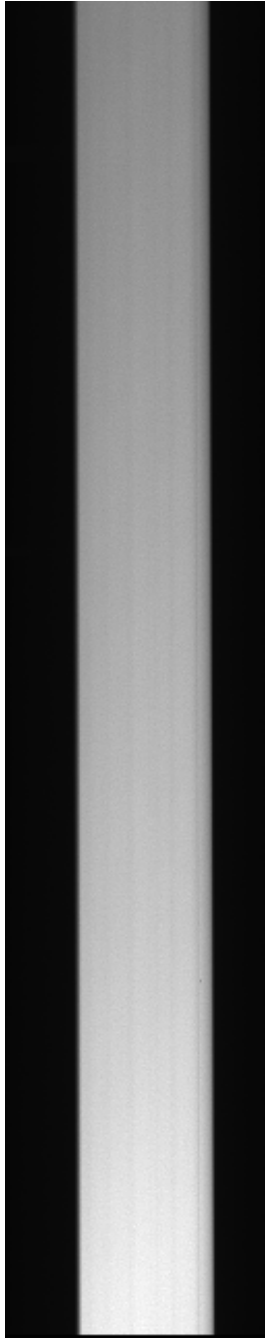


Figure 2.7: A section of one of the SpUpNIC flat frames. The overscan regions (black) can be seen on both sides of the image. These are created as part of the CCD read-out process, and do not represent actual CCD pixels.



Figure 2.8: A section of the SpUpNIC master bias frame used in the reduction of WD1201-049. This is the result of an average of one hundred bias frames collected during the observing run.

removed, this master frame can be subtracted from all other images (including flat frames and calibration arcs).

### 2.4.2 Flat Correction

Once the bias master frame has been subtracted from the images, the next intrinsic source of noise to correct for is flat noise. This is caused by the slightly non-uniform sensitivity between pixels across the CCD. These slight variations are due to physical characteristics of the system, such as small differences in the quantum efficiency of each pixel. Other sources of flat field noise can be caused by the camera optics, leading to effects such as vignetting – uneven illumination across the chip – as well as localised ring-shaped features caused by dust granules present on the filter or the CCD itself.

To create a flat field image, the SAAO 1.9 m telescope uses an illuminated white panel on the inside of the dome. Once the telescope is set up in the same way as for the science frames (i.e. same grating, angle, etc.), it is positioned to expose the CCD and obtain images of the illuminated field. Once several tens of flat images are collected – thirty frames, in the case of the SpUpNIC data presented in this work – these are then combined using the ‘flatcombine’ package in PyRAF, which performs a  $3\sigma$  clipping function to remove any existing bad pixels. The resulting frame is run through the ‘response’ script, which helps eliminate large scale effects that are due to wavelength dependent features present in the instrumentation itself. Finally, the newly created master flat image (Figure 2.9) is subtracted from the science images, thus ending the reduction process.



Figure 2.9: Section of the master flat frame used in the reduction of SpUpNIC data. This was the result of averaging thirty individual frames, as well as eliminating the wavelength dependent effects caused by the lamp illumination and the instrument itself.

### 2.4.3 Spectrum Extraction

Upon completing data reduction, the science images can be then used to extract the spectra. Figure 2.10. shows an example of one of the reduced spectra, as imaged on the CCD. Each of these images is three-dimensional: the spectrum lies along the dispersion axis; the axis perpendicular to this is known as the spatial axis; the remaining dimension stores the flux information. The extraction process will ultimately convert these images into two-dimensional plots, presenting changes in the flux of consecutive pixels (corresponding to consecutive wavelengths).

To extract the two-dimensional spectrum from an image, the PyRAF package ‘apall’ is employed. Usually, spectra will have a width of a few pixels along the spatial direction. In order to maximise the signal-to-noise ratio of the data, the flux needs to be combined into a single pixel spatial length. The script allows the user to define an aperture across the spatial axis to encompass most of the flux but as little background signal as possible. Additional background apertures on either side of the spectrum signal are then selected, ensuring no contamination from stellar flux is present within them. The script then traces these apertures along the dispersion axis automatically adjusting their positions, thus minimising the root mean square error. The user is then prompted with a graphical rendition of the aperture trace and is given the possibility to remove any discrepant points – usually due to cosmic rays affecting the spectrum at a particular pixel. Once these points are removed, the script will then extract an uncalibrated two-dimensional spectrum (Figure 2.11)

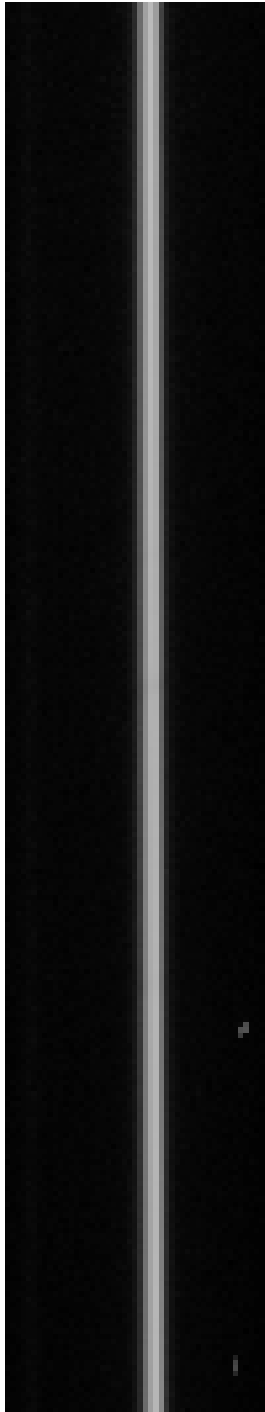


Figure 2.10: A section of a SpUpNIC spectrum, which has been bias- and flat-calibrated, as seen on the CCD before extraction. In this image, wavelength and flux calibrations have not yet been applied. The wavelength dispersion axis runs vertically along the spectrum (top to bottom), while the spatial axis lays horizontally (left to right).

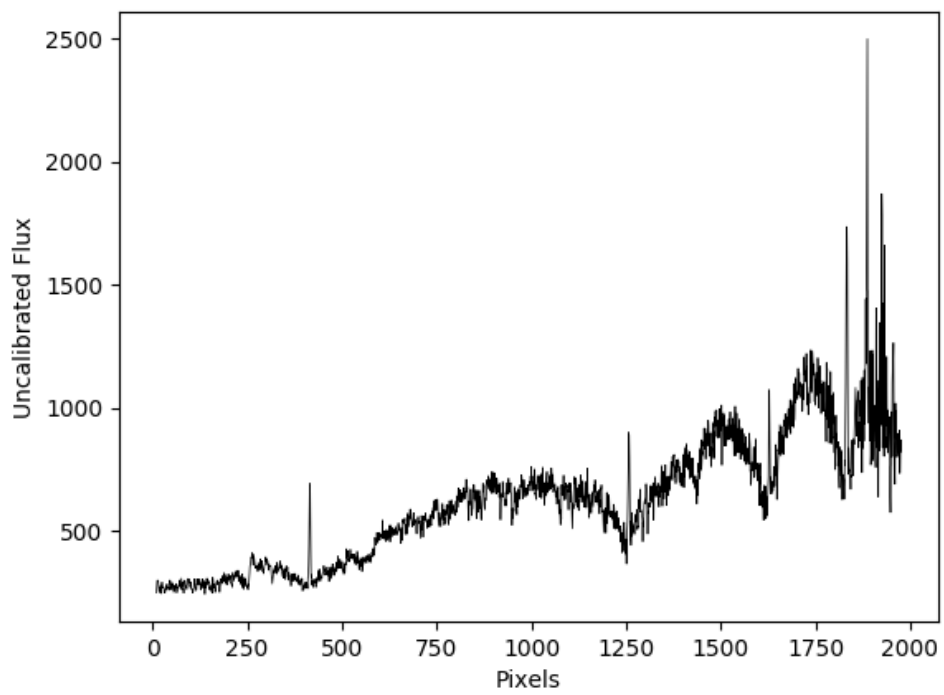


Figure 2.11: Example of a newly extracted spectrum, before wavelength calibration.

## 2.4.4 Wavelength Calibration

In order to assign a wavelength to each pixel along the dispersion axis – and hence wavelength calibrate the extracted spectra –, ‘arc’ exposures are employed. An arc is an exposure of a known lamp (a copper and argon one in this case), which will show emission lines at known wavelengths. This shows where the spectrograph causes the specific wavelengths to fall in the CCD. During the observing run in which the presented data were collected, an arc was acquired shortly before and/or after each science exposure, to account for any movement of the instrument between science exposures, which could have altered the position of the known wavelengths.

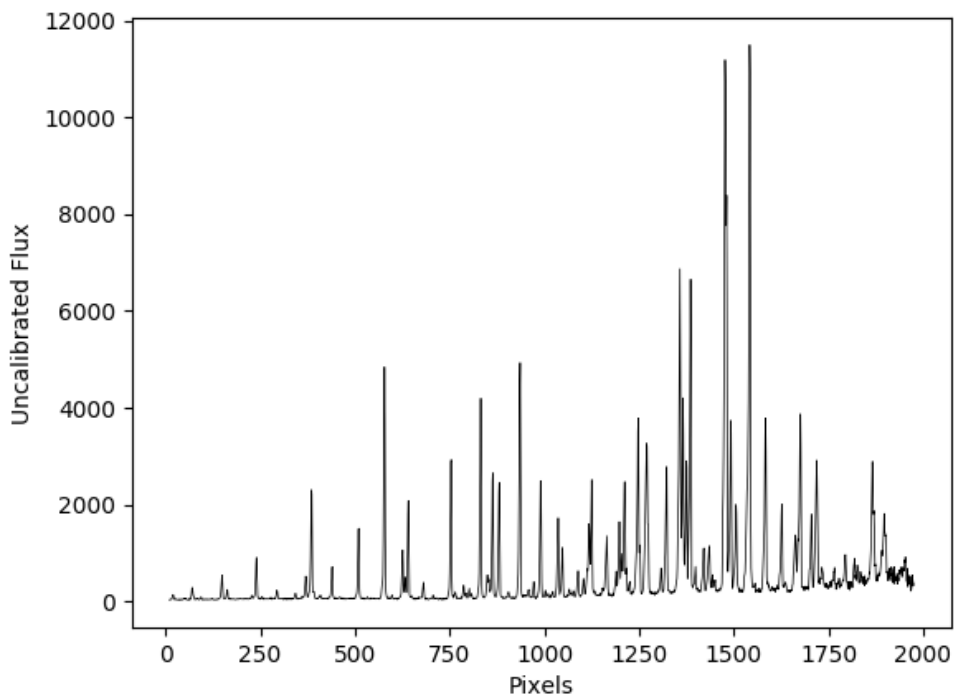


Figure 2.12: Example of an extracted arc spectrum from the SpUpNIC observation of a CuAr calibration lamp.

Any arc used to calibrate a specific science image is extracted using the same trace used on the latter (see Section 2.4.3). The result is a two-dimensional plot of the arc emission lines, as shown in Figure 2.12. To carry out the calibration, the PyRAF command ‘identify’ is used: first, a few bright lines are identified by the user from published lists; once these are entered, the script measures the distance between these lines and matches them to a database of known lines. The remaining  $\sim 30$ -50 lines in the arc spectrum are then automatically recognised and matched to their corresponding wavelengths. Subsequently, each pixel will be assigned a wavelength based on the position of the known ones. This fit is then applied to the science images, converting pixels to wavelengths (Figure 2.13).

### **2.4.5 Flux Calibration**

The final step in the extraction of a spectrum concerns the calibration of the spectral flux. The uncalibrated flux may be affected by the sensitivity of the individual pixels along the CCD as well as by the profile of the instrumentation upon using a certain grating. In order to account for and remove these effects, the observation of a few stars of known and well-modelled flux profile (also known as ‘standard’ stars) is required at intervals of a couple of hours. The spectra of these standards are extracted and wave calibrated in the same way as discussed above. They are then compared and divided by their respective modelled spectra using the PyRAF ‘sensfunc’ script. The resulting residuals provide the instrumentation profile for the required wavelength range. Lastly, the wave calibrated science spectra can be divided by this profile, producing the final, flux calibrated spectra ready for further analysis. (Figure 2.14).

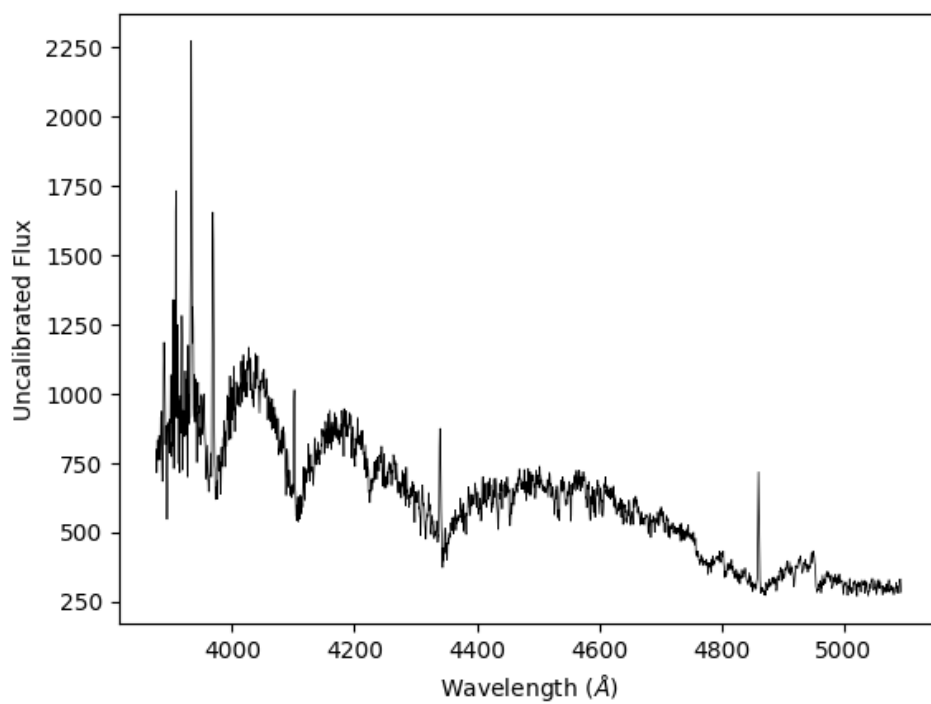


Figure 2.13: Example of a wavelength calibrated spectrum obtained using SpUpNIC.

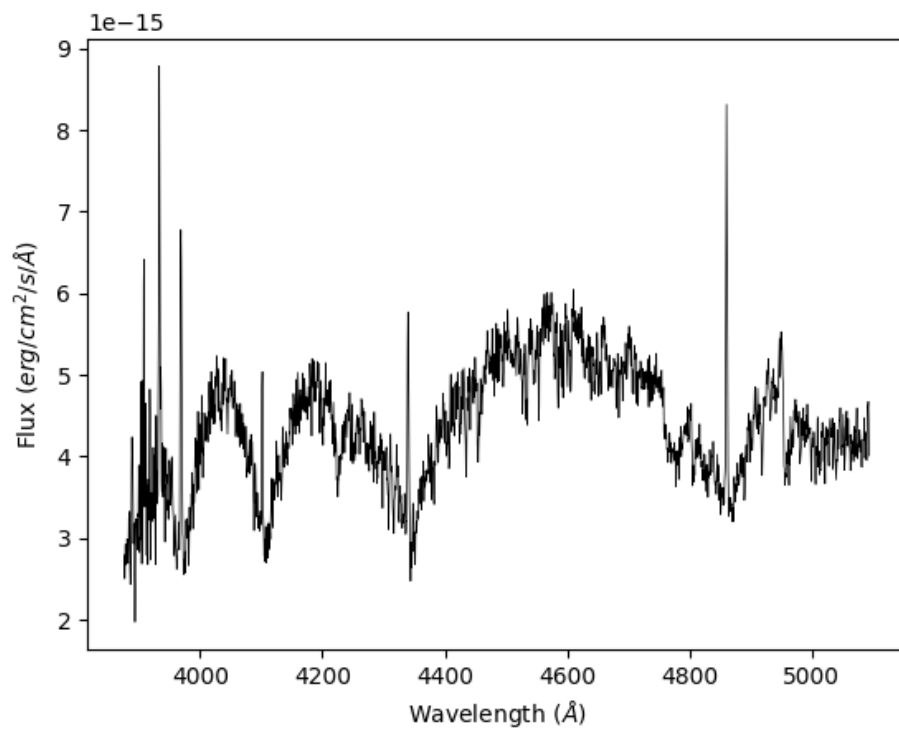


Figure 2.14: Example of a flux calibrated spectrum obtained using SpUpNIC

## 2.5 Spectroscopic Data Analysis

Reduced and calibrated spectra were analysed using MOLLY, a software developed by Tom Marsh<sup>2</sup>. Details on how the software analyses spectroscopic data are discussed below.

### 2.5.1 Normalisation and Processing

Data and their corresponding header information – including right ascension, declination, equinox and the date and time of observation – are read into the MOLLY software. If required, a heliocentric correction to the data may be applied to account for the telescope’s geographic location. Once the spectra are entered, they can then be normalised to same scale, ensuring a continuum level of  $\approx 1$ . This is achieved by creating an average spectrum – usually with the spectra acquired during one night’s observation –, and fitting a polynomial to that average (Figure 2.15). Due to the normalisation acting only on the continuum, any prominent features in the spectra (such as absorption or emission lines) are masked to be excluded from the fit (red regions in Figure 2.15). The individual spectra are consequently divided by the polynomial, resulting in normalised spectra (Figure 2.16).

In order to account for Earth’s velocity - which creates a shift in the wavelengths of the spectrum -, the normalised spectra are consequently rebinned in the heliocentric scale and in velocity space. They are then ordered according to their orbital phase. The latter is calculated according to the following equation:

---

<sup>2</sup><https://warwick.ac.uk/fac/sci/physics/research/astro/people/marsh/> University of Warwick, UK

$$\phi = \frac{t - T_0}{P} \quad (2.3)$$

In the equation,  $T_0$  is the zero-point of the ephemeris (expressed in Heliocentric Julian Days, or HJDs);  $t$  is the HJD of observation; and finally  $P$  is the orbital period (measured in fractions of a day).

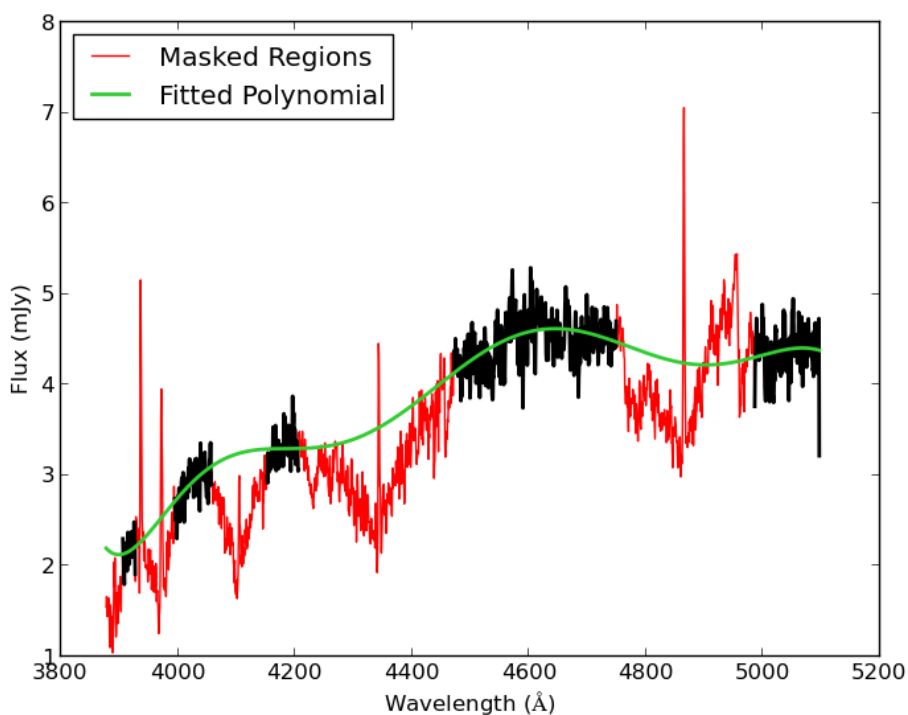


Figure 2.15: Example of a reduced spectrum from SpUpNIC data, before normalisation. The red regions represent the sections masked out during the fitting. The green line represents the polynomial function used to normalise the spectra.

## 2.5.2 Radial Velocity Measurement

The radial velocity of a celestial object is known as the velocity component along the line of sight of the observer. As a star moves closer or farther to

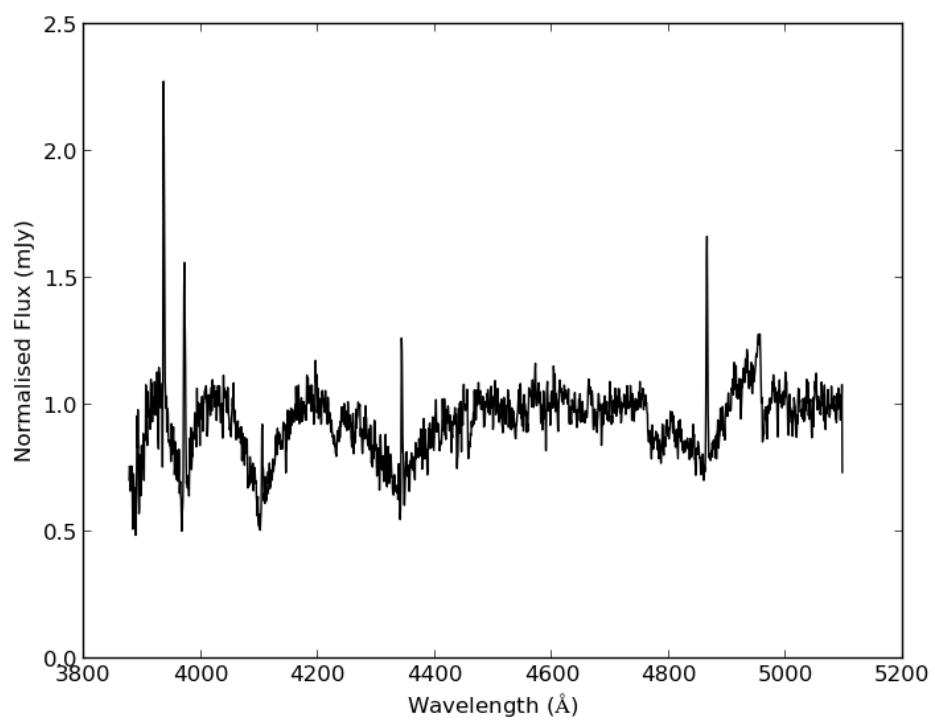


Figure 2.16: The same spectrum shown in Figure 2.15, after normalisation was applied. As expected, the continuum level is at  $\sim 1$  mJy.

the observer on this line of sight, the wavelengths at which the object's light is emitted will be shortened (or blue-shifted) or lengthened (or red-shifted) respectively. The positions at which these wavelengths are found at different points in the orbital phase of the observed star are hence altered by an effect known as Doppler Shift (Figure 2.17). Consequently, by measuring this shift, the radial velocity of a system can be calculated according to the following equation:

$$z = \frac{\Delta\lambda}{\lambda_0} = \frac{v}{c} \quad (2.4)$$

In the equation,  $\Delta\lambda$  is the shift in wavelength,  $\lambda_0$  is the rest wavelength,  $v$  is the relative velocity,  $c$  is the speed of light and  $z$  is the measured red-shift.

Measuring the radial velocity of a system – e.g. two stars in a binary orbit or a planet revolving around a star – can provide information on the masses of the objects involved. From the ratio of the amplitudes of the stars' radial velocities – which effectively represent the stars' orbits about their common centre of mass – one can determine the relative masses of the individual bodies in the system. In case only one of the objects is visible in the spectrum, one can use the following mass relation in order to determine the mass of the unseen companion (Wright, 2018):

$$f \equiv \frac{PK^3(1 - e^2)^{\frac{2}{3}}}{2\pi G} = \frac{M_{\text{unseen}}^3 \sin^3 i}{(M_{\text{unseen}} + M_{\text{seen}})^2} \quad (2.5)$$

In the equation,  $P$  is the orbital period,  $K$  is the semi-amplitude of the radial velocity variation,  $G$  is Newton’s gravitational constant,  $e$  is the eccentricity of the system,  $i$  is the inclination of the orbit compared to the observer (where  $i = 90$  represents an edge on orbit), and  $M_{\text{seen}}$  and  $M_{\text{unseen}}$  are the masses of the seen and unseen companions respectively. This relation can be also applied to exoplanetary systems. In this case, it is safe to assume that the mass of the planet ( $M_{\text{planet}} = M_{\text{unseen}}$ ) is much smaller than that of its host star ( $M_{\text{seen}} = M_*$ ) and hence  $M_{\text{planet}} \ll M_*$ . Therefore, the above equation reduces to the more familiar expression for the Doppler shift (Wright, 2018):

$$K \approx \left( \frac{2\pi G}{PM_*^2} \right)^{\frac{1}{3}} \frac{M_{\text{planet}} \sin i}{\sqrt{1 - e^2}} \quad (2.6)$$

In order to measure radial velocity, I used the MGFIT command on MOLLY. MGFIT reads the file containing all the parameters to be fit to a function that models both the continuum and a particular spectral line. The continuum is modelled with a first-degree polynomial, which pivots at the rest wavelength of the line and has two coefficients indicating its gradient and constant respectively. To model the spectral line, a combination of Gaussian functions is set up. Each function is centred at the rest wavelength of the line (in  $\text{\AA}$ ), with a velocity offset  $k$  in  $\text{kms}^{-1}$ , a systemic velocity  $\gamma$  in  $\text{kms}^{-1}$ , a full width at half maximum (FWHM) in  $\text{\AA}$ , and a peak height  $h$  in mJy. Each of these variables is given a starting value; MGFIT then uses a Levenberg-

Marquardt minimisation method to fit the Gaussians to the spectral line. The fit can be applied to each spectrum individually (resetting the parameters to their initial value for each spectrum), or to all spectra at the same time.

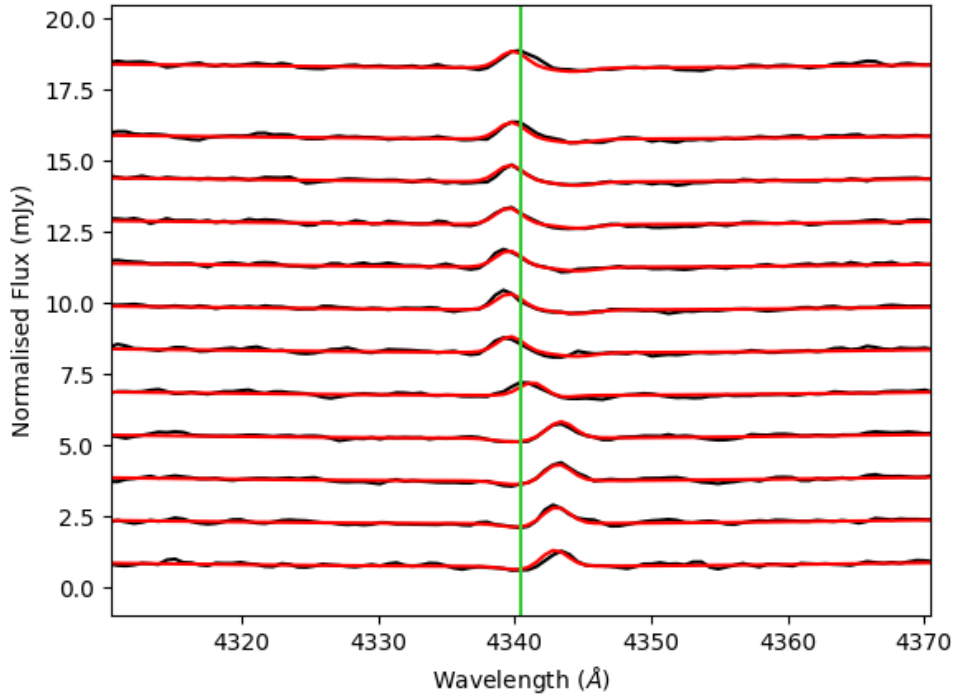


Figure 2.17: An example of a  $H\gamma$  emission line (grey) being shifted both in the red and the blue direction compared to its rest wavelength (green vertical line). The red line represents the models fit to the line to measure its radial velocity.

In the event in which the observed spectra show features from both objects in the system, MGFIT allows to fit more than one component of the line simultaneously, such as absorption and emission, as shown in Figure 2.18. However, Gaussian functions used to fit a particular feature need to have the same  $\gamma$  and  $k$  parameters, as they are all moving together in the same way.

In order to better visualise the radial velocity shift in the spectral lines

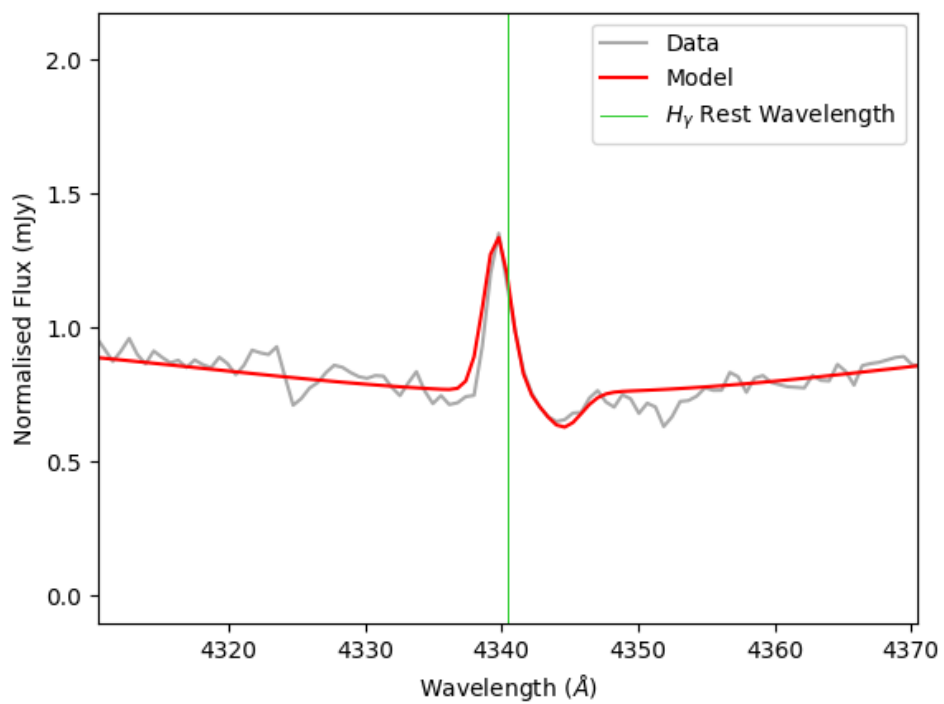


Figure 2.18: An example of fitting performed by MGFIT. Here, the  $H_\gamma$  Balmer line presents both emission and absorption, and the features are fitted simultaneously. The emission and absorption lines were fitted with one and two Gaussians respectively.

Trailed spectrum

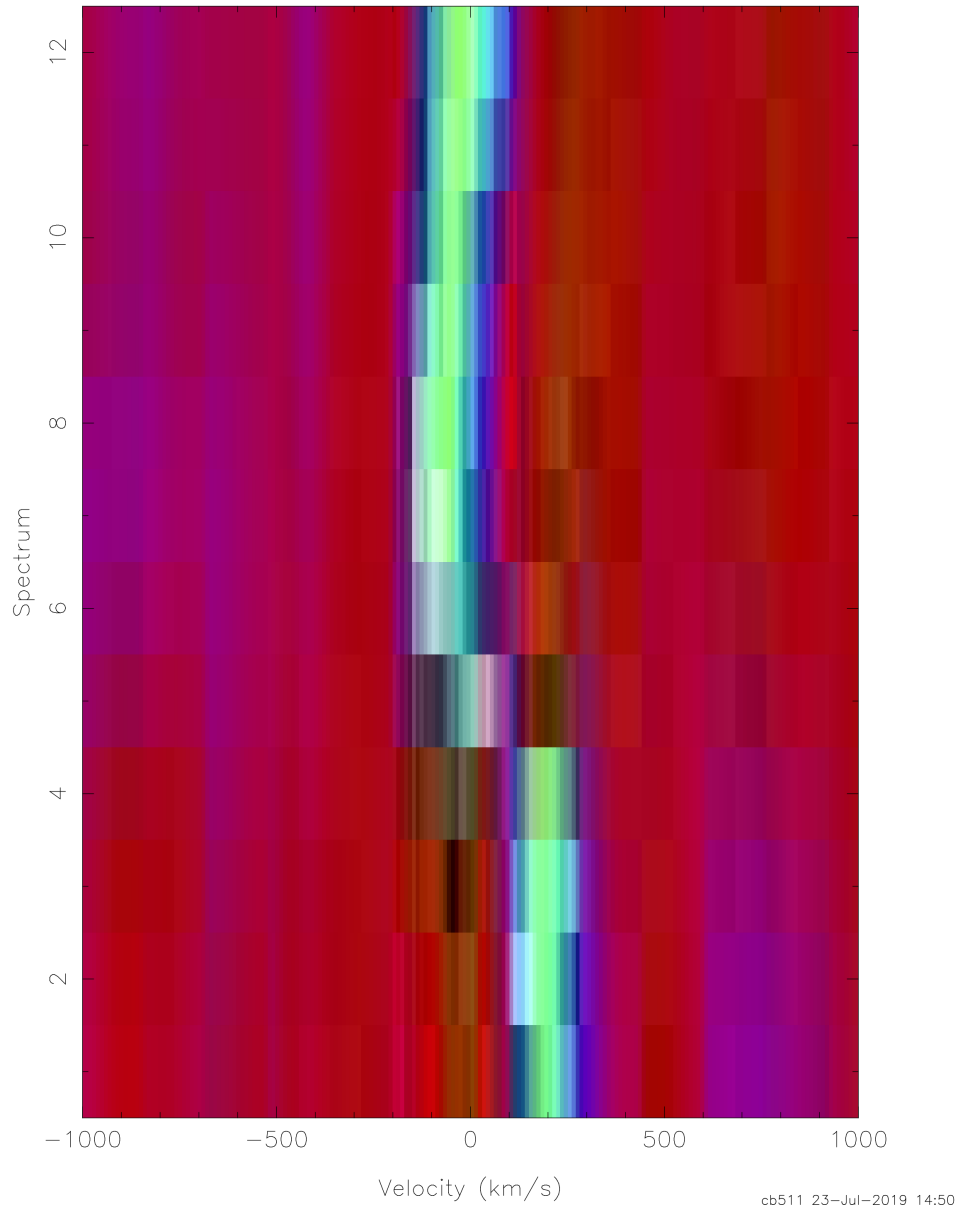


Figure 2.19: An example of trailed spectrum for  $H\gamma$ . Each horizontal line represents one spectrum. In the spectrum, the emission line is clearly visible in shades of green/blue. The x-axis shows the radial velocity of the line, centred at the rest wavelength of  $4340.462 \text{ \AA}$  for  $H\gamma$ .

of a star, one can phase fold the spectra in a data set, and hence plot them in a stack. This is known as a trailed spectrum, as it ‘trails’ the shift of a particular line. Trailed spectra are usually plotted in velocity space in order to render the Doppler shift as clearly as possible (Figure 2.19).

To find the final parameters for the Gaussian line fits, the initial parameters can be given an arbitrary initial value and then be allowed to vary freely. Upon inspecting the generated model, one can then determine which variables need to be changed or fixed in order for the model to best fit the data. To establish the accuracy of the fit, a  $\chi^2/DoF$  value (also known as reduced chi-squared, or  $\chi_\nu^2$ ) is assigned to it by MOLLY. An ideal fit reaches a value of  $\chi_\nu^2 = 1$ .

## 2.6 Summary

The methods described above were employed to reduce and analyse the data presented in the following science chapters. This includes all data collected at the South African Astronomical Observatory (SAAO) facilities, presented in Chapters 3, 4 and 6. Furthermore, MOLLY was used to analyse data from Gemini North and Kitt Peak facilities, presented in Chapters 5 and 6 respectively.

## Chapter 3

# A Ground-Based Photometric Survey of Metal Rich White Dwarfs

In Chapter 1, I explored the evolution of planetary systems once their host stars eventually leave the main sequence. Any planets surviving the RGB and AGB phase of stellar evolution will be exposed to gravitational interactions with stellar remnants and other planetary debris. These interactions will cause some planetary remnants to migrate into short-period orbits (Veras and Gänsicke, 2015). These short orbital periods (between 2 and 30 hours) coincide with the long-lived habitable zone of white dwarfs (Agol, 2011). Planets in such short period however are likely to be tidally locked to their host star or even tidally disrupted. Detections of such bodies are therefore rare, due to their short survival time, and the best strategy to discover them is to survey a large number of white dwarfs.

In this Chapter, I present an independent ground-based photometric

survey of metal-rich white dwarfs, in search for eclipses in their light curves.

### 3.1 The Discovery of WD1145+017

The first evidence for a planetary body orbiting a white dwarf was discovered in 2015. Vanderburg et al. (2015) observed eclipse-like features in the light curve of white dwarf WD1145+017, in the first field observed by the Kepler K2 mission. The light curve showed evidence of transits with varying depths, therefore excluding the hypothesis of a single non-stellar companion. Follow up observations from the ground also showed transit depths down to 40%, with durations of about 5 minutes. Subsequent Fourier analysis of these light curves revealed the presence of multiple periods between 4.5 and 4.9 hours (Vanderburg et al., 2015). Furthermore, spectroscopic follow up data identified an infra-red excess explained by the presence of a circumstellar debris disk, as well as evidence for metal contamination in the white dwarf atmosphere by at least eight heavy metals. It was therefore concluded that the observed transit events were the result of a planetesimal undergoing a disruption process and breaking off into smaller debris elements and dust clouds.

Further observations conducted by Gänsicke et al. (2016) and Rappaport et al. (2016) showed that the rate at which the depths and durations of the transits varies is relatively quick (within a couple of orbits). Rappaport et al. (2016) undertook observations with of multiple telescopes over a period of months in order to find a prominent orbital period for the disrupting body, which resulted to be 4.5004 hours. An additional 15 periods were found as a result of this analysis, however five of the original periods found by Vanderburg et al. (2015) were not identified and confirmed. It was deduced that the

dominant period can be associated with the main, parent body, and all other features observed in the light curves are the result of disrupting debris that is drifting away from the planetesimal. The rate at which these debris drift allowed a first estimate of the mass of the main body, which is approximately a tenth of the mass of Ceres, the largest asteroid in the Solar System Main Belt ( $10^{20}$  kg, Rappaport et al., 2016).

### **3.1.1 Motivation for a Metal-rich WD Survey**

The discovery of WD1145+017, a metal polluted white dwarf with a debris disk, opened up a new opportunity to study evolved planetary systems. It provided evidence for the existence and possible survival of planets after the Planetary Nebula stage of stellar evolution. Finding similar systems is of crucial importance, in order to better constrain their frequency and physical properties.

To achieve this, I surveyed 49 white dwarfs (see table 3.1) with similar properties (e.g. temperature, class, etc.) to WD1145+017. All observations were undertaken from the ground, by means of the Sutherland High Speed Optical Camera (SHOC), mounted on the 1.0 m telescope at the South African Astronomical Observatory (SAAO) in Sutherland, South Africa. Each object was observed between 1 and 7 hours, in order to sample a variety of orbital distances (and periods) similar to WD1145+017, with the aim of finding similar transit events.

## 3.2 Instrumentation

### 3.2.1 The SAAO 1.0 m Telescope

The 1.0 m telescope is found at a latitude of  $S32^{\circ}22.78'$  and a longitude of  $E20^{\circ}48.60'$ , at an altitude of 1810 m. It has a polar mount with an approximate focal ratio of  $f/16$  (Coppejans et al., 2013). For the purposes of this project, the two filter wheels available were set up with the Bessel *UBVRI* and the Sloan *u'g'r'i'z'* filters respectively. Each wheel also contains an empty slot to allow observations to be performed in white light. On this telescope, SHOC is mounted via a mounting plate at the Cassegrain focus, directly under the filter wheel box (Figure 3.1). Thanks to its lightweight design, the camera has minimal impact on the balance of the telescope.

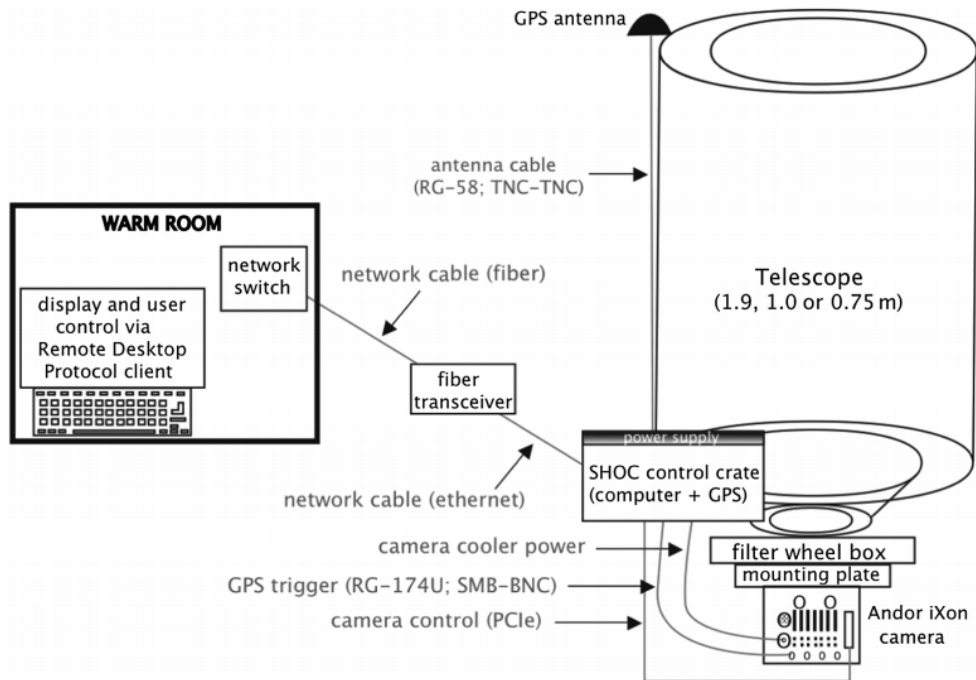


Figure 3.1: A schematic (not to scale) of SHOC setup and mount on one of the SAAO telescopes (Coppejans et al., 2013).

### 3.2.2 The Sutherland High Speed Optical Cameras

The Sutherland High Speed Optical Cameras (SHOC) are two nearly identical cameras developed to be used on the 0.75 m, the 1.0 m and the 1.9 m telescope facilities at the South African Astronomical Observatory (SAAO), effectively replacing the UCT CCD camera (O’Donoghue, 1995) in 2013. The short read-out time and high photometric precision (down to a few millimag) of SHOC makes it the ideal instrument to perform a short-cadence photometric survey on dim objects such as white dwarf stars.

Both SHOC instruments are optical imagers capable of acquiring high-quality photometric data at a fast rate (Coppejans et al., 2013). They are based on two previously existing instruments: the Portable Occultation, Eclipse and Transit Systems (POETS; Souza et al., 2006) and the Massachusetts Institute of Technology Optical Rapid Imaging System (MORIS; Gulbis et al., 2011). The main difference compared to the aforementioned instruments is the application of a larger format CCD (Andor iXon X3 888 UVB camera). The apparatus also consists of a Spectrum Instruments Inc. Intelligent Reference/TM-4<sup>TM</sup> GPS and control computer cables for network and power connections (Figure 3.1).

Each camera (SHOC 1 and 2, also renamed shocnawe and shocndisbelief) uses a 1024×1024 pixel back-illuminated, thermoelectrically-cooled CCD, with peak quantum efficiency (QE) greater than 95% at  $\lambda \sim 550$  nm. This efficiency drops to  $\sim 60\%$  at wavelengths of 400 nm and 850 nm. The thermoelectric coolers allow the camera to efficiently reach (and maintain) a temperature of  $-60^\circ\text{C}$ . Tests have shown that no dark current is detected in 20-minute-long exposures when the instrument is kept at temperatures between  $-40^\circ\text{C}$  and

-70°C. The CCD can be binned with values specified by the user. In the survey that I undertook, I used a binning value of  $4 \times 4$ . As binning occurs after the CCD is read out, this does decrease the readout time, without however affecting the dead time. Nevertheless, the total time between sequential exposures is of the order of  $\sim 10$  ms (Coppejans et al., 2013). For this project, I chose to use the Andor iXon camera conventional (CON) output amplifier with a horizontal pixel shift speed of 1 MHz as readout method. This allowed me to achieve a notably low read noise of  $\sim 6 e^- \text{ pixel}^{-1}$ .

### 3.2.3 GPS and Control Computers

In order to provide the most accurate timing possible, which is important to obtain photometry of rapidly changing objects, the Spectrum Instruments Inc. Intelligent Reference/TM-4<sup>TM</sup> global positioning system (GPS) was chosen to be mounted as part of the SHOC setup. Indeed, it has manufacturer specifications of  $\pm 25$  ns from the Universal Time Coordinated (UTC), with a root-mean-squared stability of 12.5 ns. The GPS antenna is permanently mounted on the top of the telescope tube, and due to the fixed location of the instrument, only one satellite is required to achieve an accurate time. The timing delay between the GPS input trigger and the iXon camera is accounted for by using a coaxial cable of known length.

Thanks to the addition of this instrument, SHOC has two types of image timing:

1. “internal trigger”. This uses the Andor camera’s built-in software and time-stamps a series of exposures from the control computer, with an accuracy of  $\sim 1$  s.

2. “external start trigger”. This allows a separate GPS pulse to trigger the readout of each exposure, thus reaching an accuracy of  $\sim 10 \mu\text{s}$

In the work presented in this Thesis, I used the “external start trigger” option.

### 3.3 The Ground-Based DAZ Survey

Previous, large-scale photometric surveys of white dwarfs such as SuperWASP (Faedi et al., 2011), Pan-STARRS (Fulton et al., 2014) and DECam (Belardi et al., 2016; Dame et al., 2019) were aimed at discovering planetary systems around any type of white dwarf star. However, the discovery of the disrupting planetesimals around WD1145+017 provided new information on what type of white dwarf star may be more likely to host planets. Therefore, I selected 49 metal polluted white dwarfs similar to WD1145+017. 25 of these show evidence for a debris disc, and the remaining 24 appear to have no disc.

Even though WD1145+017 does host a debris disc, the choice of including white dwarfs that do not show evidence of a disc in my survey was motivated by the fact that different plane inclinations are required to detect a disc versus a planet. Evidence for debris discs around white dwarfs is usually provided by an excess of radiation at the infra-red end of the star’s spectral energy distribution. The excess is due to the dust grains in the disc being irradiated by the white dwarf and re-emitting light at longer wavelengths. Discs are most likely to be detected if they have a face-on orientation with respect to the observer, i.e. at an inclination of  $0^\circ$ . This allows the maximum amount of re-emitted infra-red light to be detected. On the other hand, the best chance to detect a transiting planet around a star requires the orientation of the sys-

tem to be edge-on (or at  $90^\circ$ ) with respect to the observer. This allows the planet to block out the maximum amount of stellar flux. Any inclinations in between these two extremes may reveal both the presence of a disc or a planet, as in the case of WD1145+017 (Figure 3.2).

The survey was undertaken between June 2016 and May 2018. Due to observational constraints, objects were observed for different lengths of times (depending on weather conditions on site, as well as scheduling) and with different exposure times, depending on their brightness. Exposure times range between 5 seconds and 120 seconds. Observing windows range between 1 and 7 hours (see table 3.1).

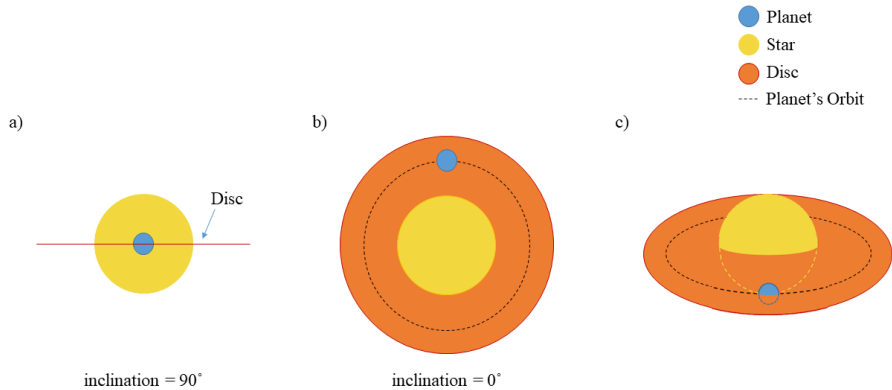


Figure 3.2: A schematic (not to scale) diagram of the different plane inclinations in which a planetary system around a white dwarf may be found. Panel a) represents the best inclination ( $i = 90^\circ$ ) required to detect a transiting planet; at this angle, none of the infra-red excess light emitted by the disc would be detected. Panel b) shows the best inclination ( $i = 90^\circ$ ) required to maximise the detected infra-red flux from the disc; a system in such inclination would present no sign of planetary eclipses. Panel c) shows an example of inclination at which both the planet and the disc could be detected: the planet is still eclipsing the star, and some of the infra-red excess from the disc is measurable.

Target Name	RA	DEC	Mag	WD Class	Date (UT)	Obs. Length (h)	Exp. Time (s)	Filter	Disc?	Ref.
HE1349-2305	13 52 44.12	-23 20 05.4	V=16.3	DBAZ	02/07/16	5	10	white	yes	a
					03/04/17	7	20	white		
WD1318+005	13 20 44.68	+00 18 55.0	V=17.3	DAZ	07/07/16	4	20	white	yes	a
GALEX1929+011	19 31 56.2	+01 17 44	V=14.2	DAZ	07/07/16	6	10	white	yes	a
WD0110-565	01 12 21.14	-56 14 27.5	V=15.69	DBAZ	07/07/16	2	20	white	yes	a
					08/07/16	2	10	white		a
WD1611-084	16 14 19.12	-08 33 26.6	V=13.43	DA	10/07/16	5	5	white	no	a
WD2157-574	22 00 43.9	-57 11 20	V=15.96	DAZ	10/07/16	6	2	white	no	a
HE2221-1630	22 24 17.43	-16 15 47.2	V=16.02	DAZ	28/09/16	5	20	white	yes	a
RE J2334-47	23 34 02.19	-47 14 26.6	V=13.46	DAZ	30/09/16	3	5	white	no	a
WD2207+121	22 09 34.9	+12 23 33	g=17.17	DBZ	01/10/16	3	30	white	yes	a
SDSSJ2007-1208	20 07 57.09	-12 08 32.0	g=16.846	DBAZH	02/10/16	2	20	white	no	b
					03/10/16	1	20	white	no	
HE0106-3253	01 08 36.03	-32 37 43.4	V=15.26	DAZ	03/10/16	5	10	white	yes	a
WD2146-433	21 49 38.93	-43 06 14.2	V=15.7	DA	04/10/16	3	20	white	no	a
G33-45	01 10 55.07	+14 39 22.3	g=16.936	DAZ	04/10/16	4	20	white	yes	a
GD40	03 02 53.10	-01 08 33.8	V=15.56	DBZ	19/10/16	2	20	white	yes	a
					22/10/16	5	30	white	yes	
NLTT6390	01 54 05.34	-30 34 32.3	V=17.08	DAZ	23/10/16	4	30	white	no	a
SDSS2247-0002	22 47 53.22	-00 02 30.3	g=18.793	DAH	24/10/16	3	60	white	no	a
WD0420-73	04 19 37.77	-73 03 44.5	V=15.61	DAZ	24/10/16	4	10/20	white	yes	a
GD56	04 11 02.17	-03 58 22.6	V=15.5	DAZ	29/11/16	3	30	white	yes	a

Continued on next page

Target Name	RA	DEC	Mag	WD Class	Date (UT)	Obs. Length (h)	Exp. Time (s)	Filter	Disc?	Ref.
WD0307+077	03 10 08.5	+07 57 33	V=16.5	DAZ	28/11/16	3	15	white	yes	a
PG1457-086	14 59 52.99	-08 49 29.6	V=15.77	DAZ	29/06/16	4	10	white	yes	a
WD2115-560	21 19 36.53	-55 50 14.5	V=14.27	DAZ	29/06/16	6	10	white	yes	a
EC11246-2923	11 27 09.25	-29 40 11.2	V=15.02	DAZ	24/03/17	3	20	white	no	a
EC11507-1519	11 53 15.26	-15 36 36.5	V=16	DA	25/03/17	3	30	white	yes	c
					02/02/18	≈1	20	white		
					03/02/18	4	20	white		
					04/02/18	2	20	white		
					05/02/18	0.75	20	white		
					06/02/18	≈0.66	20	white		
REJ0558-373	05 58 14.63	-37 34 26.0	V=14.38	DAZ	26/03/17	4	2	white	no	a
WD1201-049	12 04 21.65	-05 13 26.5	B=17.2	DAOZ	26/03/17	5	10	white	no	a
					28/04/19	5	120	I		
WD1634-573	16 38 31.2	-57 28 10.7	V=11.26	DOZ	07/07/17	3	1	white	no	a
					10/07/17	1.5	1	V		
WD1929+011	19 31 56.2	+01 17 44	V=14.2	DAZ	07/07/17	≈1	15	white	yes	a
SDSSJ2247-0002	22 47 53.23	-00 02 30.3	g=18.793	DAH	07/07/17	5	60	white	no	a
SDSSJ1617+1620	16 17 17.04	+16 20 22.5	g=17.028	DA	10/07/17	4	20	white	yes	d
					22/04/18	1.5	60	white		
					16/05/18	1.5	60	white		
					23/05/18	1	60	white		
					26/05/18	2	60	white		
					29/05/18	1	60	white		

Continued on next page

Target Name	RA	DEC	Mag	WD Class	Date (UT)	Obs. Length (h)	Exp. Time (s)	Filter	Disc?	Ref.
WD1943+163	19 45 31.76	+16 27 38.7	B=13.96	DAZ	11/07/17	2.5	30	V	no	a
					11/07/17	2.5	30	V		
WD2326+049	23 28 47.63	+05 14 54.2	B=13.17	DA	11/07/17	2	30	V	no	a
WD2053-011	20 55 46.6	-00 54 41	g=15.71	DAZ	12/07/17	5	30	V	no	a
EC00169-2205	00 19 28.22	-21 49 05.1	V=15.31	DA	18/11/17	2	10	white	yes	c
EC01071-1917	01 09 33.16	-19 01 17.5	V=16.3	DA	22/11/17	4	30	white	yes	c
EC02566-1802	02 58 59.58	-17 50 20.3	V=16.51	DA	23/11/17	3	5	white	yes	c
EC 21548-5908	21 58 23.94	-58 53 54.2	V=15.75	DA	26/11/17	3	10	white	yes	c
EC03103-6226	3 11 20.59	-62 15 16.3	V=16.05	DA	27/11/17	2	10	white	yes	c
					28/11/17	5	10	white		
2MASSJ0710-1646	07 10 39.58	-16 46 40.4	g=14.35	DAZ	24/01/18	1	10	white	no	e
					27/01/18	2	5	white		
WD0738-172	07 40 20.78	-17 24 49.1	V=13.061	DAZ	29/01/18	1	4	white	no	a
					05/02/18	1	4	white		
2MASSJ0707-1721	07 07 43.94	-17 21 16.1	g=14.31	DAZ	01/02/18	3	5	white	no	e
WD1009-184	10 11 59.6	-18 43 33	V=15.44	DZ	13/04/18	≈1	30	white	no	a
					15/04/18	≈3.5	10	I		
SDSSJ0843+0824	08 43 28.87	+08 24 38.4	g=16.176	DAZ	19/04/18	1	20	white	no	f
					20/04/18	≈2.5	20	white		
SDSSJ1228+1040	12 28 59.93	+10 40 33.0	g=16.208	DAZ	19/04/18	≈2	30	white	yes	a
					21/04/18	2.5	60	white		
					23/04/18	1.5	60	white		
SDSSJ1032-0255	10 32 48.61	-02 55 20.5	g=16.648	DBZ	21/04/18	2	60	white	no	f

Continued on next page

Target Name	RA	DEC	Mag	WD Class	Date (UT)	Obs. Length (h)	Exp. Time (s)	Filter	Disc?	Ref.
EC20036-6613	20 08 23.96	-66 04 37.1	V=15.91	DA	23/04/18	≈2	60	white		
					21/04/18	1	30	white	yes	c
					17/05/18	2	30	white		
					18/05/18	2	30	white		
					22/05/18	≈3	20	white		
WD1013-559	10 15 00.8	-56 09 54	V=15.1	DZ	24/04/18	≈3	20	white	no	a
EC20220-2243	20 24 59.46	-22 33 21.5	V=16.45	DA	25/05/18	3.5	30	white	no	g
WD1917-077	19 20 36.0	-07 39 29	V=12.28	DBZ	26/05/18	3	5	V	no	a
EC13140-1520	13 16 43.63	-15 35 51.6	V=14.86	DA	27/05/18	1	7.5	white	yes	c

a) McCook and Sion (2016)

b) Koester and Kepler (2015)

c) Dennihy et al. (2017)

d) Wilson et al. (2014)

e) Girven et al. (2011)

f) Kepler et al. (2015)

g) Downes et al. (2001)

Table 3.1: A list of astrometric and physical properties, as well as observation details for the surveyed metal-rich white dwarfs.

### 3.3.1 Survey Results

As mentioned in Section 3.3, in this project I surveyed 49 metal-polluted white dwarfs, in search for transit-like events. Details about each of the surveyed objects (such as astrometric properties, physical properties, date and length of observation, and filter) are shown in Table 3.1. In the sample, 17 objects were observed more than once, to increase the total time of observation. Of these, 5 have a total observation time of more than 5 hours. Moreover, 12 objects were observed for at least 5 continuous hours (i.e. longer than the orbital period of WD1145+017). The rest of the white dwarfs in the sample had observation windows between 4 and  $\sim 1$  hour, due to scheduling constraints.

After performing aperture and differential photometry on all the targets, I analysed each individual light curve in search for periodic variability. To perform this task, I employed PERIOD04 (Lenz and Breger, 2005), a software developed to produce Discrete Fourier Transforms (DFTs) of time-dependent sets of data, in search of significant peaks. Out of the sample, two objects showed significant peaks: WD1201-049 (further discussed in Chapter 4) and SDSS J161717.04+162022.4 (discussed in Section 3.3.4), first observed on 26 March 2017 and 10 July 2017 respectively. In both cases, upon visual inspection the light curve showed evidence of a sinusoidal variability.

The number of data points in each light curve varied between  $\sim$ few hundreds to  $\sim$ few thousands, depending on the length of observation and exposure time. For white dwarfs, planetary eclipses are expected to last 2-5 minutes, amounting to a small number of consecutive data points. In order to find eclipse-like events in the light curves, I therefore searched for consecutive data points that deviated more than  $4\sigma$  from the mean flux.

Target Name	Magnitude (mag)	Minimum Transit Depth (%)
WD1611-084	$V = 11.26$	1.024
REJ2334-47	$V = 13.46$	1.163
EC11246-2923	$V = 15.02$	1.457
HE1349-2305	$V = 16.30$	5.360
NLTT6390	$V = 17.08$	9.072
SDSS2247-0002	$g = 18.79$	30.802

Table 3.2: Minimum detectable transit depth for white dwarfs of different brightnesses in my sample.

No eclipse-like features were detected within a  $4\sigma$  significance limit. However, the detectability of a transit is strictly dependent on the brightness of the white dwarf. Brighter stars will show less scatter in their light curves, allowing the detection of shallower eclipses. Table 3.2 shows the minimum percentage depth required to detect eclipses at the  $4\sigma$  limit for a range of magnitudes present in my sample of white dwarfs. While the minimum depth increases for dimmer objects, all the values are consistent with the depth of the transits observed around WD1145+017. Hence, if disrupting asteroids or other planetary remnants were to eclipse the white dwarfs in my sample, they would be detected.

### 3.3.2 Detection Rate

The planetesimal around WD1145+017 has an orbital period of  $\sim 4.5$  hours (Vanderburg et al., 2015). It is therefore reasonable to assume that planets or planetesimals could exist around a white dwarf star at similar periods. Based on the different observing windows employed during the survey, I calculated the frequency of detection of transiting objects around a white dwarf, assuming every observed star had at least one orbiting planetesimal at an inclination

suitable for detection. This was achieved by simulating sets of light curves with lengths spanning between 1 and 5 hours – in increments of 1 hour –, each with integration times of 60 seconds. The simulated light curves were injected with 3-data-point-long eclipses, at periods ranging from 0.5 to 30 hours, with increments of 30 minutes. Subsequently, I matched the simulated light curves with each observing window and shifted the eclipses to start at different times of the night in order to probe every possible combination. The total probability of detecting at least one transit over each observing window was then calculated using the following equation:

$$P_{Detection} = \frac{n_{tot}}{n_{Period}} \times 100\% \quad (3.1)$$

In this equation,  $n_{tot}$  is the total number of data points associated to a transit detected over the entire observing window, summed over all the possible combinations, while  $n_{Period}$  is the number of data points in one period.

Figure 3.3 shows the probability of detection over all the investigated orbital periods, for each observing window between 1 and 7 hours. The overall trend shows a decrease in probability as the orbital period increases. Table 3.3 shows the cumulative probability of detecting a transiting planet in the sample for each of the sampled observing windows. This is done under the assumption that each of the white dwarfs observed has a detectable planetesimal orbiting it. The table also shows the cumulative detection rate considering that the actual probability of eclipse for an Earth-like planet orbiting in the habitable zone of a white dwarf is 1% (Agol, 2011). As an example, the cumulative probability of detection for a 6-hour-long observation is 51.53%. This corresponds

Observing Window Length (hours)	Cumulative Chance of Detection from Simulations (%)	Predicted Number of Detected Planets (per 1000 white dwarfs)
1	13.93	1
2	23.98	2
3	32.3	3
4	39.49	3-4
5	45.85	4
6	51.53	5
7	56.66	5-6

Table 3.3: Cumulative detection probability for each of the sampled observing windows. The predicted number of detected planets is also shown, as a result of applying the actual 1% chance of detecting a planet around a white dwarf to the simulated data.

to an actual expected detection rate of  $\sim 0.5\%$ . Hence, we would expect to find 0.5 planets in a sample of 100 white dwarfs, or 5 planets in a sample of 1000. However, these numbers only represent an upper limit, as it is not expected for every white dwarf to host a planet, detectable or otherwise.

### 3.3.3 Statistical Implications of the Survey

As the detection rate discussed in Section 3.3.2 inferred, the lack of eclipsing planets detected in the sample is not surprising. The observing strategy and time set strong limitations on the probability of detecting an eclipsing event (see table 3.3 and Figure 3.3). With a continuous observation length of maximum 7 hours and  $\sim 3$  hours on average, I would only detect transit-like events with periods similar to WD1145+017 or shorter.

However, this survey helps estimate an upper limit for the occurrence of systems like WD1145+017. If the latter were to be added to the sample listed in table 3.1, one would find that there is a probability of at least 1 in

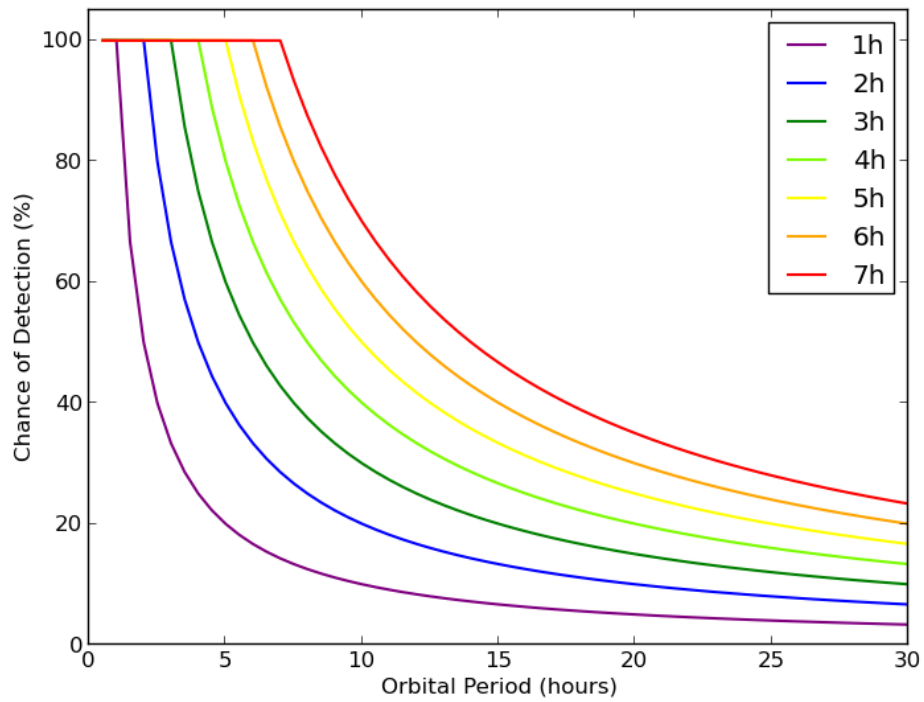


Figure 3.3: A plot of the probability of detecting a transit around a white dwarf for observing windows ranging between 1 and 7 hours, as function of the orbital period. The range of orbital periods was chosen based on the extent of the Habitable Zone of  $0.6 M_{\odot}$  white dwarf, as well as on the period of WD1145+017.

50 (or 2%) for a transiting planet to be hosted by a metal-rich white dwarf. Although this is only an upper limit, based on a relatively small sample, it indicates that eclipsing evolved planetary systems around this particular type of stellar remnants are rare, but should be easily detectable in a larger sample of stars and with a prolonged observing window and duration.

A further interesting comment on the results of this survey concerns white dwarf SDSSJ1228+1040. This star was observed as part of this survey for a cumulative time of  $\approx 8$  hours (Table 3.1). The collected light curves do not show any sign of significant photometric variability (i.e. greater than  $4\sigma$ ). However, Manser et al. (2019) find that this white dwarf is the host of a planetesimal, embedded in the debris disc, which orbits the star with a period of 123.4 minutes. Evidence for the presence of this planetary remnant was provided by a variability in the strength and shape of the Ca II emission line triplet. These findings reveal that, while no eclipse-like events are present, some of the stars in my sample may still be the hosts of unseen planetary systems which can only be detected spectroscopically.

### **3.3.4 SDSS J161717.04+162022.4**

SDSS J161717.04+162022.4 (or SDSS J1617+1620 hereafter) is a DA white dwarf with a circumstellar debris and gas disc. In particular, the gaseous disc shows evidence of spectroscopic variability in the Ca II emission lines (Wilson et al., 2014). While most white dwarfs showing evidence for this gas emission are also hosts of dust discs detected through IR excess, only a small fraction of metal-polluted white dwarfs are found to be the hosts of gaseous discs (e.g. Gänsicke et al., 2007; Vennes et al., 2010; Klein et al., 2011; Farihi et al., 2012).

Both types of discs are found around white dwarfs with temperatures between  $\sim 13,000$  K and  $\sim 22,000$  K (Gänsicke et al., 2006a, 2007, 2008; Dufour et al., 2012; Farihi et al., 2012; Melis et al., 2012). The formation of such systems is therefore not universal, and the reasons for this still remain uncertain.

The radius of the gas disc around SDSS J1617+1620 is found to be  $\sim 0.5$ - $1.5 R_{\odot}$ . Since only a low fraction of white dwarfs show evidence for gaseous discs, and a high surface temperature is required for Ca II emission, one can rule out that the gas originates from sublimating dust within the radiation field of the star.

Wilson et al. (2014) obtained optical time-series spectroscopy of SDSS J1617+1620 between 2008 and 2014. In 2008 the data showed strong, double-peaked Ca II emission, which was then observed to steadily fade over the rest of the monitoring time. They therefore suggested two possible explanations for the formation of this transient feature. The first scenario sees the impact of a small body onto a pre-existing dust disc orbiting the white dwarf (Jura, 2008). The absence of Balmer emission lines in the spectra of the white dwarf suggests a body of rocky nature, such an asteroid or a small planetesimal. Upon impact with the debris disc and after entering the Roche lobe, the incoming asteroid would start breaking up and vaporising. Subsequently, the gas would spread into a disc due to viscous angular momentum, and heating by radiation from the white dwarf would result in the observed Ca II emission. The weakening of the emission lined observed over time could be explained by the gas eventually being accreted onto the white dwarf, thus decreasing in density.

A second, similar scenario instead assumes that the dust disc around SDSS J1617+1620 is young, and the Ca II emission is due to the disc impacting a debris tail left behind by the original disruption of planetary bodies.

Simulations of the tidal disruption of a rubble pile asteroid over many orbital cycles showed that the debris forms a highly eccentric and collisionless ring, unless additional forces come into play (Veras et al., 2014). In order to fan out the debris train and form a close-in circular circumstellar disc, forces such as sublimation are required over many orbital cycles, which implies time-scales of up to thousands of years. During this period of time, there would be multiple impacts from leftover debris. It would therefore be expected to see another flare-up of gas emission in the next decade. Although spectroscopic variability is well sampled, no evidence for photometric variations have ever been published. Upon observing this object in July 2017, I detected a  $\sim 1\%$  modular variation in its light curve (Figure 3.4).

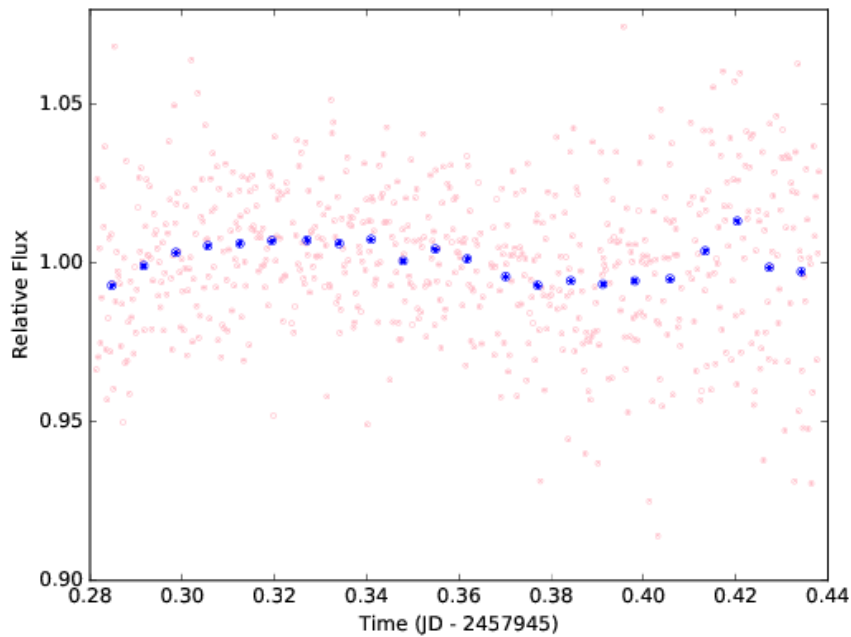


Figure 3.4: A light curve of the photometric data collected for SDSS J1617+1620 on 10 July 2017. A clear,  $\sim 1\%$  peak-to-peak variation is noticeable in the data. The pink data points represent the unbinned data collected. The blue data points show the data binned to intervals of 10 minutes.

The variability was subsequently confirmed by the Discrete Fourier

Transform (DFT). Figure 3.5 shows a significant peak at a period of  $\sim 9.571$  cycles/day ( $\sim 2.51$  hours). In the plot, the red dashed line and the blue dotted lines represent the amplitude value equivalent to three and four times the median values ( $3\langle A \rangle$  and  $4\langle A \rangle$ ), respectively. The highest peak in the DFT has an amplitude equal to  $\sim 3.73$  times the median value and is therefore a significant detection.

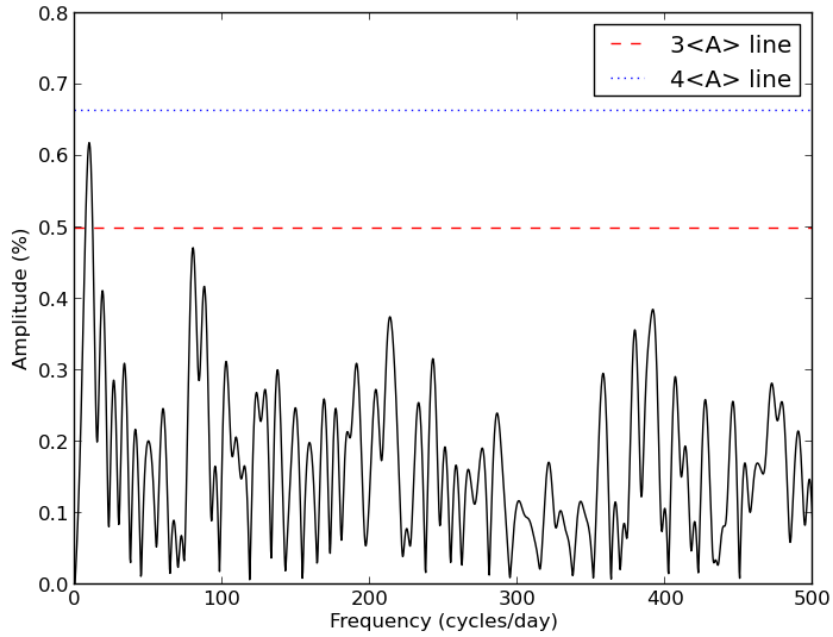


Figure 3.5: A plot of SDSS J1617+1620 discrete Fourier Transform. The red dashed line represents the  $3\langle A \rangle$  limit, while the blue dotted line represents the  $4\langle A \rangle$  limit.

Due to the results of this observation, further follow-up observations were scheduled and carried out in the months of April and May of the following year (details can be found in Table 3.4). Unfortunately, due to weather and scheduling restrictions, none of the follow-up observations were long enough to sample a full period. Moreover, adverse weather conditions affected the

Date of Observation	Length of Observation (hours)	Airmass	Exposure Time (s)	Filter
22/04/18	1.5	1.52-1.88	60	None
16/05/18	1.5	1.58-2.03	60	None
23/05/18	1	1.52	60	None
26/05/18	2	1.53-2.04	60	None
29/05/18	1	1.55	60	None

Table 3.4: A table showing dates and lengths of all photometric follow-up observations of SDSS J1617+1620.

quality of the data, resulting in a scatter in the data sets much larger than the  $\sim 1\%$  variability I previously detected. No variation was detected in the follow-up photometric data.

The photometric variability could shed a new light on the source of the Ca II emission variations, by confirming the hypothesis of an unseen, disrupting body embedded in the circumstellar disc. To obtain further proof that could confirm or disprove the presence of an unseen companion, time-series spectroscopic data is required to search for radial velocity variations.

To achieve this, I submitted a proposal to the Isaac Newton Group of Telescopes, in order to observe SDSS J1617+1620 with the Intermediate-dispersion Spectrograph and Imaging System (ISIS) mounted on the William Herschel Telescope (WHT). I was awarded one night in the 2018A semester to observe the object using both the red and blue arms of the instrument simultaneously, allowing both the  $H\beta$  Balmer absorption line and the Ca II emission lines to be observed. The proposal was accepted on 20 December 2017 and time was awarded, and the observation was queued as part of the service program with a high priority status. The observations were finally carried out in August 2019, and I was therefore unable to carry out the analysis before

the submission of this work.

Both scenarios suggested by Wilson et al. (2014) to explain the source of the Ca II emission variability involve the presence of a planetary remnant interacting with the disc. If this were to be the case, the photometric variability detected in the SAAO observation of SDSS 1617+1620 could be the result of these planetary debris embedded in the disc and reflecting some of the radiation from the white dwarf. Radial velocity variations resulting from the analysis of time-series spectroscopy (e.g. Manser et al., 2019) will enable us to confirm whether this white dwarf does have a hidden planetary companion, and provide us with some constraints on the mass of this object.

### 3.4 Summary

Following the discovery of the disrupting planetesimal orbiting WD 1145+017, I undertook a ground-based survey of 52 metal-polluted white dwarfs in search for similar systems as to the one mentioned above.

Out of the sampled white dwarfs, none showed eclipse-like features in their light curves. If an object like WD1145+017 were to be observed as part the sample, 2% of surveyed objects would show transits. This represents an upper limit, indicating that such systems are rare, but should be easily detectable when surveying a larger ( $\sim 1000$ ) number of stars.

Moreover, two objects (SDSS 1617+1620 and WD 1201-049) presented sinusoidal modulations of 1% and 2% respectively. SDSS 1617+1620 is known to have a strongly variable Ca II emission line in its spectrum. Upon discovery, it was suggested that this spectroscopic variability could be due to a disrupting planetary remnant interacting with the already present debris disc around the

star. I therefore applied for – and obtained – time to collect time-series spectra using the ISIS instrument mounted on the William Herschel Telescope in La Palma. Time was awarded as part of the service queue, and observations did not take place in time to be submitted as part of this work.

WD1201-049 will be further discussed in Chapter 4.

## Chapter 4

# WD1201-049: A Variable White Dwarf in the DAZ Survey

WD1201-049 was first identified as a hot, hydrogen rich (DAO) white dwarf in a survey lead by Gianninas et al. (2010). The star has an effective temperature of 57,260 K, and a surface gravity of  $\log g = 7.61$  (with a mass of  $0.55 M_{\odot}$ ). Specifically, the presence of a carbon absorption line (C IV, at wavelength 4658 Å) classifies it as a DAOZ white dwarf. The intensity of the C IV line has been observed to decrease in strength over the span of almost six years, which could indicate diffusing of metals out of the atmosphere as the star cools.

A short-cadence observation from my photometric survey on metal-rich white dwarfs revealed a photometric variability sinusoidal in nature. Although no eclipse was recorded, the variability could indicate an unseen companion, which may also be responsible for the presence of metals in the stellar atmosphere.

In order to help determine the cause of variability, the next steps re-

quired obtaining follow up data, both photometric and spectroscopic. Observing the star using different photometric filters was needed to determine whether the variability is caused by an unseen substellar companion orbiting the star. As described by Maoz et al. (2015), a cool, tidally locked companion at a short orbital distance from a white dwarf would have one half of its surface constantly irradiated by the white dwarf. The sub-stellar object would consequently re-emit the acquired thermal energy, and as a result a sinusoidal variation would be observed as the orbital phase of the object changes. Due to the thermal radiation being mostly re-emitted at redder wavelengths, the amplitude of the modulation is expected to increase when observed through a red filter (e.g. Casewell et al., 2015). Another strategy that can be adopted to confirm the presence of an unseen companion is looking for radial velocity variations in the spectral absorption lines of the star. This can be achieved by obtaining time-series spectroscopy data, later discussed in section 4.3.2.

## 4.1 Observations

WD1201-049 was first observed for  $\sim 5$  hours, as part of my photometric metal-rich white dwarf survey on 26 March 2017. The observation was performed in white light. The data were subsequently reduced by means of the SAAO pipeline developed by Marissa Kotze<sup>1</sup>. Table 4.1 shows the photometric and astrometric properties of the object. Based on its luminosity, consecutive exposures of 10 seconds each were collected to reach the required signal, without saturating the nearby stars used as comparison objects.

As a result of the analysis, the photometric data showed sinusoidal

---

<sup>1</sup><https://shoc.sao.ac.za/Pipeline/>

Property	Value	info
Ra	12 04 21.65	
Dec	-05 13 26.5	
Distance	724.83±49.9 pc	Gaia
M <sub>WD</sub>	0.55 M <sub>☉</sub>	Gianninas et al. (2010)
FUV	14.509±0.0137	<i>Galex</i>
FUV	14.923±0.0109	<i>Galex</i>
G	16.53±0.0016	Gaia
<i>g</i>	16.326±0.0059	PAN-STARRS
<i>r</i>	16.8206±0.0065	PAN-STARRS
<i>i</i>	17.2496±0.0059	PAN-STARRS
<i>z</i>	17.5385±0.0094	PAN-STARRS
Y	17.354±0.34	VISTA
J	17.579±0.34	VISTA
H	17.784±0.344	VISTA
Ks	18.108±0.34	VISTA

Table 4.1: Photometry and literature parameters for WD1201-049.

modulations (see Figure 4.3, later discussed in Section 4.5.1). Hence, follow up photometric and spectroscopic observations were undertaken to establish whether the variability was caused by an unseen companion. New photometric data was collected on 28 April 2019 using SHOC in the I filter, searching for modulations with a higher amplitude. Furthermore, time-resolved spectra were collected over the course of 6 nights in April 2019 using the SpUpNIC (Spectrograph Upgrade: Newly Improved Cassegrain) instrument mounted on the 1.9 m telescope at SAAO. Instrument details are discussed in the following section.

## 4.2 Instrumentation - SpUpNIC

Both photometric and spectroscopic observations were obtained at SAAO facilities, using the 1.0 m and 1.9 m telescopes respectively. The SHOC instrument

mounted on the 1.0 m telescope was employed to obtain light curves, and technical details about this camera have been previously described in Chapter 3 (section 3.2).

Spectroscopic observations were obtained through the The Spectrograph Upgrade: Newly Improved Cassegrain (SpUpNIC, Crause et al., 2016) long-slit instrument mounted on the Grubb Parsons 1.9 m reflecting telescope. With a focal ratio of 18 at the Cassegrain focus, its focal length is 34.2 m. SpUpNIC was first mounted in 2015 as an upgrade to the previous low-resolution spectrograph (Cassie). The instrument is placed at the Cassegrain focus of the telescope, and the upgrade centred on replacing the collimator and camera optics, the detector systems as well as various electrical and mechanical mechanisms (Crause et al., 2016).

### **4.2.1 Instrument Layout**

The instrument (Figure 4.1) is attached to the Cassegrain weight plate, which is located behind the primary mirror. The setup can be divided into two sections, referred to as upper and lower box respectively. The upper box contains all the components that deal with acquisition and wavelength calibration processes. All of these components were part of Cassie and consequently improved, however none were replaced.

The lower box contains the spectrograph optics components (such as the collimator, camera and diffraction grating) and the detector. A new collimator was installed as part of the upgrade, as well as a new USB camera which helped streamline the acquisition process (Crause et al., 2016).

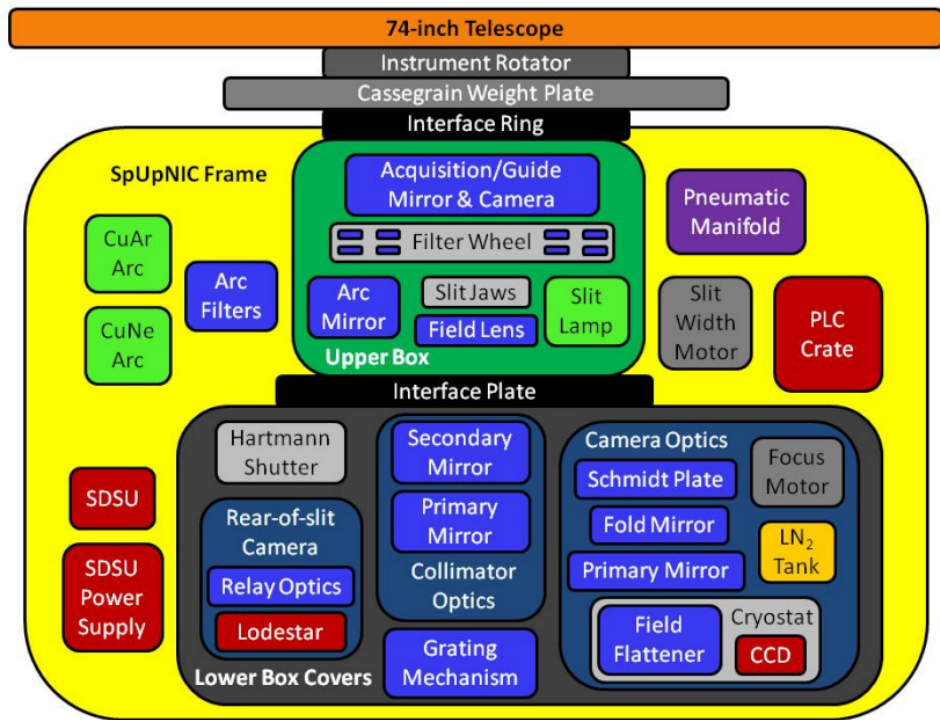


Figure 4.1: A diagram for SpUpNIC. The upper and lower boxes are represented by the dark green section and the black section respectively. The optical elements of the instrument are shown in blue, the electronic parts are red, and the lamps are light green. The yellow area represents the instrument frame attached to the telescope, which is coloured in orange (Crause et al., 2016).

## **Upper Box**

As previously mentioned, all the components present in the upper box were upgraded. That included revamping the acquisition/guiding camera, which is carried by XY slides that enable offset guiding while the telescope is exposing. The upgrade also included a new housing for the arc lamps, which are used to wavelength calibrate spectra. An upgraded slit mechanism was implanted, allowing the slit to be adjusted to widths between 0.15 and 4.2 arcseconds (with 0.15 arcsecond increments) depending on the atmospheric seeing conditions and the required resolution.

## **Lower Box**

The new components of the lower box constitute the real upgrade of SpUp-NIC. Crause et al. (2016) report the installation of a new carbon fibre cover that shields the apparatus from dust and light. While the diffraction gratings have not changed, a new housing was implanted to facilitate installation, and the gratings themselves were magnetically encoded to be automatically recognised; this way, grating information as well as wavelength identification can be directly identified by the software. Properties for all the gratings are listed in Table 4.2. Furthermore, a new Hartmann shutter (composed by a single shutter driven by two pneumatic cylinders) was added, allowing the spectrograph to be re-focussed daily and whenever a new diffraction grating is adopted (Crause et al., 2016). Moreover, to allow a reliable way of ensuring that the target is properly placed in the centre of the slit, a new camera was placed in the instrument to permanently view the slit from its rear. By moving a small mirror in the beam, one can hence check the positioning and focus of

Grating	Lines per mm	Blaze Wavelength ( $\text{\AA}$ )	Wavelength Range ( $\text{\AA}$ )	Dispersion ( $\text{\AA pix}^{-1}$ )	Resolving Power
G4	1200	4600	1250	0.625	2500
G5	1200	6800	1100	0.525	6500
G6	600	4600	2800	1.36	1000
G7	300	4600	5550	2.72	700
G8	400	7800	4100	2.21	1200
G9	830	7800	1700	0.835	2500
G10	1200	10000	950	0.470	5400
G11	600	10000	2600	1.25	1200
G12	300	10000	5600	2.75	1000

Table 4.2: Parameters for the available SpUpNIC gratings (Crause et al., 2016).

the target in the slit, before auto-guiding and exposing start.

## Software

All of the new and improved features of the SpUpNIC instrument can be controlled from a machine in the telescope control room. All the clients are bundled together and can be operated using a Python graphical user interface (GUI). The latter provides an interactive schematic of the instrument set up which can be used to configure the spectrograph for different functions such as observations, wavelength calibrations and rear-of-slit acquisitions. This enables the user to monitor the state of the apparatus in real time, thus avoiding time wastage due to taking long science exposures while one of the other mirrors were in the beam or while one of the arc lamps was accidentally left on. Furthermore, a quick-look data reduction GUI provides real time sky-subtracted and wavelength calibrated spectra, thus enabling the observer to check each science exposure (Crause et al., 2016).

## 4.3 Observing Strategy for WD1201-049

### 4.3.1 SHOC Observations

WD1201-049 was first observed in white light on 26 March 2017. As it was part of the metal rich white dwarf photometric survey, the purpose of which was to find eclipse-like events, it was first observed in white light to maximise the intensity of the signal. The target has a maximum magnitude (in the G filter) of  $\sim 16.5$  mag (see Table 4.1), and thanks to the favourable weather conditions, an exposure time of 10 seconds was chosen, in order to avoid saturation of the comparison stars surrounding the object. The star was then observed for  $\sim 5$  hours, obtaining 1740 images.

Follow up observations were then performed upon discovery of the object's photometric variability. To further investigate the possible source of variability, these observations were performed in the I filter with SHOC, as a red unseen companion would produce modulations with higher amplitudes at redder wavelengths. These data were obtained on 28 April 2019, and the observation had a duration of  $\sim 5$  hours. Due to the reduced signal intensity caused by the presence of a filter, as well as WD1201-049 having an  $i$  magnitude of  $\sim 17.25$  mag, the exposure time was increased to 120 seconds. A total of 150 images were collected.

### 4.3.2 SpUpNIC Observations

WD1201-049 has an effective temperature of  $\sim 57,000$  K and thus emits most of its light in the blue wavelength range. Therefore, a grating centred on shorter wavelengths was required to capture prominent absorption features such as the

Date	Number of Spectra	Exposure Time (s)	Seeing (arcsec)	Weather Conditions
03/04/19	4	1200	2.10	High/medium clouds
05/04/19	7	1200	1.95	High humidity
06/04/19	10	1200	2.54	Medium/low clouds
07/04/19	5	1200	1.95	Some clouds/rain
08/04/19	11	1200	1.05	High clouds
09/04/19	3	1200	2.24	High clouds

Table 4.3: Observing details and weather conditions for WD1201-049 spectroscopy with SpUpNIC.

$H\beta$  and  $H\gamma$  Balmer lines. Moreover, due to the scope of these observations, i.e. searching for possible minor changes in the radial velocity of the star to confirm the presence of an unseen companion, the highest possible resolving power was required. For these reasons, the best choice of grating was Grating 4. This offers a wavelength range between  $\sim 4000\text{--}5300$  Å when the grating is kept at the standard angle, and a medium resolution of 2500, resulting in  $\sim 1.85$  Å separation.

Furthermore, due to the G magnitude of the target being  $\sim 16.5$  mag (thus quite faint), the exposure time was set to 1200 s. Choosing a shorter exposure time would have not met the required S/N, while a longer exposure would have resulted into smearing of the variation in radial velocity, if present.

The star was observed over the course of 7 nights between 3-9 April 2019, however the night of April 4 was lost due to adverse weather. Table 4.3 shows details about the observations carried out on each night, such as number of consecutive exposures taken and weather conditions.

Finally, I used the CuAr lamp in order to take arcs before and after every science exposure. Each arc frame had an exposure time of 20 seconds.

## 4.4 Data Reduction

### 4.4.1 Reducing and Extracting Photometric Data

The photometric data was reduced using the SAAO data reduction pipeline developed by Marissa Kotze, and subsequently extracted performing aperture photometry, as previously described in Chapter 2 (section 2.2).

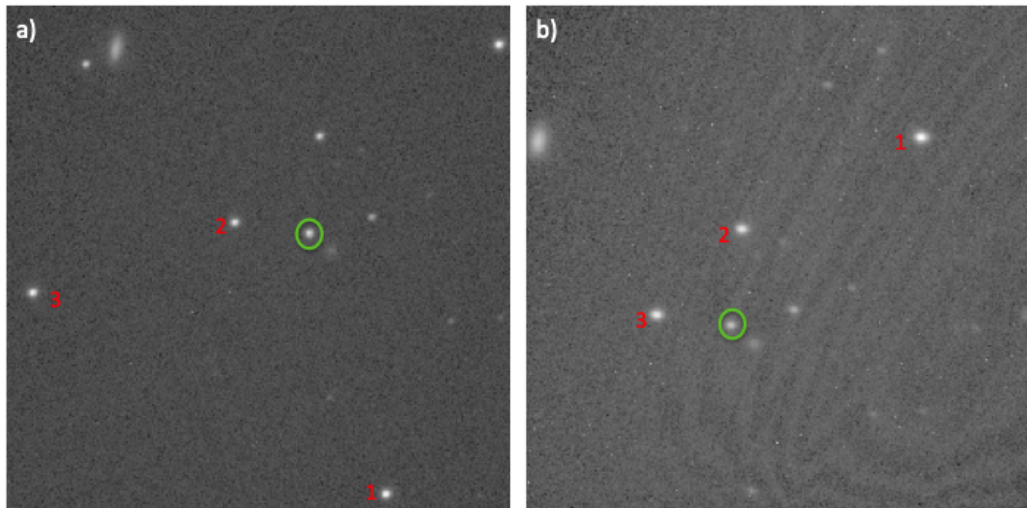


Figure 4.2: Examples of field of view (FOV) of the observations of WD1201-049 in white light (a) and I filter (b). In both panels, the target is circled in green and the comparison stars employed in differential photometry are marked with numbers from 1 to 3.

Upon extracting the light curves, the best signal to noise ratio was achieved using a 3 pixel aperture in white light, and a 5 pixel aperture in the I filter. To perform differential photometry on the target, three comparison

stars were chosen in the white light images, as shown in Figure 4.2(a). Due to the follow-up data being acquired two years later by a different observer, it was not possible to use the same three stars as comparison stars due to a difference in pointing, and instead the 3 stars shown in Figure 4.2(b) were employed. The comparison stars were individually inspected to ensure they were not variable objects, thus causing a false variability detection on the targeted white dwarf (for further details, see Section 4.5.1).

## 4.4.2 Reducing and Extracting Spectroscopic Data

Once obtained, I reduced and extracted the SpUpNIC spectra using the methods described in Chapter 2 (section 2.3). All the spectra were bias and flat field subtracted. I then extracted and wavelength-calibrated the spectra using arcs that were collected before and after each science exposure, to ensure maximum precision. Finally, I carried out the flux calibration by extracting and wavelength-calibrating the spectra of standard star Hiltner 600 (Hamuy et al., 1992, 1994). This is an spectro-photometric standard star of spectral type B1, with brightness  $V = 10.44$  mag. It is found at coordinates RA: 06 45 13.37 and Dec: 02 08 14.7. The star was observed each night, using an exposure time of 900 seconds.

## 4.5 Results

### 4.5.1 Preliminary Results

WD1201-049 was first observed as part of the ground-based survey of metal-polluted white dwarfs, previously described in Chapter 3. Upon visually in-

pecting the newly extracted white-light light curve, a clear modulation could be observed (Figure 4.3).

To confirm the veracity of the variation, as well as to better determine the period, PERIOD04 was used in order to produce a periodogram of the light curve. The resulting Fourier Transform showed a clear peak at  $\sim 6.723$  cycles/day ( $\sim 0.1487$  days), with an amplitude of  $\sim 0.9424\%$  ( $\sim 11$  times the mean amplitude value) as shown in Figure 4.4.

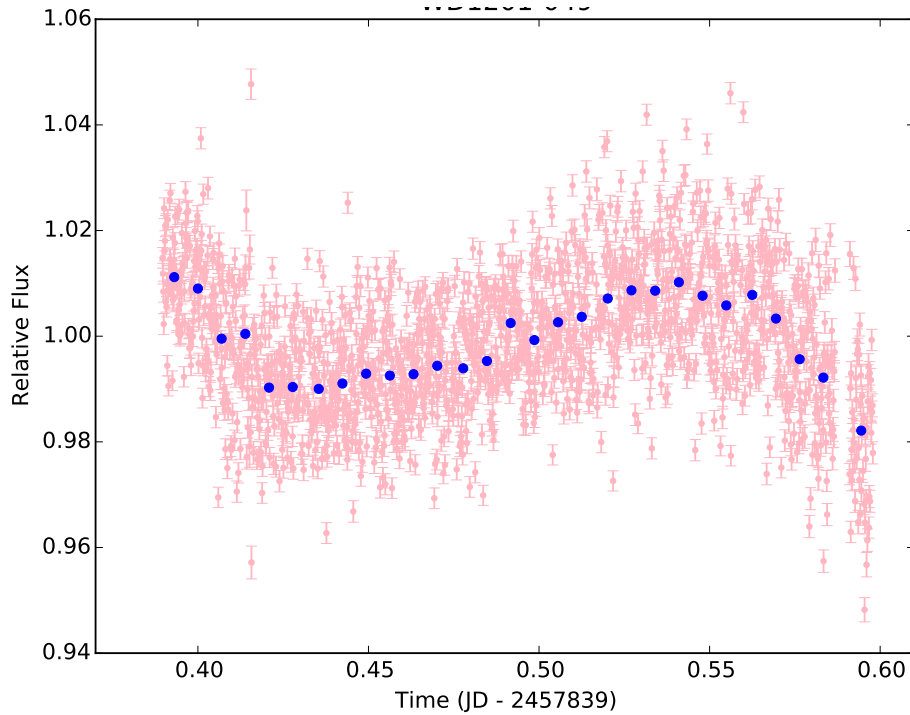


Figure 4.3: Calibrated light curve of WD1201-049, observed in white light. The pink data points represent the unbinned data collected. The blue data points show the data binned to intervals of 10 minutes. The light curve shows a sinusoidal modulation, with peak-to-peak amplitude of  $\sim 2\%$ .

A further step in confirming the variability consisted of inspecting the comparison stars used (both visually and through their periodograms) to ensure the same variability was not present in any of them, thus ruling out the

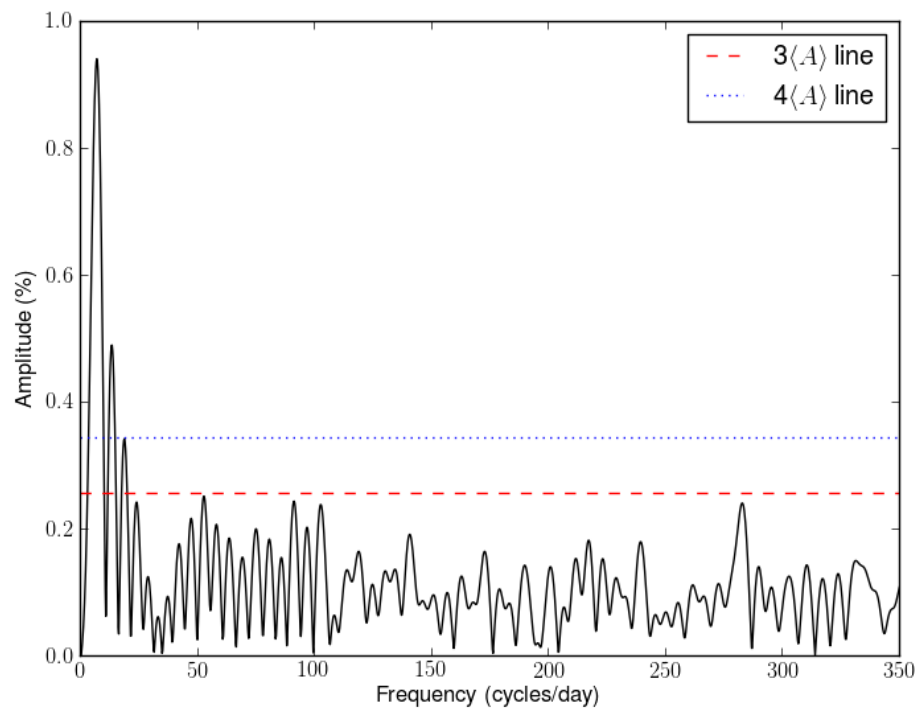


Figure 4.4: Periodogram of WD1201-049, as seen in white light. The red dashed line represents the  $3\langle A \rangle$  limit, while the blue dotted line shows the  $4\langle A \rangle$  limit.

chance of a false positive. Figure 4.5 shows a comparison between the target light curve and those of the three comparison stars. In the plot, the comparison stars were corrected and normalised through differential photometry and airmass correction in the same process as the target. The figure clearly shows the sinusoidal modulation in the target not being present in any of the other stars. This was further confirmed by the periodograms extracted from the comparison stars. The Fourier Transforms of these stars do not show any sign of variability at  $\sim 0.1487$  days, as shown in Figure 4.6. All three comparison stars do however present significant peaks at  $\sim 6$  hours. These are typical periodicities related to airmass correction and the observing window. A period of  $\sim 6$  hours corresponds to the approximate time a star spends in the sky at airmass  $\leq 2$ . As mentioned before, the effect of airmass on the brightness of a star is strongly dependent to the star’s colour. Consequently, differential photometry – and even a second-degree polynomial fitting – may not eliminate this effect completely, resulting in the alias observed in the three comparison stars.

A final method of testing the accountability of the variation is to ascertain whether the detected peak in the star’s periodogram is real. To do so, I used the method proposed by Alcock et al. (2000) and Lawrie et al. (2013b) to calculate the False Alarm Probability (FAP) of the significant peak. To measure the significance of the highest peak in the DFT the following equation was used:

$$S_g = \frac{A_{\max} - \langle A \rangle}{\sigma_A} \quad (4.1)$$

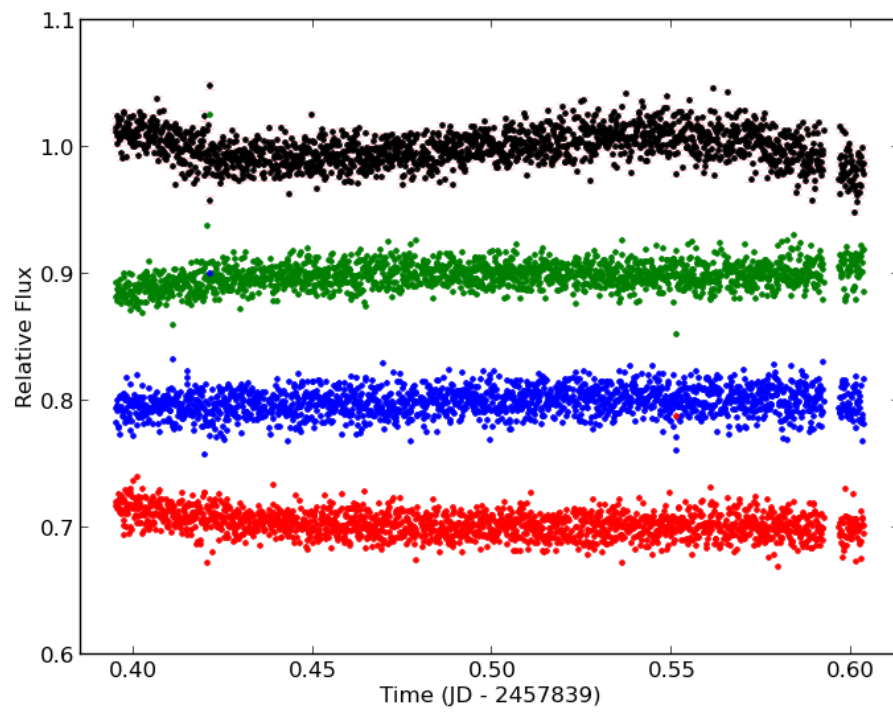


Figure 4.5: A plot of the calibrated and normalised light curves for WD1201-049 (black), and Comparison stars 1 (green), 2 (blue) and 3 (red).

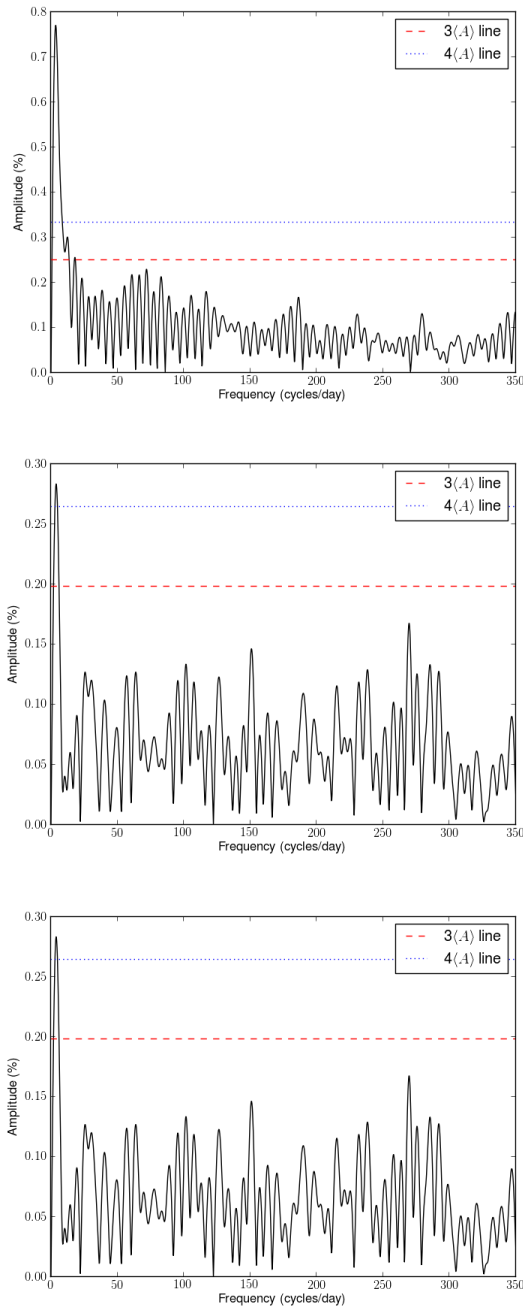


Figure 4.6: Periodograms for comparison star 1, 2 and 3 (top, middle and bottom panels respectively). The red dashed lines represent the  $3\langle A \rangle$  limit, while the blue dotted lines show the  $4\langle A \rangle$  limit. All three stars show a significant peak at  $\sim 6$  hours.

In equation 4.1,  $A_{\max}$  is the amplitude of the highest peak in the periodogram,  $\langle A \rangle$  is the average amplitude and  $\sigma_A$  is the standard deviation of the amplitude in the sampled frequency range. This procedure is carried out on the original light curve, as well as 1000 fake light curves generated by shuffling the target light curve at random. The periodogram analysis is carried out on each of the fake light curves, generating a probability distribution.

The FAP on the light curve of WD1201-049 amounted to 0.1% (i.e. the peak in the periodogram has a 99.9% significance), confirming the detected variability as real.

## 4.5.2 Follow-up Results - Spectroscopy

Once the photometric variability in white light was confirmed to be real, the next step in the analysis concerned searching for variability in the radial velocity of the white dwarf. If present, it would indicate the presence of an unseen companion. After extraction, the spectra were analysed using MOLLY. Details on how the software analyses spectroscopic data are discussed in Chapter 2 (Section 2.3).

### Trailed Spectra

MOLLY is capable of creating trails of spectra in velocity space, centred at the rest wavelength of a particular line. If the photometric variability observed in WD1201-049 were to be caused by an unseen companion and reflecting part of the light, we would expect to see evidence of such companion in the form of Doppler shift in the absorption lines of the star (e.g. Mayor et al., 1995). WD1201-049 did not show any sign of emission lines in its spectrum.

I chose to trail and model the  $H\beta$  hydrogen absorption line, which has a rest wavelength of  $4861.327 \text{ \AA}$ . I used MGFIT, as described in Chapter 2, to fit three Gaussian functions to the absorption line simultaneously (Figure 4.7). The three functions were given the same values for  $k$  and  $\gamma$ , but had different widths (FWHMs) and heights ( $h$ ). Each Gaussian was allowed to vary as  $\gamma + k \sin(2\pi\phi)$ , where  $\phi$  is the orbital phase. The continuum was fitted using a first-degree polynomial centred at  $H\beta$ .

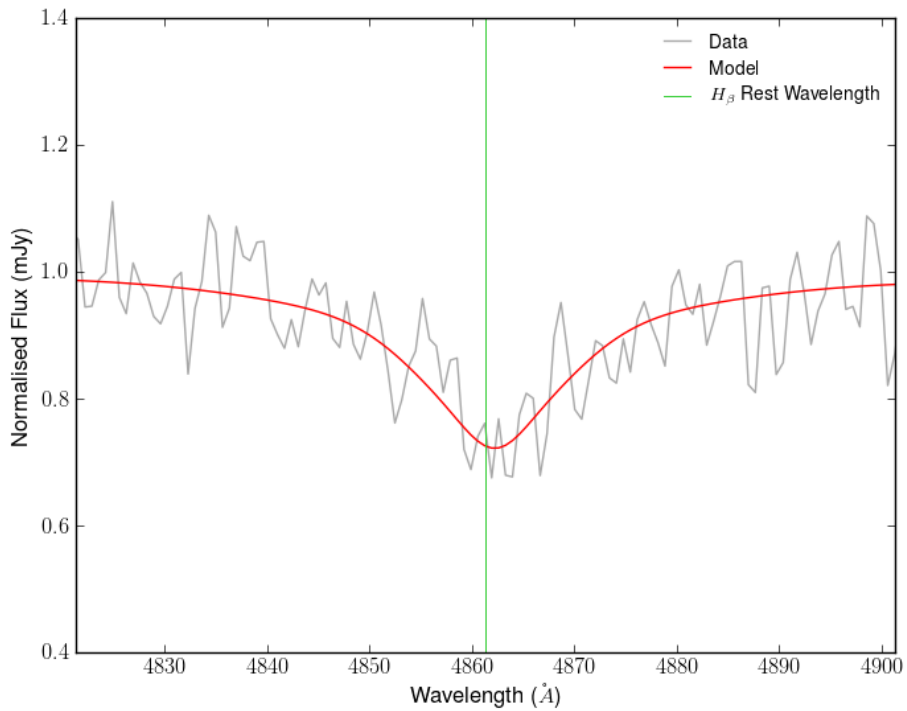


Figure 4.7: An example of the MGFIT model (red) applied to the  $H\beta$  line (dark grey). In order to reproduce the shape of the line, three Gaussian functions were fitted simultaneously. The continuum was fitted with a first-degree polynomial pivoted at the central wavelength.

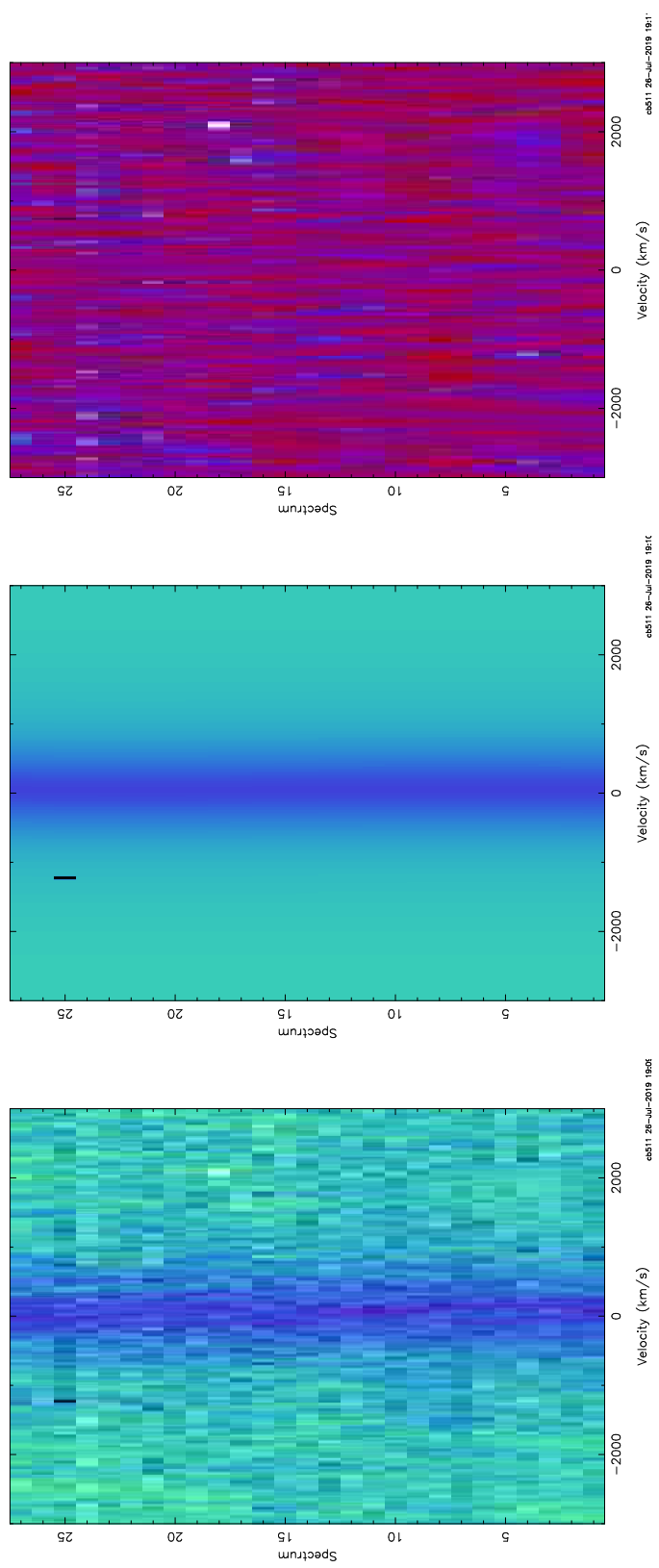


Figure 4.8: Trailed SpUpNIC spectra centred on the H $\beta$  absorption line. The plots show the data (left panel), the model generated from the Gaussian fitting (central panel) and the residuals to the fit (right panel).

The resulting model trail was subsequently subtracted from the trailed data, in order to test accuracy of the fit based on the value of the residuals (Figure 4.8). The model fit results showed  $k$  (the velocity offset) and  $\gamma$  (the systemic velocity) values of  $\gamma = 52.22 \pm 10.54 \text{ kms}^{-1}$  and  $k = 4.74 \pm 13.65 \text{ kms}^{-1}$ .

The high errors are due to the quality of the data, which directly depends on the brightness of the star, as well as the resolution of the spectra. The error on  $k$  is significantly larger than the value of  $k$  itself ( $\sim 3$  times larger), making this result imprecise. However, the model accurately fits the data, as shown by the  $\chi^2_\nu$  value of 0.41659 and the residuals to the fit in the third panel of Figure 4.8.

### 4.5.3 Follow-up Results: Photometry

Shortly after observing the white dwarf with SpUpNIC, WD1201-049 was observed again with SHOC, in the I filter. The observation was carried out in order to confirm the photometric variability, as well as to investigate any changes in the amplitude of the modulation. The presence of an unseen companion would increase the amplitude of the sinusoidal variation, due to the re-emitted light from the sub-stellar object being mostly at longer, redder wavelengths.

After performing aperture and differential photometry on the data, the resulting, normalised light curve is shown in Figure 4.9. In the light curve, no sign of sinusoidal modulation is visible, and similarly, the DFT does not present any significant peaks around the period detected in the white light data (Figure 4.10).

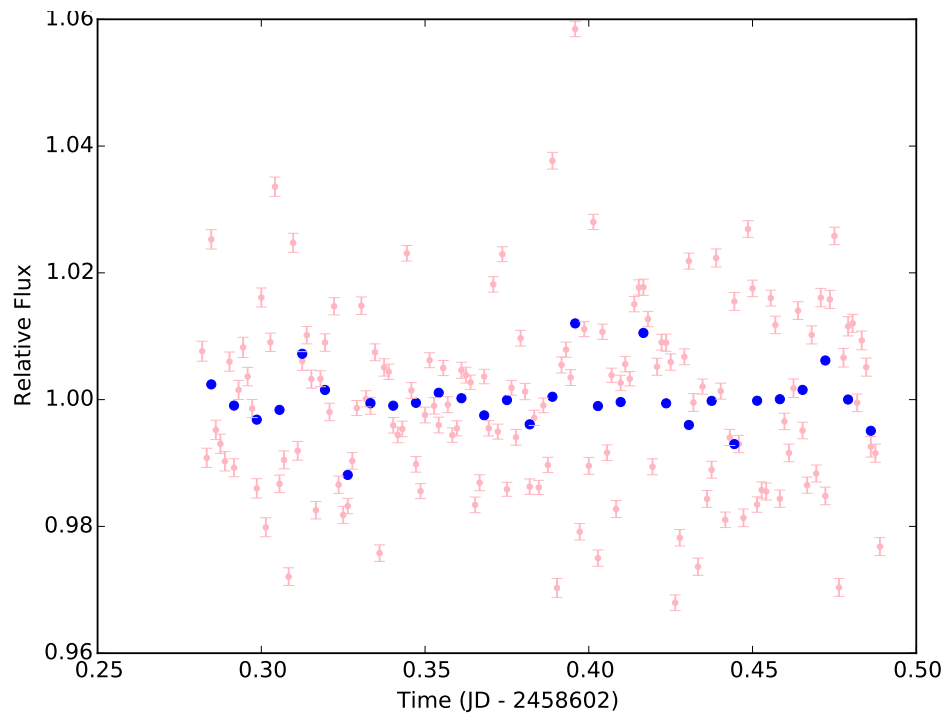


Figure 4.9: Calibrated light curve of WD1201-049, observed in the I filter. The pink data points represent the unbinned data collected. The blue data points show the data binned to intervals of 10 minutes. The light curve shows no sign of sinusoidal variation.

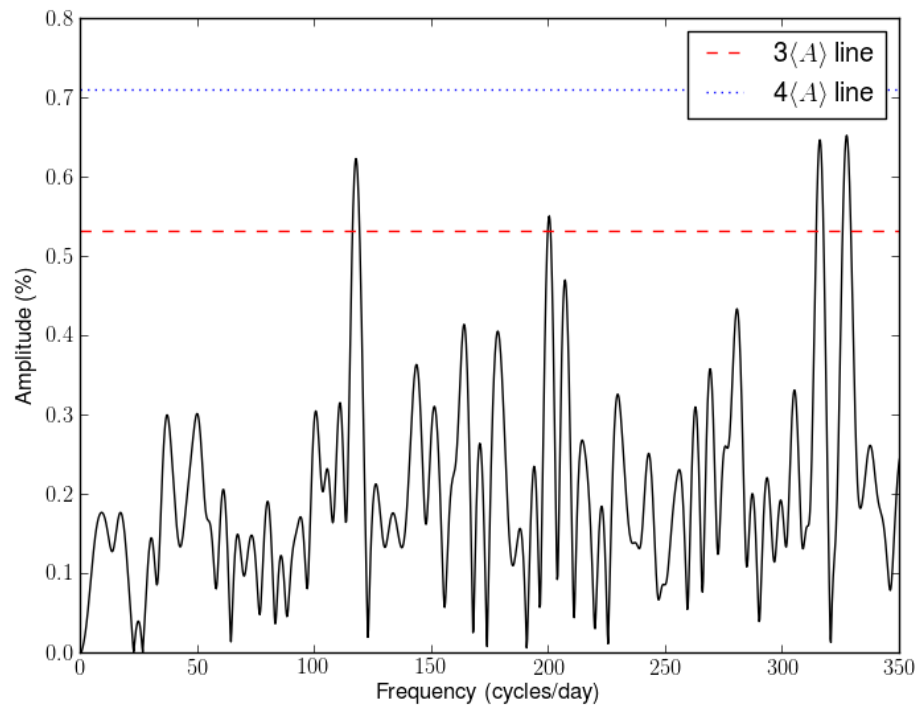


Figure 4.10: Periodogram of WD1201-049, as seen in the I filter. The red dashed line represents the  $3\langle A \rangle$  limit, while the blue dotted line shows the  $4\langle A \rangle$  limit.

## 4.6 Discussion

The lack of modulation in the follow-up I-filter photometric data suggests an unseen companion is unlikely. Therefore, it is not surprising that no radial velocity variations were noted in the stars spectral trail.

Further confirmation of the lack of a red companion can also be seen from fitting the photometry from Table 4.1 to a model white dwarf spectrum. To do this, I used a model white dwarf spectrum for a DAO white dwarf with  $T_{\text{eff}} = 57,200$  K and  $\log g = 7.61$ , generated by my colleague Simon Preval using TLUSTY and SYNSPEC, softwares by Hubeny and Lanz (1995) which produce 1-dimensional models of stellar atmospheres and spectra. Figure 4.11 shows WD1201-049 photometric data points in the UV (from *Galex*), visible (from PAN-STARRS) and infra-red (from VISTA) sides of the spectrum fitted to the model DAO spectral energy distribution (SED). While the data is generally in agreement with the model, there seems to be a lack of flux in the infra-red (especially in the Ks filter). However, if one considers the error on each data point to be  $1\sigma$ , the *Y*, *J*, *H* and *Ks* photometry still lies within  $3\sigma$  of the model. The larger error bars are also to be expected, due to the high effective temperature of the star.

The nature of the detected photometric variability in white light remains unsure. The absence of variability in the *I* filter, of radial velocity variations in the trailed spectra and of infra-red excess in the spectral energy distribution rule out the presence of an unseen companion. Gianninas et al. (2010) reports a significant decrease in the strength of the C IV line (at  $\lambda = 4658 \text{ \AA}$ ) in observations carried out between May 2004 and January 2010, and hypothesises that the metal is diffusing out of the atmosphere. Figure 4.12 shows the trail

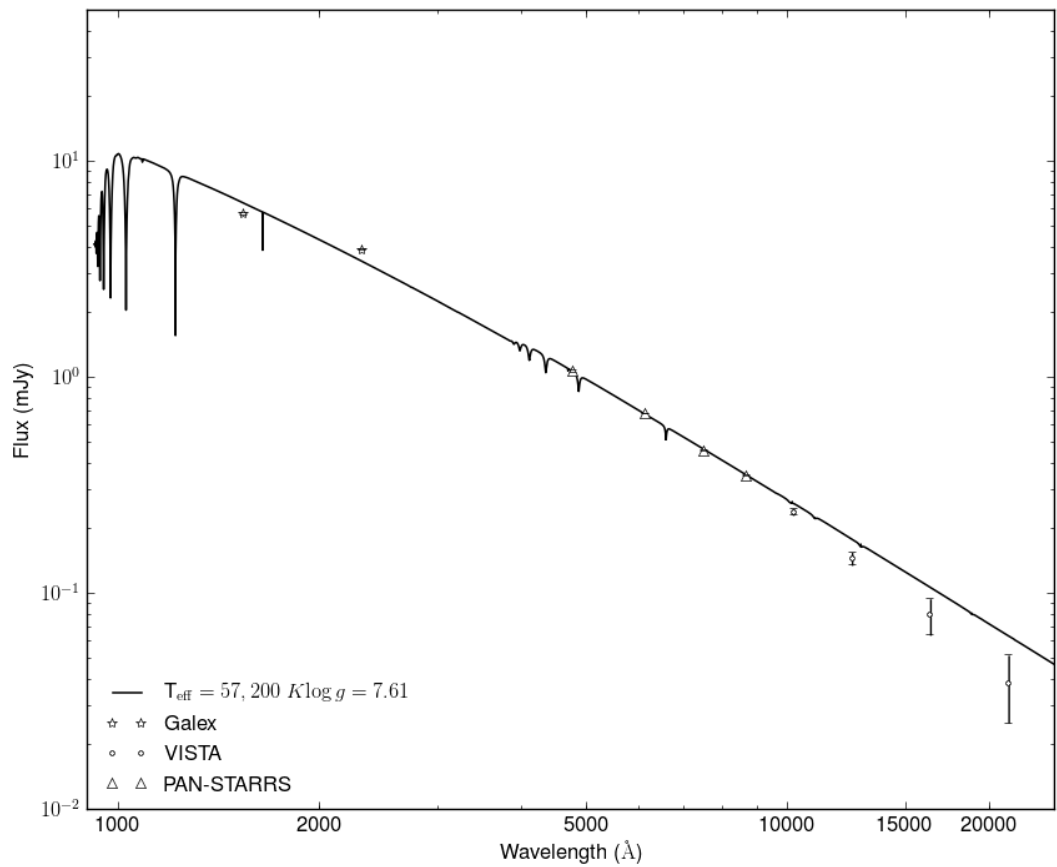


Figure 4.11: Model spectrum of a  $T_{\text{eff}} = 57,200 \text{ K}$ ,  $\log g = 7.61$  DAO white dwarf fitted to the photometric data from *Galex* (stars), PAN-STARRS (triangles) and VISTA (circles) of WD1201-049.

of spectra from the SpUpNIC data previously presented in this Chapter, this time centred at the C IV line. In the spectra, it is unclear whether the line is present, however this could be due to insufficient signal-to-noise.

A likely explanation for the observed, inconsistent variability could be given by sporadic accretion events onto the white dwarf's atmosphere from surrounding circumstellar material. The flow of accreting materials could create hot spots on the photosphere of the star, resulting in an inhomogeneous surface brightness (Maoz et al., 2015). The inhomogeneity is due to a fraction of the energy of the UV photons that are absorbed by the metals being re-emitted in the optical range of the spectrum, in a phenomenon known as fluorescence. Both Koester et al. (2014) and Maoz et al. (2015) find that 50% of metal polluted white dwarfs show evidence of this UV opacity. An extreme example of this is white dwarf GD 394, which shows extreme UV variations with an amplitude of 25% and a period of 1.15 days (e.g. Dupuis et al., 2000).

In this particular case, the accretion might not be happening in a steady flow, causing both the observed decrease in strength in the carbon line and the change in photometric variability seen in the SHOC data two years after the first observation. The star might be undergoing sporadic accretion events, followed by periods of quiescence. However, to confirm this hypothesis, extensive photometric observations in multiple filters are required.

Another possible explanation for the inconsistent variability arises from the discovery of a new system, shortly before the submission of this Thesis. Vanderbosch et al. (2019) report the detection of eclipsing circumstellar material around white dwarf ZTF J013906.17+524536.89. The star was observed for 210 days by the Zwicky Transient Facility (ZTF, Masci et al., 2019; Bellm et al., 2019). This system is substantially different from WD1145+017, pre-

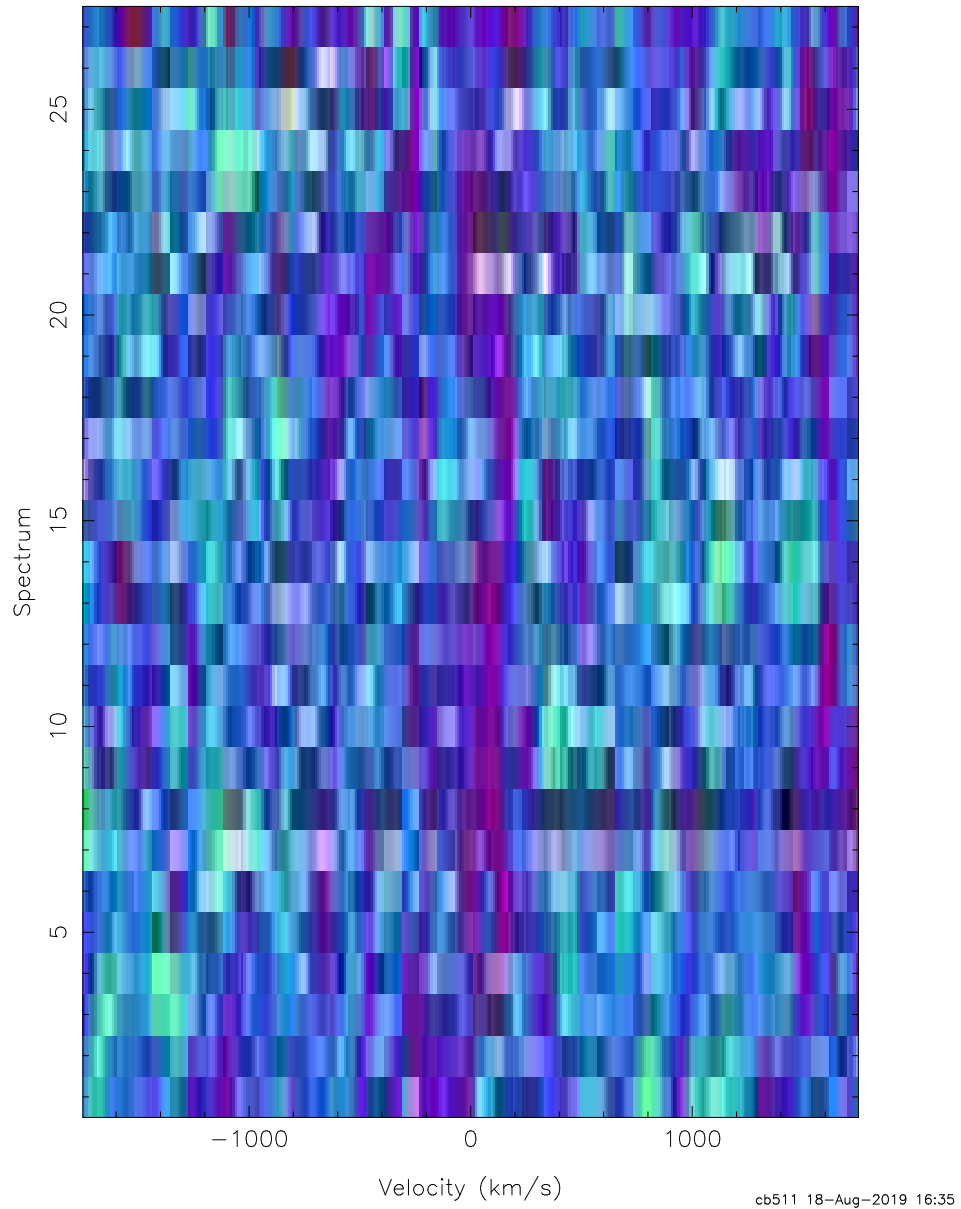


Figure 4.12: Trailed SpUpNIC spectra centred at the C IV line ( $\lambda = 4658 \text{ \AA}$ ) discussed by Gianninas et al. (2010). The trail does not show any evidence of C IV at this wavelength.

senting only two transits separated by  $\approx 110$  days, each lasting  $\approx 25$  days and showing depths of 30-45%. The variability in transit shape and depth is consistent with a cloud of disrupted circumstellar debris. With an orbit of 110 days however, the material is too distant from the star to be tidally disrupted. Vanderbosch et al. (2019) find the best explanation to be a highly eccentric ( $e > 0.97$ ) orbit (Veras et al., 2014), in which the circumstellar material passes within the white dwarf’s tidal disruption radius.

The ground-based survey I presented in this work was designed to detect systems similar to WD1145+017 (see Chapter 3). However, the discovery of ZTF J013906.17+524536.89 confirms the presence of planetary remnants at a wider range of orbital separations and eccentricities. The observed variability in WD1201-049 could hence be associated to one of these systems, in which irregular transits occur over longer timescales. This hypothesis can be verified through continuous photometric observations over the course of several days or weeks, thus increasing the likelihood of detecting another transit.

## 4.7 Summary

In this chapter, I presented the discovery of photometric variability in the light curve of WD1201-049. The white-light light curve shows evidence of sinusoidal modulations with a period of  $\sim 3.6$  hours and a peak-to-peak amplitude of  $\sim 2\%$ . The variability is not present in the three comparison stars employed in the differential photometry process, and the false alarm probability test confirms the periodicity to be of 99.9% significance. I first attributed the variability to the possible presence of an unseen companion, and therefore collected time-resolved spectra using SpUpNIC at the 1.9 m telescope

at SAAO, as well as follow-up photometric data in a redder filter ( $I$ ). The spectra revealed no variations in the radial velocity of the star. Similarly, no variability was detected in the  $I$ -filter photometry (which was collected two years after the original white light data). SpUpNIC is able to detect radial velocity variations down to  $\sim 10 \text{ km s}^{-1}$  (see Chapter 6). Assuming an orbital period equal to that of the measured variation, I used equation 2.6 to calculate the minimum detectable mass for an unseen companion, which amounted to  $0.02 M_{\text{Jup}}$ . Any brown dwarf sized body would have therefore produced a detectable radial velocity variation. Moreover, due to the high temperature of the white dwarf, even a Jupiter-sized body would have produced a detectable infrared excess due to irradiation. Therefore, the absence of an infra-red excess in the star's SED, the absence of radial velocity variations and the lack of photometric variability in  $I$  helped rule out the hypothesis of a sub-stellar companion to the white dwarf.

As magnetic dichroism can be also ruled out due to the high temperature of the host star, the most likely scenario is explained by inhomogeneous, sporadic accretion of circumstellar left-over metals to the star's atmosphere. However, this needs further investigation, requiring higher resolution spectroscopy to better sample the variability of the C IV metal line, as well as longer photometric observations in both white light and UV filters.

A second likely scenario arises from the discovery of disrupting material around white dwarf ZTF J013906.17+524536.89 (Vanderbosch et al., 2019), which eclipses the star every  $\sim 110$  days, with transit lengths of  $\sim 25$  days. This system provides evidence for the existence of eclipsing planetary material at much larger separations than WD1145+017. Extensive photometric observations of WD1201-049 would therefore help confirming whether the observed

variability is due to highly eccentric circumstellar debris eclipsing the star over large timescales.

## Chapter 5

# A New Eclipsing White Dwarf + Brown Dwarf System in the Kepler K2 Mission

In the early 1990's, the first exoplanet was discovered orbiting a pulsar (Wolszczan and Frail, 1992). As this was a rather unexpected location, the method used to detect the planet was very specific to this particular system; pulsars are known for their well-defined rotation periods, and the presence of a planet was determined by monitoring the variations in the star's pulse arrival times.

Since it was determined that planets exist outside of our Solar System, the scientific community devised a few methods to detect these systems. The first extra-solar system discovered by searching for radial velocity variations was that around 51 Pegasi (Mayor et al., 1995). Since then, hundreds of planets have been detected using this technique. However, when searching for planets around white dwarf stars, this method is not optimal. Planets usually produce small ( $\sim 2-100 \text{ ms}^{-1}$ ) variations in the velocity of their parent

stars. In order to detect these changes, large telescopes and high-resolution spectrographs are needed. Furthermore, due to the low brightness and pressure broadening of the white dwarf spectral lines, such small variations are not easily detectable. Where possible however, studying the variations in radial velocity remains an important step to determine some of the properties of sub-stellar companions to white dwarfs. If detectable in the spectral trails, these variations can provide a lower limit on the mass of the companion. In order to have a precise mass measurement, the inclination of the system needs to be known. This information, as well as information about the size of the companion, cannot be extrapolated from radial velocity data alone, and hence a complimentary method for planet detection must be used.

This second method involves a photometric search for variations in the light of the parent star. A transiting object will produce periodic dips in the stellar flux, with a characteristic ‘flat-bottomed’ shape. The first planet to be detected by this technique was HD209458b (Charbonneau et al., 2000; Henry et al., 2000), as part of a follow-up observation after radial velocity variations had been discovered in the system.

Upon inspecting the periodic dips in the stellar brightness, their shape provides information on the radius of the transiting object as well as on their inclination. The probability of detecting a planet transiting a star ( $P_{tr}$ ) is strictly dependent on the radii of both the star ( $R_*$ ) and the planet ( $R_{Planet}$ ), and the semi-major axis of the orbit ( $a$ ), as shown in the following expression (Faedi et al., 2011):

$$P_{tr} = \frac{R_* + R_{Planet}}{a} \quad (5.1)$$

Therefore, in order to maximise the chances of detection, one requires a large planet to orbit a small star at a short orbital distance. This way, the transits will be deeper, increasing the chance of observation even at lower levels of signal-to-noise ratio, and will occur more often, increasing the probability of being observed and confirmed.

For main sequence stars, dips tend to be rather small – a Jovian planet would only produce a variation of  $\sim 1\%$  when transiting a solar-type star – and will occur over larger periods of time. Hence, the best observing strategy is to monitor several thousands of objects for extended periods of time. However, the small ( $\sim R_{\oplus}$ ) size of typical white dwarfs and the short separation at which we expect to find their sub-stellar companions make this the best method of detection. Moreover, as my previous ground-based survey (discussed in Chapter 3) proved, smaller telescopes are still able to detect variations of  $\sim 1\%$  in the light curves of these stars, thus facilitating the data collection process.

One of the largest, ground-based surveys aimed at searching for transiting extrasolar planets was the Wide Angle Survey for Planets (WASP, Polacco et al., 2006), which was able to detect  $\sim 130$  planets using a grid of small camera lenses. WASP’s cadence and precision, as well as its observational constraints (such as the Earth’s orbital phase and the day/night cycle) only allowed the discovery of gas giant planets in relatively short orbits ( $\sim$ days). The newest large-scale survey for transiting is the Next Generation Transit Survey (NGTS, Wheatley et al., 2018) which has now allowed the discovery of smaller, Neptune-sized planets in short period orbits to be detected (e.g. West et al., 2019), due to the survey’s focussed search for systems around small, red main sequence stars (for details about the NGTS survey, see Chapter 6).

While a vast number of planets has been discovered orbiting main sequence and even evolved stars, other sub-stellar objects - known as brown dwarfs - seem to be much rarer.

A brown dwarf is defined as a celestial object massive enough to be able to ignite deuterium burning in its core, but not enough to burn hydrogen into helium (Boss et al., 2003). Hence masses for these bodies span between  $\sim 13 M_{\text{Jup}}$  and  $\sim 80 M_{\text{Jup}}$ . The lack of these objects as companions to main sequence stars is known as “brown dwarf desert”. For instance, Grether and Lineweaver (2006) found that  $\sim 16\%$  of solar-type stars have close companions (with orbital periods shorter than 5 years) with higher masses than Jupiter, but less than 1% of these are brown dwarfs. Steele et al. (2011) found that brown dwarfs in close systems with white dwarfs are an even rarer occurrence, with only 0.5% of white dwarfs hosting such companions. To date, only nine of these systems are confirmed to be in non-interacting orbits (Dobbie et al., 2005; Burleigh et al., 2006; Casewell et al., 2012; Steele et al., 2013; Beuermann et al., 2013; Littlefair et al., 2014; Parsons et al., 2017; Rappaport et al., 2017; Casewell et al., 2018). Of these, only two are eclipsing. In this Chapter, I present my discovery of third known eclipsing detached white dwarf + brown dwarf system.

## 5.1 The Kepler Mission

Although ground-based surveys are an efficient way of searching for short-period planets around relatively bright stars, they are constrained by atmospheric factors such as airmass and weather, and other factors such as night-time length and the Earth’s orbital cycle around the Sun. In order to survey a

larger number of stars for longer, continuous periods of time ( $\sim$ years), space-based surveys are required, such as the Kepler Space Telescope. Although the Kepler Mission was not focussed on white dwarfs, the large field of view of the telescope still allowed to observe a significant number of these stellar remnants and their systems, such as the one later discussed in this chapter.

The original Kepler mission was first launched in March 2009. Its primary aim was to survey a sample of  $\sim 150,000$  solar-type stars in the constellations of Cygnus and Lyra, in order to detect Earth-like planets ( $\leq 2.5 R_{\oplus}$ ) in the habitable zone of their hosts.

### 5.1.1 Telescope Design

The Kepler Space Telescope (Borucki et al., 2004; Koch et al., 2010) (Figure 5.1) is a reflective Schmidt telescope. Its primary mirror has a diameter of 1.4 m, while the Schmidt corrector plate has a diameter of 0.95 m. It has a focal length of 1399.2 mm, and a focal ratio of 1.473.

The telescope has a total of 21 E2V CCDs employed to collect data, and an additional 4 are used for fine guidance. A field flattener was placed above each of these devices, in order to minimise the field curvature at the imaging plane, as well as to determine the telescope bandpass. Each CCD has a grid of  $2200 \times 2048$  pixels, resulting in a total of  $\sim 94.6$  million pixels. Each pixel has a size of  $27 \times 27$  micrometers, and covers an area of  $3.98''$  in the sky. Therefore, upon launch, Kepler had a total field of view of  $\sim 116$  square degrees. In November 2017, however, three of the science CCDs failed.

As the telescope was originally designed to only observe one field, so the fine pointing was designed to be maintained by 4 reaction wheels (one for

each axis, and a spare).

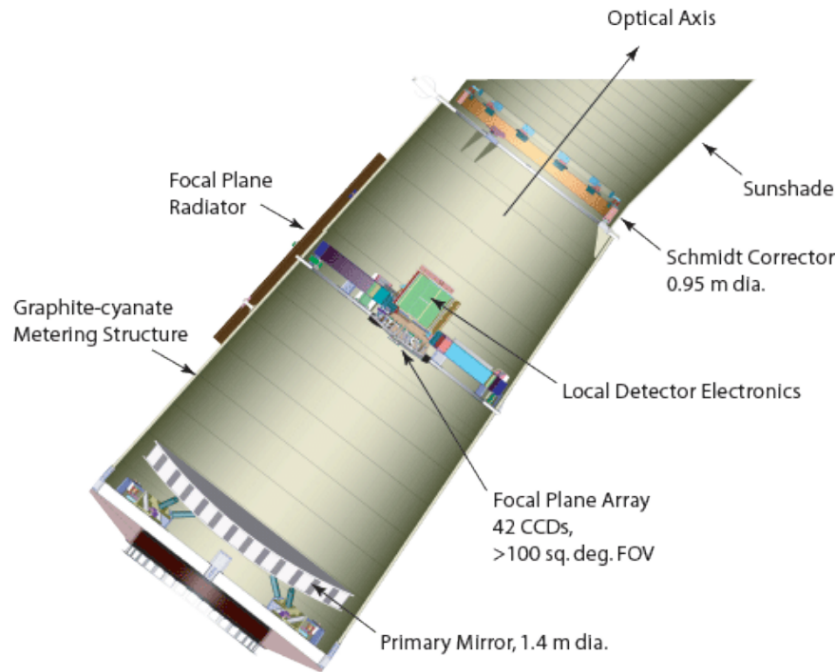


Figure 5.1: A schematic of the Kepler Space Telescope (from the NASA Kepler Instrument Handbook).

### 5.1.2 Original Mission Design

The original mission of the Kepler Space Telescope entailed observing the same field for a continuous period. The field was chosen to be in the constellations of Cygnus and Lyra, due to the location being rich in star (more than 100,000 stars) and observable throughout the year without interference from the Sun.

The telescope collected exposures with an integration time of 6.02 seconds, and a readout time of 0.52 seconds. As a standard procedure on all targets, 270 exposures were combined towards creating a longer cadence data point of 29.4 minutes. However, a small subset of targets ( $\sim 510$ ) were observed with a shorter cadence of 58.86 s, resulting from the combination of 9 single

exposures. The telescope only allowed 5.4 million pixels to be stored, therefore a pixel mask was applied to only record pixels around the selected targets and subsequently download them to the database on Earth. The photometric precision was suitable for the detection of planets around white dwarfs, amounting to  $\leq 15\%$  for an 18<sup>th</sup> magnitude star observed in long-cadence.

The original Kepler mission monitored the selected field for nearly four years. However, in May 2013 the second reaction wheel failed, and fine pointing could no longer be maintained, effectively putting an end to the mission.

### 5.1.3 The Kepler K2 Mission

The failure of the reaction wheel on one of the axes signified the end of the original purpose of the Kepler telescope. However, tests showed that the instrument could be repurposed and continue to take observations in a different *modus operandi* (Howell et al., 2014). By pointing the telescope along the ecliptic plane, solar pressure could be balanced across one axis and managed by the instrument's thrusters in case of any deviation. The other two axes could be maintained by the remaining two reaction wheels. This new observing strategy however was constrained by the Sun eventually entering the field of view of the telescope. Thus, instead of limiting the mission to observing one field, the schedule was divided into multiple campaigns, each observing one particular field for  $\sim 80 - 90$  days. In total, 19 campaigns were scheduled and performed, covering most of the ecliptic plane (Figure 5.2). The last campaign ended in September 2018, when eventually the thrusters ran out of fuel.

For each campaign, the telescope could be positioned either in the same or opposite direction compared to the direction of motion. The forward di-

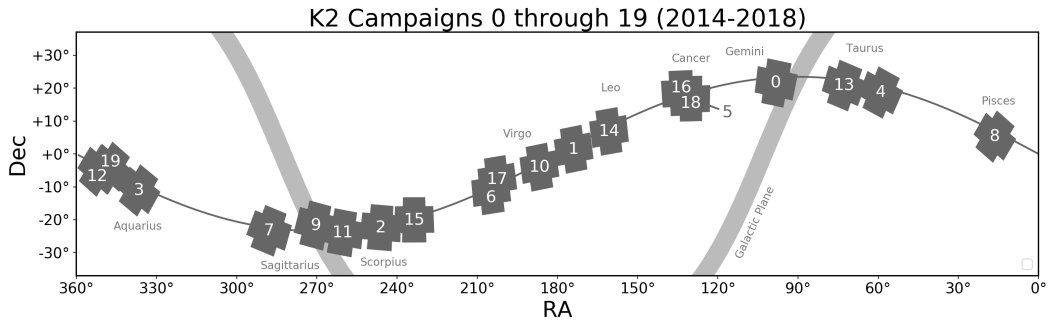


Figure 5.2: The proposed – and ultimately observed – Kepler K2 campaigns. The Kepler mission had to be repurposed after the failure of two reaction wheels. Each K2 campaign was observed for  $\sim 80$  - 90 days (Image credits: <https://keplerscience.arc.nasa.gov/>).

rection allowed ground-based observations to be performed at the same time as the campaign. Keeping the telescope in the reverse direction was however preferable as it minimised the chance of Earth passing through the field of view.

Following initial analysis, Howell et al. (2014) estimated the photometric precision to be two to four times worse than the original mission. This was due to the repurposing of the telescope operations. Even though solar pressure could keep the telescope relatively stable, accuracy in pointing had to be ensured by readjusting the positioning through use of the thrusters every  $\sim 6$  hours (or 0.245 days). In between these adjustments, targets would slowly drift out of their aperture, until the telescope would be brought back to its original alignment. Due to this, the raw K2 light curves present a very characteristic “saw-tooth” feature. The regular thruster firings also require for additional pixels to be added to the target masks, to ensure the targets remained within one mask at all times. Therefore, due to the limited number of storable pixels, the star sample in one individual field had to be reduced to  $\sim 30,000$  for long-cadence targets and  $\sim 130$  for short-cadence ones.

A final difference between the original and the K2 campaign concerned the selection of the observed targets. In K2, they were all proposed by members of the astronomical community. This was a great opportunity to search for planetary systems around objects such as white dwarfs, which were previously only marginally observed by the mission.

#### **5.1.4 Kepler and K2 Light Curve Processing**

Each time the data were downloaded from the Kepler Space Telescope, they were processed by the Kepler Science Operation Centre (Jenkins, 2017).

Initially, each pixel was corrected to remove instrument-related artefacts. This included bias, flat and dark current corrections, as well as any noise due to electronics. Subsequently, any background noise arising from cosmic rays, zodiacal light or similar occurrences was removed from each aperture. For each object, the aperture was tweaked to account for differences in pointing and focus. Aperture photometry was then performed to create light curves. The systematic errors produced by the telescope operations in the K2 mission were additionally calibrated either by the Kepler Guest Observer Office (Van Cleve et al., 2016) or using the Self Flat Fielding method (SFF) developed by Vanderburg and Johnson (2014). Any other outliers were then removed to produce a Presearch Data Conditioning (PDC) light curve (Jenkins, 2017).

The generated data were then uploaded to the Mikulski Archive for Space Telescopes (MAST). As well as the generated light curves, calibrated pixel files were also added to the archive, in order to allow the user to self-extract the light curves if required.

### 5.1.5 Target Selection

The white dwarf research group at the University of Leicester played a significant role in selecting and proposing white dwarf targets for the Kepler K2 campaigns. For each campaign, spectroscopically identified white dwarfs brighter than 19.5 magnitudes were selected in order to search for eclipse-like events in their light curves.

The targets were identified by my colleague Ian Braker (Braker, 2019) in a variety of catalogues, such as McCook and Sion (2016), SDSS (Kleinman et al., 2013; Kepler et al., 2015, 2016) and LAMOST (Guo et al., 2015). Moreover, any other targets from photometric catalogues with a  $>60\%$  chance of being white dwarfs were also included (Gentile Fusillo et al., 2015b,a, 2017). Generally, any white dwarf in a known binary system or with a brighter star in their immediate vicinity (within a few pixels) was not included in the sample. Due to these constraints, the number of surveyed targets in each campaign varied from a few tens to a few hundred objects.

Although the Kepler K2 mission was not the primary focus of my work, I was involved in the analysis of Campaign 14 observed white dwarfs, which consisted of 368 targets brighter than 20 magnitudes, in search for eclipse-like events. This campaign lasted 81 days (May 31, 2017 – August 19, 2017) and was centred at coordinates  $RA = 10:42:44$  and  $Dec = 06:51:06$ .

Running the analysis consisted in creating Discrete Fourier Transforms (DFTs) of the downloaded MAST light curves, in search for periodicities. In the presence of a significant peak in the periodogram of a star, the 81 day-long light curve was folded over the relevant period and then inspected to search for characteristic features as well as to confirm the veracity of the variation.

## 5.2 WD1032+011: A New Eclipsing WD+BD System - Discovery and Preliminary Results

In the process of analysing the K2 Campaign 14 data, one of the targets (EPIC248433650) showed a prominent eclipse-like feature, with a period of  $\sim 133$  minutes.

The target, known as WD1032+011, was first identified as a hydrogen-rich (DA) white dwarf by Vennes et al. (2002), as part of the 2df QSO survey. The object was surveyed by the Sloan Digital Sky Survey (SDSS), and those spectra were used by Eisenstein et al. (2006) to measure the star's effective temperature ( $T_{\text{eff}}$ ) and surface gravity ( $\log g$ ), which are  $9904 \pm 109$  K and  $8.13 \pm 0.15$  respectively. Later analysis of the star's Spectral Energy Distribution (SED) with data from SDSS and UKIDSS (UKIRT Infrared Deep Sky Survey) revealed an infra-red excess indicative of a redder substellar companion, most likely a brown dwarf of class L5 and mass of  $55 \pm 4 M_{\text{Jup}}$  (Steele et al., 2011). All photometric parameters are shown in Table 5.2.

The number of observed brown dwarfs in eclipsing systems with their host stars is very low. About 20 of these objects are known to exist in close orbits around main sequence stars (e.g. Grether and Lineweaver, 2006). Previous to my discovery discussed in this chapter, only 5 non-interacting eclipsing brown dwarfs had been confirmed to be in the post-common envelope stage of the binary evolution. Three of these are found around hot subdwarf stars (Geier et al., 2011; Schaffenroth et al., 2014, 2015), and two around white dwarfs: SDSS J141126.20+200911.1 (Beuermann et al., 2013; Littlefair et al.,

Property	Value	info
Ra	10 34 48.93	
Dec	+00 52 01.4	
Distance	326.78±45.58 pc	Gaia
M <sub>wd</sub>	0.68±0.1 M <sub>⊙</sub>	Steele et al. (2011)
K2	19.073±0.01	K2
fuv	22.670±0.224	<i>Galex</i>
nuv	20.152±0.037	<i>Galex</i>
<i>u</i>	19.547±0.032	SDSS
<i>g</i>	19.034±0.010	SDSS
<i>r</i>	19.076±0.012	SDSS
<i>i</i>	19.169±0.019	SDSS
<i>z</i>	19.240±0.076	SDSS
<i>Y</i>	18.820±0.042	UKIDSS LAS
<i>J</i>	18.648±0.056	UKIDSS LAS
<i>H</i>	18.202±0.107	UKIDSS LAS
<i>K</i>	18.034±0.141	UKIDSS LAS

Table 5.1: Photometry and literature parameters for WD1032+011.

2014) and SDSS J120515.80-024222.6 (Parsons et al., 2017).

### 5.2.1 Photometry: Kepler K2

I initially retrieved the light curve for WD1032+011 provided by the Kepler Guest Observer Office (Van Cleve et al., 2016) from MAST, in order to run a preliminary periodogram and hence detect any significant variability. To perform this, I used the NASA Periodogram Tool provided by the NASA Exoplanet Science Institute<sup>1</sup>, which uses the Lomb-Scargle method (Lomb, 1976; Scargle, 1982) to produce a Fourier Transform of the data. Although a matched transit filter algorithm might be more effective to detect transit-like events, due to the large number of data points in the Kepler K2 light curves, as well as the long cadence of the data, I found that using Discrete

<sup>1</sup>(<https://exoplanetarchive.ipac.caltech.edu/cgi-bin/Pgram/nph-pgram>)

Fourier Transforms (DFTs) as a detection tool was sufficient. This is further supported by the discovery of WD1145+017 in the Kepler K2 data.

The software identified a period of  $\sim 0.092$  days (approximately 2.2 hours). I proceeded to fold the original light curve file over the detected period (Figure 5.3) and finally binned it (Figure 5.4). The phase-folded light curve clearly reveals a primary eclipse feature, which however appears shallower and broader than a companion to a white dwarf in such period would be expected to produce. This is due to the short  $\sim 6$  s exposures being combined into a cadence of 29.4 minutes, which covers approximately one quarter of the  $\sim 133$  minute orbit.

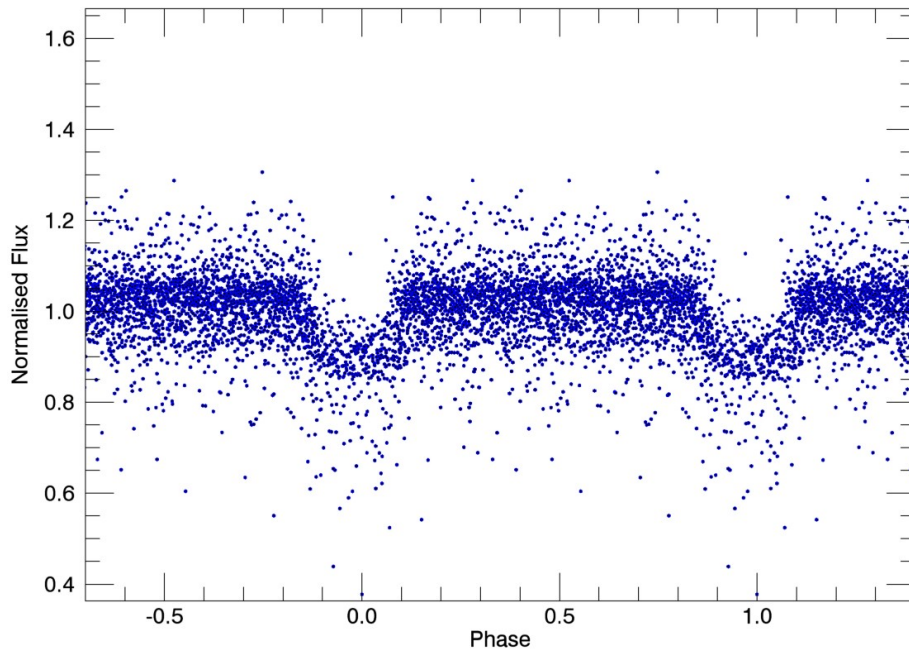


Figure 5.3: The phase-folded K2 light curve of WD1032+011, on a period of  $\sim 0.092$  days. The plot displays two periods for clarity. Eclipse-like features are clearly present, although they appear shallower and broader than they are in reality, due to K2 long cadence of 29.4 minutes.

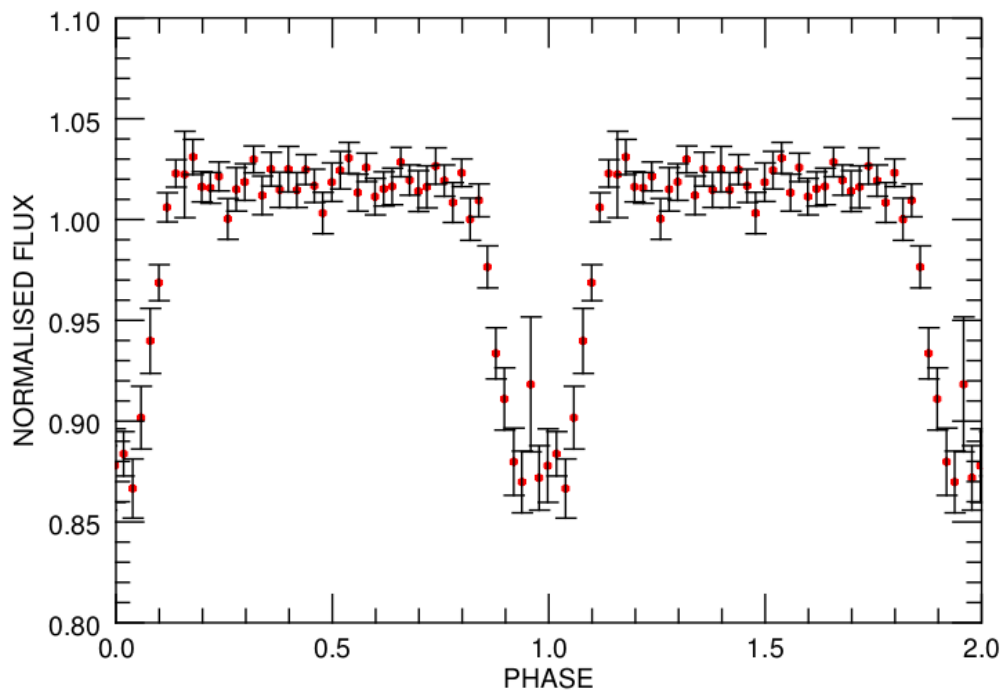


Figure 5.4: The binned and phase-folded K2 light curve of WD1032+011, on a period of  $\sim 0.092$  days. The plot displays two periods for clarity. The primary eclipse feature is evident. No sign of a secondary eclipse (which should appear at phase 0.5) is present.

Night	Filters	Seeing	Airmass	Exposure
20180119	$u'g'r'$	1.4''	1.24–1.36	6 s
20180123	$u'g'r'$	1.0''	1.56–1.77	6 s
20180119	$u'g'i'$	0.7''	1.41–1.49	4.5 s

Table 5.2: ULTRACAM observations of WD1032+011

### 5.2.2 Photometry: ULTRACAM

Due to the Kepler K2 long cadence altering the shape of the eclipse, follow-up photometry was needed in order to model the system and determine the radii of the two components and their inclination.

My collaborator Steven Parsons observed three eclipses of WD1032+011, over the course of two nights (19 and 23 January 2019) using ULTRACAM (Dhillon et al., 2007), mounted on the ESO New Technology Telescope (NTT). ULTRACAM is able to observe in three filters simultaneously, so data was collected in  $u'$ ,  $g'$  and  $r'$  bands for two of the eclipses, and  $u'$ ,  $g'$  and  $i'$  bands for the third one (Table 5.2). The data were reduced by collaborators using the ULTRACAM pipeline software. Once reduced, the source flux of the target was extracted performing aperture photometry on all the images, using variable aperture sizes, dependent on the source’s full width at half maximum. The flux for a comparison star in the field was also extracted and used to perform differential photometry on the target, thus eliminating any weather and atmosphere related variations. Ultimately, in order to achieve the required signal-to-noise ratio, the  $u'$  band data was coadded upon collection to an exposure time of 18 s (3 exposures per bin).

Since different comparison stars were used on different nights, the continuum level flux was determined for each light curve, and was then used to normalise each light curve to a continuum level of  $\sim 1$ . Finally, the light curves

in each of the observed filters were phase-folded over the period extracted from the K2 data.

### 5.2.3 Photometry: Brown Dwarf Spectral Type

Upon discovery of this eclipsing system, I created combined white dwarf-brown dwarf models in order to match them to the Galex, SDSS and UKIDSS photometry in Table 5.2.

The first step in creating a combined model involved producing a normalised model for the white dwarf at 10 pc. This was done by matching a  $T_{\text{eff}} = 10,000$  K and  $\log g = 8.0$  white dwarf model spectrum from Koester (2010) to the absolute magnitudes of a white dwarf with the same properties found in Holberg and Bergeron (2006); Tremblay et al. (2011). I then repeated the same process for a few brown dwarf spectral types (L3, L4, L5 and L6), this time sourcing the absolute magnitudes from Dupuy and Liu (2012) and the template spectra from Burgasser et al. (2004), Burgasser et al. (2010), Reid et al. (2006) and Cruz et al. (2004), which are archived in the SpeX Prism Spectral Libraries. The absolute magnitudes for both the white dwarf and the L dwarfs were converted into flux density  $F_\nu$  (measured in units of Janskys) through the following equation:

$$F_\nu = F_0 * 10^{-\frac{M}{2.5}} \quad (5.2)$$

where  $M$  is the absolute magnitude, and  $F_0$  is the zero-point flux of the relevant filter, obtained from the SVO Filter Service (Rodrigo et al., 2012). Moreover, as the flux densities of the template spectra was given as a function of

wavelength ( $F_\lambda$ ), these were converted into  $F_\nu$  using the basic formula:

$$F_\nu = \frac{\lambda^2}{c} F_\lambda \quad (5.3)$$

where  $\lambda$  is the wavelength (in m), and  $c$  is the speed of light (in  $\text{ms}^{-1}$ ). In the particular case in which the wavelengths are in units of Ångstroms, equation 5.3 can be rewritten as:

$$\frac{F_\nu}{Jy} = 3.34 * 10^4 \left( \frac{\lambda^2}{\text{Å}} \right) \frac{F_\lambda}{\text{erg cm}^{-2} \text{s}^{-1} \text{Å}^{-1}} \quad (5.4)$$

Once the spectra were all normalised to the same flux scale, I interpolated each one to ensure they all were on the same wavelength scale. Subsequently I combined the normalised white dwarf model spectrum with each of the brown dwarf normalised template spectra. I then normalised them all to the  $i$  band SDSS photometry, and plotted them with the Galax, SDSS and UKIDSS photometry data points (Figure 5.5). The UKIDSS magnitudes were consistent with the WD+L5 model of the system, as expected from Steele et al. (2011). These were however preliminary results, and an infra-red spectrum was required to better constrain the spectral type of the brown dwarf companion.

#### 5.2.4 Spectroscopy: FORS

Prior to my discovery of photometric variability, WD1032+011 had been observed by my collaborator Sarah Casewell as part of a bad-weather programme using the visual and near-ultraviolet FOcal Reducer and low dispersion Spec-

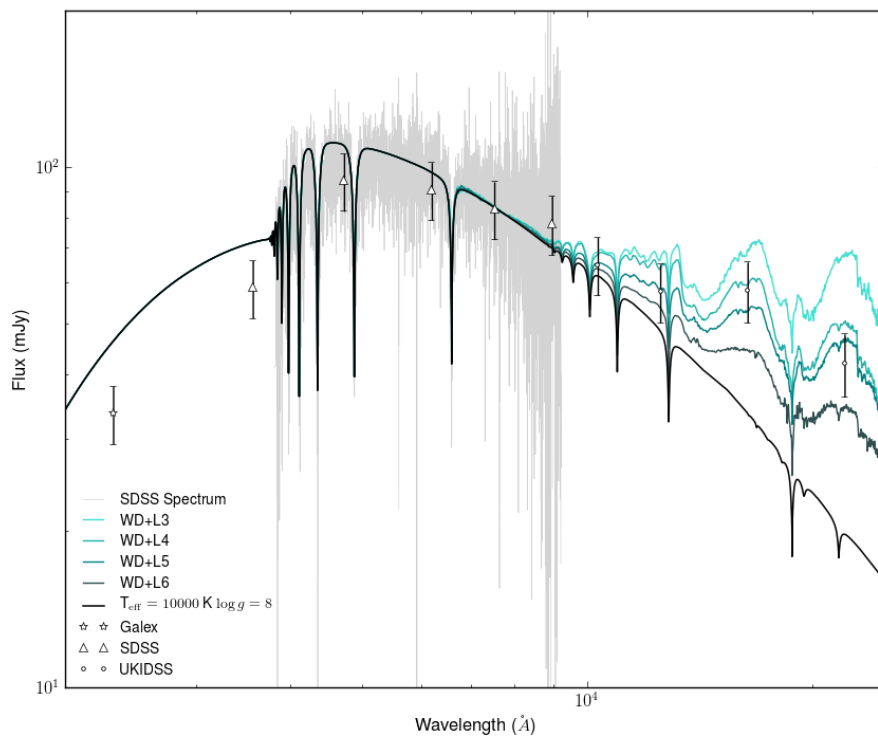


Figure 5.5: SDSS spectrum of WD1032+011 matched to various white dwarf + brown dwarf template spectra. The Gailex (stars), SDSS (triangles) and UKIDSS (diamonds) magnitudes are also shown.

trograph (FORS; Appenzeller et al., 1998), mounted on the Very Large Telescope (VLT). Using the G1200B grism and the 1" slit, they were able to sample most Balmer lines – including  $H\beta$ , but excluding  $H\alpha$ . The star was observed in blocks of one hour a night over the course of three nights (January 05-06-24, 2016). The collected spectra had exposure times of 420 seconds, resulting in 6 spectra for each of the 1-hour slots, and 18 spectra in total. The data were reduced using the FORS REFLEX pipeline (Freudling et al., 2013). A trailed spectrum was then created using MOLLY, by phase-folding the spectra according to the K2 orbital period (Figure 5.6) While it is clear from the trail that the white dwarf is moving according to the K2 period, the resolution was not sufficient to determine a radial velocity for WD1032+011.

## 5.3 Follow-up Spectroscopy

As Figure 5.6 shows, the FORS spectra were insufficient in resolution for a model to be fit to them. Therefore, our team submitted a proposal to the Gemini-North observatory in order to observe WD1032+011 with both the Gemini Multi-Object Spectrograph (GMOS; Hook et al., 2004), and the Gemini Near-Infrared Spectrograph (GNIRS; Elias et al., 2006). The target was observed on three different nights (11-13 January 2019), collecting a total of 24 spectra with GMOS and 8 with GNIRS.

### 5.3.1 GMOS: Design and Observing Strategy

The Gemini Multi-Object Spectrographs (GMOS; Hook et al., 2004) North and South are almost identical twin instruments mounted on the two Gemini

Trailed spectrum

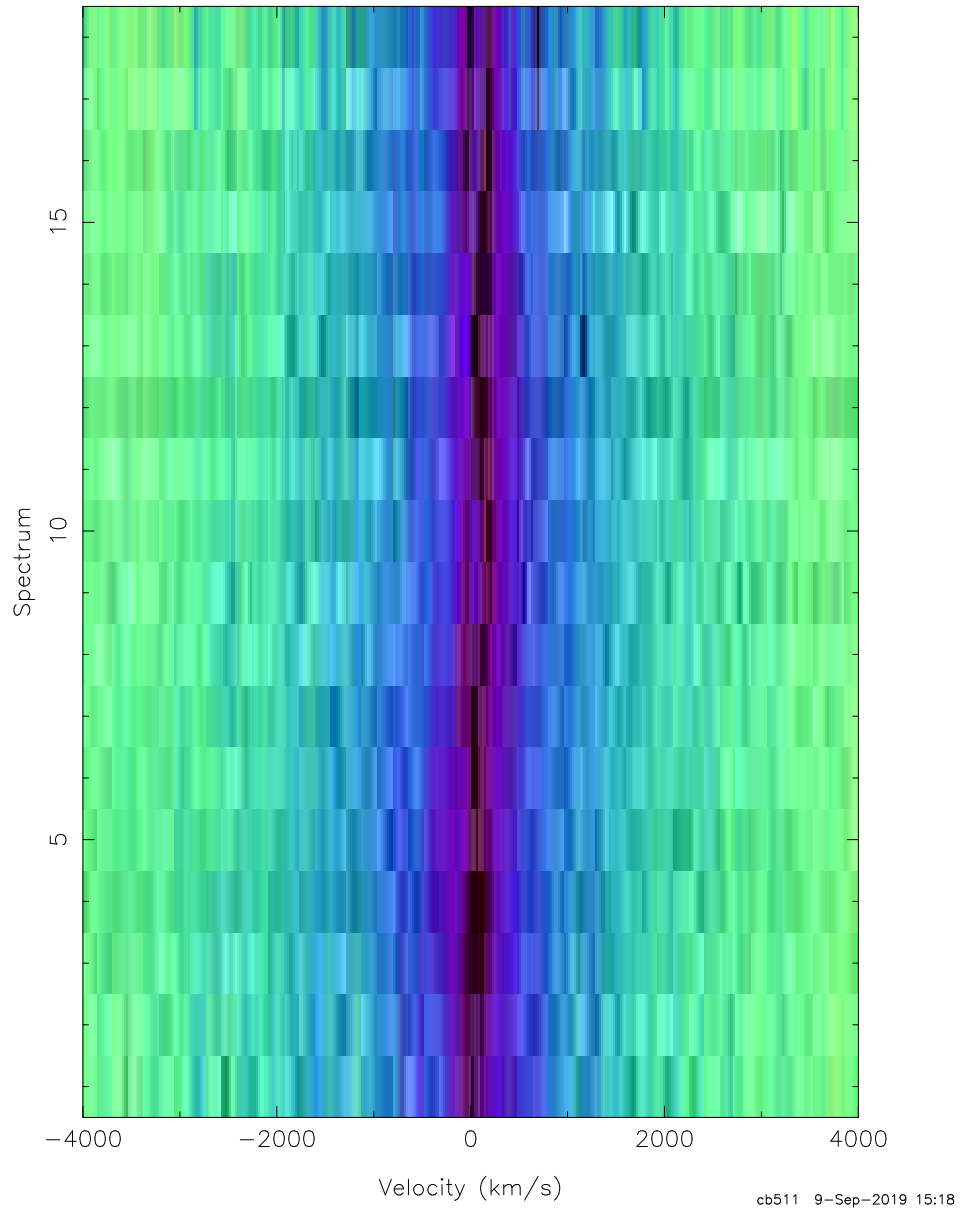


Figure 5.6: FORS trailed spectra (sorted in order of phase) of the  $H\beta$  line for WD1032+011. A clear sinusoidal movement can be seen in the trail. However, as the spectra were collected as part of a bad-weather programme, the resolution was not high enough to fit the spectra and extract a radial velocity measurement.

telescopes. Gemini North (Figure 5.7, from the GMOS fact sheet<sup>2</sup>) is an 8.1 m optical/infrared telescope situated at the Mauna Kea Observatory in Hawaii. The spectrograph covers a spectral range of 0.36 - 1.03  $\mu\text{m}$ , sampling 0.0807" per pixel.

The instrument provides a choice of 7 long slits (with a length of 330"). In this work, we used the 0.75" slit, with a binning of  $2 \times 2$ . It also offers 6 gratings, with resolving powers ranging between  $\sim 630 - 4400$ . For this work, the R831 grating, centred at a wavelength of 5750  $\text{\AA}$ , and thus covering a wavelength range between 4600  $\text{\AA}$  and 6900  $\text{\AA}$ . The 24 collected spectra had an exposure time of 900 s.

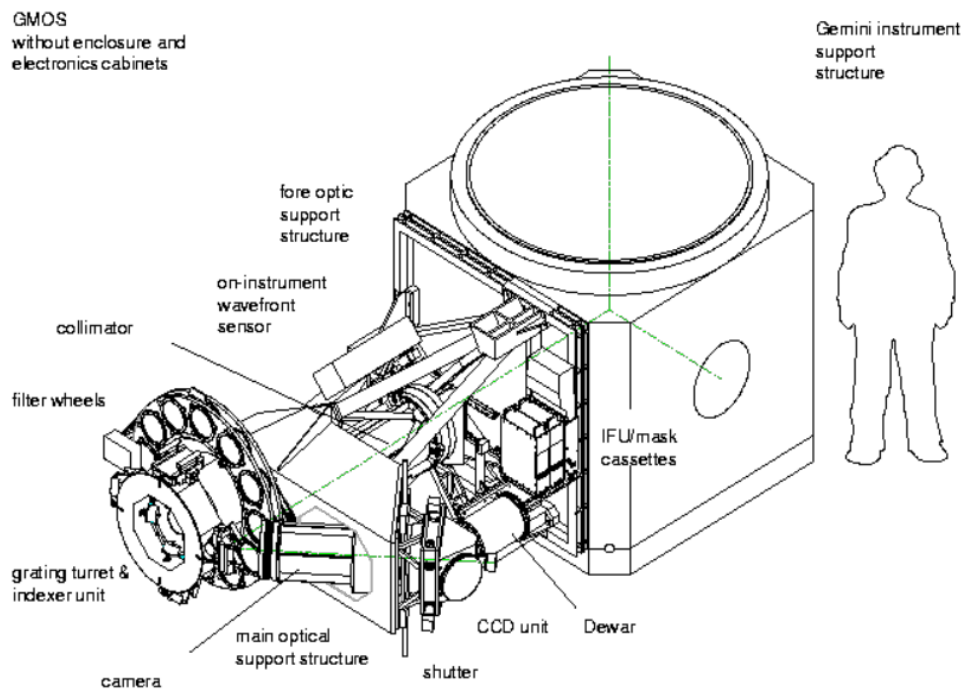


Figure 5.7: A diagram representing the main structure and components of GMOS (from the GMOS fact sheet).

<sup>2</sup><https://www.gemini.edu/sciops/instruments/factsheet/Factsheet-GMOSN-v14.pdf>

### 5.3.2 GNIRS: Design and Observing Strategy

To better constrain the nature of the infrared excess in the UKIDSS flux of WD1032+011, the Gemini Near-Infrared Spectrograph (GNIRS) was used to collect infrared spectra of the star (Figure 5.8, from the GNIRS fact sheet<sup>3</sup>).

GNIRS covers a spectral range of  $0.8 - 2.5 \mu\text{m}$ , and provides a range of low to high resolutions modes that can be achieved by choosing one of four camera mode options. In this work, the short camera option was used, which provides a slit length of  $7''$  and a resolution of  $\sim 500$  over the entire spectral range. The chosen slit width was of  $1.0''$ . A total of 8 exposure was collected, each with an exposure time of 440 s. These were subsequently combined at the data reduction stage, in order to achieve a higher signal-to-noise ratio.

### 5.3.3 Data Reduction

Both GMOS and GNIRS data were reduced and extracted by collaborators. GMOS spectra were reduced using a specific IRAF package for long-slit spectroscopy (Tody, 1986). The data was subsequently wave-calibrated and flux calibrated using observations of standard star Hiltner 600. GNIRS data were reduced using K. Allers's adaptation for GNIRS [K. Allers, private comm.] of the SPEXTOOL v4.1 software (Cushing et al., 2004). The spectra were then telluric corrected using the XTELLCORR software (Vacca et al., 2003) and a standard star of class A0V.

---

<sup>3</sup><https://www.gemini.edu/sciops/instruments/factsheet/Factsheet-GNIRS-v1.4.pdf>

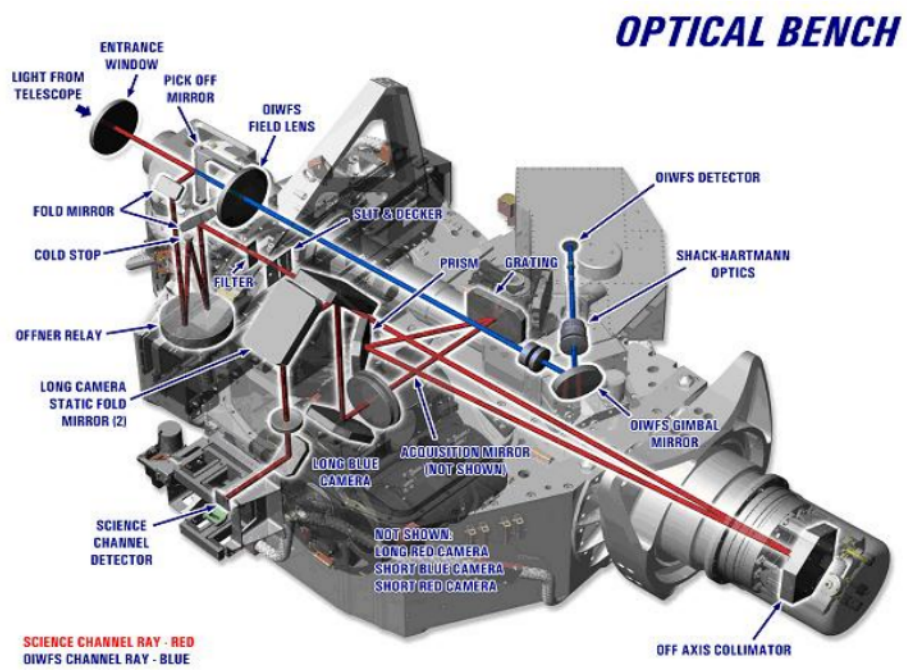


Figure 5.8: A diagram representing the main structure and components of GNIRS (from the GNIRS fact sheet).

## 5.4 Results

### 5.4.1 Radial Velocity

Once the 24 GMOS spectra were reduced and calibrated, I analysed them using the MOLLY software, as described in Chapter 2 (section 2.5). I used the ephemeris ( $T_0$ ) found from the ULTRACAM data fitting and the period from the K2 light curves to phase fold the spectra and produce a trail of the H $\alpha$  absorption feature of the white dwarf. I used ‘mgfit’ to fit three Gaussian functions to the feature using the same  $k$  and  $\gamma$  velocities (an example shown in Figure 5.9). I allowed these to vary around the orbit according to the radial velocity formula:

$$V_r = \gamma + k \sin(2\pi\phi) \quad (5.5)$$

where  $\phi$  is the orbital phase of the system. Although MOLLY does not provide any errors associated with the calculated phases, an error in the K2 period of  $\pm 0.00000000003$  days makes systematic errors due to ephemeris drifting unlikely.

The trails for the data, the model fit and the residuals are shown in Figure 5.11. The errors on the radial velocity parameters that I used were found by multiplying the errors associated to the data by a factor of 4.2, in order to achieve a reduced  $\chi^2$  value of  $\chi^2_\nu \sim 1$ . The final fit resulted in velocities of  $k = 48.8 \pm 2.64 \text{ kms}^{-1}$  and  $\gamma = 122.08 \pm 1.94 \text{ kms}^{-1}$ .

Unfortunately, there were no hydrogen emission features that could be attributed to the brown dwarf in the spectra (e.g. Casewell et al., 2015;

Longstaff et al., 2017), so parameters for the brown dwarf’s radial velocity could not be measured from the GMOS data. In addition, I searched the spectra for some of the characteristic metal lines present in irradiated brown dwarfs, such as Na I and Mg I (e.g. Longstaff et al., 2017), but none were present.

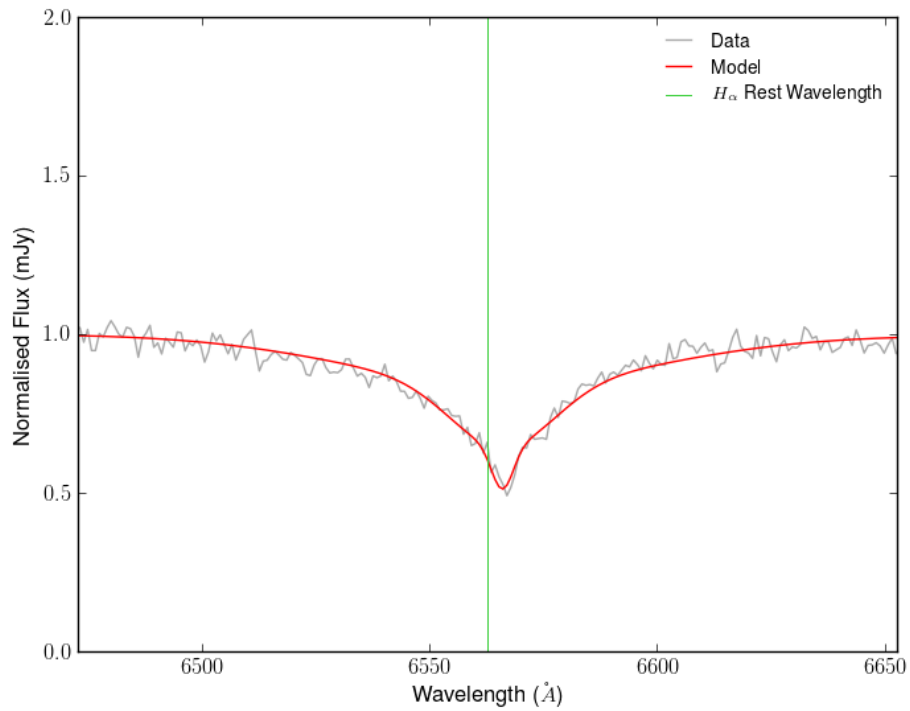


Figure 5.9: An example of the ‘mgfit’ fit to the  $H_{\alpha}$  absorption line of WD1032+011. I used a combination of three Gaussian functions to produce the model, which was then fit to all the 24 GMOS spectra.

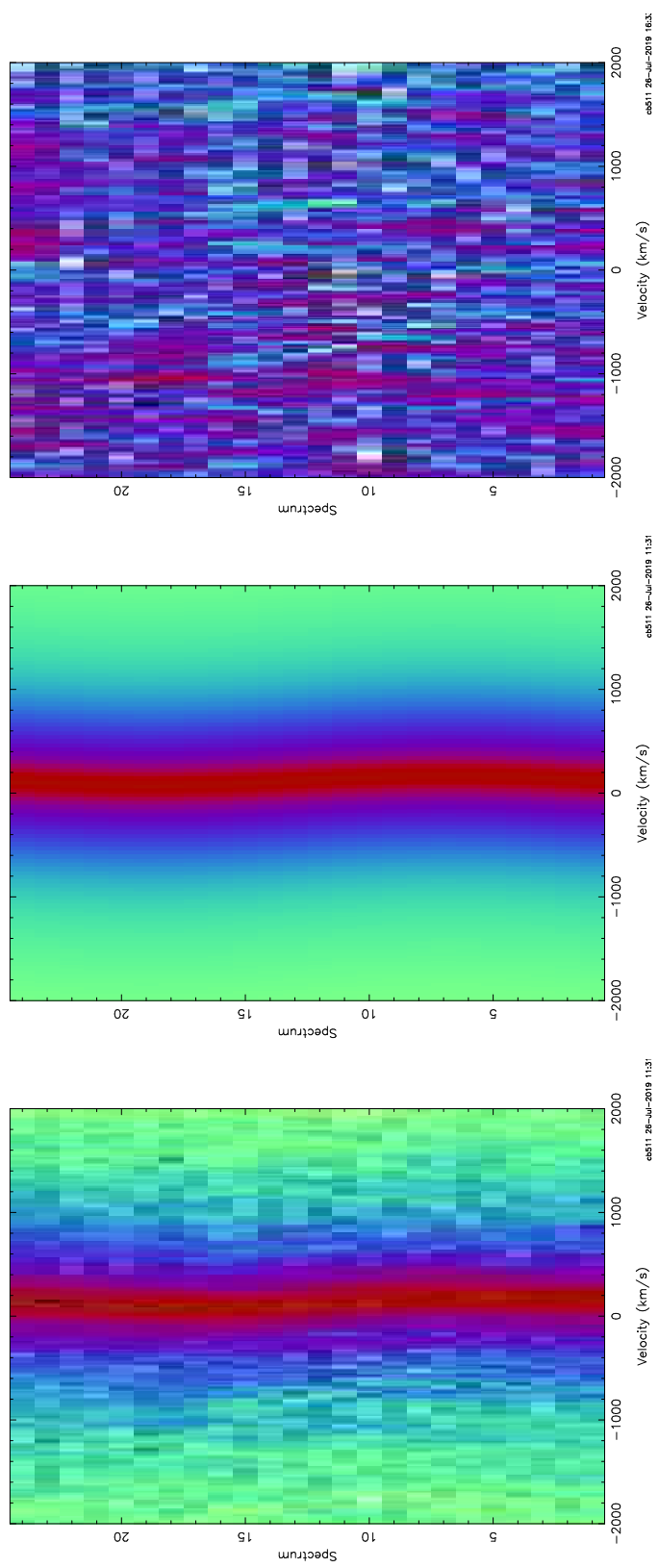


Figure 5.10: Trailed GMOS spectra (in order of phase) centred on the H $\alpha$  absorption line. The plots show the data (left panel), the model generated from the Gaussian fitting (central panel) and the residuals to the fit (right panel).

### 5.4.2 Follow-Up on the Brown Dwarf Spectral Type

Once the GNIRS infrared spectra were coadded to reach the required signal-to-noise ratio, I added them to the plot shown in Figure 5.5 to verify the spectral type of the brown dwarf companion to WD1032+011. The new plots are shown in Figures 5.11 and 5.12 (zoomed into the near-infrared side of the SED).

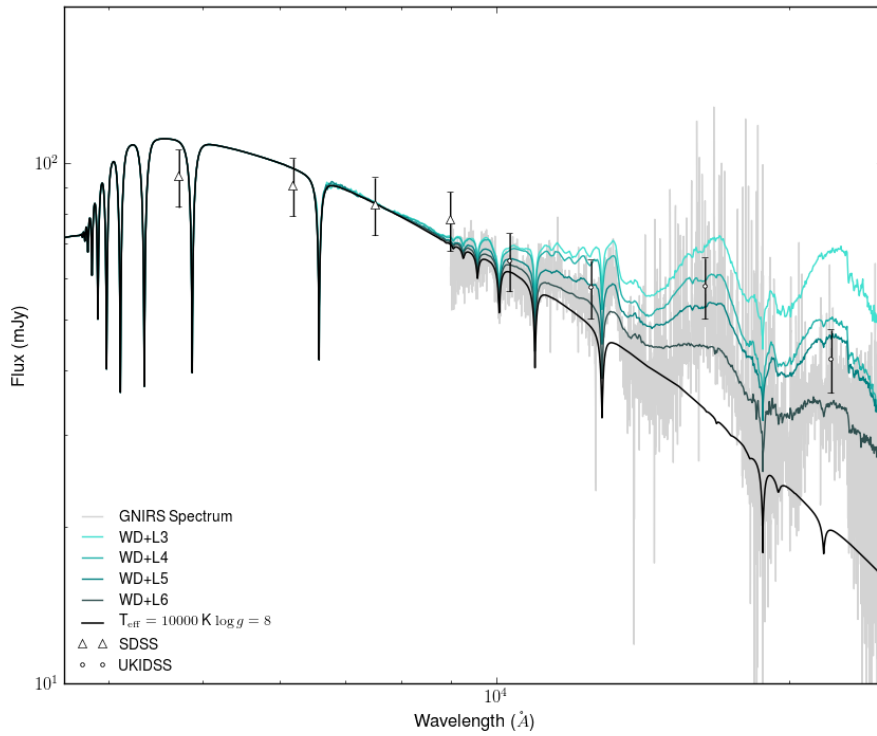


Figure 5.11: GNIRS infrared spectrum of WD1032+011 matched to various white dwarf + brown dwarf template spectra. The SDSS (triangles) and UKIDSS (diamonds) magnitudes are also shown.

In the plots, the GNIRS spectrum confirms L5 to be the most probable spectral type for the brown dwarf, in agreement with Steele et al. (2011). However, Figure 5.12 shows that while, in general, the photometry agrees with an

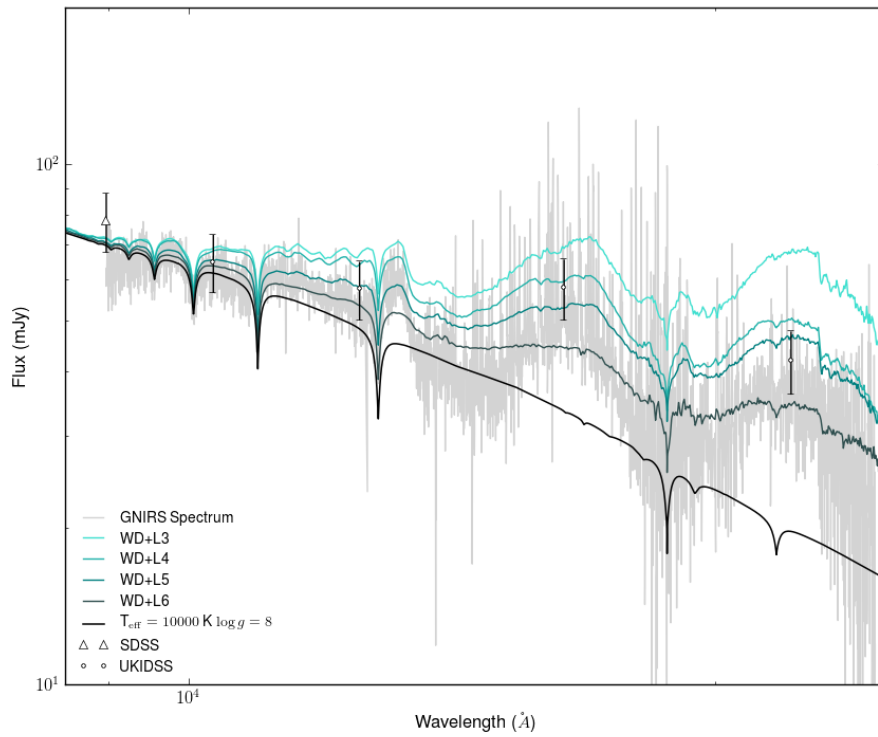


Figure 5.12: GNIRS infrared spectrum of WD1032+011 matched to various white dwarf + brown dwarf and white dwarf + late M-dwarf template spectra, zoomed in to the near-infrared. The SDSS (triangles) and UKIDSS (diamonds) magnitudes are also shown.

L5 brown dwarf, the UKIDSS  $H$  and  $K$  bands show some discrepancies with the model. In the  $H$ -band the photometry is more consistent with an L4-L5 type, while the  $K$ -band is closer to an L5-L6. The  $K$ -band discrepancy is particularly interesting, as other systems such as SDSS J141126.20+200911.1 (Casewell et al., 2018) and WD0137-349B (Casewell et al., 2015) show a  $K$ -band brightening due to UV flux from the white dwarf irradiating the brown dwarf companion. What is observed in the spectrum of WD1032+011 could be explained by the UKIDSS  $K$ -band photometry being obtained while the system was eclipsing, however due to the short eclipse duration this is perhaps unlikely. Otherwise, it could be due to a reflection effect. This second option is however also unlikely, as the optical light curves (both in the K2 and ULTRACAM data) show no sign of a reflection feature, which suggests the the near-infrared magnitudes should not change significantly over an orbit.

### 5.4.3 $T_{\text{eff}}$ and $\log g$ Calculation

Although the FORS spectra were of insufficient resolution to obtain a radial velocity solution for the system, they were employed to better constrain the effective temperature and surface gravity of the white dwarf. To do this, the 18 spectra were analysed with the FITSB2 codes, using DA white dwarf models from Koester (2010) as reference.

The model grid consisted of a set of DA white dwarfs with a  $T_{\text{eff}}$  range between 6,000 K and 40,000 K (in steps of 1000 K) and a  $\log g$  range between 6.5 dex and 9.5 dex (with increments of 0.25 dex). Assuming an uncertainty in effective temperature of 2.3% and in surface gravity of 0.07 dex (Napiwotzki et al., 1999), the new values were estimated to be  $T_{\text{eff}} = 9,991 \pm 230 \text{ K}$

and  $\log g = 8.054 \pm 0.07$ . Comparing these values to Fontaine et al. (2001) evolutionary models for thick-H layer white dwarfs, the resulting radius, mass and cooling time for WD1032+011 are  $R_{WD} = 0.0122R_{\odot}$ ,  $M_{WD} = 0.615M_{\odot}$  and  $t_{cool} = 0.715$  Gyr.

#### 5.4.4 Light Curve Fitting

The ULTRACAM light curves were then fitted by Sarah Casewell using LCURVE (Copperwheat et al., 2010) to better constrain the orbital period and the radii of both the white dwarf and the white dwarf. The mass ratio, radii, inclination and limb darkening parameters of the system were allowed to vary. LCURVE runs Markov-Chain Monte-Carlo (MCMC) simulations to find a best fit to all these parameters. Results to the fit for the  $u'$ ,  $g'$  and  $r'$  ULTRACAM light curves are shown in Figure 5.13.

### 5.5 Discussion

Once parameters such as the mass ratio ( $q$ ), the fractional radii ( $R_{WD}/a$  and  $R_{BD}/a$ ), inclination ( $i$ ) and radial velocity of the white dwarf ( $k$ ) were obtained from fitting a model to the ULTRACAM light curves and to the GMOS spectra, these were then used to obtain mass and radius measurements for both components of the system (Littlefair et al., 2014). This was done by running a Monte-Carlo simulation which selects random values  $10^5$  times. As the light curve fitting and the spectral line fitting already provided us with likely solutions and errors for the system's radial velocity and the white dwarf mass, these were used to put limits to the random distributions for  $M_{WD}$  fed to the simulation. Once these values were constrained, they were then used in

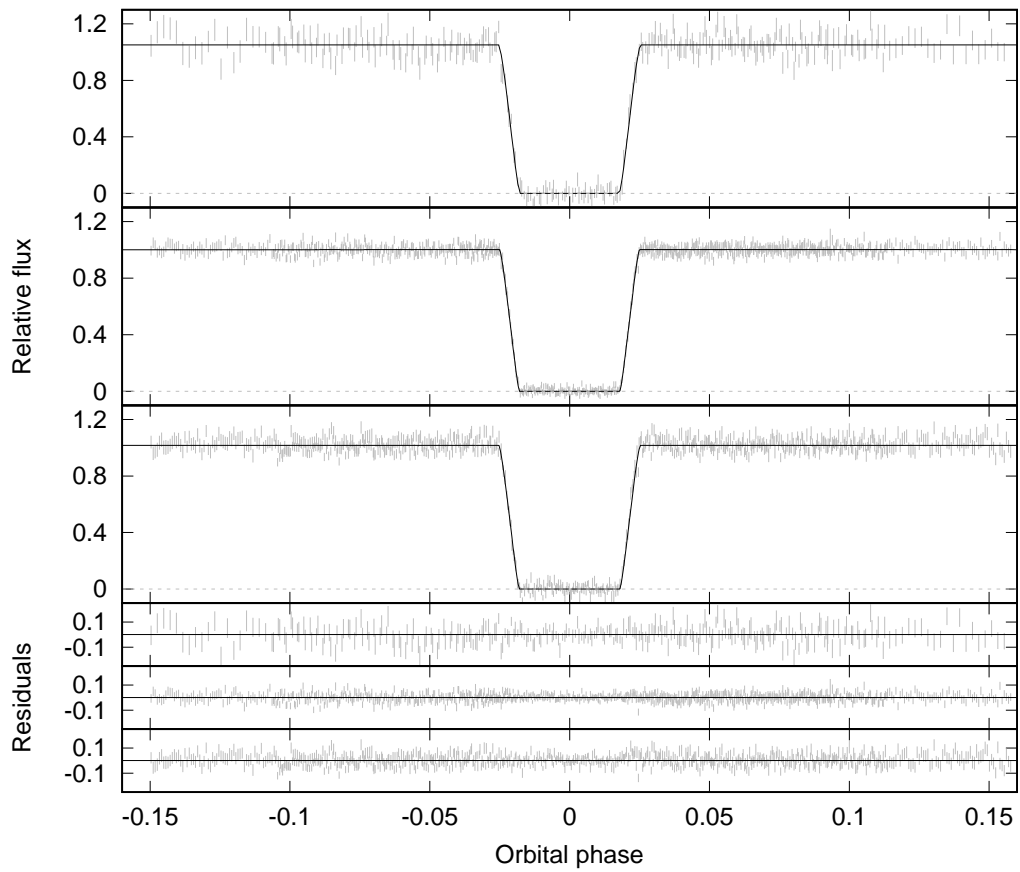


Figure 5.13: ULTRACAM light curve in  $u'$  (top),  $g'$  (middle) and  $r'$  (bottom) bands, shown with their best fitting models and respective residuals. The system totally eclipses in all three bands (Casewell et al., in prep.).

equation 5.6 to give a solution for the brown dwarf mass ( $M_{BD}$ ).

$$\frac{P}{2\pi G} k = \frac{M_{BD}^3}{(M_{WD} + M_{BD})^2} \sin^3 i \quad (5.6)$$

In the equation,  $P$  is the orbital period of the system and  $G$  is the Gravitational constant. Finally, the resulting masses were used in equation 5.7 (Kepler's third law) to find the semi major axis  $a$  of the orbit, which was subsequently used to obtain the white dwarf and brown dwarf radius values from their fractional radii ( $R_{WD}/a$  and  $R_{BD}/a$  respectively).

The resulting parameters for the WD1032+011AB system are shown in Table 5.3.

$$a^3 = \frac{G(M_{WD} + M_{BD})}{4\pi^2} P^2 \quad (5.7)$$

Parameter	Value
Mass Ratio $q$	$0.091 \pm 0.011$
inclination( $^\circ$ )	$87.560 \pm 0.720$
$R_{WD}$ ( $R_\odot$ )	$0.016011 \pm 0.001394$
$R_{BD}$ ( $R_\odot$ )	$0.114753 \pm 0.010463$
$M_{WD}$ ( $M_\odot$ )	$0.588877 \pm 0.043005$
$M_{BD}$ ( $M_\odot$ )	$0.079004 \pm 0.005952$

Table 5.3: WD1032+011AB parameters from fitting the mass function.

From this fit, the calculated mass for the sub-stellar companion was too high for an L5 brown dwarf. As the fit to the mass function (Equation 5.6) was strictly dependent on the previously calculated white dwarf mass, this discrepancy in the results suggested a wrong estimate for the star's mass had

been used.

WD1032+011 was observed by the *Gaia* Mission. The measured *Gaia* parallax to the star is  $p \approx 3.062$  mas. From parallax, the distance to a star (in parsecs) can be calculated as:

$$d = \frac{1}{p} \quad (5.8)$$

with the parallax in arcseconds. Once I calculated the distance, I used the SDSS *ugriz* apparent magnitudes (Table 5.2) to calculate the absolute *ugriz* magnitudes for the star, using the following formula:

$$M = m - 5.0 \log_{10} \left( \frac{d}{10pc} \right) \quad (5.9)$$

Comparing the calculated magnitudes to the Holberg and Bergeron (2006) DA model magnitudes, these are more consistent with a  $T_{\text{eff}} = 10,000$  K and  $\log g = 7.5$  white dwarf. In light of this new information, the FORS spectra were modelled to produce a better estimate of the white dwarf  $T_{\text{eff}}$  and  $\log g$ . The fit (Figure 5.14) returned most likely values of  $T_{\text{eff}} = 10196 \pm 235$  K and  $\log g = 7.81 \pm 0.07$ . The final parameters for both the white dwarf and the brown dwarf are shown in Table 5.4.

Parameter	Value
inclination( $^{\circ}$ )	$87.560 \pm 0.720$
$R_{WD} (R_{\odot})$	$0.0145 \pm 0.0006$
$R_{BD} (R_{\odot})$	$0.108643 \pm 0.009923$
$M_{WD} (M_{\odot})$	$0.496 \pm 0.036$
$M_{BD} (M_{\odot})$	$0.070820 \pm 0.005321$

Table 5.4: WD1032+011AB final parameters.

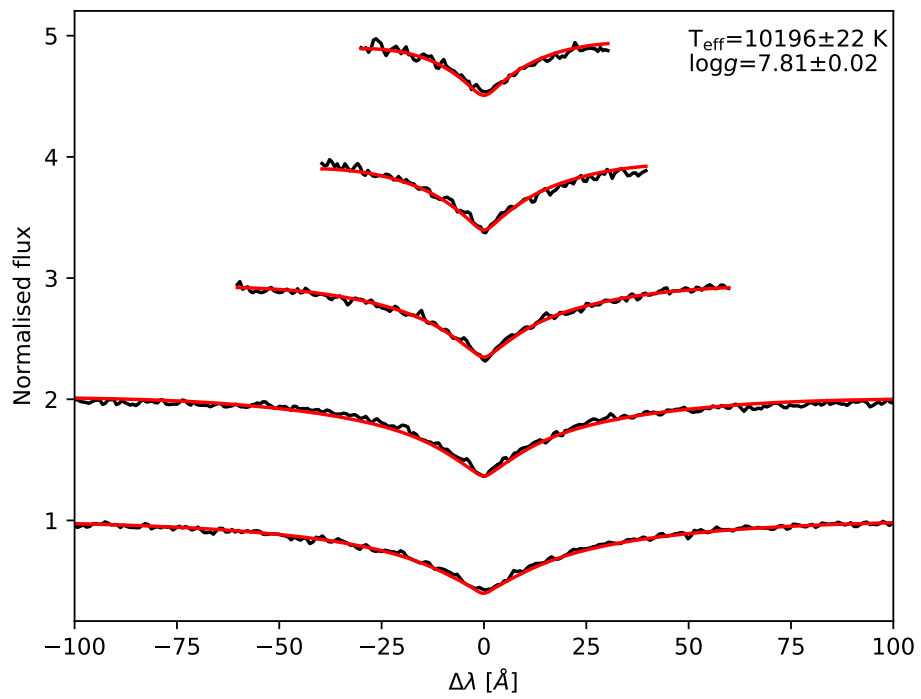


Figure 5.14: Best fit (red line) to the combined FORS spectrum of WD1032+011. The best fitting model is  $T_{\text{eff}} = 10196 \pm 235$  K and  $\log g = 7.81 \pm 0.07$ .

Comparing the final brown-dwarf parameters to the Baraffe et al. (2015) mass-radius relation models, these still result to be inconsistent with what it would be expected (see Figure 5.15).

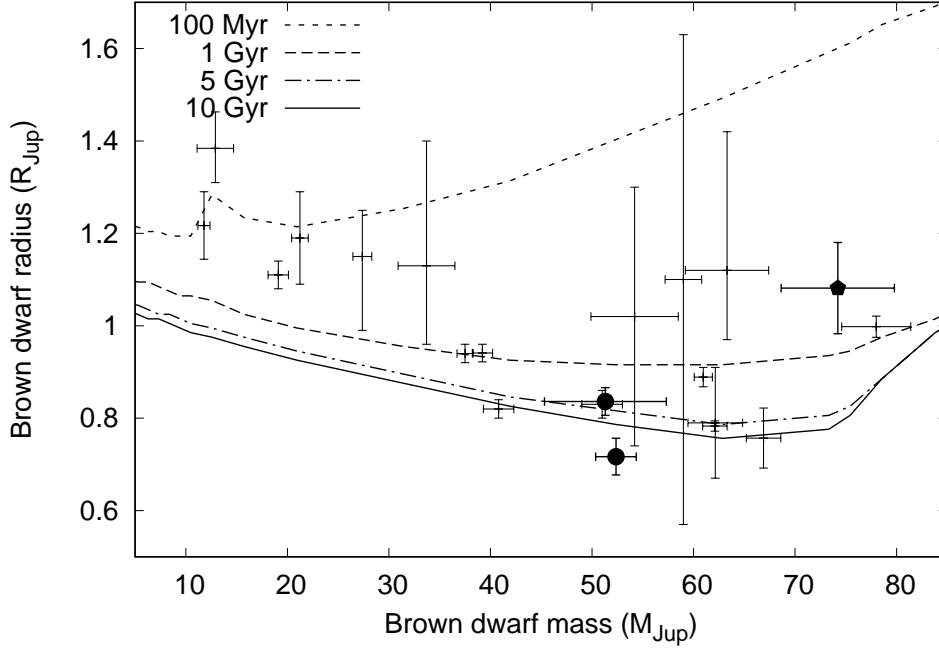


Figure 5.15: The mass-radius relation for the brown dwarf in WD1032+011. In the plot, different isochrones from Baraffe et al. (2015) are shown as solid and dashed lines. The black pentagon represents WD1032+011, while the two black circles represent the only other eclipsing white dwarf + brown dwarf systems. The rest of the objects plotted represent known main sequence star + brown dwarf systems.

According to the Baraffe et al. (2015) models, a brown dwarf with the same parameters as WD1032+011 would have an effective temperature of 2395 K and an age of 428 Myr, which are inconsistent with an L5 spectral type and the cooling age of the white dwarf companion, respectively. The most likely reason is that the fit to the white dwarf Balmer lines is still not optimal. Comparing the final white dwarf parameters to the Holberg and Berg-

eron (2006) DA models, the Gaia absolute magnitude should be 11.83 mag. However, through the method discussed above, the observed absolute Gaia magnitude for the system is  $\sim 9.27$ , more consistent with a  $\log g = 7.5$  white dwarf.

A lower white dwarf mass (and a larger radius) would result in lower parameters (mass and radius) for its brown dwarf companion. Therefore, a future step will involve a new fit of the Balmer lines, using UV data to better take into account the extinction of the system.

## 5.6 Summary

In this Chapter, I present my discovery of the third eclipsing white dwarf + brown dwarf system. Systems such as this are immensely helpful to determine the characteristic of brown dwarfs, as they allow to determine physical properties such as masses and radii with higher precision than systems involving hot – and probably pulsating – subdwarfs.

My collaborators used FORS spectra, combined to the *Gaia* parallax of  $p \approx 3.062$  mas, to determine an effective temperature for the white dwarf  $T_{\text{eff}} = 10196 \pm 235$  K and a surface gravity of  $\log g = 7.81 \pm 0.07$ . These correspond to a mass of  $M_{WD} = 0.496 \pm 0.036 M_{\odot}$  and radius of  $R_{WD} = 0.0145 \pm 0.0006 R_{\odot}$ . They used LCURVE to fit a model to ULTRACAM  $u'g'r'$  observations of the primary eclipse, thus extrapolating the inclination of the system, as well as the mass ratio  $q$  and the fractional radii of the components. I then used the MOLLY software on the GMOS time-resolved spectra to obtain a white dwarf radial velocity measurement of  $k = 48.8 \pm 2.64$   $\text{kms}^{-1}$ . I then fitted the GNIRS stacked spectrum, SDSS  $ugriz$  photometry and UKIDSS  $JHK$  photometry to

SED models of various white dwarf + brown dwarf systems to confirm the spectral type of the brown dwarf companion to be L5. Finally, the radial velocity and mass solution of the white dwarf – combined with the estimated inclination and the fractional radii – were used to create a fit to the mass function (Equation 5.6), resulting in a mass and radius solution for the brown dwarf of  $M_{BD} = 0.0708 \pm 0.0053 M_{\odot}$  and  $R_{BD} = 0.1086 \pm 0.0099 R_{\odot}$ . The brown dwarf shows no signs of irradiation, neither in the spectra nor in the photometric data.

## Chapter 6

# NOI-101535 and NOI-103465: Two Newly Discovered Eclipsing WD+MS Systems in NGTS

Transit surveys offer a unique opportunity to detect and extract intrinsic properties of extrasolar planets, such as their radii, inclinations and orbital separations. When paired with radial velocity data – which determine the mass – photometric detections of planets also allow us to determine the bulk compositions of the transiting planets (e.g. Baraffe et al., 2008).

Space-based telescopes such as Kepler (Borucki et al., 2010) and *CoRoT* (Auvergne et al., 2009) were able, through higher precision photometry and without being affected by the Earth’s atmosphere, to discover planets with masses and sizes comparable to Earth around bright stars. However, while the space setting allows the detection of small, rocky planets (e.g. Léger et al.,

2009; Queloz et al., 2009; Batalha et al., 2011), these are also usually found around stars that are too faint to be observed from the ground for radial velocity determination. Hence their masses remain unconstrained most of the time.

On the other hand, the most successful ground-based large-scale transit surveys such as WASP (Pollacco et al., 2006) only allowed the discovery of larger, Jovian planets around solar-type stars. This is due to Earths and super-Earths only producing very shallow dips in the stellar flux, too shallow to be detected from Earth. However, Neptune-sized planets around late main sequence stars should be detectable from the ground due to their sufficient transit depths. This is confirmed by the discovery of planets such as HAT-P-11b (Bakos et al., 2010) and the seven Earth-like planets around TRAPPIST-1 (Gillon et al., 2016, 2017).

To better investigate the transition region between super-Earths and Neptune-like planets, a new ground-based survey was designed, as both a discovery instrument for new exoplanets in the aforementioned region, and a method of following up planet candidates identified in space missions. This new survey has also proven useful in identifying extreme stellar binary systems, such as white dwarfs being eclipsed by main sequence companions. In this Chapter, I present the discovery of two such systems in the Next Generation Transit Survey.

## **6.1 The Next Generation Transit Survey**

The Next Generation Transit Survey (NGTS; Wheatley et al., 2018) has the primary science goal of detecting extrasolar planets with sizes down to at least

that of Neptune, thus increasing the sample of transiting planets visible from Earth that can be followed up for radial velocity confirmation. In addition, the NGTS facility can be used to follow up planet candidates detected in space missions such as the Transiting Exoplanet Survey Satellite (TESS; Ricker et al., 2015).

To accomplish this goal, NGTS was designed to detect transit depths down to 0.1%, corresponding to a super-Earth sized planet transiting an early M dwarf star (Wheatley et al., 2018). Moreover, to ensure the possibility of spectroscopic follow-up, the survey was set to sample stars brighter than 13 and 15 mag (depending on the employed spectrograph: HARPS or ESPRESSO respectively (Mayor et al., 2003; Pepe et al., 2014)). Due to atmospheric constraints linked to ground-based photometry, the NGTS facility was built (during 2014-2015) at the Cerro Paranal site in Chile, which ensures a high fraction of clear skies as well as low extinction. Other effects such as variable sky background due to Moon or Sun illumination (Noll et al., 2012) and scintillation caused by atmospheric turbulence (Osborn et al., 2015). Taking these effects into account, the required photometric precision of 0.1% was achievable for targets brighter than  $I = 14$  mag (on dark nights) and  $I = 13$  mag (at full Moon).

### **6.1.1 NGTS Design**

To minimise the atmospheric refraction effect which causes the field of view of ground-based telescopes to stretch, thus limiting the amount of sky over which autoguiding is possible, NGTS was designed as an array of 12 individual 20 cm telescopes. Each telescope is mounted on an individual equatorial mount, and

positioned in two rows of 6 telescopes along the East-West direction (Figure 6.1). The individual mounts allow each telescope to be slewed independently, making the survey efficient at following up multiple transit candidates at once. The telescopes have an individual field of view of approximately 8 square degrees, which results in a potential total field of view of  $\sim 100$  square degrees.

Each telescope has a hyperbolic primary mirror with a 20 cm diameter, a focal ratio of  $f/2.8$ , a flat secondary mirror with a 9 cm diameter, and a four-element corrector lens. The mirrors are coated with protected aluminium, which is the most stable compound at the instrument location. The coating on the corrector lenses is optimised to span over the NGTS filter wavelength range (520 to 890 nm). The chosen filter has the best sensitivity to K and early M type stars.

A  $2048 \times 2048$  CCD is fitted to each of the 12 telescopes. The CCDs are packed into custom versions of the Andor iKon-L 936 camera, an upgraded version of the cameras used for the WASP survey (Pollacco et al., 2006). Each pixel in the devices has a size of  $13 \mu\text{m}$ , and each device has an image area of  $27.6 \times 27.6 \text{ nm}$ . All the cameras are equipped with a thermoelectric cooler which allows them to operate at a temperature of  $-70^\circ\text{C}$ .

### **6.1.2 NGTS Observing Strategy and Operations**

NGTS is completely robotic. The enclosure opens every night 1 hour before sunset, to allow the instrumentation to reach the temperature of the surroundings. While the Sun is between  $-4.5^\circ$  and  $-8.5^\circ$ , the telescopes take 100 flat frames, while pointing to the anti-Solar azimuth. Subsequently, each camera runs a focus check and will occasionally adjust to its optimal focus. While



Figure 6.1: The two arrays of 20 cm telescopes used at the NGTS facility (Wheatley et al., 2014).

the sun is  $15^\circ$  below the horizon, science frames are collected. After morning twilight, the telescopes perform a second focus check and collect another 100 flat frames, followed by a sequence of dark and bias frames after the structure's roof is shut, to minimise light contamination.

Each night, each telescope can operate in two different mode. In either of these, the telescopes have exposure times of 10 s.

When in 'survey' mode, a telescope usually observes two pre-assigned fields per night, observed for as long as possible while they are higher than  $30^\circ$ . Each field is followed by the assigned telescope every night in which it is visible to maximise the coverage, which usually amounts to  $\sim 500$  hours spread over  $\sim 250$  nights a year. The fields are selected according to criteria such as the density of stars ( $\leq 15,000$  stars brighter than  $I = 16$  mag), the fraction of dwarf stars in the sample ( $\geq 70\%$ ), their positions with respect to the ecliptic and Galactic planes (usually more than  $30^\circ$  and  $20^\circ$  away respectively) and their proximity with very bright objects.

When in 'follow-up' mode, a telescope is assigned to observe a particular star, which is positioned in the centre of the field of view – where the differential atmospheric refraction effect is at a minimum (Wheatley et al., 2018).

The photometric precision of the instruments is maintained by a closed-loop guiding system that operates while exposing. In particular, the algorithm is an upgraded version of DONUTS (McCormac et al., 2013), and uses a master image of the field to re-acquire the next exposure to the same sub-pixel position as previous exposures and previous nights.

### 6.1.3 Data Storage and Reduction

The NGTS telescopes generate an average of 200 GB of data per night. These are stored into a 2 TB hard disc, which is sent to the University of Warwick every two weeks. The data are transferred into a local database, backed up, and then the removable hard discs are sent back to Chile to be formatted and reused.

The images are then reduced by using mean-combined master bias and flat frames. In particular, the flat frames are sigma-clipped to ensure no stars contaminate the field. Dark current is negligible in the NGTS CCDs, but the master dark frames are monitored.

Before performing aperture photometry, a World Coordinate System (WCS) astrometric solution is calculated for each image, which ensures each aperture is precisely placed on its target. Aperture photometry is carried out using the `CASUTOOLS IMCORE_LIST` software (Irwin et al., 2004). Apertures have a standard size of 3 pixels (which corresponds to 15 arcseconds). Differential photometry is then performed on the newly extracted raw light curves. This is done by calculating a mean light curve that is used as a proxy for a comparison star. Other sources of systematic variability are caused by airmass and Moon illumination. These show as periodic signals, and to eliminate them, the light curves are analysed for variance. Any significant periodicity is then inspected to ensure it does not have a transit-like shape, and is subsequently removed. This helps improve the transit detection rate by 10-30%, and to reduce the false detection probability by 50%.

### 6.1.4 Transit Detection

In order to detect transit-like features in the detrended light curves, the data is run through a Box-Least-Squares (BLS, Kovács et al., 2002) algorithm using the ORION code (previously used to detect most of the transit in the WASP survey). The algorithm is based on the work by Collier Cameron et al. (2006), but was enhanced to encompass box profiles with a wide range of widths (sampling transit durations from 1.5 to 3.75 hours, with increments of 0.75 hours). This allows a better match for eclipsing planets in inclined orbits, which have shorter eclipses.

Transit candidates detected by ORION are consequently vetted through an automated algorithm known as CANVAS (CANdidates Vetting, Analysis and Selection). The algorithm uses the BATMAN code (Kreidberg, 2015) to fit the transit model by Mandel and Agol (2002) to each transit feature detected. The spectral class of each star detected in the survey is determined by fitting the available magnitudes (provided by various surveys such as SDSS, SkyMapper, 2MASS, APASS, Gaia, etc.) to spectral energy distribution (SED) models of main sequence and giant stars, and by choosing the model with the minimum  $\chi^2$  value. Combined with the results from BATMAN, CANVAS is then able to provide a first estimate for planet radii, orbital distances, impact parameters and stellar densities. Subsequently, the algorithm rules out detections with known periods (which are most likely aliases dependent on the observing window or airmass), detections that have variabilities with large amplitudes (most likely variable stars) and detections with poor phase coverage. Finally, CANVAS searches for evidence of secondary eclipses, the presence of which suggests the transits are caused by a binary stellar system rather than by a planet.

While this method is widely efficient in detecting planet candidates and ruling out binary systems, some extreme systems may still be flagged as planetary transits.

## 6.2 Two New Eclipsing White Dwarf + main sequence Star Systems

About one quarter of binary systems involving two main sequence stars are found at relatively close separations ( $\approx$ few AU). In these cases, when the more massive star evolves to the red giant branch (RGB) – thus expanding – the two stars start interacting in a process known as Roche lobe overflow (Willems and Kolb, 2004). When this happens, the two stars will form a common envelope, and the secondary star will migrate inwards while transferring angular momentum to the envelope, leading to its ejection (Webbink, 1984; Ivanova et al., 2013). As a result, the newly formed post common envelope binary (PCEB) will consist of a white dwarf remnant in a short period system with a main sequence companion. To date, there are  $\sim$ 200 such systems known (e.g. Nebot Gómez-Morán et al., 2011; Parsons et al., 2013).

A large number of such systems were identified within the Sloan Digital Sky Survey (SDSS, York et al., 2000). Thousands of PCEB candidates were found within surveys using SDSS data (Silvestri et al., 2007; Rebassa-Mansergas et al., 2010; Steele et al., 2011; Girven et al., 2011). Due to a selection bias, most PCEB systems are found to contain a relatively hot white dwarf in orbit with a cool, red dwarf companion. In these cases, the hot white dwarf will dominate the flux at the blue end of the spectrum, while the cooler

M dwarf companion will dominate the flux at the near-IR and IR end. This allows the two components to be split by spectroscopic colour and then analysed photometrically. Older systems with cooler white dwarfs and M dwarf components are much harder to identify as the M dwarf flux tends to dominate in a larger portion of the spectrum. In some cases – such as for SDSS J121010.1+334722.9, a metal polluted DA white dwarf ( $T_{\text{eff}} = 6000$  K) with an M5 companion (Rebassa-Mansergas et al., 2010; Pyrzas et al., 2012) – the spectral energy distribution of the system still showed an excess from the white dwarf at the shorter wavelengths. However, systems with even cooler white dwarfs are much more difficult to detect as the white dwarf flux is almost completely invisible compared to that of the M dwarf. The only way to identify such systems is through a careful spectral analysis. The influence of the stellar wind from the M dwarf on the chromosphere of the white dwarf can produce emission lines, which can allow us to determine radial velocity variations for both components of the system. An example of this is SDSS J013851.54-001621.6 (Parsons et al., 2012a), a PCEB with a  $0.53 M_{\odot}$  white dwarf with a surface temperature of 3571 K and a  $0.132 M_{\odot}$  M dwarf companion (Figure 6.2). Surveys like NGTS, with extensive orbital coverage and short cadences, are ideal to detect these types of systems, as they present very characteristic eclipse signatures. When the M dwarf companion eclipses the white dwarf, it produces extremely short ( $\approx 15$  minutes) deep transits, especially if observed in blue optical wavelengths, where the flux from the M dwarf is negligible.

Due to the detection limitations for old, cool post common envelope binaries, these systems are incredibly rare. To date, the only system where the white dwarf has a temperature of less than 4000 K is SDSS J013851.54-

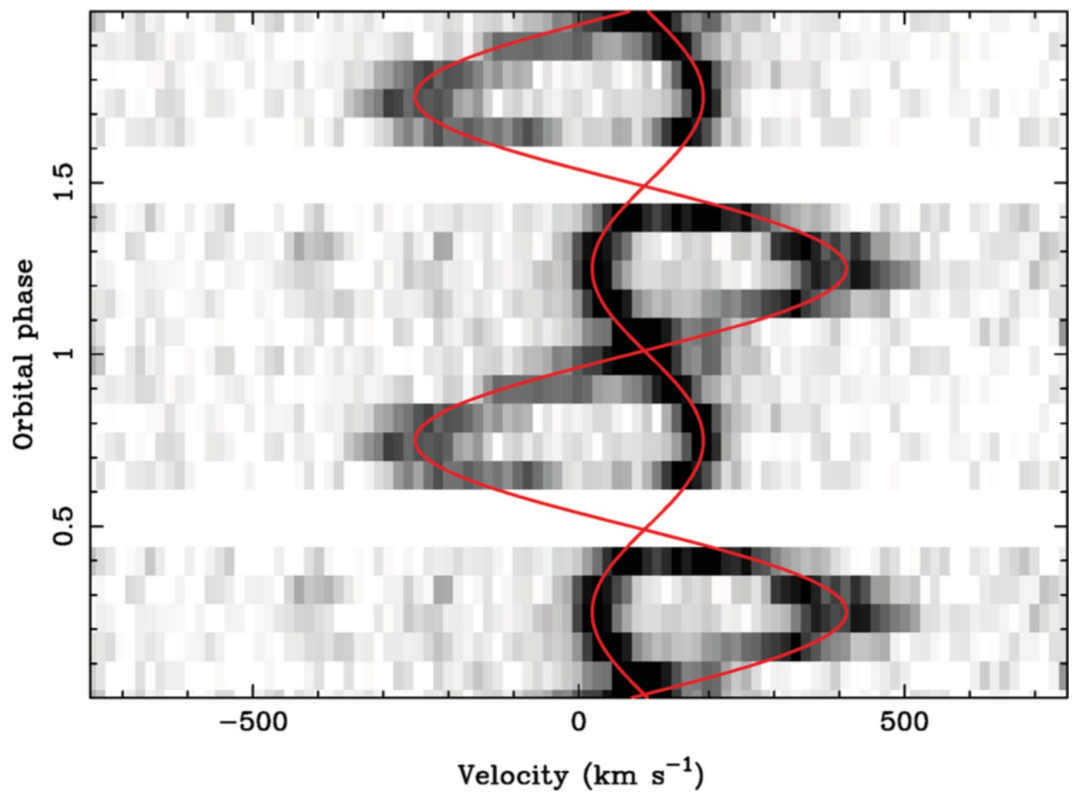


Figure 6.2: Traced spectra of SDSS J013851.54-001621.6, centred on the Ca II line at 3934 Å. Emission is seen from both the white dwarf (stronger line with smaller amplitude) and the M-dwarf (weaker line with larger amplitude). The red lines track the motion of each component (Parsons et al., 2012a).

001621.6 (Parsons et al., 2012a), which was originally identified by Becker et al. (2011) as a transiting candidate from SDSS photometry.

At the moment, the masses and radii of isolated cool white dwarfs are identified through their spectral profiles and absolute magnitudes. Current models however do not include pressure effects, and are hence not yet considered reliable. Therefore, eclipsing systems that also present double lined white dwarfs (such as SDSS J013851.54-001621.6, Parsons et al., 2012a) are particularly important to determine the mass and radii of cool white dwarfs independently.

## **6.3 NOI-101535**

### **6.3.1 Optical Observations**

#### **NGTS Photometry**

NOI-101535 is the first post common-envelope binary system discovered in NGTS. It was observed by NGTS between April 21 and December 2, 2016, for a total of 169,722 images. The images were reduced using the standard pipeline described in section 6.1.3 (Wheatley et al., 2018). The light curve shows a sharp eclipse feature with a depth of 10% and a duration of approximately 10 minutes, lacking the characteristic ingress and egress features produced by planetary transit (Figure 6.3). These properties made it clear that the transit was produced by a main sequence star eclipsing a white dwarf. For an eclipse of such shape, the BLS algorithm is not the best method for fitting the data. Hence the light curve was fitted again using `BATMAN` (Kreidberg, 2015), to better determine the ephemeris and period of the system. Due to the dip in the

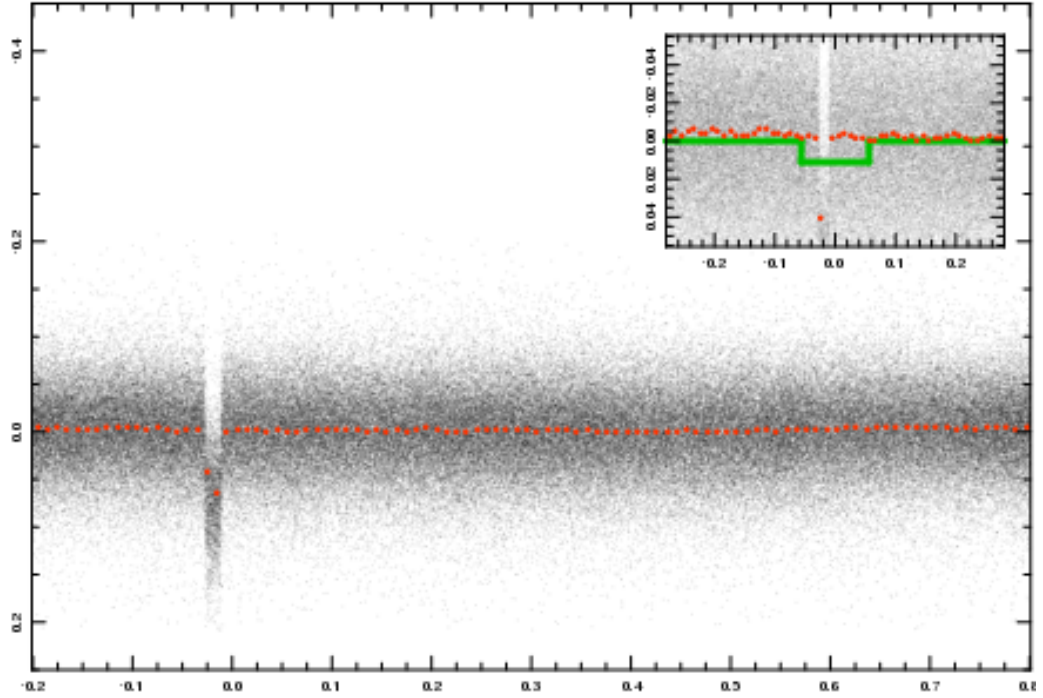


Figure 6.3: NGTS light curve for NOI-101535. The top panel shows the initial BLS fitting (green line).

light curve being an eclipse rather than a transit, the eclipse model in BATMAN produces a more accurate fit. The period of the system was estimated to be 18.87 hours, with a transit duration of 15.605 minutes (Table 6.1).

### Follow-up Photometry: SHOC

To better constrain the parameters of the two companions, follow-up photometric data was collected by Liam Raynard and Ian Braker at the South African Astronomical Observatory (SAAO) using two of the SHOC cameras, mounted on the 1.0 m and the 1.9 m telescopes respectively. Simultaneous observations of the primary eclipse were performed from both telescopes on the night of 23<sup>rd</sup> September 2017 in  $z'$  (at the 1.0 m telescope) and  $V$  bands (at the 1.9 m telescope). An additional observation in  $B$  band was performed

Property	Value	Source
Astrometric Properties		
R.A.	$20^h53^m29.4$	2MASS
Dec	$-01^\circ37'06.1''$	2MASS
2MASS I.D.	20532935-0137061	2MASS
Gaia source I.D.	6916925365694417152	Gaia DR2
$\mu_{\text{R.A.}}$ (mas y <sup>-1</sup> )	$2.183 \pm 0.112$	Gaia DR2
$\mu_{\text{Dec.}}$ (mas y <sup>-1</sup> )	$-94.349 \pm 0.066$	Gaia DR2
parallax (mas)	$16.572 \pm 0.066$	Gaia DR2
Photometric Properties		
U (mag)	$18.518 \pm 0.029$	SkyMapper
g (mag)	$17.12 \pm 0.025$	SkyMapper
r (mag)	$16.363 \pm 0.042$	SkyMapper
i (mag)	$14.939 \pm 0.004$	SkyMapper
z (mag)	$14.271 \pm 0.005$	SkyMapper
G (mag)	15.751	Gaia DR2
$G_{RP}$ (mag)	14.574	Gaia DR2
$G_{BP}$ (mag)	17.049	Gaia DR2
NGTS (mag)	$14.56 \pm 0.01$	this work
J (mag)	$12.860 \pm 0.033$	2MASS
H (mag)	$12.354 \pm 0.039$	2MASS
K (mag)	$12.099 \pm 0.033$	2MASS
Derived Properties		
T0 (HJD)	$2457500.200141 \pm 0.000107$	NGTS BATMAN fit
P (days)	$0.577926999 \pm 0.000000476$	NGTS BATMAN fit
2MASS (Skrutskie et al., 2006); SkyMapper (Wolf et al., 2018); Gaia DR2 (Gaia Collaboration et al., 2018b)		

Table 6.1: Stellar Properties for NOI-101535

at the 1.0 m telescope on 27<sup>th</sup> September 2017, however significant scattered clouds adversely affected the quality of the data.

The data were bias and flat calibrated using the SAFPHOT Python package developed by Alex Chaushev and Liam Raynard. SAFPHOT was also employed to perform aperture photometry on the target and surrounding comparison stars using the ‘SEP’ package (Barbary, 2016). ‘SEP’ subtracts the sky background by producing a background map. This is done by masking the stars in the field, and then adopting box size and filter width parameters that minimise the background residuals across the image. The box sizes had widths of 16 and 32 pixels for the  $V$  and  $z'$  bands respectively, while a filtering value of 0 was adopted in both bands, in order to account to possible overestimation due to the presence of nearby bright stars. Subsequently, aperture sizes that maximised the signal-to-noise ratio were chosen, resulting in sizes of 4.0 and 3.4 pixels for the  $V$  and  $z'$  bands respectively. After extracting raw light curves for the target and surrounding stars, three comparison stars were chosen to perform differential photometry on the target. Figure 6.4 shows the simultaneous light curves. As expected, the depth of the primary eclipse at bluer wavelengths is much deeper ( $> 5$  times) than that in the  $z'$  filter, with depths of  $\sim 7\%$  in  $z'$  and  $\sim 40\%$  in  $V$ .

### **Follow-up Photometry: NITES**

Additional photometric follow-up data were collected by James McCormac using the the Near-Infrared Transiting ExoplanetS telescope (NITES, McCormac et al., 2014) in La Palma. Observations were carried out on the night of September 9, 2017. 491 images were obtained in the  $I$  band filter, with an exposure time of 30 seconds.

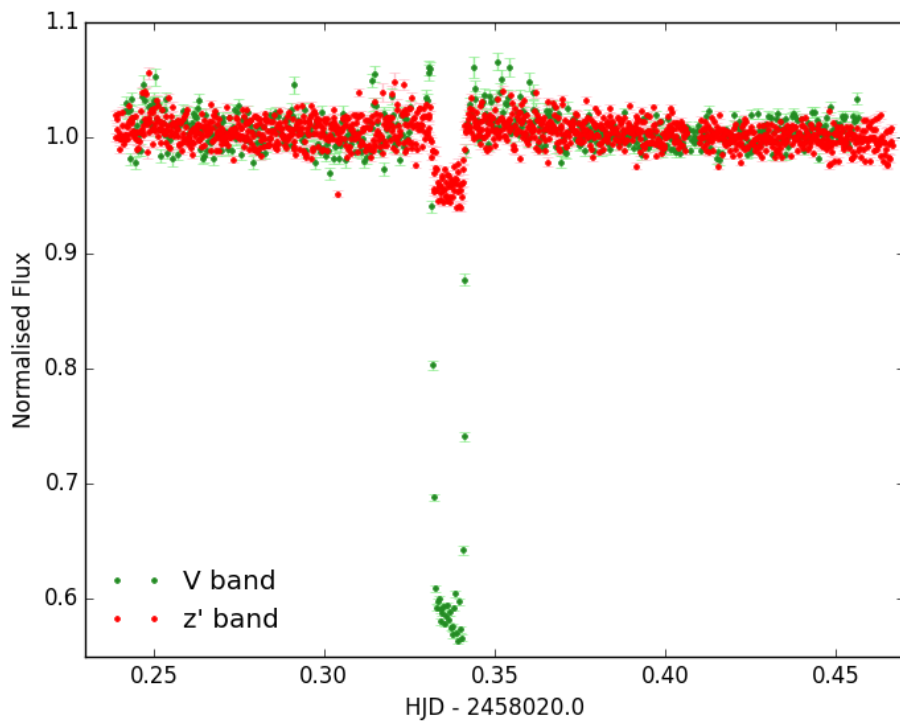


Figure 6.4: Simultaneous observations of the primary eclipse of NOI-101535 from the SAAO 1.0 m and 1.9 m facilities in the  $z'$  band (red) and  $V$  band (green) respectively.

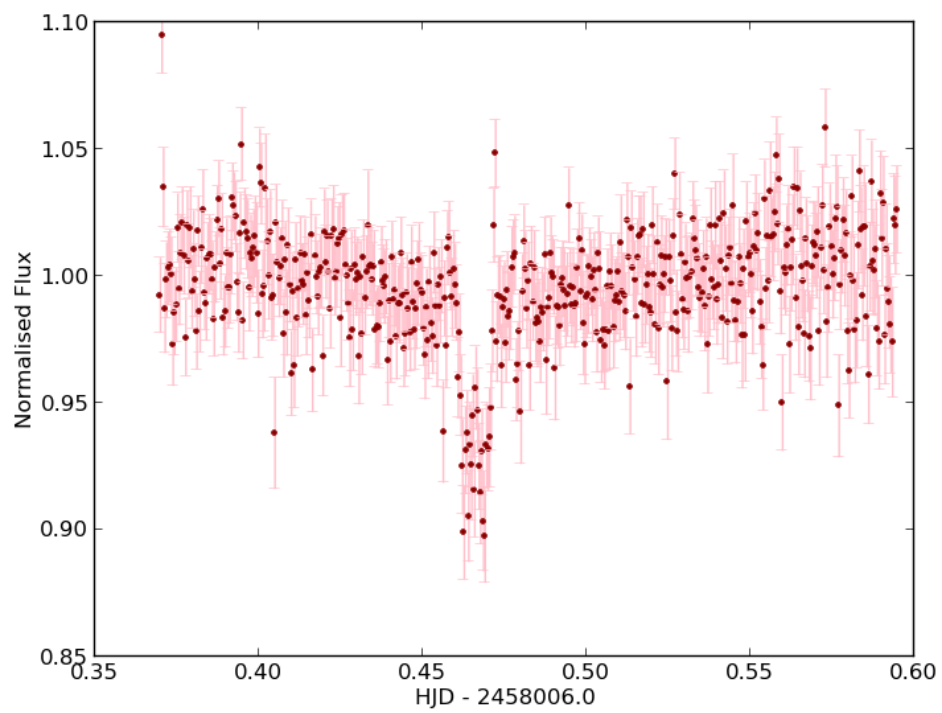


Figure 6.5: NITES observations of the primary eclipse of NOI-101535 in *I* band.

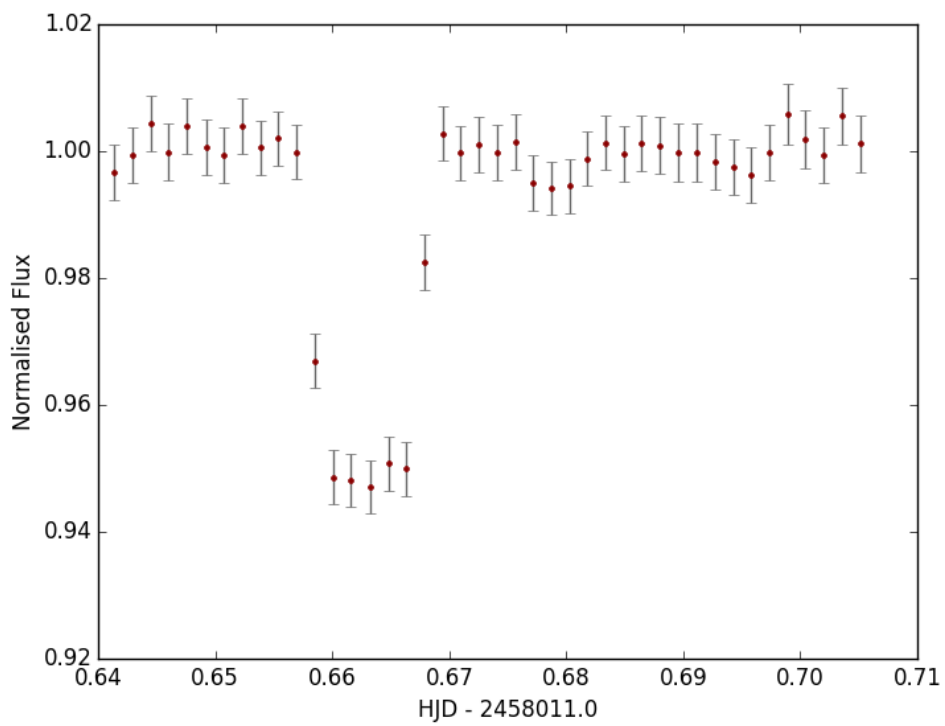


Figure 6.6: Eulercam observations of the primary eclipse of NOI-101535 in ZG band.

The data were reduced using the CCDPROC package in Python (Craig et al., 2015). The images were calibrated using a master bias and a master flat frame. ‘SEP’ (Barbary, 2016) was then used to perform aperture photometry on the target as well as non-variable nearby stars, which were then used as comparisons upon performing differential photometry. The NITES light curve is shown in Figure 6.5.

### **Follow-up Photometry: Eulercam**

The last follow-up photometric run was carried out with Eulercam, mounted on the 1.2 m Swiss Euler telescope in La Silla. Observations were carried out by Gael Ottoni on the night of September 14, 2017. A total of 42 images were collected in the ZG filter, with exposure times of 120 seconds.

The data were reduced by Oliver Turner using the ‘ePipe’ photometric reduction pipeline developed by Sergi Blanco-Cuaresma (e.g. Roelens et al., 2016). An aperture with 11 pixels in radius was used to perform aperture photometry on the target and two comparison stars in the field. Figure 6.6 shows the resulting light curve.

### **Follow-up Spectroscopy: WiFeS**

As mentioned in section 6.2, fitting the system’s spectrum to a model SED can provide information on the effective temperature of the white dwarf component, as well as insight on the spectral class of its M-dwarf companion (e.g. Pyrzas et al., 2012). Therefore, medium resolution spectra of NOI-101535 were obtained on the night of October 14, 2017, using the Wide Field Spectrograph (WiFeS, Dopita et al., 2007), mounted on the ANU 2.3 m telescope at Sliding Spring Observatory (Australia). WiFeS is an image-slicing integral field

spectrograph with two arms. Both blue and red arms were used with gratings B3000 and R3000 respectively, delivering a resolving power of  $\approx 3000$  and a wavelength range between 3500 and 9000 Å. The spectra were wavelength-calibrated using arc exposures of a NeAr lamp, and flux calibrated using a spectrophotometric standard star. The extraction process was performed using the standard method described in .

SkyMapper images with higher spatial resolution than that of NGTS revealed that NOI-101535 appears to have a nearby star at a distance of  $\sim 5$  arcseconds (Figure 6.7).

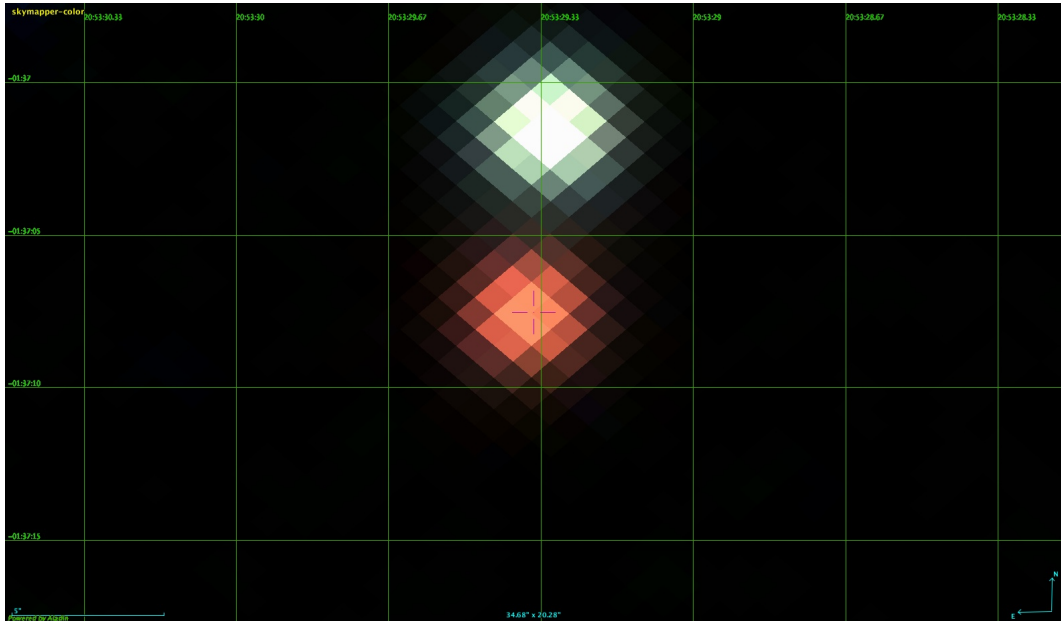


Figure 6.7: A three-colour image from SkyMapper showing NOI-101535 (red star, marked with crosshair) and its close, K-dwarf neighbour (green star to the north).

The two objects appeared as a single source in the NGTS image (which has a 4.97 pixel/arcsec plate scale). Gaia DR2 (Gaia Collaboration et al., 2018b) identifies the nearby source as a K-dwarf, and confirms that the two stars are not physically associated. However, the photometric data from sur-

veys such as WISE and APASS are affected by this close neighbouring star. The NGTS centroiding algorithm (Günther et al., 2017) confirmed that the eclipses were originating from the M-dwarf. Figure 6.8 shows an upward shift in the x-direction of the aperture centroid. This is due to the centre-of-light shifting towards the brighter object in the blended region, while the target is being eclipsed by its companion.

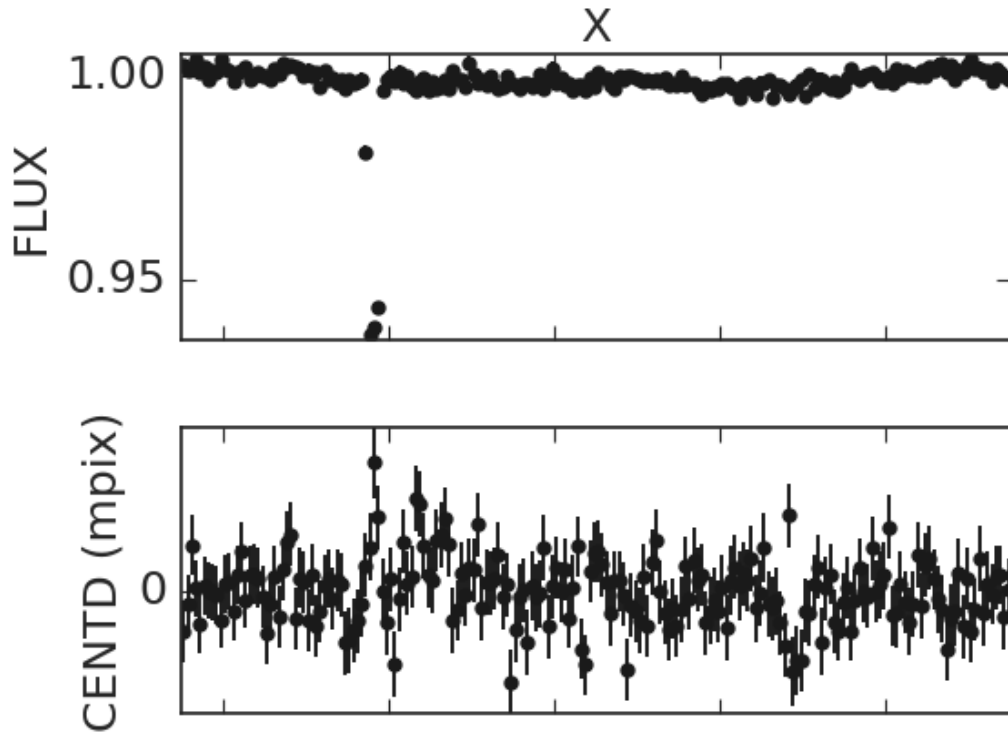


Figure 6.8: The centroid position shift in the x-direction (bottom panel) during a primary eclipse of NOI-101535 observed in the NGTS data (top panel). The image is directly taken from the OPIS database. The x-axis shows the phase of the system, while the y-axis shows relative flux (top panel) and centroiding shift (bottom panel).

The 1 arcsec per image-slice spatial resolution provided by WiFeS, combined with the good seeing conditions on the night of observations enabled us to separate the two neighbouring stars, and to extract spectra for both NOI-

101535 and the K-dwarf (Figure 6.9).

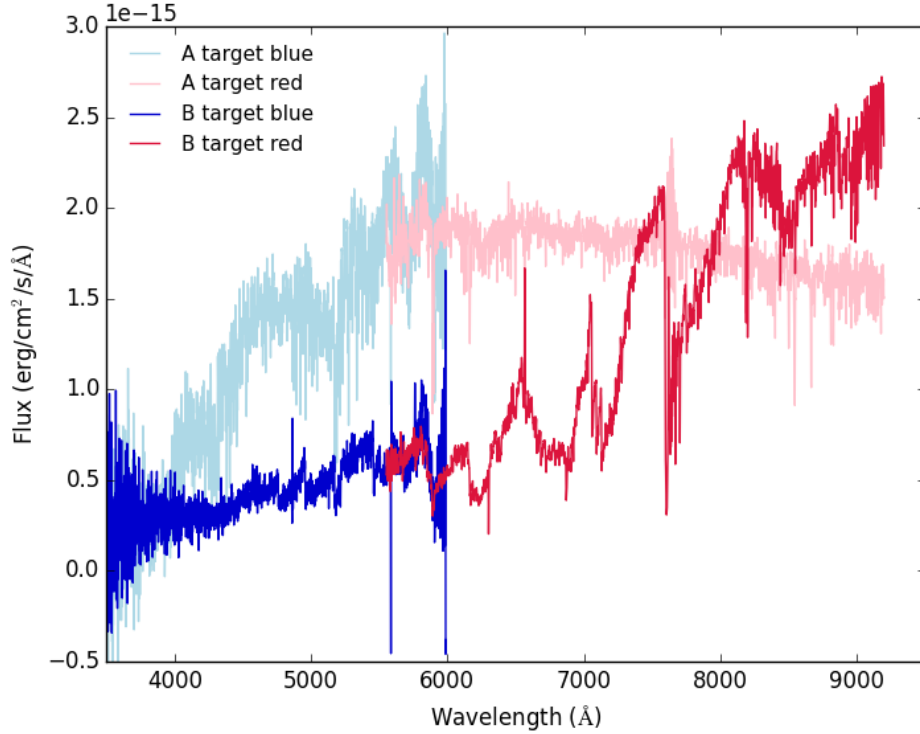


Figure 6.9: The extracted red and blue WiFeS spectra for the K-dwarf neighbour to NOI-101535 (Star A) and for the target itself (Star B).

### Follow-up Spectroscopy: KOSMOS

The last important follow up set of observations was that involving time-resolved spectroscopy. With consecutive spectra, MOLLY could provide radial velocity solutions for both components of this cool PCEB system. NOI-101535 was observed for three nights (14-15-16 October 2017) using the Kitt Peak National Observatory Ohio State Multi-Object Spectrograph (KOSMOS, Martini et al., 2014), mounted on the 4 m Mayall Telescope. The target was observed in longslit mode, using the blue grism and the E2V CCD. Details about the individual exposures can be found in Table 6.2. The data were reduced and

wave calibrated using the standard IRAF packages I previously described in Chapter 2 (Section 2.4). Flux calibration was carried out using a bolometric standard star as reference.

### 6.3.2 Results: Light Curve Fitting

To determine the fractional radii of both the white dwarf and the M-dwarf, as well as to constrain the inclination of the system, I fitted a model to the photometric data collected with SHOC (in  $V$  and  $z'$  bands) and NITES (in  $I$  band) using JKTEBOP (Popper and Etzel, 1981; Etzel, 1981; Nelson and Davis, 1972; Southworth et al., 2004). Details on this software are described in Chapter 2 (Section 2.3.1). The photometry obtained from Eulercam was not suitable for the fitting process, due to the insufficient amount of data points covering the ingress and egress features.

While running the fitting algorithm, I allowed the fractional radii, the inclination and the period to vary. Once these parameters were finalised, I let the Monte Carlo algorithm run to obtain the uncertainties in the fitted parameters, creating 10,000 datasets of fake observational data, to which simulated Gaussian noise was added, and re-fitting the parameters to each dataset. The final uncertainties were given by the range in parameter value, as explained in the JKTEBOP website<sup>1</sup>. While the results from all three fitted light curves were consistent, the best fit (with a  $\chi^2_\nu$  value closest to 1) was given by the  $V$  band data, and was therefore chosen to be the best solution to the system. Figure 6.10 shows the generated best fit models to the three light curves, and the final parameter values for all three filters are found in table 6.3.

---

<sup>1</sup>(<https://www.astro.keele.ac.uk/jkt/codes/jktebop.html>)

Date (UT)	Time (UT)	HJD	Phase	Exp time (s)	Comments
14/10/17	02:27:20	2458040.60463	0.070	1200	
14/10/17	02:41:04	2458040.61417	0.087	1200	
15/10/17	02:49:50	2458041.62017	0.827	600	
15/10/17	03:00:25	2458041.62752	0.840	600	
15/10/17	03:27:20	2458041.64621	0.872	600	
15/10/17	03:40:14	2458041.65517	0.888	600	
15/10/17	03:52:52	2458041.66394	0.903	600	
15/10/17	04:04:16	2458041.67185	0.917	600	
15/10/17	04:15:38	2458041.67975	0.930	600	
15/10/17	04:26:51	2458041.68754	0.944	600	
15/10/17	04:38:18	2458041.69549	0.958	600	
15/10/17	04:49:48	2458041.70347	0.971	600	
15/10/17	05:08:04	2458041.71616	0.993	600	Eclipse
15/10/17	05:21:05	2458041.72519	0.009	600	
15/10/17	05:32:20	2458041.73301	0.023	600	
16/10/17	02:17:38	2458042.59772	0.519	1200	
16/10/17	02:38:53	2458042.61248	0.544	1200	
16/10/17	03:48:27	2458042.66078	0.628	1200	
16/10/17	04:09:38	2458042.67549	0.653	1200	
16/10/17	04:30:47	2458042.69018	0.679	1200	
16/10/17	04:51:40	2458042.70468	0.704	1200	
16/10/17	05:20:04	2458042.7244	0.738	1200	Quadrature
16/10/17	05:41:14	2458042.7391	0.763	1200	

Table 6.2: Observations taken using KOSMOS on the 4m Mayall Telescope

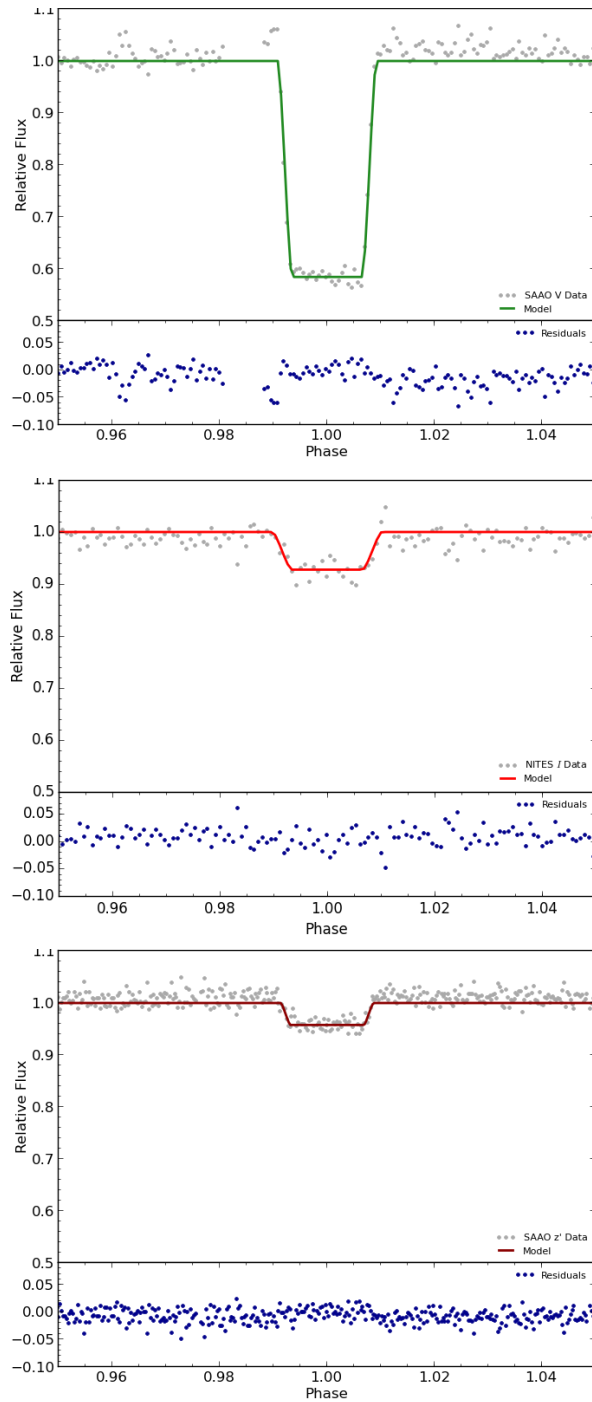


Figure 6.10: Light curve fitting of SAAO data in  $V$  band (top panel) and  $z'$  band (bottom panel), and NITES data in  $I$  band (middle panel). All three plots are maintained at the same flux scale to show the difference in eclipse depth in the different filters. Although only the eclipse is depicted in these plots, all data points in the light curve were used to determine the flux level. The residuals for each light curve represent the model fit - the data.

Parameter	$V$	$I$	$z'$
$R_*/a$	$0.12582 \pm 0.00029$	$0.12705 \pm 0.0104$	$0.12143 \pm 0.0292$
$R_{\text{WD}}/a$	$0.003243 \pm 0.00043$	$0.004264 \pm 0.01331$	$0.00244 \pm 0.00155$
$i$ ( $^\circ$ )	$83.351 \pm 0.034$	$83.366 \pm 0.142$	$85.173 \pm 1.936$
$\chi_\nu^2$	1.66	2.28	2.26

Table 6.3: Radial velocity fitting parameters for NOI-101535.

### 6.3.3 Results: Radial Velocity Measurements

I used MOLLY (details in Chapter 2, Section 2.5) to normalise each spectrum individually, dividing them by a  $10^{\text{th}}$  order polynomial fitted to the continuum flux. I then used the ephemeris and orbital period measured from the BATMAN fit to phase bin the data.

The spectra show a clear emission feature at the  $\text{H}\beta$  Balmer line moving with the M-dwarf, as well as broader and shallower absorption feature at the same position, moving with the white dwarf. I used MGFIT (as explained in Chapter 2, Section 2.5.2) to fit two Gaussians to the  $\text{H}\beta$  line: one broad and shallow varying in position as  $\gamma_1 + k_1 \sin(2\pi\phi)$  to the absorption, and one narrow and sharp moving as  $\gamma_{\text{em}} + k_{\text{em}} \sin(2\pi\phi)$  and with a variable strength of  $(1 - \cos\phi)/2$  (where  $\phi$  is the orbital phase of the system) to the emission. The resulting fit (Figure 6.11) had a reduced  $\chi^2$  value of 0.96. The final  $k$  and  $\gamma$  values are shown in Table 6.4, while the trailed spectra for the data and model are shown in Figure 6.12. The large errors on  $k_1$  and  $\gamma_1$  reflect the difficulty in fitting such a weak absorption feature with data of this quality.

The observed M-dwarf emission line is a result of the star's surface being irradiated from the white dwarf flux. Due to it arising from the heated side of the star facing the white dwarf, this line tracks the centre-of-light of the emission region, rather than the centre of mass. Therefore, a correction needs

to be applied to the radial velocity measurement of the line, to shift it to the centre of mass (Parsons et al., 2017). The correction goes as follows:

$$k_{\text{MS}} = \frac{k_{\text{em}}}{1 - f(1 + q)\frac{R_2}{a}} \quad (6.1)$$

where  $R_2/a$  is the fractional radius of the M-dwarf (see Section 6.3.2 , and  $f$  is a constant between 0 and 1 which depends on the position of the centre of light (Parsons et al., 2012b). The centre of light is dependent on the optical depth of the emission. When  $f = 0$ , the emission is evenly spread across the surface of the star, and the centre of line and mass coincide. When  $f = 1$ , the emission flux is completely concentrated on the M-dwarf's surface point that is closest to the white dwarf. I therefore assumed a value of  $f = 0.5$  (e.g. Parsons et al., 2012c) and consequently applied the correction.

I subsequently used the radial velocity solutions to calculate the mass ratio of the system  $q$ :

$$q = \frac{k_1}{k_{\text{em}}} = \frac{M_*}{M_{\text{WD}}} = 0.6064 \pm 0.1082 \quad (6.2)$$

where  $M_*$  is the mass of the M-dwarf and  $M_{\text{WD}}$  is the mass of the white dwarf.

Furthermore, Kepler's third law can be rearranged to calculate the mass of the white dwarf as follows (Parsons et al., 2012c):

$$M_{\text{WD}} = \frac{Pk_{\text{em}}(k_1 + k_{\text{em}})^2}{2\pi G \sin^3 i} = 0.7069 \pm 0.1260 M_{\odot} \quad (6.3)$$

where  $P$  is the orbital period,  $i$  the orbital inclination and  $G$  is the gravitational constant. The inclination is constrained by fitting the light curves, as discussed in Section 6.3.2.

Parameter	Value
$k_{\text{em}}$	$164.901 \pm 2.542 \text{ kms}^{-1}$
$k_1$	$99.993 \pm 17.756 \text{ kms}^{-1}$
$\gamma_{\text{em}}$	$19.155 \pm 1.665 \text{ kms}^{-1}$
$\gamma_1$	$7.802 \pm 11.582 \text{ kms}^{-1}$

Table 6.4: Radial velocity fitting parameters for NOI-101535.

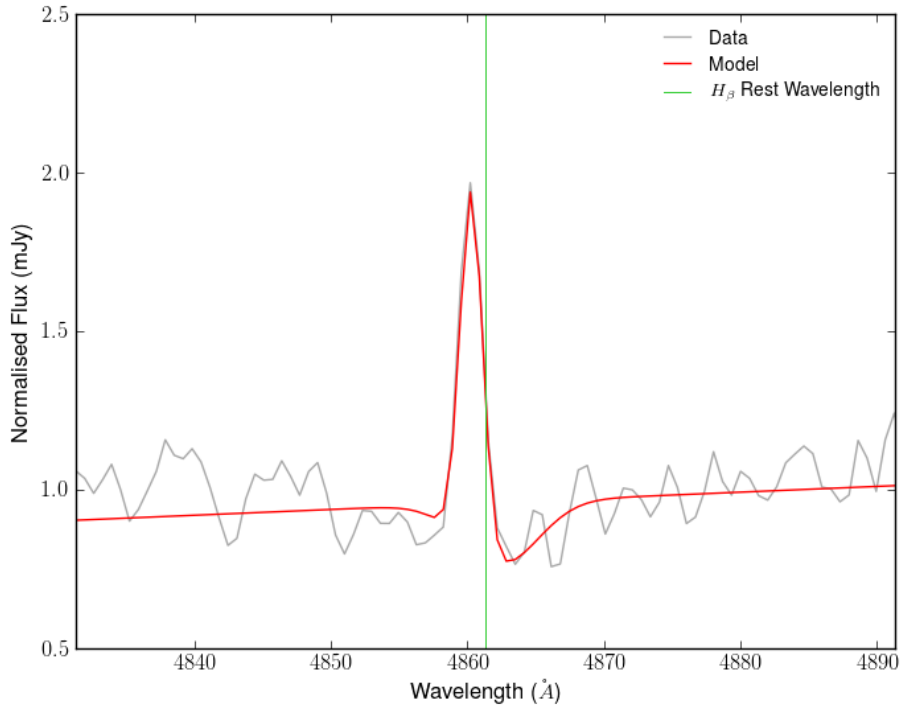


Figure 6.11: An example of MGFIT model fit to the  $H\beta$  emission and absorption lines in one of the KOSMOS spectra of NOI-101535.

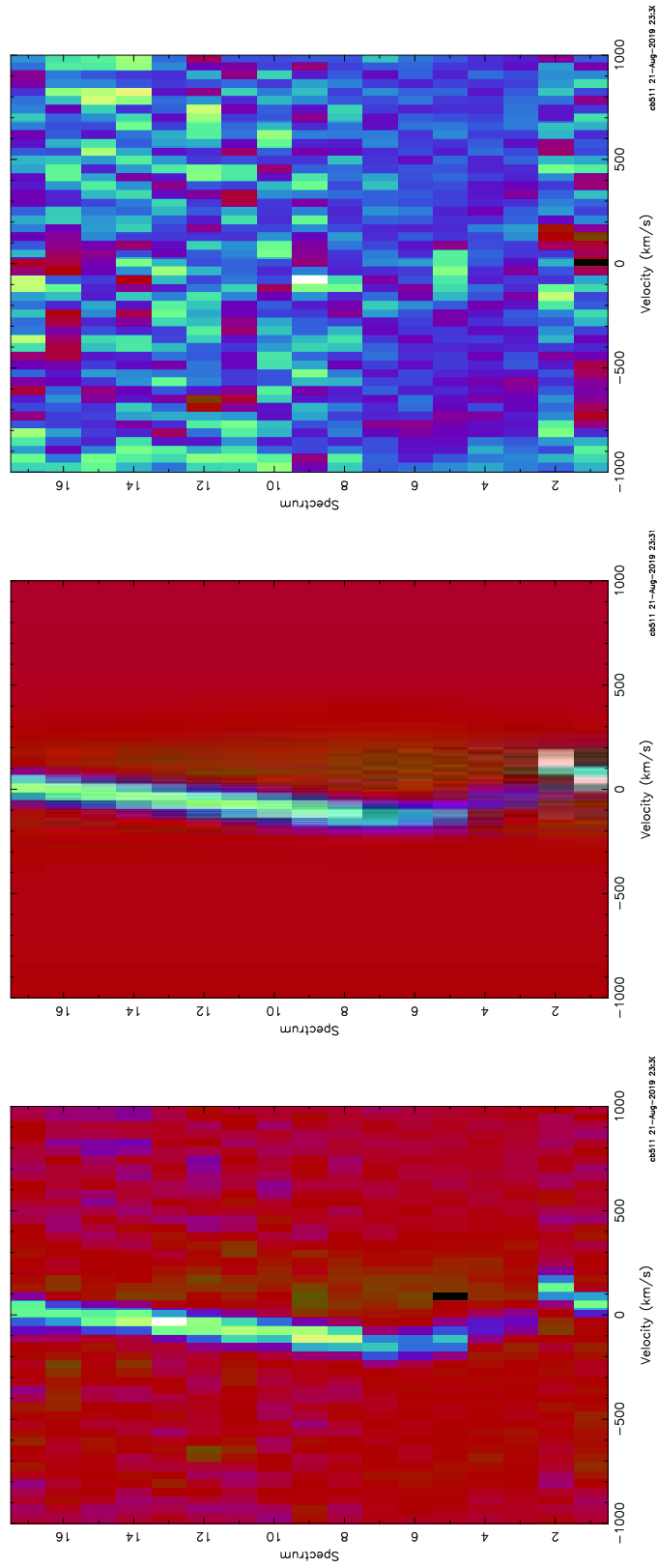


Figure 6.12: Trailed KOSMOS spectra (in order of phase) of NOI-101535, centred on the  $H\beta$  emission and absorption lines. The plots show the data (left panel), the model generated from the Gaussian fitting (central panel) and the residuals to the fit (right panel).

### 6.3.4 Results: M-Dwarf Spectral Type

As previously mentioned, the WiFeS spectra were collected to constrain the spectral type of the M-dwarf component of this binary system. I used a similar method to that described in Chapter 5 (Section 5.2.3), i.e. by combining white dwarf and M-dwarf spectra, after normalising them to the same magnitude scale. However, in this case there was no previous estimate for the white dwarf effective temperature and gravity. For this reason, I assumed a  $\log g$  of 8.0 (corresponding to the mass of an average white dwarf), and then I used three estimates for the white dwarf temperature (7000, 7500 and 8000 K respectively). The temperature range was estimated based on SDSS J121010.1+334722.9 (Pyrzas et al., 2012), in which the white dwarf has a temperature of  $\sim 6000$  K. I matched the three model spectra from Koester (2010) to the corresponding absolute magnitudes from Holberg and Bergeron (2006) and Tremblay et al. (2011). I then repeated the procedure for a few M-dwarf spectral type (M3, M4, M5 and M6), sourcing the averaged template spectra from Bochanski et al. (2007). The absolute magnitudes were calculated using apparent magnitudes and Gaia parallaxes of M-dwarf standards listed the SpeX Prism Spectral libraries<sup>2</sup>.

Once normalised to the absolute magnitudes, the model white dwarf and the M-dwarf template spectra were interpolated to fall on the same wavelength scale. Subsequently, each white dwarf model was combined to the template M-dwarfs. This was done taking into account that, as estimated from the light curve fits, the white dwarf only contributes  $\approx 5\%$  to the light of the system at redder wavelengths ( $I$  and  $z'$  filters).

---

<sup>2</sup><http://pono.ucsd.edu/~adam/browndwarfs/spexprism/>

I compared each of the three generated white dwarf + M-dwarf models to the observed WiFeS spectra to establish the spectral class of the M-dwarf companion, as well as to estimate (to 500 K) the most likely temperature for the white dwarf.

Figures 6.13, 6.14 and 6.15 show that the most likely spectral type of the M-dwarf component is M4. While all three white dwarf temperature choices seem to agree with our observed data, the best fit model was yet to be determined. To do so, I combined the three white dwarf spectra only with the template spectrum of an M4 dwarf, and then compared these three new models to the observed WiFeS spectrum, to refine the effective temperature of the white dwarf. As Figure 6.16 reveals, the best fit is given by a white dwarf of  $\log g = 8$  and  $T_{\text{eff}} = 7500$  K. However, this is only an estimate, as the spectrum is heavily dominated by the redder companion to the white dwarf.

### 6.3.5 Results: Final Parameters

Once the fractional radii and inclination were determined, I used equation 6.3 to calculate the mass of the white dwarf. Consequently, the mass of the M-dwarf companion was measured from the mass ratio  $q$  of the system. The radial velocities of the two components were used to find the sum of the unprojected orbital speeds, defined as:

$$V_s = \frac{k_1 + k_{\text{em}}}{\sin i} \quad (6.4)$$

Hence, the orbital separation  $a$  was calculated to be (Parsons et al., 2012c):

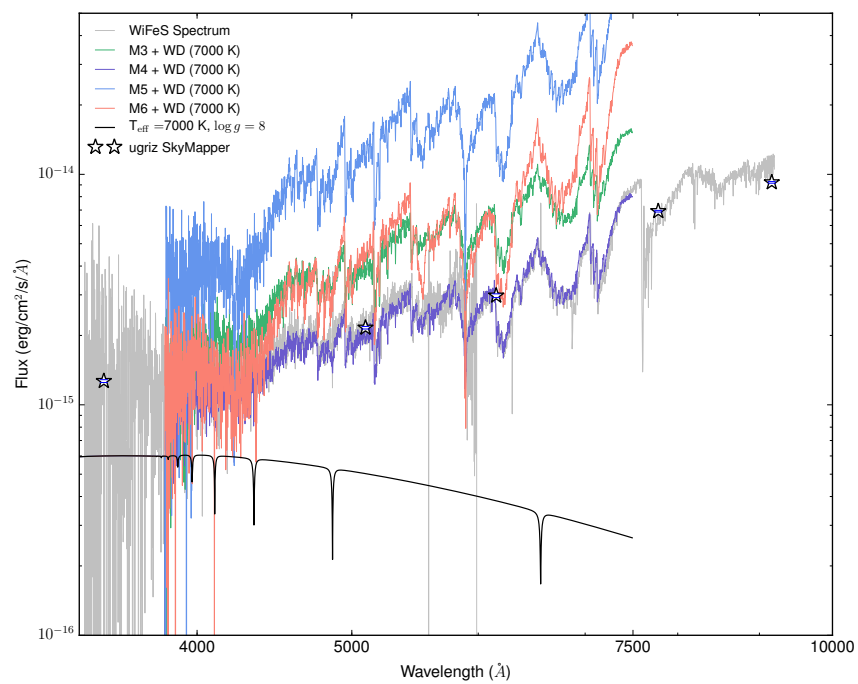


Figure 6.13: WiFeS spectrum and SkyMapper *ugriz* photometry compared to the combined SED of a  $T_{\text{eff}} = 7000$  K and  $\log g = 8$  white dwarf and multiple M-dwarf type spectra. The data best fits with an M4 spectral type.

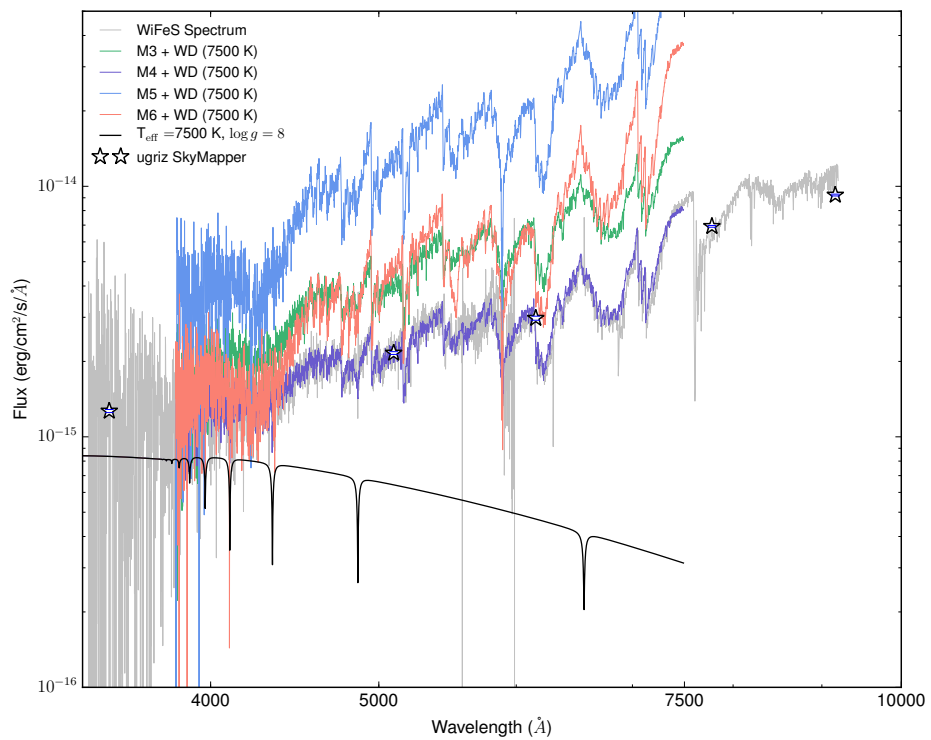


Figure 6.14: WiFeS spectrum and SkyMapper *ugriz* photometry compared to the combined SED of a  $T_{\text{eff}} = 7500 \text{ K}$  and  $\log g = 8$  white dwarf and multiple M-dwarf type spectra. The data best fits with an M4 spectral type.

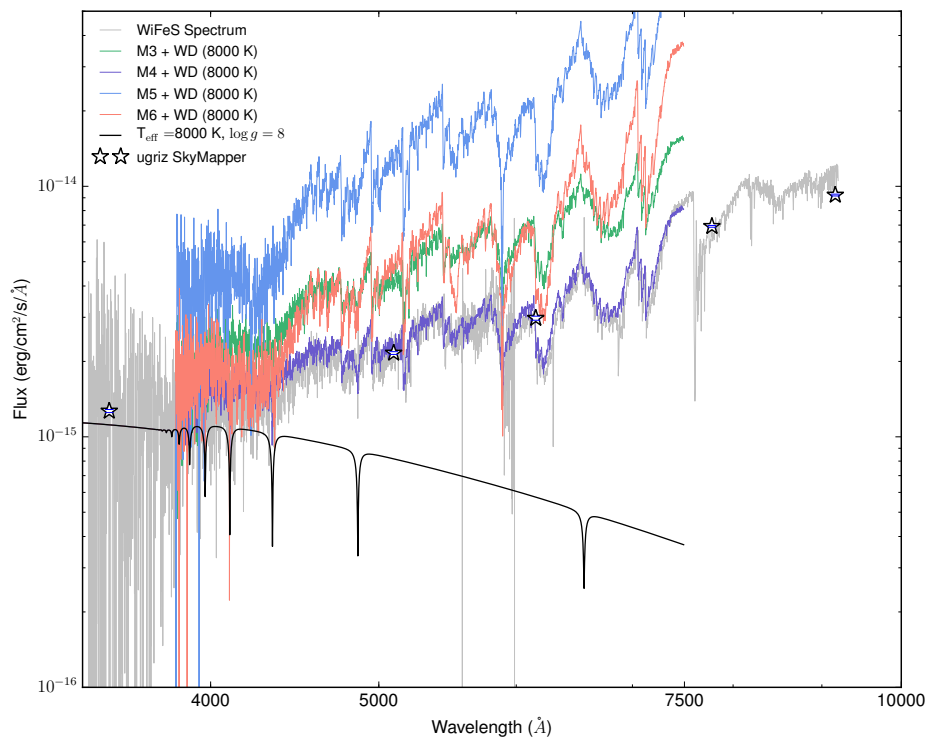


Figure 6.15: WiFeS spectrum and SkyMapper *ugriz* photometry compared to the combined SED of a  $T_{\text{eff}} = 8000 \text{ K}$  and  $\log g = 8$  white dwarf and multiple M-dwarf type spectra. The data best fits with an M4 spectral type.

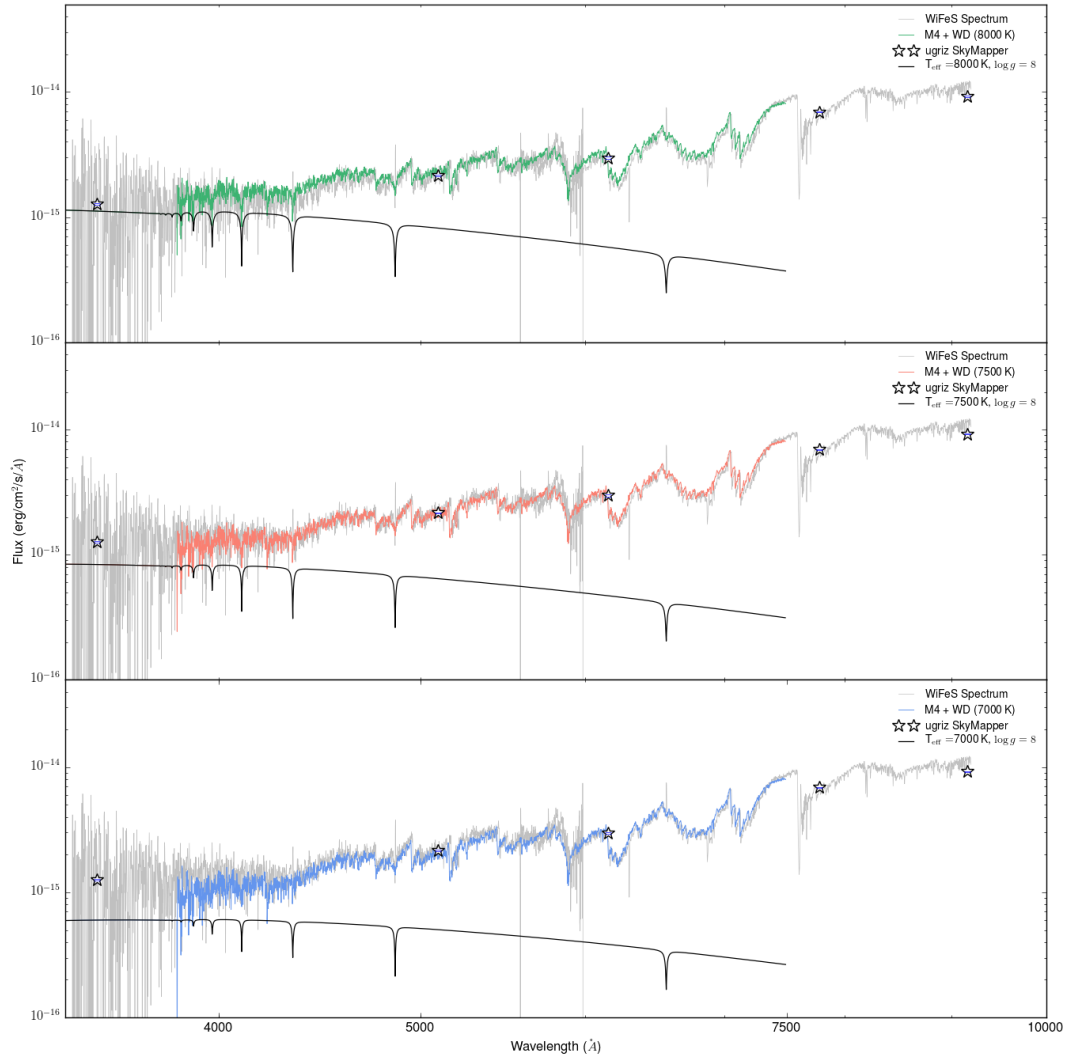


Figure 6.16: WiFeS spectrum and SkyMapper *ugriz* photometry compared to the combined SEDs of an M4 dwarf with white dwarfs spectra of  $T_{\text{eff}} = 8000$  K (top),  $T_{\text{eff}} = 7500$  K (middle) and  $T_{\text{eff}} = 7000$  K (bottom). The data best fits with a  $T_{\text{eff}} = 7500$  K and  $\log g = 8$  white dwarf.

$$a = \frac{V_s}{2\pi} P = \frac{(k_1 + k_{\text{em}})P}{2\pi \sin i} \quad (6.5)$$

Once the orbital separation was known, the white dwarf and M-dwarf radii ( $R_{\text{WD}}$  and  $R_*$  respectively) were extrapolated from the fractional radius values. The resulting final masses and radii are shown in table 6.5.

Parameter	Value
$R_*$ ( $R_\odot$ )	$0.3834 \pm 0.068$
$R_{\text{WD}}$ ( $R_\odot$ )	$0.0099 \pm 0.0022$
$M_*$ ( $M_\odot$ )	$0.4286 \pm 0.1081$
$M_{\text{WD}}$ ( $M_\odot$ )	$0.7069 \pm 0.1260$
$a$ ( $R_\odot$ )	$3.0472 \pm 0.543$

Table 6.5: Calculated masses, radii and orbital separation for the NOI-101535 system components.

With the white dwarf physical parameters constrained, I used the following equation to obtain an estimate of the white dwarf's gravitational redshift:

$$z = 0.635 \left( \frac{M_{\text{WD}}}{M_\odot} \right) \left( \frac{R_\odot}{R_{\text{WD}}} \right) \text{ kms}^{-1} \quad (6.6)$$

where WD and  $R_{\text{WD}}$  are the mass and radius of the white dwarf respectively. Through this method, I obtained a value of  $z = 44.714 \pm 12.964 \text{ kms}^{-1}$ . This is consistent with the Fontaine et al. (2001) evolutionary models, which predict a gravitational redshift of  $z = 41.3 \text{ kms}^{-1}$  for a  $T_{\text{eff}} = 7500 \text{ K}$  and  $\log g = 8.21$  ( $0.708 M_\odot$ ) white dwarf. Another method for calculating the white dwarf's

gravitational redshift consists of calculating the difference between the  $\gamma$  velocities of the system. Through this method, I obtained a  $z$  value of:

$$z = \gamma_{\text{em}} - \gamma_1 = 11.353 \pm 11.701 \text{ kms}^{-1} \quad (6.7)$$

This is inconsistent, within the errors, with the value obtained through equation 6.6. Assuming normal distributions for both calculated  $z$  values, using the Student's t-test I find a p-value of 0.0001, which makes the difference between the two calculations extremely significant. However, this inconsistency is most likely due to the large errors on the radial velocity fit to the white dwarf absorption line.

### 6.3.6 Discussion

The white dwarf radius obtained from JKTEBOP is in agreement with the Fontaine et al. (2001) evolutionary models, which predict  $R_{\text{WD}} = 0.0109 R_{\odot}$ . Moreover, I compared the resulting white dwarf mass and radius to the theoretical mass-radius tracks from Renedo et al. (2010), as shown in Figure 6.17. The results shown in table 6.5 are consistent with the models. The large errors on the mass are due to the radial velocity fit to the white dwarf absorption line, which is dominated by the M-dwarf absorption and barely visible.

Figure 6.18 shows the mass-radius plot for the M-dwarf in NOI-101535. In the plot, the solid and dashed lines represent isochrones for low mass stars from Baraffe et al. (2015). The age of the M-dwarf was estimated from West et al. (2008), who provide timescales for different M-dwarf classes to be active. In particular, they find an activity lifetime for an M4 dwarf of  $4.5 \pm_{1.0}^{0.5}$  Gyr. Due to the lack of metal emission lines in NOI-101535 spectra, and the lack of

flares in the light curves, the M-dwarf is assumed to not be active, hence older than the age cited above. To this first estimate, one needs to add the predicted age of the white dwarf, which results to be 1.837 Gyr (Fontaine et al., 2001). I therefore used isochrone tracks of 5 and 8 Gyrs in Figure 6.18.

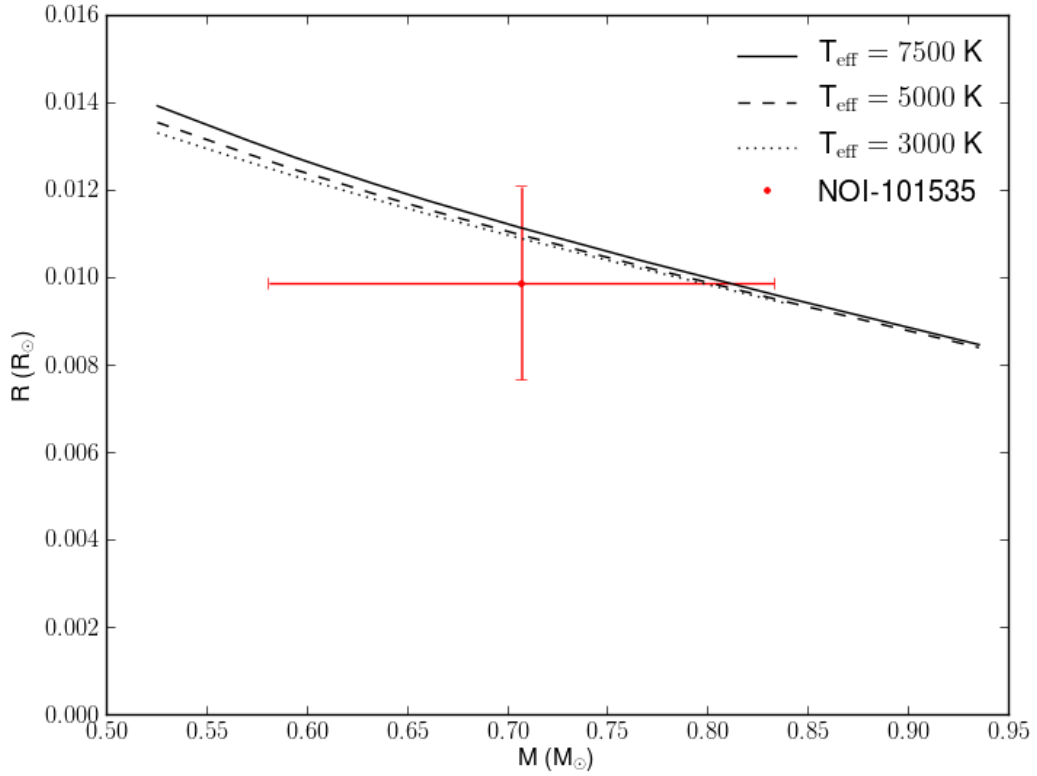


Figure 6.17: Mass-radius plot for the white dwarf component in NOI-101535. The black solid, dashed and dotted lines represent tracks from Renedo et al. (2010) for a  $T_{\text{eff}} = 7500$  K,  $T_{\text{eff}} = 5000$  K and  $T_{\text{eff}} = 3000$  K white dwarf respectively.

### 6.3.7 Summary

In summary, following the NGTS discovery of NOI-101535 I used photometric and spectroscopic data to constrain the masses and radii of this old, cool

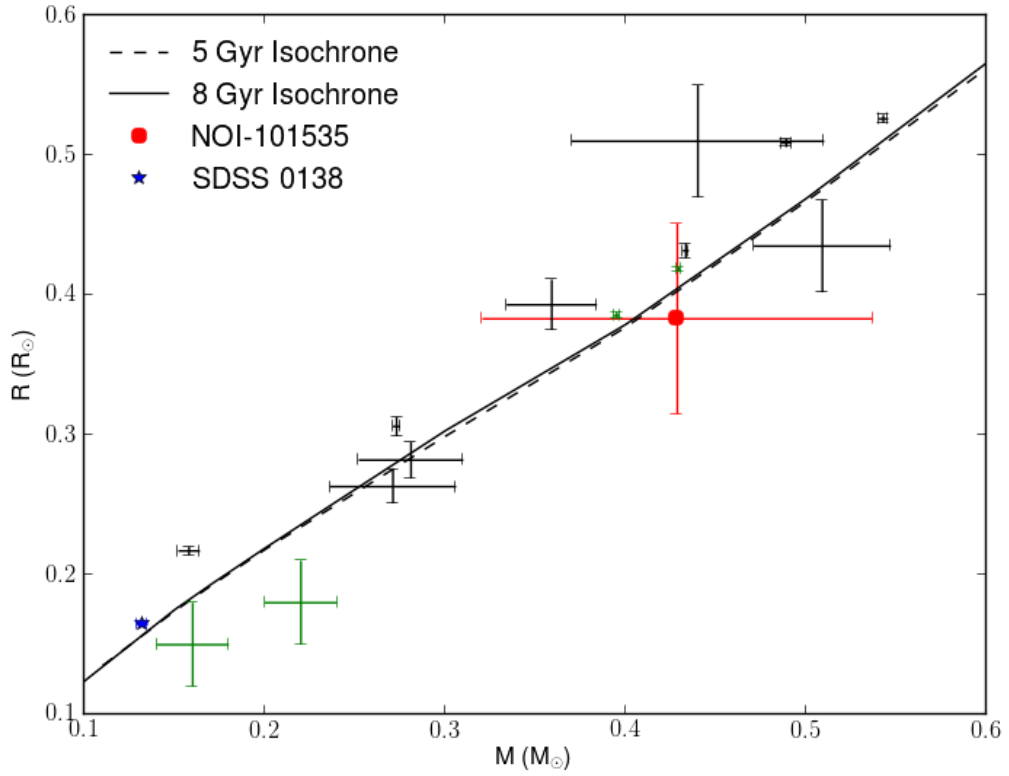


Figure 6.18: Mass-radius plot for the M-dwarf component in NOI-101535. The black solid and dashed lines represent the 8 Gyr and 5 Gyr isochrones respectively from Baraffe et al. (2015). The blue star-shaped data point shows the M dwarf in SDSS 0138-0016 (Parsons et al., 2012a), the only WD + M-dwarf systems in which the white dwarf has a temperature cooler than 4000 K. The black error bars represent other M-dwarfs in eclipsing PCEBs from Pyrzas et al. (2012); Parsons et al. (2012c,b) and Beatty et al. (2007). Finally, the green error bars show M-dwarfs in double M-dwarf binaries from Leinert et al. (1990) and Wilson et al. (2017)

PCEB system. From the combined SED, I estimated the temperature of the white dwarf to be  $T_{\text{eff}} \approx 7500$  K. From spectral and photometric analysis, I measured the white dwarf to have a mass of  $0.7069 \pm 0.1260 M_{\odot}$  and a radius of  $0.0099 \pm 0.0022 R_{\odot}$ . These values are consistent with Fontaine et al. (2001) evolutionary models, and with a cooling age of 1.837 Gyr.

I compared the collected spectra to combined SEDs of a white dwarf and several types of M-dwarf, finding the most likely to be an M4. The measured mass and radius for the secondary component in NOI-101535 were estimated to be  $0.4286 \pm 0.1081 M_{\odot}$   $0.3834 \pm 0.068 R_{\odot}$  respectively. These were found to be in good agreement with Baraffe et al. (2015) models for a  $\sim 8$  Gyr M-dwarf.

## 6.4 NOI-103465

### 6.4.1 Optical Observations

#### NGTS Photometry

NOI-103465 is the second post common envelope binary system discovered in NGTS. It was observed as part of the survey between 16 August 2017 and 18 March 2018, for a total of 204,154 images. The images were reduced using the standard pipeline described in section 6.1.3 (Wheatley et al., 2018). Similar to NOI-101535, the light curve shows a sharp eclipse feature lacking the characteristic ingress and egress features produced by planetary transit (Figure 6.19). This time however, the eclipse shows a depth of  $\sim 4\%$ , with a duration of  $\sim 25$  minutes and a period of 0.60784 days ( $\approx 14.6$  hours). Table 6.6 shows a list of astrometric and photometric properties for the system.

Property	Value	Source
Astrometric Properties		
R.A.	04:52:33.43	2MASS
Dec	-36:32:12.0	2MASS
2MASS I.D.	J04523343-3632120	2MASS
Gaia source I.D.	4818744300120317440	Gaia DR2
$\mu_{\text{R.A.}}$ (mas y <sup>-1</sup> )	70.082±0.032	Gaia DR2
$\mu_{\text{Dec.}}$ (mas y <sup>-1</sup> )	152.890±0.037	Gaia DR2
parallax (mas)	13.2382±0.0208	Gaia DR2
Photometric Properties		
u (mag)	16.082±0.016	SkyMapper
v (mag)	15.934±0.023	SkyMapper
g (mag)	14.684±0.011	SkyMapper
r (mag)	14.036±0.004	SkyMapper
i (mag)	12.940±0.007	SkyMapper
z (mag)	12.496±0.005	SkyMapper
G (mag)	13.6681±0.0004	Gaia DR2
NGTS (mag)	11.17±0.01	this work
J (mag)	11.211±0.023	2MASS
H (mag)	10.608±0.022	2MASS
K (mag)	10.383±0.019	2MASS
Derived Properties		
T0 (HJD)	2457982.10466698±0.0000102	NGTS BATMAN fit
P (days)	0.60793933±0.000000105	NGTS BATMAN fit
2MASS (Skrutskie et al., 2006); SkyMapper (Wolf et al., 2018); Gaia DR2 (Gaia Collaboration et al., 2018b)		

Table 6.6: Stellar Properties for NOI-103465

## Follow-up Photometry: SHOC

As for NOI-101535, follow up photometry was required in order to constrain the parameters of the two components of this PCEB system. I therefore collected photometric data covering the primary eclipse using the SHOC instrument mounted on the 1.0 m telescope at SAAO. Data were collected in  $I$  band and  $V$  band, on the nights of 3 and 9 October 2018 respectively. In the  $I$  band, I collected a total of 550 exposures, with an exposure time of 20 seconds. In the  $V$  band, I collected a total of 525 exposures, with an integration time of 30 seconds. I reduced and calibrated the data using the standard SHOC reduction pipeline, and then performed aperture photometry, and used one comparison star in the field of view to conduct differential photometry. Details on this method are described in Chapter 2, Section 2.1. Figures 6.20 and 6.21 show

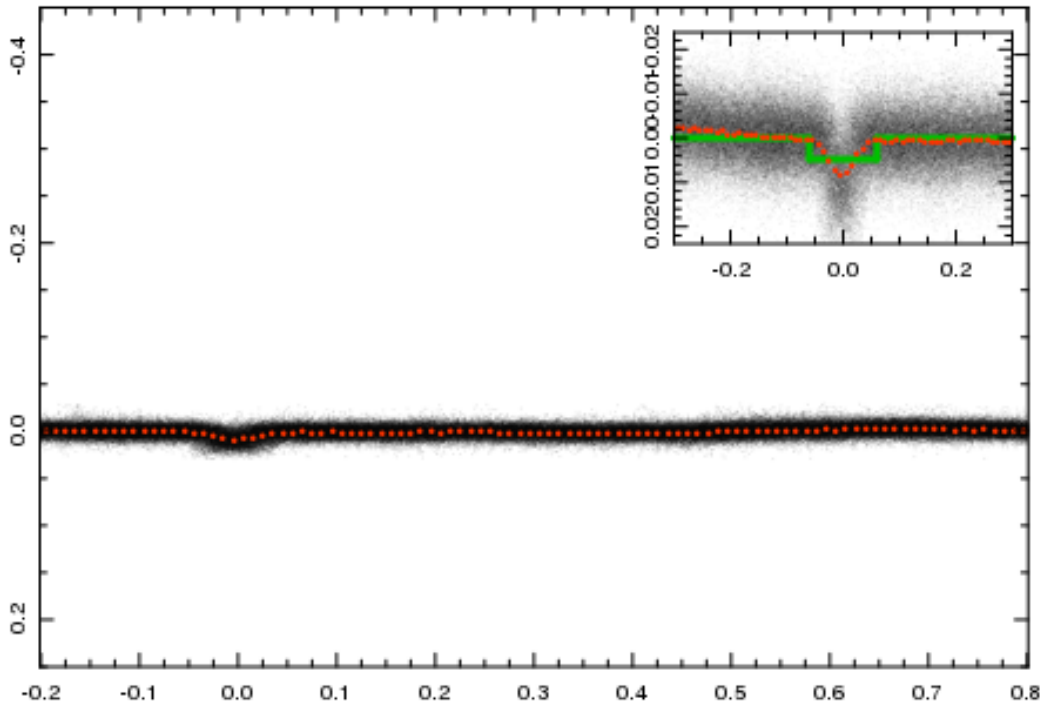


Figure 6.19: NGTS light curve for NOI-103465. The top panel shows the initial BLS fitting (green line).

the normalised SHOC light curves. The  $I$  band light curve shows a gradual brightening after the transit, hinting to a reflection effect in the system. This reflection effect is also seen in the NGTS phase folded data, as shown in figure 6.22.

Moreover, the  $V$  band light curve shows a clear flare feature shortly before the eclipse, which indicates the main sequence (MS) companion is still active.

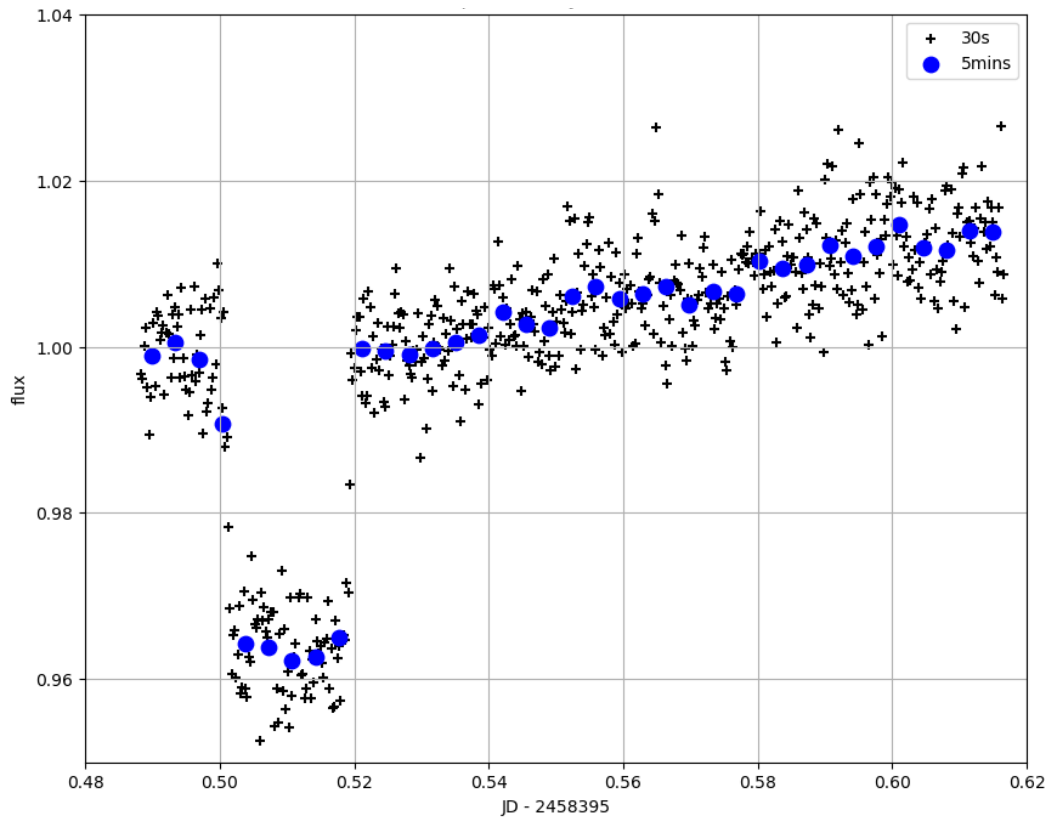


Figure 6.20: SHOC light curve for NOI-103465 in  $I$  band.

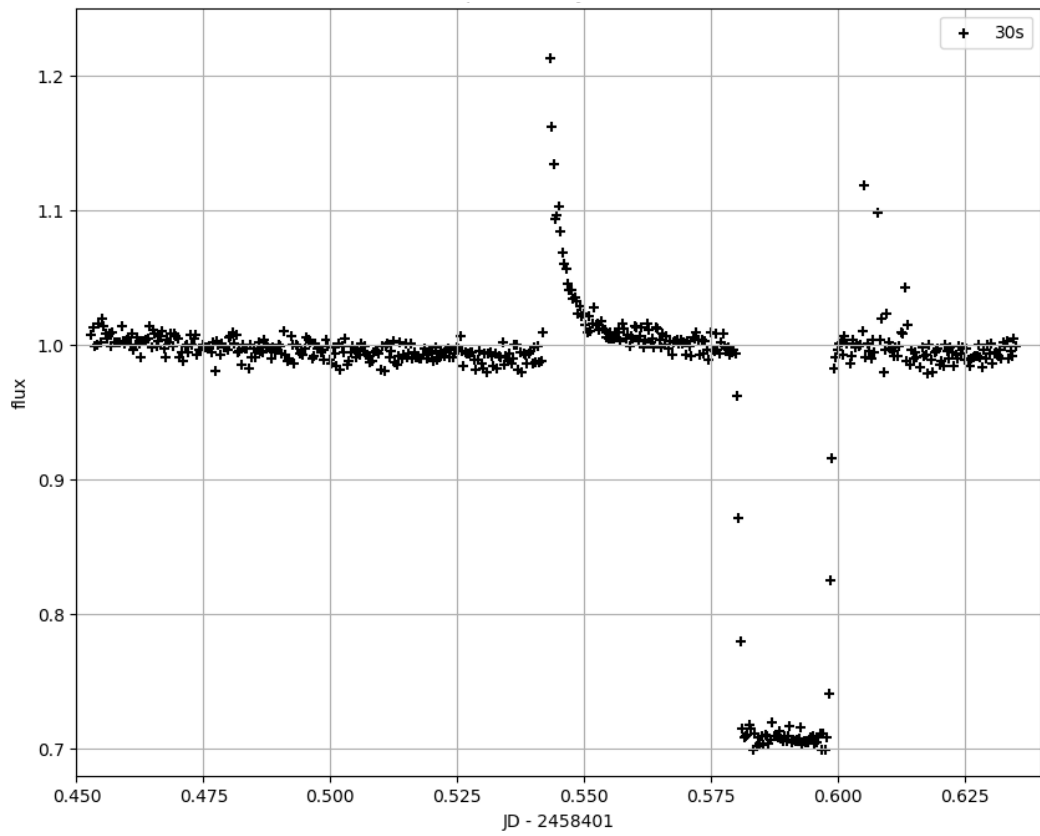


Figure 6.21: SHOC light curve for NOI-103465 in  $V$  band. Just before the eclipse, a flare feature is visible, indicating activity in the MS star's atmosphere.

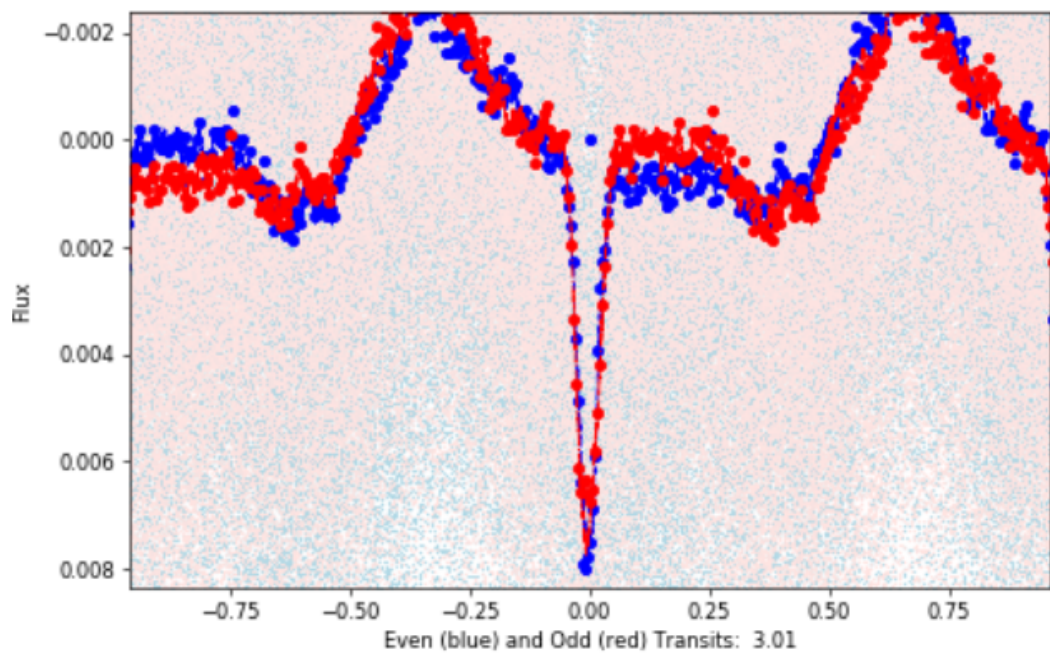


Figure 6.22: Phase folded and binned NGTS light curve from the OPIS database. The plot shows relative flux for the even (blue) and odd (red) eclipses as a function of phase. A significant asymmetric reflection effect can be observed between eclipses.

### **Follow-up Photometry: Eulercam**

Additional photometric data was collected with the 1.2 m Swiss Euler telescope + Eulercam, at the La Silla Observatory. Observations were carried out by Helen Giles, on the night of November 21, 2018. A total of 93 exposures in the *R* band were collected. The starting exposure time was 10 seconds, however it was incremented to 90 seconds as the observation progressed to achieve a suitable signal-to-noise ratio.

The data were reduced by Oliver Turner using the ‘ePipe’ pipeline developed by Sergi Blanco-Cuaresma (e.g. Roelens et al., 2016). An aperture radius of 9 pixels was chosen to perform aperture photometry on the target and four comparison stars, which were then employed in differential photometry. Figure 6.23 shows the final, normalised Eulercam light curve. Similar to the *V* band SHOC data, there appears to be a flare feature occurring just after the transit.

### **Follow-up Spectroscopy: SpUpNIC**

Time-resolved spectroscopic data is of vital importance to determine the radial velocity variations and hence the masses of the components of this binary system. I therefore observed NOI-103465 with the Spectrograph Upgrade: Newly Improved Cassegrain (SpUpNIC, Crause et al., 2016) instrument, mounted on the 1.9 m telescope at SAAO. I observed the target over the course of 5 nights between 5 and 9 April, 2019. I used Grating 4, which offers a wavelength range between  $\sim 3800\text{--}5150$  Å and a medium resolution of 2500. I used the standard IRAF tools (described in Chapter 2, section 2.4) to perform bias and flat correction on all the spectra. The spectra were then wavelength calibrated

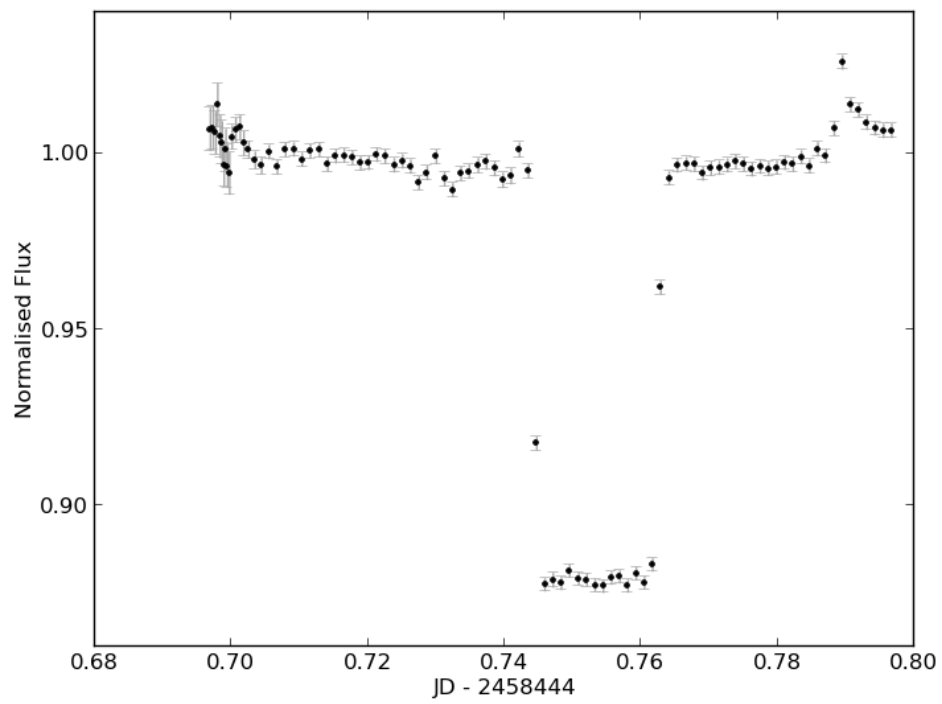


Figure 6.23: Eulercam light curve for NOI-103465 in  $R$  band. Just after the eclipse, a flare feature is visible, indicating activity in the MS star's atmosphere.

using arcs from SpUpNIC’s CuAr lamp, and flux calibrated using the standard star Hiltner 600. Table 6.7 shows detailed information about each exposure.

Date (UT)	Time (UT)	HJD	Exp Time (s)	Phase
05/04/19	17:29:47	2458579.224770526	900	0.13436
05/04/19	17:45:31	2458579.235696094	900	0.15233
05/04/19	18:17:20	2458579.257790994	900	0.18867
06/04/19	17:49:38	2458580.238577272	900	0.80197
06/04/19	18:06:41	2458580.250425796	900	0.82146
06/04/19	18:22:26	2458580.261358993	900	0.83944
07/04/19	18:48:23	2458581.279408152	900	0.51403
08/04/19	18:14:21	2458582.255787817	900	0.12008
09/04/19	17:13:21	2458583.213456937	900	0.69535
09/04/19	17:30:35	2458583.225428000	900	0.71504
09/04/19	17:46:38	2458583.236566624	900	0.73336
09/04/19	18:02:22	2458583.247496871	900	0.75134

Table 6.7: Observations taken using SpUpNIC on the 1.0 m SAAO telescope.

## 6.4.2 Results: Radial Velocity Measurements

I used MOLLY (details in Chapter 2, Section 2.4), to normalise each spectrum by fitting and then dividing the continuum flux by a 10<sup>th</sup> degree polynomial. I then used the system’s ephemeris and orbital period to phase bin the data.

Contrary to NOI-101535, the white dwarf’s absorption features at the Balmer lines is quite prominent, thus suggesting that this system is hotter and younger than the latter. This is also confirmed by the flaring activity on the MS star’s photosphere.

To obtain radial velocity solutions for both components of NOI-103465, I used MGFIT to fit two Gaussian functions to the H $\gamma$  absorption line, as

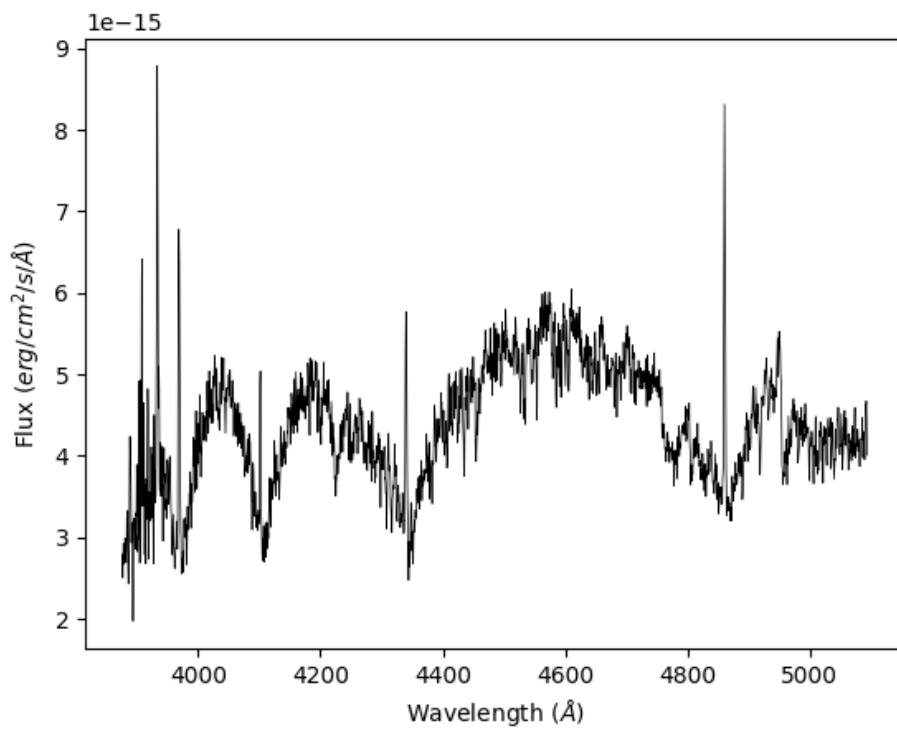


Figure 6.24: One of the SpUpNIC spectra collected at SAAO. Prominent broad absorption features related to the white dwarf can be observed at  $H\beta$ ,  $H\gamma$ ,  $H\delta$  and  $H\epsilon$ , as well as narrow emission lines at the same wavelengths, related to the active main sequence companion.

well as a single, narrow Gaussian function to the emission feature at the same wavelength (Figure 6.25). The white dwarf Gaussians were assumed to vary as  $\gamma_1 + k_1 \sin(2\pi\phi)$ , while the MS companion model emission was allowed to vary in position as  $\gamma_{\text{em}} + k_{\text{em}} \sin(2\pi\phi)$ , and in strength as  $(1 - \cos \phi)/2$ , where  $\phi$  is the orbital phase of the system. The resulting trailed spectra for the data, model and residuals to the fit are shown in Figure 6.26. The final fit had a reduced  $\chi^2$  value of 1.03, and the resulting values for the  $k$  and  $\gamma$  velocities are listed in table 6.8.

Subsequently, I used Equation 6.2 to calculate the mass ratio of the system, which resulted to be  $q = 1.2344 \pm 0.0494$ .

Parameter	Value
$k_{\text{em}}$	$136.758 \pm 2.297 \text{ kms}^{-1}$
$k_1$	$168.815 \pm 9.896 \text{ kms}^{-1}$
$\gamma_{\text{em}}$	$76.062 \pm 1.898 \text{ kms}^{-1}$
$\gamma_1$	$120.835 \pm 8.691 \text{ kms}^{-1}$

Table 6.8: Radial velocity fitting parameters for NOI-103465.

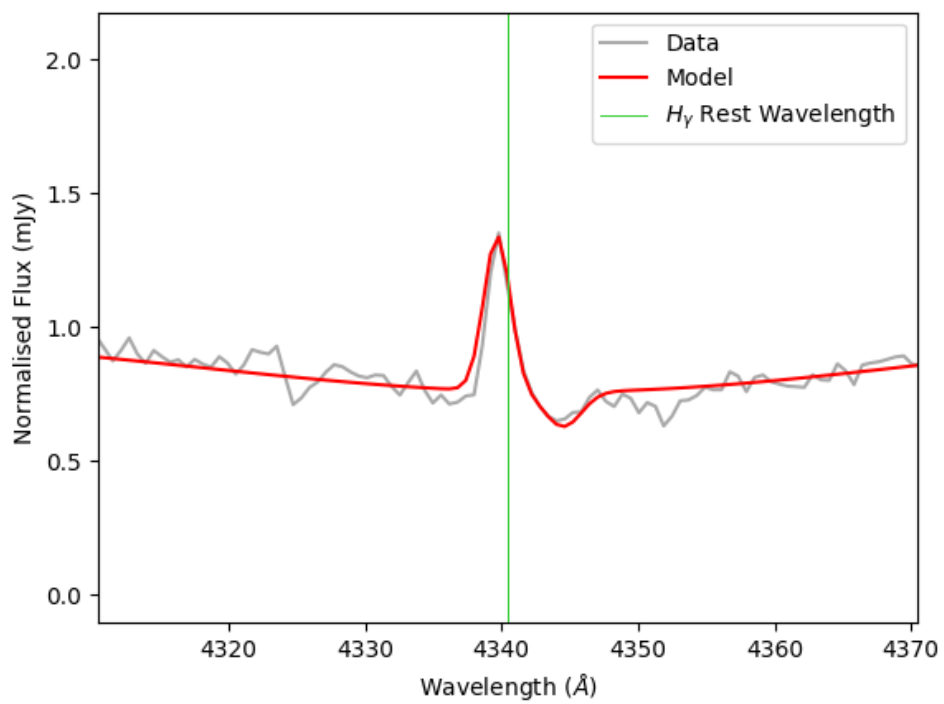


Figure 6.25: An example of model fit performed by MGFIT to the H $\gamma$  emission and absorption lines in one of the spectra of NOI-103465 collected at SAAO.

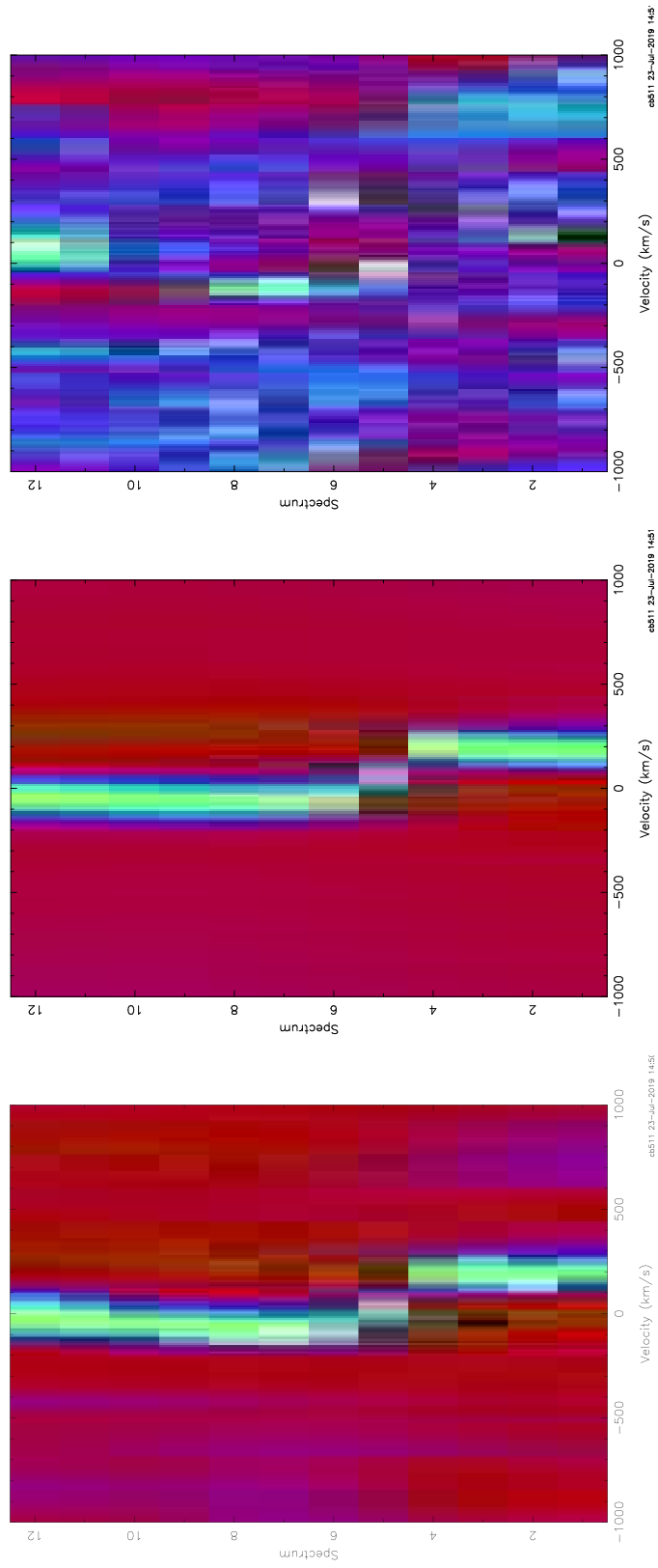


Figure 6.26: Trailed SpUpNIC spectra of NOI-103465, centred on the H $\gamma$  emission and absorption lines. The plots show the data (left panel), the model generated from the Gaussian fitting (central panel) and the residuals to the fit (right panel).

### 6.4.3 Results: White Dwarf Parameters

While contaminated by the brighter MS companion, the spectra collected at SAAO show the  $H\beta$ ,  $H\gamma$ ,  $H\delta$  and  $H\epsilon$  Balmer absorption lines belonging to the white dwarf spectrum. These features were fitted with a pure-hydrogen Non-Local Thermal Equilibrium (NLTE) model by my collaborator Simon Joyce, in order to obtain an estimate for the white dwarf  $T_{\text{eff}}$  and  $\log g$ .

The stellar models were generated with TLUSTY (Hubeny and Lanz, 1995), and the resulting spectral models were calculated using the SYNSPEC software (Hubeny and Lanz, 2017).

While the depth and broadness of the lines are mainly dependent on the white dwarf's  $T_{\text{eff}}$  and  $\log g$ , there are many other factors that could influence the shape of the lines. Therefore, the results shown below are only to be treated as an estimate at this stage.

The fitting was carried out in XSPEC (Arnaud, 1996), which uses  $\chi^2$  minimisation to find the best fit to the data. The MS companion affects the slope of the continuum, and since its effect had not been modelled at the time of fitting, the best option was to fit the normalised spectra earlier obtained from MOLLY. This improved the overall fit, but there still appeared to be a residual slope at longer wavelengths. Due to this, the  $H\beta$  and  $H\gamma$  lines were not suitable for fitting with a pure-hydrogen model. Therefore, the fitting was only applied to the sampled Balmer lines at shorter wavelengths. Lastly, the emission features from the MS companion had to be removed, affecting the core of the absorption features that were being modelled.

Out of the 5 fitted spectra, three returned a  $\log g$  of  $\sim 8.5$  and the fourth showed a slightly lower solution ( $\log g \sim 8.4$ ). The last one returned

a much lower value of 7.78, which appeared to be inconsistent with the rest of the results but did not show any obvious problems with the spectrum. All spectra returned temperatures between 18,000 and 19,000 K. An example of the spectral line fitting is shown in Figure 6.27.

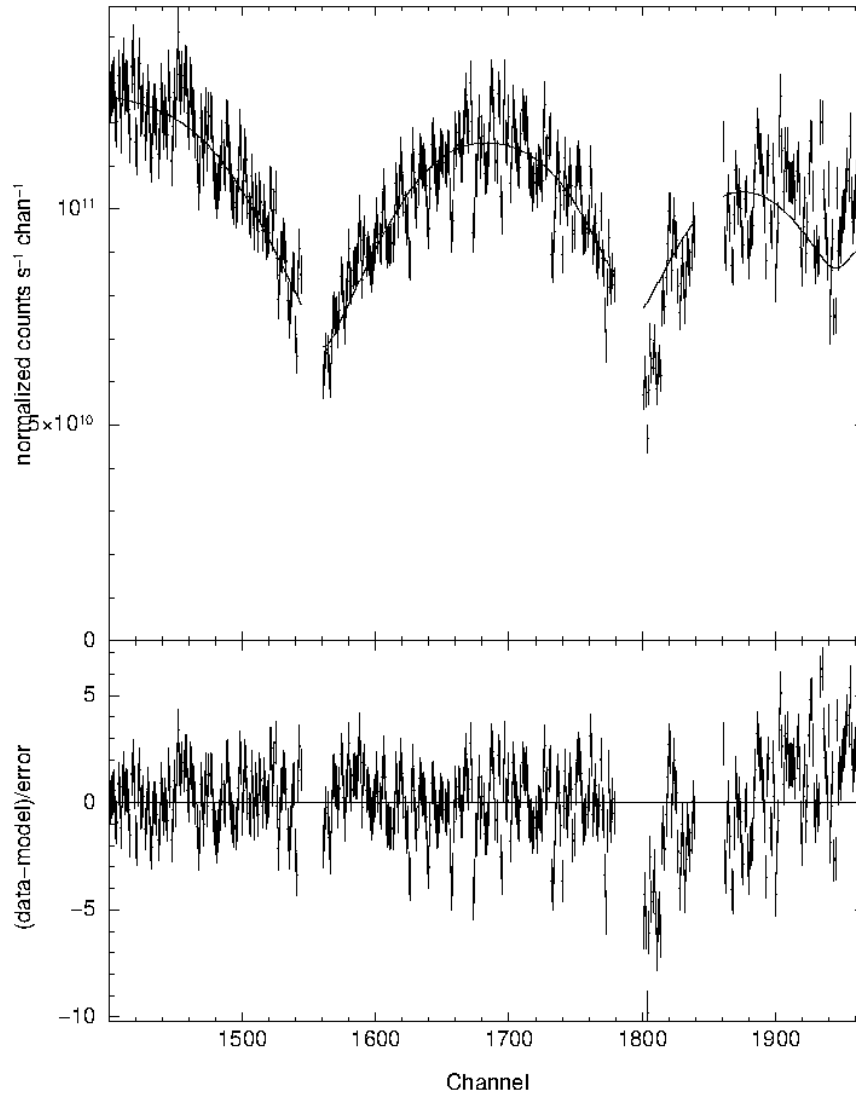


Figure 6.27: An example of model fit performed through XSPEC to the H $\delta$  and H $\epsilon$  absorption lines in one of the spectra of NOI-103465 collected at SAAO. This fit estimated a  $T_{\text{eff}}$  and  $\log g$  of 18,000 K and 8.48 respectively.

#### 6.4.4 Results: Light Curve Fitting

In a similar way to NOI-101535, I used JKTEBOP (Popper and Etzel, 1981; Etzel, 1981; Nelson and Davis, 1972; Southworth et al., 2004) to find the best fitting model to the SHOC light curves (in  $V$  and  $I$  bands) and the Eulercam light curve in  $R$  band, as described in Chapter 2 (Section 2.3.1).

As the light curves (particularly the SHOC  $I$  band, Figure 6.20) showed evidence of reflection effects, upon running the algorithm I allowed the two fractional radii, the inclination of the system and the reflection coefficients to vary. I used linear limb darkening parameters from Gianninas et al. (2013) for the white dwarf and Claret and Hauschildt (2003) for the MS star. Once the best solution for these values was determined, I ran the Monte Carlo algorithm to obtain the robust uncertainties of the fitted parameters. Being the only light curve lacking flare activity, the most reliable solution was obtained from the  $I$  band data (with a  $\chi^2_\nu$  value of 2.11), and was thus selected as the final solution to the system's parameters. Figure 6.28 shows the best fit models generated by JKTEBOP for the three light curves, while the final values for the fractional radii and inclination are found in table 6.9.

Parameter	Value
$R_*/a$	$0.2804 \pm 0.0003$
$R_{WD}/a$	$0.00226 \pm 0.0003$
$i$ ( $^\circ$ )	$74.607 \pm 0.022$

Table 6.9: Radial velocity fitting parameters for NOI-101535.

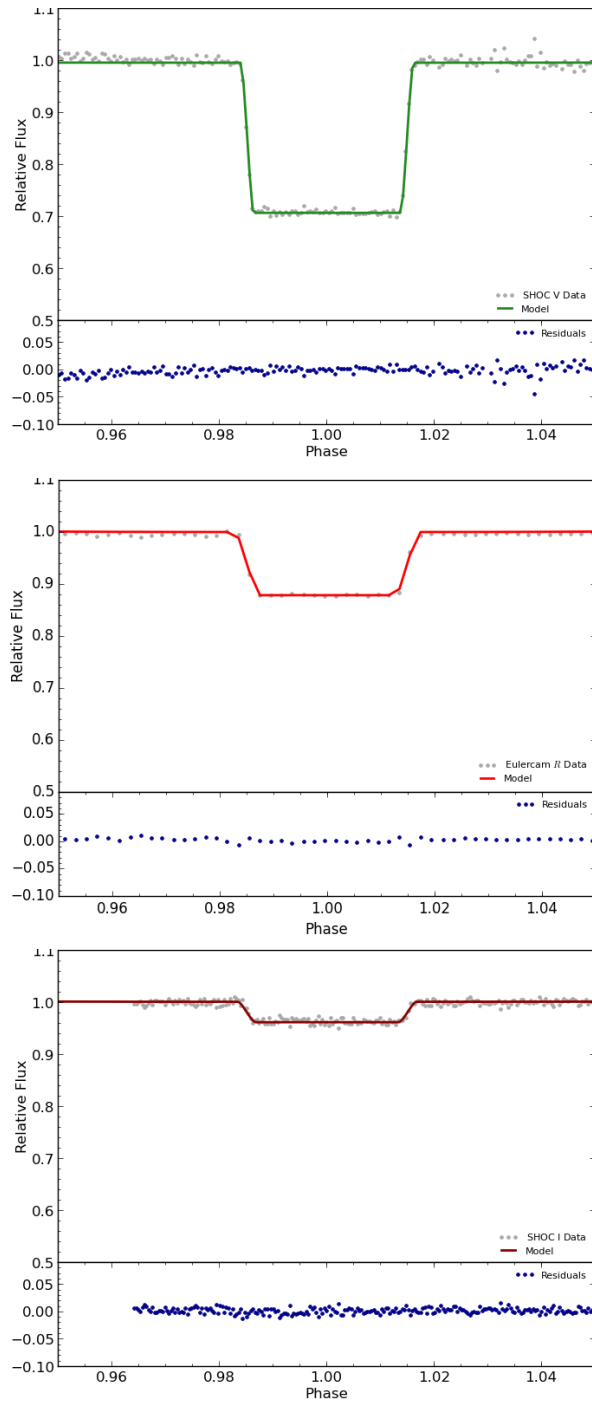


Figure 6.28: Light curve fitting of SAAO data in  $V$  band (top panel) and  $I$  band (bottom panel), and Eulercam data in  $R$  band (middle panel). All three plots represent the primary eclipse, and are maintained at the same flux scale to show the difference in eclipse depth in the different filters. The residuals under each light curve represent the difference between the model fit and the data.

### 6.4.5 Results: Final Parameters

Once the fractional radii and inclination of the system were determined, I used equation 6.3 to calculate the mass of the white dwarf. The mass was consequently used to determine the mass of the companion from the mass ratio  $q$ . I then used equations 6.4 and 6.5 to measure the orbital separation of the system, and hence the radii of both stellar components. The final solution for the masses and radii is shown in table 6.10.

Knowing the mass and radius of the white dwarf, I obtained a precise measurement of the star's gravitational redshift using equation 6.6. Through this method, I obtained a value of  $z = 66.213 \pm 10.868 \text{ kms}^{-1}$ , which is in agreement with Fontaine et al. (2001) evolutionary models, predicting a value of  $65.0 \text{ kms}^{-1}$ . The white dwarf's gravitational redshift was also calculated from equation 6.7 and resulted to be  $z = 44.773 \pm 8.896 \text{ kms}^{-1}$ . The inconsistency with the measured redshift from the difference in the  $\gamma$  velocities may be due to the larger uncertainty in the absorption feature fit.

Parameter	Value
$R_*$ ( $R_\odot$ )	$1.0682 \pm 0.065$
$R_{\text{WD}}$ ( $R_\odot$ )	$0.0086 \pm 0.0013$
$M_*$ ( $M_\odot$ )	$1.107 \pm 0.098$
$M_{\text{WD}}$ ( $M_\odot$ )	$0.8973 \pm 0.0547$
$a$ ( $R_\odot$ )	$3.8096 \pm 0.232$

Table 6.10: Calculated masses, radii and orbital separation for the NOI-101535 system components.

### 6.4.6 Discussion

The white dwarf mass is in good agreement with the solution obtained through fitting the absorption lines. At  $T_{\text{eff}} = 18,000$  K, a  $\log g$  value of 8.5 corresponds to a mass of  $0.910 M_{\odot}$ , which is consistent with the value estimated from radial velocity measurements. Moreover, the white dwarf evolutionary tracks by Fontaine et al. (2001) predict a white dwarf radius of  $0.0089 M_{\odot}$ , which is again in perfect agreement with my findings.

The final parameters for the MS companion identify it as a solar type star (of spectral type G). However, this is inconsistent with the spectral data obtained at SAAO. A G-type star is on average  $10^3$  times brighter than a white dwarf, hence the spectral energy distribution of the system should be dominated by the MS star, and the white dwarf's absorption features should not be visible.

Further confirmation of this inconsistency is given by Gaia data. The mean Gaia magnitude for the system is 13.6681 (Table 6.6), and its colour (given by the difference between the Gaia BP and RP magnitudes) has a value of 1.975 mag. Using the parallax information from Gaia (Gaia Collaboration et al., 2018b), the absolute mean magnitude of the system was found to be 9.277 mag. I used the cooling model tables for hydrogen-rich white dwarfs<sup>3</sup> (Holberg and Bergeron, 2006) to obtain absolute Gaia magnitudes for a  $T_{\text{eff}} = 18000$  K,  $\log g = 8.5$  model white dwarf. These were then subtracted from the absolute magnitude and colour of the system, in order to find the luminosity and colour contribution of the MS star alone, without contamination from the white dwarf. The MS star in this system has a mean Gaia

---

<sup>3</sup><http://www.astro.umontreal.ca/~bergeron/CoolingModels>

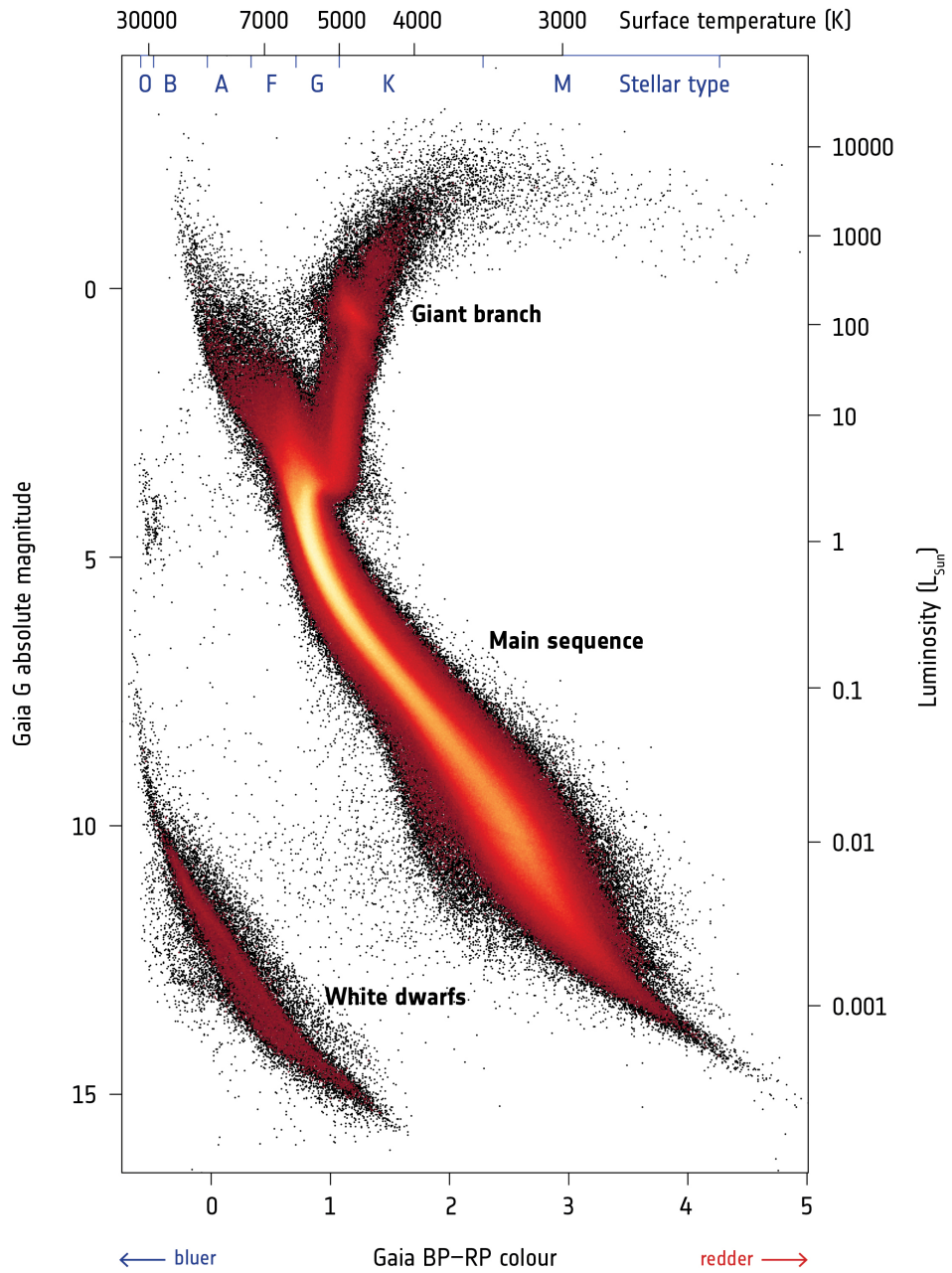


Figure 6.29: Hertzsprung-Russell Diagram of stars in Gaia DR2 (Gaia Collaboration et al., 2018a)

magnitude of  $\sim 9.382$  and a BP-RP colour of  $\sim 2.21$ . Comparing these values to the Gaia Hertzsprung-Russell (HR) Diagram (Figure 6.29, Gaia Collaboration et al., 2018a), the MS star in the NOI-103465 system should be of spectral class late-K or early-M.

It is uncertain what the nature of this inconsistency is. One possible explanation for the high value of the MS star's mass obtained in my results could be given by mass transfer in the system. Each of the stars in the the system is surrounded by an area of gravitational dominance known as the Roche lobe. When one of the stars exceeds the lobe, it will start transferring mass to its companion, in a process known as Roche lobe overflow (Paczynski, 1971; Eggleton, 1983). A first calculation of the size of a star's Roche lobe was given by Eggleton (1983). This was later improved by Breedt et al. (2012), who measured it to be:

$$\frac{R_L}{a} = \frac{0.5126q^{0.7388}}{0.6710q^{0.7349} + \ln(1 + q^{0.3983})} \quad (6.8)$$

where  $q$  is the mass ratio of the system and  $a$  is the orbital separation. Using the values found in this work, I obtained a Roche lobe size of  $1.5 \pm 0.13 R_\odot$ . Comparing this value to the radius of the MS star, it can be estimated that the the star is filling  $\approx 70\%$  of its lobe. Mass transfer is therefore not occurring at this stage, and it cannot be responsible for the large, solar-type mass obtained through the radial velocity solution.

On the other hand, the larger radius of the MS star obtained through fitting light curves with JKTEBOP may be a result of the star being distorted by the gravity of the white dwarf. Oblateness of a star is defined as percentage

difference between its equatorial radius (where the star is largest) and its polar radius (where the star would be smallest), as shown in equation 6.9.

$$Obl = \frac{R_{eq} - R_{pol}}{R_{eq}} \quad (6.9)$$

Therefore, a perfectly spherical star would have an oblateness value of 0. In NOI-103465, the MS component has an oblateness of 0.0394. As the equatorial radius is  $1.0682 \pm 0.065 R_{\odot}$ , the polar radius would be  $1.0261 \pm 0.083 R_{\odot}$ . This is still consistent with a G-type main sequence star.

Future steps that may help constrain the real parameters of this system involve more spectroscopic and photometric observations. First of all, collecting data of the secondary eclipse (if at all present) will provide a better measurement of the radii of both companions. Spectra encompassing a wider range of wavelengths in the optical and near-infrared will help constrain the spectral type of the secondary star in this system. And finally, higher resolution spectra of the Balmer hydrogen lines will help refine the radial velocity solution, providing a better measurement for the masses of the two stars.

#### 6.4.7 Summary

Compared to NOI-101535, NOI-103465 is a much younger and hotter PCEB system. Based on the follow-up data collected at SAAO, the white dwarf appears to be rather massive ( $0.8973 \pm 0.0547 M_{\odot}$ ), with an estimated effective temperature of  $\sim 18,000$  K. Based on its Gaia luminosity and colour, the MS companion to the white dwarf should be a late-K or early-M dwarf. However, the solution obtained from the presented data is inconsistent with this infor-

mation, identifying the star as a solar-type G-dwarf. This is inconsistent with the observed spectral profile. I explored a few possible explanations to this inconsistency, such as Roche-lobe overflow and stellar oblateness, but none of these helped explain the observed results.

Therefore, at the time of writing this thesis, the work on this object is still in progress. Higher resolution spectra may be required to refine the radial velocity solutions for both objects in the binary. A spectrum encompassing redder wavelengths (both optical and near-infrared) will allow a better spectral type classification for the MS component. And finally, photometric follow-up data of both the primary and secondary eclipses (thus encompassing a whole orbital phase) will provide a more accurate measurement of the radii.

## Chapter 7

# Conclusions and Future Applications

This last chapter is aimed at summarising the work presented in this thesis. In Chapter 1 I introduced the properties of white dwarfs, and explored the possibility of them being the hosts of planetary system remnants. The main aim of this work was to search for eclipse-like events in the light curves of white dwarfs. The sample of white dwarfs stars were observed as part of three main surveys, using both ground- and space- based instruments.

In Chapter 2 I described the main techniques involved in the reduction and analysis processes performed on the collected data. While photometric data were the preferred form of detection, follow-up analysis involved searching for radial velocity variations in the spectral lines of the stars. I therefore discussed the method of extracting and calibrating light curves through aperture and differential photometry, as well as the method of extracting, calibrating and analysing spectra.

Below is a summary of the results of my work, as well as brief a discus-

sion about the further steps to be taken for a more complete analysis.

## 7.1 Chapter 3: The SAAO DAZ Survey

In 2015, the first confirmed eclipsing planetesimal around a white dwarf was discovered, orbiting WD1145+017 (Vanderburg et al., 2015). The star is a known metal-polluted white dwarf, as well as the host of a debris disc. Following this discovery, I dedicated part of my research time to collecting time-series photometry of a sample of 49 metal polluted white dwarfs, in search for similar transit-like events. The data were collected using SHOC, an instrument mounted on the 1.0 m telescope at SAAO, over the course on approximately three years.

After extracting the light curves and calibrating them through differential photometry and airmass correction, none of the sampled objects displayed eclipse-like features. This was highly dependent on the limitations of the observing window, as well as on the low probability of detecting a transit around a white dwarf. However, the results of this survey provide an upper limit on the frequency of transiting planetesimals around metal-rich white dwarfs. The probability of detecting a transit around a white dwarf could be increased by modifying the design of the experiment. Increasing the observing window length would allow better sampling of longer orbital periods, as well as increasing the chance of detecting systems with short ( $< 5$  hours) periods.

However, two white dwarfs in the survey displayed evidence of sinusoidal variability in their light curves. The first of these objects is SDSS J1617+1620, a metal rich white dwarf with a known gas and dust disc, as well as a strong Ca II variable emission feature in its spectrum. The spectroscopic variability

was first discovered by (Wilson et al., 2014), who suggested it could be due to a disrupting planetary remnant interacting with the circumstellar disc.

Following the discovery of the star’s photometric variation, I collected follow-up photometric data at SAAO to confirm its periodicity. However, the repeatedly adverse weather conditions at SAAO impaired the observations, both in length and in quality, preventing the detection of the periodicity over the scatter in the data.

### **7.1.1 Future Work**

Future analysis of SDSS J1617+1620 requires the collection of time-resolved spectroscopic data to search for variations in the radial velocity of the star, which would indicate the presence of a companion. I proposed an observation of at least three full orbits at the William Herschel Telescope in La Palma. I was awarded observing time through the service queue in December 2017. At the time of writing this (August 2019), only part of the observations have been carried out.

Upon obtaining the data, I will use the MOLLY software to search for radial velocity variations, using both the balmer lines and the Ca II emission lines (e.g. Manser et al., 2019). This will confirm whether the nature of the variability is due to an unseen sub-stellar companion/remnant.

## **7.2 Chapter 4: WD1201-049**

In this chapter, I discussed the second variable object I discovered in the photometric survey of metal-rich white dwarfs I conducted at SAAO. The star was first identified as a metal rich, hot DAOZ by Gianninas et al. (2010), showing

variable C IV lines in its spectra. No previous indication of photometric variability had been documented, however the SAAO light curve showed a clear sinusoidal modulation with a peak-to-peak amplitude of  $\sim 2\%$  and a period of  $\sim 3.5$  hours.

I collected time-resolved spectra using SpUpNIC (mounted on the 1.9 m telescope at SAAO) and follow-up photometry in  $I$  band with SHOC, in order to establish whether the observed variability was due to an unseen companion orbiting the white dwarf. Spectral analysis revealed no variations in the radial velocity of the star, and the  $I$  band light curve did not show any sign of photometric variability. Lastly, no infra-red excess was detected in the spectral energy distribution of the star. For these reasons, the possibility of an unseen companion was ruled out.

The most likely explanation for the observed, non-persistent variability of the system is an inhomogeneous flow of circumstellar material accreting on the white dwarf, causing spots onto the stellar photosphere which will appear as a sinusoidal variation as the star rotates. However a new likely scenario arised from the recent discovery of a second system in which a white dwarf is eclipsed by a cloud of disrupting rocky material. Unlike WD1145+017, the transits last  $\sim 25$  days and occur every  $\sim 110$  day. The detected variability in the light curve of WD1201-049 may therefore be due to an irregularly shaped transit caused by circumstellar material, over large timescales.

### **7.2.1 Future Work**

The conclusions mentioned above can only be confirmed by extensive photometric monitoring over the span of several weeks (when searching for other

transit-like events) or years (when monitoring the inhomogeneous accretion episodes). Variability due to the accretion of materials would manifest itself mostly in the UV and bluer optical wavelengths, so photometric observations should be carried out in both UV and optical filters. The C IV line was shown to decrease in strength over the course of  $\sim 6$  years (Gianninas et al., 2010), suggesting that, if present, the inhomogeneous accretion occurs over relatively short timescales. The spectra collected at SAAO did not offer sufficient resolution to detect the C IV line, therefore I could not determine whether it was present. Hence, future observations should involve high resolution spectroscopy to monitor the activity of this metal absorption feature.

### 7.3 Chapter 5: WD1032+011, a New WD+BD system

Alongside my SAAO survey, I took part in the analysis of white dwarfs observed in Kepler K2 Campaign 14. In the data, I discovered the third known eclipsing system involving a brown dwarf orbiting a white dwarf. These systems offer a unique opportunity to study the physical characteristics of brown dwarfs.

My collaborators to this project used FORS spectra to determine the effective temperature and surface gravity of the white dwarf, which were found to be  $T_{\text{eff}} = 10196 \pm 235$  K and  $\log g = 7.81 \pm 0.07$ . Moreover, they determined the inclination of the system, as well as the fractional radii and the mass ratio of the white dwarf and its companion through fitting a model to ULTRACAM  $u'g'r'$  light curves of the primary eclipse. Using MOLLY on the

GMOS spectra, I found the best solution for the white dwarf’s radial velocity,  $k = 48.8 \pm 2.64 \text{ kms}^{-1}$ . This was used, combined with the inclination, fractional radii and white dwarf mass, to determine the mass and radius of the brown dwarf ( $M_{BD} = 0.0708 \pm 0.0053 M_{\odot}$  and  $R_{BD} = 0.1086 \pm 0.0099 R_{\odot}$ , respectively). Lastly, I generated template spectra for a white dwarf with the same  $\log g$  and  $T_{\text{eff}}$  as WD1032+011 combined with brown dwarf companions of different spectral types. I then matched the GNIRS spectrum to these models to determine the most likely spectral type of the brown dwarf. This resulted to be L5, as already predicted by Steele et al. (2011).

### 7.3.1 Future Work

The work on this particular system is mostly complete, however there is still a slight inconsistency with the final mass and radius of the brown dwarf. To solve this, the white dwarf’s Balmer absorption lines will be fit again, this time using UV photometric data to obtain a better estimate of the extinction affecting the system. Nonetheless, in the era of large scale surveys searching for exoplanets such as TESS and NGTS, more of these systems could be discovered and constrained, helping populate the brown dwarf desert. Moreover, close systems such as WD1032+011 allow us to constrain the age of the brown dwarf from knowing the white dwarf’s age, and hence to use these as benchmark objects.

## 7.4 Chapter 6: NOI-101535 and NOI-103465

The Next Generation Transit Survey (NGTS) has the primary goal of finding new transiting planets around low-mass main sequence stars. However, its short exposure time and its observing strategy allow the discovery of other

types of systems. In Chapter 6, I presented the discovery of two new PCEB systems in NGTS.

#### 7.4.1 NOI-101535

NOI-101535 is an old system, consisting of a cool ( $T_{\text{eff}} \approx 7500$  K) white dwarf in a  $\sim 0.578$  day orbit with an M4 dwarf. The spectral type of the M-dwarf was determined by comparing the system's spectrum to combined SEDs of a white dwarf and multiple types of M-dwarfs. I used the emission (from the M-dwarf) and absorption (from the white dwarf) features at  $H\beta$  to find radial velocity solutions for both components of the system, which provided estimates for their masses. I then found the best fit model to the system's light curve to measure the individual radii.

The final parameters for the white dwarf resulted in a mass of  $0.7069 \pm 0.1260 M_{\odot}$  and a radius of  $0.0099 \pm 0.022 R_{\odot}$ . These values are in good agreement with Fontaine et al. (2001) white dwarf evolutionary models.

The M-dwarf companion's final mass and radius were measured to be  $0.4286 \pm 0.1081 M_{\odot}$  and  $0.3834 \pm 0.068 R_{\odot}$  respectively. These are consistent with Baraffe et al. (2015) mass-radius models for an  $\sim 8$  Gyr M-dwarf. The age of the star was estimated taking into account the age of the white dwarf (1.897 Gyrs, Fontaine et al., 2001) and the lifetime of its progenitor star.

#### 7.4.2 NOI-103465

NOI-103465 is a much younger binary system. First estimates of the white dwarf's temperature and mass were obtained through fitting the Balmer absorption lines with model spectra, and resulted to be  $\sim 18,000$  K and  $\sim 0.9 M_{\odot}$

respectively. The mass of the white dwarf was confirmed through fitting the  $H\gamma$  absorption line in the spectra collected at SAAO, and the radius was measured (from fitting the primary eclipse light curves) to be  $0.0086 \pm 0.0013 R_{\odot}$ , which is consistent with the Fontaine et al. (2001) evolutionary models.

While the parameters obtained for the white dwarf were in perfect agreement with models, the final solution for the MS component of the system was not in agreement with expectations. Based on the object's Gaia absolute magnitude and colour, the star's most likely spectral type is late-K or early-M. However, the parameters obtained from fitting the light curves and spectra indicate a star with mass  $1.107 \pm 0.098 M_{\odot}$  and radius  $1.0682 \pm 0.065 R_{\odot}$ , which indicates a G spectral type. This inconsistency is not due to Roche-lobe overflow or stellar oblateness, and at this stage remains uncertain.

### 7.4.3 Future Work

The work on NOI-101535 is mostly completed, and the findings presented in this work are in the process of being submitted as a journal article. NOI-103465 is still in the process of being studied, and will require additional data in order to verify the source of the inconsistency in the results presented in this work. Additional photometric data - including the secondary eclipse of the system - is required in order to obtain a more accurate measurement of the individual radii. Moreover, obtaining higher resolution spectra of the Balmer lines will result in a more refined radial velocity solution for both the white dwarf and the MS star, constraining the masses to a higher precision. Finally, obtaining a spectrum encompassing optical and near-infrared wavelengths will allow an accurate classification of the spectral type of the MS companion.

## 7.5 Final Remarks

The main aim of this work was focussed on the search for eclipse-like events in the light curves of white dwarf stars, in order to constrain the properties of evolved planetary systems.

To date, only two white dwarfs (Vanderburg et al., 2015; Vanderbosch et al., 2019) are known to host eclipsing planetary material. Both stars show evidence of metals in their spectra, however the properties of these systems (orbital periods, length of the transits, depth of the transits) are extremely different. This shows that these events may be rare, but also very different from one another. The survey I presented in Chapter 3 was designed to find eclipsing bodies at short orbital separations ( $\sim$ few hours) from their host white dwarf. Hence, the results only provide an upper limit for the frequency of eclipsing planetesimals in systems similar to WD1145+017. Longer observing windows over an extended period of time may help constrain the frequency of all kinds of evolved planetary systems around metal-polluted white dwarfs. Moreover, one of the white dwarfs in the sample was found to host a planetesimal without being eclipsed by it or causing any other photometric variability (Manser et al., 2019). This shows that while not all white dwarfs may be the hosts of planetary remnants, some may be in systems that cannot be photometrically detected.

Nevertheless, high-cadence photometric surveys, such as the one presented in this work, also offer an opportunity to find other forms of variability in the light curves of white dwarfs, which can be due to other factors, such as accretion (see Chapter 4).

Finally, eclipse-like features in the light curves of white dwarfs can be caused by other objects such as brown dwarfs (Chapter 5) and main sequence

stars (Chapter 6). Brown dwarfs eclipsing white dwarfs are a rare occurrence. This is due to the apparent lack of these sub-stellar objects around main sequence star (the “brown dwarf desert”, Grether and Lineweaver, 2006). Thus, the discovery in this work of a new eclipsing system contributed in constraining the properties of this class of objects.

# Bibliography

- P. A. Aannestad, S. J. Kenyon, G. L. Hammond, and E. M. Sion. Cool Metallic-Line White Dwarfs, Radial Velocities, and Interstellar Accretion. , 105:1033, Mar 1993. doi: 10.1086/116491.
- E. Agol. Transit Surveys for Earths in the Habitable Zones of White Dwarfs. , 731(2):L31, Apr 2011. doi: 10.1088/2041-8205/731/2/L31.
- C. Alcock and A. Illarionov. The surface chemistry of stars. I - Diffusion of heavy ions in white dwarf envelopes. II - Fractionated accretion of interstellar matter. , 235:534–553, Jan 1980. doi: 10.1086/157656.
- C. Alcock, C. C. Fristrom, and R. Siegelman. On the Number of Comets around Other Single Stars. , 302:462, Mar 1986. doi: 10.1086/164005.
- C. Alcock, R. Allsman, D. R. Alves, T. Axelrod, A. Becker, D. Bennett, C. Clement, K. H. Cook, A. Drake, K. Freeman, et al. The MACHO Project Large Magellanic Cloud Variable-Star Inventory. IX. Frequency Analysis of the First-Overtone RR Lyrae Stars and the Indication for Nonradial Pulsations. , 542(1):257–280, Oct 2000. doi: 10.1086/309530.
- I. Appenzeller, K. Fricke, W. Fürtig, W. Gässler, R. Häfner, R. Harke, H. J. Hess, W. Hummel, P. Jürgens, R. P. Kudritzki, et al. Successful commissioning of FORS1 - the first optical instrument on the VLT. *The Messenger*, 94:1–6, Dec 1998.
- K. A. Arnaud. XSPEC: The First Ten Years. In G. H. Jacoby and J. Barnes, editors, *Astronomical Data Analysis Software and Systems V*, volume 101 of *Astronomical Society of the Pacific Conference Series*, page 17, Jan 1996.

- M. Auvergne, P. Bodin, L. Boisdard, J. T. Buety, S. Chaintreuil, G. Epstein, M. Joutet, T. Lam-Trong, P. Levacher, A. Magnan, et al. The CoRoT satellite in flight: description and performance. , 506(1):411–424, Oct 2009. doi: 10.1051/0004-6361/200810860.
- G. Á. Bakos, G. Torres, A. Pál, J. Hartman, G. Kovács, R. W. Noyes, D. W. Latham, D. D. Sasselov, B. Sipőcz, et al. HAT-P-11b: A Super-Neptune Planet Transiting a Bright K Star in the Kepler Field. , 710(2):1724–1745, Feb 2010. doi: 10.1088/0004-637X/710/2/1724.
- I. Baraffe, G. Chabrier, and T. Barman. Structure and evolution of super-Earth to super-Jupiter exoplanets. I. Heavy element enrichment in the interior. , 482(1):315–332, Apr 2008. doi: 10.1051/0004-6361:20079321.
- I. Baraffe, D. Homeier, F. Allard, and G. Chabrier. New evolutionary models for pre-main sequence and main sequence low-mass stars down to the hydrogen-burning limit. , 577:A42, May 2015. doi: 10.1051/0004-6361/201425481.
- K. Barbary. SEP: Source Extractor as a library. *The Journal of Open Source Software*, 1(6):58, Oct 2016. doi: 10.21105/joss.00058.
- S. D. Barber, A. J. Patterson, M. Kilic, S. K. Leggett, P. Dufour, J. S. Bloom, and D. L. Starr. The Frequency of Debris Disks at White Dwarfs. , 760(1):26, Nov 2012. doi: 10.1088/0004-637X/760/1/26.
- M. A. Barstow, S. Jordan, D. O’Donoghue, M. R. Burleigh, R. Napiwotzki, and M. K. Harrop-Allin. RE J0317-853: the hottest known highly magnetic DA white dwarf. , 277(3):971–985, Dec 1995. doi: 10.1093/mnras/277.3.971.
- M. A. Barstow, J. K. Barstow, S. L. Casewell, J. B. Holberg, and I. Hubeny. Evidence for an external origin of heavy elements in hot DA white dwarfs. , 440(2):1607–1625, May 2014. doi: 10.1093/mnras/stu216.
- N. M. Batalha, W. J. Borucki, S. T. Bryson, L. A. Buchhave, D. A. Caldwell, J. Christensen-Dalsgaard, D. Ciardi, E. W. Dunham, F. Fressin, I. Gautier, Thomas N., et al. Kepler’s First Rocky Planet: Kepler-10b. , 729(1):27, Mar 2011. doi: 10.1088/0004-637X/729/1/27.

- T. G. Beatty, J. M. Fernández, D. W. Latham, G. Á. Bakos, G. Kovács, R. W. Noyes, R. P. Stefanik, G. Torres, M. E. Everett, and C. W. Hergenrother. The Mass and Radius of the Unseen M Dwarf Companion in the Single-Lined Eclipsing Binary HAT-TR-205-013. , 663(1):573–582, Jul 2007. doi: 10.1086/518413.
- A. C. Becker, J. J. Bochanski, S. L. Hawley, Ž. Ivezić, A. F. Kowalski, B. Sesar, and A. A. West. Periodic Variability of Low-mass Stars in Sloan Digital Sky Survey Stripe 82. *The Astrophysical Journal*, 731(1):17, Apr 2011. doi: 10.1088/0004-637X/731/1/17.
- C. Belardi, M. Kilic, J. A. Munn, A. Gianninas, S. D. Barber, A. Dey, and P. B. Stetson. The DECam minute cadence survey - I. , 462(3):2506–2517, Nov 2016. doi: 10.1093/mnras/stw1834.
- E. C. Bellm, S. R. Kulkarni, M. J. Graham, R. Dekany, R. M. Smith, R. Riddle, F. J. Masci, G. Helou, T. A. Prince, S. M. Adams, et al. The Zwicky Transient Facility: System Overview, Performance, and First Results. , 131(995):018002, Jan 2019. doi: 10.1088/1538-3873/aaecbe.
- K. Beuermann, S. Dreizler, F. V. Hessman, U. Backhaus, A. Boesch, T. O. Husser, L. Nortmann, A. Schmelev, and R. Springer. The eclipsing post-common envelope binary CSS21055: a white dwarf with a probable brown-dwarf companion. , 558:A96, Oct 2013. doi: 10.1051/0004-6361/201322241.
- S. Bloemen, T. R. Marsh, R. H. Østensen, S. Charpinet, G. Fontaine, P. Degroote, U. Heber, S. D. Kawaler, C. Aerts, E. M. Green, J. Telting, P. Brassard, B. T. Gänsicke, G. Handler, D. W. Kurtz, R. Silvotti, V. Van Grootel, J. E. Lindberg, T. Porsimo, P. A. Wilson, R. L. Gilliland , H. Kjeldsen, J. Christensen-Dalsgaard, W. J. Borucki, D. Koch, J. M. Jenkins, and T. C. Klaus. Kepler observations of the beaming binary KPD 1946+4340. , 410(3):1787–1796, Jan 2011. doi: 10.1111/j.1365-2966.2010.17559.x.
- J. J. Bochanski, A. A. West, S. L. Hawley, and K. R. Covey. Low-Mass Dwarf Template Spectra from the Sloan Digital Sky Survey. , 133:531–544, Feb. 2007. doi: 10.1086/510240.

- W. Borucki, D. Koch, A. Boss, E. Dunham, A. Dupree, J. Geary, R. Gilliland, S. Howell, J. Jenkins, Y. Kondo, D. Latham, J. Lissauer, and H. Reitsema. The Kepler mission: a technical overview. In F. Favata, S. Aigrain, and A. Wilson, editors, *Stellar Structure and Habitable Planet Finding*, volume 538 of *ESA Special Publication*, pages 177–182, Jan 2004.
- W. J. Borucki, D. Koch, G. Basri, N. Batalha, T. Brown, D. Caldwell, J. Caldwell, J. Christensen-Dalsgaard, W. D. Cochran, E. DeVore, et al. Kepler Planet-Detection Mission: Introduction and First Results. *Science*, 327 (5968):977, Feb 2010. doi: 10.1126/science.1185402.
- A. P. Boss, G. Basri, S. S. Kumar, J. Liebert, E. L. Martín, B. Reipurth, and H. Zinnecker. Nomenclature: Brown Dwarfs, Gas Giant Planets, and ? In E. Martín, editor, *Brown Dwarfs*, volume 211 of *IAU Symposium*, page 529, Jun 2003.
- I. P. Braker. *Variability and Transits in Kepler White Dwarfs*. PhD thesis, University of Leicester, 2019.
- E. Breedt, B. T. Gänsicke, J. Girven, A. J. Drake, C. M. Copperwheat, S. G. Parsons, and T. R. Marsh. The evolutionary state of short-period magnetic white dwarf binaries. , 423(2):1437–1449, Jun 2012. doi: 10.1111/j.1365-2966.2012.20965.x.
- C. S. Brinkworth, T. R. Marsh, L. Morales-Rueda, P. F. L. Maxted, M. R. Burleigh, and S. A. Good. Rotational period of WD 1953-011- a magnetic white dwarf with a star-spot. , 357(1):333–337, Feb 2005. doi: 10.1111/j.1365-2966.2005.08649.x.
- C. S. Brinkworth, M. R. Burleigh, K. Lawrie, T. R. Marsh, and C. Knigge. Measuring the Rotational Periods of Isolated Magnetic White Dwarfs. , 773 (1):47, Aug 2013. doi: 10.1088/0004-637X/773/1/47.
- A. J. Burgasser, M. W. McElwain, J. D. Kirkpatrick, K. L. Cruz, C. G. Tinney, and I. N. Reid. The 2MASS Wide-Field T Dwarf Search. III. Seven New T Dwarfs and Other Cool Dwarf Discoveries. , 127:2856–2870, May 2004. doi: 10.1086/383549.

- A. J. Burgasser, K. L. Cruz, M. Cushing, C. R. Gelino, D. L. Looper, J. K. Faherty, J. D. Kirkpatrick, and I. N. Reid. SpeX Spectroscopy of Unresolved Very Low Mass Binaries. I. Identification of 17 Candidate Binaries Straddling the L Dwarf/T Dwarf Transition. *Astronomical Journal*, 710:1142–1169, Feb. 2010. doi: 10.1088/0004-637X/710/2/1142.
- M. R. Burleigh, E. Hogan, P. D. Dobbie, R. Napiwotzki, and P. F. L. Maxted. A near-infrared spectroscopic detection of the brown dwarf in the post common envelope binary WD0137-349. *Astronomical Journal*, 373(1):L55–L59, Nov 2006. doi: 10.1111/j.1745-3933.2006.00242.x.
- M. R. Burleigh, F. J. Clarke, E. Hogan, C. S. Brinkworth, P. Bergeron, P. Dufour, P. D. Dobbie, A. J. Levan, S. T. Hodgkin, D. W. Hoard, and S. Wachter. The ‘DODO’ survey - I. Limits on ultra-cool substellar and planetary-mass companions to van Maanen’s star (vMa2). *Astronomical Journal*, 386(1):L5–L9, May 2008. doi: 10.1111/j.1745-3933.2008.00446.x.
- S. L. Casewell, M. R. Burleigh, G. A. Wynn, R. D. Alexander, R. Napiwotzki, K. A. Lawrie, P. D. Dobbie, R. F. Jameson, and S. T. Hodgkin. WD0837+185: The Formation and Evolution of an Extreme Mass-ratio White-dwarf-Brown-dwarf Binary in Praesepe. *Astronomical Journal*, 759(2):L34, Nov 2012. doi: 10.1088/2041-8205/759/2/L34.
- S. L. Casewell, S. P. Littlefair, M. R. Burleigh, and M. Roy. Spectroscopically confirmed brown dwarf members of Coma Berenices and the Hyades. *Monthly Notices of the Royal Astronomical Society*, 441(3):2644–2649, Jul 2014. doi: 10.1093/mnras/stu746.
- S. L. Casewell, K. A. Lawrie, P. F. L. Maxted, M. S. Marley, J. J. Fortney, P. B. Rimmer, S. P. Littlefair, G. Wynn, M. R. Burleigh, and C. Helling. Multiwaveband photometry of the irradiated brown dwarf WD0137-349B. *Monthly Notices of the Royal Astronomical Society*, 447(4):3218–3226, Mar 2015. doi: 10.1093/mnras/stu2721.
- S. L. Casewell, S. P. Littlefair, S. G. Parsons, T. R. Marsh, J. J. Fortney, and M. S. Marley. The direct detection of the irradiated brown dwarf in the white dwarf-brown dwarf binary SDSS J141126.20+200911.1. *Monthly Notices of the Royal Astronomical Society*, 481(4):5216–5222, Dec 2018. doi: 10.1093/mnras/sty2599.

- S. Chandrasekhar. The Maximum Mass of Ideal White Dwarfs. , 74:81, Jul 1931. doi: 10.1086/143324.
- D. Charbonneau, T. M. Brown, D. W. Latham, and M. Mayor. Detection of Planetary Transits Across a Sun-like Star. , 529(1):L45–L48, Jan 2000. doi: 10.1086/312457.
- P. Chayer, S. Vennes, A. K. Pradhan, P. Thejll, A. Beauchamp, G. Fontaine, and F. Wesemael. Improved Calculations of the Equilibrium Abundances of Heavy Elements Supported by Radiative Levitation in the Atmospheres of Hot DA White Dwarfs. , 454:429, Nov 1995. doi: 10.1086/176494.
- S. Ciceri, J. Lillo-Box, J. Southworth, L. Mancini, T. Henning, and D. Barrado. Kepler-432 b: a massive planet in a highly eccentric orbit transiting a red giant. , 573:L5, Jan 2015. doi: 10.1051/0004-6361/201425145.
- A. Claret and P. H. Hauschildt. The limb-darkening for spherically symmetric NextGen model atmospheres: A-G main-sequence and sub-giant stars. , 412:241–248, Dec 2003. doi: 10.1051/0004-6361:20031405.
- A. Collier Cameron, D. Pollacco, R. A. Street, T. A. Lister, R. G. West, D. M. Wilson, F. Pont, D. J. Christian, W. I. Clarkson, B. Enoch, A. Evans, A. Fitzsimmons, C. A. Haswell, C. Hellier, S. T. Hodgkin, K. Horne, J. Irwin, S. R. Kane, F. P. Keenan, A. J. Norton, N. R. Parley, J. Osborne, R. Ryans, I. Skillen, and P. J. Wheatley. A fast hybrid algorithm for exoplanetary transit searches. *Monthly Notices of the Royal Astronomical Society*, 373(2):799–810, Dec 2006. doi: 10.1111/j.1365-2966.2006.11074.x.
- R. Coppejans, A. A. S. Gulbis, M. M. Kotze, D. L. Coppejans, H. L. Worters, P. A. Woudt, H. Whittal, J. Cloete, and P. Fourie. Characterizing and Commissioning the Sutherland High-Speed Optical Cameras (SHOC). , 125(930):976, Aug 2013. doi: 10.1086/672156.
- C. M. Copperwheat, T. R. Marsh, V. S. Dhillon, S. P. Littlefair, R. Hickman, B. T. Gänsicke, and J. Southworth. Physical properties of IP Pegasi: an eclipsing dwarf nova with an unusually cool white dwarf. , 402(3):1824–1840, Mar 2010. doi: 10.1111/j.1365-2966.2009.16010.x.

- M. W. Craig, S. M. Crawford, C. Deil, C. Gomez, H. M. Günther, N. Heidt, A. Horton, J. Karr, S. Nelson, J. P. Ninan, P. Pattnaik, E. Rol, W. Schoenell, M. Seifert, S. Singh, B. Sipocz, C. Stotts, O. Streicher, E. Tollerud, N. Walker, and ccdproc contributors. ccdproc: CCD data reduction software, Oct 2015.
- L. A. Crause, D. Carter, A. Daniels, G. Evans, P. Fourie, D. Gilbank, M. Hendricks, W. Koorts, D. Lategan, E. Loubser, et al. SpUpNIC (Spectrograph Upgrade: Newly Improved Cassegrain) on the South African Astronomical Observatory's 74-inch telescope. In , volume 9908 of *Society of Photo-Optical Instrumentation Engineers (SPIE) Conference Series*, page 990827, Aug 2016. doi: 10.1117/12.2230818.
- K. L. Cruz, A. J. Burgasser, I. N. Reid, and J. Liebert. 2MASS J05185995-2828372: Discovery of an Unresolved L/T Binary. , 604:L61–L64, Mar. 2004. doi: 10.1086/383415.
- M. J. Currie, D. S. Berry, T. Jenness, A. G. Gibb, G. S. Bell, and P. W. Draper. Starlink Software in 2013. In N. Manset and P. Forshay, editors, *Astronomical Data Analysis Software and Systems XXIII*, volume 485 of *Astronomical Society of the Pacific Conference Series*, page 391, May 2014.
- M. C. Cushing, W. D. Vacca, and J. T. Rayner. Spextool: A Spectral Extraction Package for SpeX, a 0.8-5.5 Micron Cross-Dispersed Spectrograph. , 116(818):362–376, Apr 2004. doi: 10.1086/382907.
- K. Dame, C. Belardi, M. Kilic, A. Rest, A. Gianninas, S. Barber, and W. R. Brown. The DECam Minute Cadence Survey II: 49 Variables but No Planetary Transits of a White Dwarf. , page 405, Feb 2019. doi: 10.1093/mnras/stz398.
- J. H. Debes and S. Sigurdsson. Are There Unstable Planetary Systems around White Dwarfs? , 572(1):556–565, Jun 2002. doi: 10.1086/340291.
- J. H. Debes, D. W. Hoard, S. Wachter, D. T. Leisawitz, and M. Cohen. The WIRED Survey. II. Infrared Excesses in the SDSS DR7 White Dwarf Catalog. , 197(2):38, Dec 2011. doi: 10.1088/0067-0049/197/2/38.

- E. Dennyhy, J. C. Clemens, J. H. Debes, B. H. Dunlap, D. Kilkenney, P. C. O'Brien, and J. T. Fuchs. WIRED for EC: New White Dwarfs with WISE Infrared Excesses and New Classification Schemes from the Edinburgh-Cape Blue Object Survey. *The Astrophysical Journal*, 849(2):77, Nov 2017. doi: 10.3847/1538-4357/aa8ef2.
- V. S. Dhillon, T. R. Marsh, M. J. Stevenson, D. C. Atkinson, P. Kerry, P. T. Peacocke, A. J. A. Vick, S. M. Beard, D. J. Ives, D. W. Lunney, S. A. McLay, C. J. Tierney, J. Kelly, S. P. Littlefair, R. Nicholson, R. Pashley, E. T. Harlaftis, and K. O'Brien. ULTRACAM: an ultrafast, triple-beam CCD camera for high-speed astrophysics. *MNRAS*, 378(3):825–840, Jul 2007. doi: 10.1111/j.1365-2966.2007.11881.x.
- P. D. Dobbie, M. R. Burleigh, A. J. Levan, M. A. Barstow, R. Napiwotzki, J. B. Holberg, I. Hubeny, and S. B. Howell. A near-infrared spectroscopic search for very-low-mass cool companions to notable DA white dwarfs. *MNRAS*, 357(3):1049–1058, Mar 2005. doi: 10.1111/j.1365-2966.2005.08720.x.
- M. Dopita, J. Hart, P. McGregor, P. Oates, G. Bloxham, and D. Jones. The Wide Field Spectrograph (WiFeS). *MNRAS*, 310(3-4):255–268, Aug 2007. doi: 10.1007/s10509-007-9510-z.
- R. A. Downes, R. F. Webbink, M. M. Shara, H. Ritter, U. Kolb, and H. W. Duerbeck. A Catalog and Atlas of Cataclysmic Variables: The Living Edition. *Publications of the Astronomical Society of the Pacific*, 113(784):764–768, Jun 2001. doi: 10.1086/320802.
- P. Dufour, M. Kilic, G. Fontaine, P. Bergeron, C. Melis, and J. Bochanski. Detailed Compositional Analysis of the Heavily Polluted DBZ White Dwarf SDSS J073842.56+183509.06: A Window on Planet Formation? *MNRAS*, 749(1):6, Apr 2012. doi: 10.1088/0004-637X/749/1/6.
- J. Dupuis, G. Fontaine, C. Pelletier, and F. Wesemael. A Study of Metal Abundance Patterns in Cool White Dwarfs. I. Time-dependent Calculations of Gravitational Settling. *Astronomical Journal*, 82:505, Oct 1992. doi: 10.1086/191728.
- J. Dupuis, G. Fontaine, C. Pelletier, and F. Wesemael. A Study of Metal

- Abundance Patterns in Cool White Dwarfs. II. Simulations of Accretion Episodes. , 84:73, Jan 1993a. doi: 10.1086/191746.
- J. Dupuis, G. Fontaine, and F. Wesemael. A Study of Metal Abundance Patterns in Cool White Dwarfs. III. Comparison of the Predictions of the Two-Phase Accretion Model with the Observations. , 87:345, Jul 1993b. doi: 10.1086/191808.
- J. Dupuis, P. Chayer, S. Vennes, D. J. Christian, and J. W. Kruk. Adding More Mysteries to the DA White Dwarf GD 394. , 537(2):977–992, Jul 2000. doi: 10.1086/309079.
- J. Dupuis, P. Chayer, S. Vennes, D. J. Christian, and J. W. Kruk. The Mysteries of GD394. In J. L. Provençal, H. L. Shipman, J. MacDonald, and S. Goodchild, editors, *12th European Workshop on White Dwarfs*, volume 226 of *Astronomical Society of the Pacific Conference Series*, page 257, Jan 2001.
- T. J. Dupuy and M. C. Liu. The Hawaii Infrared Parallax Program. I. Ultracool Binaries and the L/T Transition. , 201(2):19, Aug 2012. doi: 10.1088/0067-0049/201/2/19.
- P. P. Eggleton. Approximations to the radii of Roche lobes. , 268:368–369, May 1983. doi: 10.1086/160960.
- D. J. Eisenstein, J. Liebert, H. C. Harris, S. J. Kleinman, A. Nitta, N. Silvestri, S. A. Anderson, J. C. Barentine, H. J. Brewington, J. Brinkmann, M. Harvanek, J. Krzesiński, J. Neilsen, Eric H., D. Long, D. P. Schneider, and S. A. Snedden. A Catalog of Spectroscopically Confirmed White Dwarfs from the Sloan Digital Sky Survey Data Release 4. , 167(1):40–58, Nov 2006. doi: 10.1086/507110.
- J. H. Elias, R. R. Joyce, M. Liang, G. P. Muller, E. A. Hileman, and J. R. George. Design of the Gemini near-infrared spectrograph. In , volume 6269, page 62694C, Jun 2006. doi: 10.1117/12.671817.

- P. B. Etzel. A Simple Synthesis Method for Solving the Elements of Well-Detached Eclipsing Systems. In *Photometric and Spectroscopic Binary Systems*, page 111, Jan 1981.
- F. Faedi, R. G. West, M. R. Burleigh, M. R. Goad, and L. Hebb. Detection limits for close eclipsing and transiting substellar and planetary companions to white dwarfs in the WASP survey. , 410(2):899–911, Jan 2011. doi: 10.1111/j.1365-2966.2010.17488.x.
- J. Farihi, E. E. Becklin, and B. Zuckerman. Low-Luminosity Companions to White Dwarfs. , 161(2):394–428, Dec 2005. doi: 10.1086/444362.
- J. Farihi, M. A. Barstow, S. Redfield, P. Dufour, and N. C. Hambly. Rocky planetesimals as the origin of metals in DZ stars. , 404(4):2123–2135, Jun 2010. doi: 10.1111/j.1365-2966.2010.16426.x.
- J. Farihi, B. T. Gänsicke, P. R. Steele, J. Girven, M. R. Burleigh, E. Breedt, and D. Koester. A trio of metal-rich dust and gas discs found orbiting candidate white dwarfs with K-band excess. , 421(2):1635–1643, Apr 2012. doi: 10.1111/j.1365-2966.2012.20421.x.
- L. Ferrario, S. Vennes, D. T. Wickramasinghe, J. A. Bailey, and D. J. Christian. EUVE J0317-855: a rapidly rotating, high-field magnetic white dwarf. , 292(1):205–217, Nov 1997. doi: 10.1093/mnras/292.2.205.
- G. Fontaine and P. Brassard. The Pulsating White Dwarf Stars. , 120(872):1043, Oct 2008. doi: 10.1086/592788.
- G. Fontaine and G. Michaud. Diffusion time scales in white dwarfs. , 231:826–840, Aug 1979. doi: 10.1086/157247.
- G. Fontaine and F. Wesemael. Recent advances in the theory of white dwarf spectral evolution. In A. G. D. Philip, D. S. Hayes, and J. W. Liebert, editors, *IAU Colloq. 95: Second Conference on Faint Blue Stars*, pages 319–326, Jan 1987.
- G. Fontaine, P. Brassard, and P. Bergeron. The Potential of White Dwarf Cosmochronology. , 113:409–435, Apr. 2001. doi: 10.1086/319535.

- R. H. Fowler. On dense matter. , 87:114–122, Dec 1926. doi: 10.1093/mnras/87.2.114.
- W. Freudling, M. Romaniello, D. M. Bramich, P. Ballester, V. Forchi, C. E. García-Dabó, S. Moehler, and M. J. Neeser. Automated data reduction workflows for astronomy. The ESO Reflex environment. , 559:A96, Nov 2013. doi: 10.1051/0004-6361/201322494.
- B. J. Fulton, J. L. Tonry, H. Flewelling, W. S. Burgett, K. C. Chambers, K. W. Hodapp, M. E. Huber, N. Kaiser, R. J. Wainscoat, and C. Waters. A Search for Planetary Eclipses of White Dwarfs in the Pan-STARRS1 Medium-deep Fields. , 796(2):114, Dec 2014. doi: 10.1088/0004-637X/796/2/114.
- Gaia Collaboration, C. Babusiaux, F. van Leeuwen, M. A. Barstow, C. Jordi, A. Vallenari, D. Bossini, A. Bressan, T. Cantat-Gaudin, M. van Leeuwen, A. G. A. Brown, et al. Gaia Data Release 2. Observational Hertzsprung-Russell diagrams. , 616:A10, Aug 2018a. doi: 10.1051/0004-6361/201832843.
- Gaia Collaboration, A. G. A. Brown, A. Vallenari, T. Prusti, J. H. J. de Bruijne, C. Babusiaux, C. A. L. Bailer-Jones, M. Biermann, D. W. Evans, L. Eyer, F. Jansen, et al. Gaia Data Release 2. Summary of the contents and survey properties. *Astronomy and Astrophysics*, 616:A1, Aug 2018b. doi: 10.1051/0004-6361/201833051.
- B. T. Gänsicke, T. R. Marsh, J. Southworth, and A. Rebassa-Mansergas. A Gaseous Metal Disk Around a White Dwarf. *Science*, 314(5807):1908, Dec 2006a. doi: 10.1126/science.1135033.
- B. T. Gänsicke, T. R. Marsh, J. Southworth, and A. Rebassa-Mansergas. A Gaseous Metal Disk Around a White Dwarf. *Science*, 314(5807):1908, Dec 2006b. doi: 10.1126/science.1135033.
- B. T. Gänsicke, T. R. Marsh, and J. Southworth. SDSSJ104341.53+085558.2: a second white dwarf with a gaseous debris disc. , 380(1):L35–L39, Sep 2007. doi: 10.1111/j.1745-3933.2007.00343.x.
- B. T. Gänsicke, D. Koester, T. R. Marsh, A. Rebassa-Mansergas, and J. Southworth. SDSSJ084539.17+225728.0: the first DBZ white dwarf with a metal-

- rich gaseous debris disc. , 391(1):L103–L107, Nov 2008. doi: 10.1111/j.1745-3933.2008.00565.x.
- B. T. Gänsicke, D. Koester, J. Farihi, J. Girven, S. G. Parsons, and E. Breedt. The chemical diversity of exo-terrestrial planetary debris around white dwarfs. , 424(1):333–347, Jul 2012. doi: 10.1111/j.1365-2966.2012.21201.x.
- B. T. Gänsicke, A. Aungwerojwit, T. R. Marsh, V. S. Dhillon, D. I. Sahman, D. Veras, J. Farihi, P. Chote, R. Ashley, S. Arjyotha, S. Rattanasoon, S. P. Littlefair, D. Pollacco, and M. R. Burleigh. High-speed Photometry of the Disintegrating Planetesimals at WD1145+017: Evidence for Rapid Dynamical Evolution. , 818(1):L7, Feb 2016. doi: 10.3847/2041-8205/818/1/L7.
- S. Geier, V. Schaffenroth, H. Drechsel, U. Heber, T. Kupfer, A. Tillich, R. H. Østensen, K. Smolders, P. Degroote, P. F. L. Maxted, B. N. Barlow, B. T. Gänsicke, T. R. Marsh, and R. Napiwotzki. Binaries Discovered by the MUCHFUSS Project: SDSS J08205+0008—An Eclipsing Subdwarf B Binary with a Brown Dwarf Companion. , 731(2):L22, Apr 2011. doi: 10.1088/2041-8205/731/2/L22.
- N. P. Gentile Fusillo, B. T. Gänsicke, and S. Greiss. A photometric selection of white dwarf candidates in Sloan Digital Sky Survey Data Release 10. , 448(3):2260–2274, Apr 2015a. doi: 10.1093/mnras/stv120.
- N. P. Gentile Fusillo, A. Rebassa-Mansergas, B. T. Gänsicke, X. W. Liu, J. J. Ren, D. Koester, Y. Zhan, Y. Hou, Y. Wang, and M. Yang. An independent test of the photometric selection of white dwarf candidates using LAMOST DR3. , 452(1):765–773, Sep 2015b. doi: 10.1093/mnras/stv1338.
- N. P. Gentile Fusillo, R. Raddi, B. T. Gänsicke, J. J. Hermes, A. F. Pala, J. T. Fuchs, B. Chehade, N. Metcalfe, and T. Shanks. A catalogue of white dwarf candidates in VST ATLAS. , 469(1):621–629, Jul 2017. doi: 10.1093/mnras/stx777.
- A. Gianninas, P. Bergeron, J. Dupuis, and M. T. Ruiz. Spectroscopic Analysis of Hot, Hydrogen-rich White Dwarfs: The Presence of Metals and the Balmer-line Problem. , 720(1):581–602, Sep 2010. doi: 10.1088/0004-637X/720/1/581.

- A. Gianninas, B. D. Strickland, M. Kilic, and P. Bergeron. Limb-darkening Coefficients for Eclipsing White Dwarfs. , 766(1):3, Mar 2013. doi: 10.1088/0004-637X/766/1/3.
- M. Gillon, E. Jehin, S. M. Lederer, L. Delrez, J. de Wit, A. Burdanov, V. Van Grootel, A. J. Burgasser, A. H. M. J. Triaud, C. Opitom, B.-O. Demory, D. K. Sahu, D. Bardalez Gagliuffi, P. Magain, and D. Queloz. Temperate Earth-sized planets transiting a nearby ultracool dwarf star. , 533(7602): 221–224, May 2016. doi: 10.1038/nature17448.
- M. Gillon, A. H. M. J. Triaud, B.-O. Demory, E. Jehin, E. Agol, K. M. Deck, S. M. Lederer, J. de Wit, A. Burdanov, J. G. Ingalls, et al. Seven temperate terrestrial planets around the nearby ultracool dwarf star TRAPPIST-1. , 542(7642):456–460, Feb 2017. doi: 10.1038/nature21360.
- J. Girven, B. T. Gänsicke, D. Steeghs, and D. Koester. DA white dwarfs in Sloan Digital Sky Survey Data Release 7 and a search for infrared excess emission. , 417(2):1210–1235, Oct 2011. doi: 10.1111/j.1365-2966.2011.19337.x.
- D. Grether and C. H. Lineweaver. How Dry is the Brown Dwarf Desert? Quantifying the Relative Number of Planets, Brown Dwarfs, and Stellar Companions around Nearby Sun-like Stars. , 640(2):1051–1062, Apr 2006. doi: 10.1086/500161.
- A. A. S. Gulbis, S. J. Bus, J. L. Elliot, J. T. Rayner, W. E. Stahlberger, F. E. Rojas, E. R. Adams, M. J. Person, R. Chung, A. T. Tokunaga, and C. A. Zuluaga. First Results from the MIT Optical Rapid Imaging System (MORIS) on the IRTF: A Stellar Occultation by Pluto and a Transit by Exoplanet XO-2b. , 123(902):461, Apr 2011. doi: 10.1086/659636.
- M. N. Günther, D. Queloz, E. Gillen, J. McCormac, D. Bayliss, F. Bouchy, S. R. Walker, R. G. West, P. Eigmüller, A. M. S. Smith, et al. Centroid vetting of transiting planet candidates from the Next Generation Transit Survey. , 472(1):295–307, Nov 2017. doi: 10.1093/mnras/stx1920.
- J. Guo, J. Zhao, A. Tziamtzis, J. Liu, L. Li, Y. Zhang, Y. Hou, and Y. Wang.

- White dwarfs identified in LAMOST DR 2. , 454(3):2787–2797, Dec 2015. doi: 10.1093/mnras/stv2104.
- I. Hachisu, M. Kato, and K. Nomoto. Final Fates of Rotating White Dwarfs and Their Companions in the Single Degenerate Model of Type Ia Supernovae. , 756(1):L4, Sep 2012. doi: 10.1088/2041-8205/756/1/L4.
- M. Hamuy, A. R. Walker, N. B. Suntzeff, P. Gigoux, S. R. Heathcote, and M. M. Phillips. Southern Spectrophotometric Standards. I. , 104:533, Jul 1992. doi: 10.1086/133028.
- M. Hamuy, N. B. Suntzeff, S. R. Heathcote, A. R. Walker, P. Gigoux, and M. M. Phillips. Southern Spectrophotometric Standards. II. , 106:566, Jun 1994. doi: 10.1086/133417.
- G. W. Henry, G. W. Marcy, R. P. Butler, and S. S. Vogt. A Transiting “51 Peg-like” Planet. , 529(1):L41–L44, Jan 2000. doi: 10.1086/312458.
- S. T. Hodgkin, B. R. Oppenheimer, N. C. Hambly, R. F. Jameson, S. J. Smartt, and I. A. Steele. Infrared spectrum of an extremely cool white-dwarf star. , 403(6765):57–59, Jan 2000. doi: 10.1038/47431.
- E. Hogan, M. R. Burleigh, and F. J. Clarke. The DODO survey - II. A Gemini direct imaging search for substellar and planetary mass companions around nearby equatorial and Northern hemisphere white dwarfs. , 396(4):2074–2086, Jul 2009. doi: 10.1111/j.1365-2966.2009.14565.x.
- J. B. Holberg and P. Bergeron. Calibration of Synthetic Photometry Using DA White Dwarfs. , 132(3):1221–1233, Sep 2006. doi: 10.1086/505938.
- J. B. Holberg and S. B. Howell. The Kepler Light Curve of the Unique DA White Dwarf BOKS 53856. , 142(2):62, Aug 2011. doi: 10.1088/0004-6256/142/2/62.
- J. B. Holberg, M. A. Barstow, and E. M. Sion. Elemental abundances in hot white dwarfs. In S. E. Solheim and E. G. Meistas, editors, *11th European Workshop on White Dwarfs*, volume 169 of *Astronomical Society of the Pacific Conference Series*, page 485, Jan 1999.

- J. B. Holberg, E. M. Sion, T. Oswalt, G. P. McCook, S. Foran, and J. P. Subasavage. A New Look at the Local White Dwarf Population. , 135(4): 1225–1238, Apr 2008. doi: 10.1088/0004-6256/135/4/1225.
- I. M. Hook, I. Jørgensen, J. R. Allington-Smith, R. L. Davies, N. Metcalfe, R. G. Murowinski, and D. Crampton. The Gemini-North Multi-Object Spectrograph: Performance in Imaging, Long-Slit, and Multi-Object Spectroscopic Modes. , 116(819):425–440, May 2004. doi: 10.1086/383624.
- S. B. Howell, C. Sobeck, M. Haas, M. Still, T. Barclay, F. Mullally, J. Troeltzsch, S. Aigrain, S. T. Bryson, D. Caldwell, W. J. Chaplin, W. D. Cochran, D. Huber, G. W. Marcy, A. Miglio, J. R. Najita, M. Smith, J. D. Twicken, and J. J. Fortney. The K2 Mission: Characterization and Early Results. , 126(938):398, Apr 2014. doi: 10.1086/676406.
- I. Hubeny and T. Lanz. Non-LTE Line-blanketed Model Atmospheres of Hot Stars. I. Hybrid Complete Linearization/Accelerated Lambda Iteration Method. , 439:875, Feb 1995. doi: 10.1086/175226.
- I. Hubeny and T. Lanz. A brief introductory guide to TLUSTY and SYN-SPEC. *arXiv e-prints*, art. arXiv:1706.01859, Jun 2017.
- M. J. Irwin, J. Lewis, S. Hodgkin, P. Bunclark, D. Evans, R. McMahon, J. P. Emerson, M. Stewart, and S. Beard. VISTA data flow system: pipeline processing for WFCAM and VISTA. In P. J. Quinn and A. Bridger, editors, , volume 5493 of *Society of Photo-Optical Instrumentation Engineers (SPIE) Conference Series*, pages 411–422, Sep 2004. doi: 10.1117/12.551449.
- N. Ivanova, S. Justham, X. Chen, O. De Marco, C. L. Fryer, E. Gaburov, H. Ge, E. Glebbeek, Z. Han, X. D. Li, G. Lu, T. Marsh, P. Podsiadlowski, A. Potter, N. Soker, R. Taam, T. M. Tauris, E. P. J. van den Heuvel, and R. F. Webbink. Common envelope evolution: where we stand and how we can move forward. *Astronomy and Astrophysics Review*, 21:59, Feb 2013. doi: 10.1007/s00159-013-0059-2.
- J. H. Jeans. Cosmogonic problems associated with a secular decrease of mass. , 85:2, Nov 1924. doi: 10.1093/mnras/85.1.2.

- J. M. Jenkins. Kepler Data Processing Handbook: Overview of the Science Operations Center. Technical report, Jan 2017.
- M. Jura. A Tidally Disrupted Asteroid around the White Dwarf G29-38. , 584(2):L91–L94, Feb 2003. doi: 10.1086/374036.
- M. Jura. Pollution of Single White Dwarfs by Accretion of Many Small Asteroids. , 135(5):1785–1792, May 2008. doi: 10.1088/0004-6256/135/5/1785.
- M. Jura and S. Xu. The Survival of Water Within Extrasolar Minor Planets. , 140(5):1129–1136, Nov 2010. doi: 10.1088/0004-6256/140/5/1129.
- M. Jura, S. Xu, B. Klein, D. Koester, and B. Zuckerman. Two Extrasolar Asteroids with Low Volatile-element Mass Fractions. , 750(1):69, May 2012. doi: 10.1088/0004-637X/750/1/69.
- A. Kawka, S. Vennes, G. D. Schmidt, D. T. Wickramasinghe, and R. Koch. Spectropolarimetric Survey of Hydrogen-rich White Dwarf Stars. , 654(1):499–520, Jan 2007. doi: 10.1086/509072.
- S. O. Kepler, I. Pelisoli, S. Jordan, S. J. Kleinman, D. Koester, B. Külebi, V. Peçanha, B. G. Castanheira, A. Nitta, J. E. S. Costa, D. E. Winget, A. Kanaan, and L. Fraga. Magnetic white dwarf stars in the Sloan Digital Sky Survey. , 429(4):2934–2944, Mar 2013. doi: 10.1093/mnras/sts522.
- S. O. Kepler, I. Pelisoli, D. Koester, G. Ourique, S. J. Kleinman, A. D. Romero, A. Nitta, D. J. Eisenstein, J. E. S. Costa, B. Külebi, S. Jordan, P. Dufour, P. Giommi, and A. Rebassa-Mansergas. New white dwarf stars in the Sloan Digital Sky Survey Data Release 10. , 446(4):4078–4087, Feb 2015. doi: 10.1093/mnras/stu2388.
- S. O. Kepler, I. Pelisoli, D. Koester, G. Ourique, A. D. Romero, N. Reindl, S. J. Kleinman, D. J. Eisenstein, A. D. M. Valois, and L. A. Amaral. New white dwarf and subdwarf stars in the Sloan Digital Sky Survey Data Release 12. , 455(4):3413–3423, Feb 2016. doi: 10.1093/mnras/stv2526.
- M. Kilic, E. Agol, A. Loeb, D. Maoz, J. A. Munn, A. Gianninas, P. Canton, and S. D. Barber. Habitable Planets Around White Dwarfs: an Alternate

- Mission for the Kepler Spacecraft. *arXiv e-prints*, art. arXiv:1309.0009, Aug 2013.
- B. Klein, M. Jura, D. Koester, and B. Zuckerman. Rocky Extrasolar Planetary Compositions Derived from Externally Polluted White Dwarfs. , 741(1):64, Nov 2011. doi: 10.1088/0004-637X/741/1/64.
- S. J. Kleinman, S. O. Kepler, D. Koester, I. Pelisoli, V. Peçanha, A. Nitta, J. E. S. Costa, J. Krzesinski, P. Dufour, F. R. Lachapelle, P. Bergeron, C.-W. Yip, H. C. Harris, D. J. Eisenstein, L. Althaus, and A. Córscico. SDSS DR7 White Dwarf Catalog. , 204(1):5, Jan 2013. doi: 10.1088/0067-0049/204/1/5.
- D. G. Koch, W. J. Borucki, G. Basri, N. M. Batalha, T. M. Brown, D. Caldwell, J. Christensen-Dalsgaard, W. D. Cochran, E. DeVore, E. W. Dunham, et al. Kepler Mission Design, Realized Photometric Performance, and Early Science. , 713(2):L79–L86, Apr 2010. doi: 10.1088/2041-8205/713/2/L79.
- D. Koester. *Chemical Stratification in White Dwarf Atmospheres and Envelopes*, volume 328, page 206. 1989. doi: 10.1007/3-540-51031-1\_20.
- D. Koester. White dwarf spectra and atmosphere models . , 81:921–931, 2010.
- D. Koester and S. O. Kepler. DB white dwarfs in the Sloan Digital Sky Survey data release 10 and 12. *Astronomy and Astrophysics*, 583:A86, Nov 2015. doi: 10.1051/0004-6361/201527169.
- D. Koester, B. T. Gänsicke, and J. Farihi. The frequency of planetary debris around young white dwarfs. , 566:A34, Jun 2014. doi: 10.1051/0004-6361/201423691.
- G. Kovács, S. Zucker, and T. Mazeh. A box-fitting algorithm in the search for periodic transits. *Astronomy and Astrophysics*, 391:369–377, Aug 2002. doi: 10.1051/0004-6361:20020802.
- L. Kreidberg. batman: BAsic Transit Model cAlculation in Python. *Publications of the Astronomical Society of the Pacific*, 127(957):1161, Nov 2015. doi: 10.1086/683602.

- A. U. Landolt. A New Short-Period Blue Variable. , 153:151, Jul 1968. doi: 10.1086/149645.
- K. A. Lawrie, M. R. Burleigh, C. S. Brinkworth, T. R. Marsh, S. T. Hodgkin, D. E. A. Baker, P. Cossins, O. M. Littlejohns, A. E. Scott, and P. R. Steele. Photometric Variability of Magnetic White Dwarfs. In J. Krzesiński, G. Stachowski, P. Moskalik, and K. Bajan, editors, *18th European White Dwarf Workshop*, volume 469 of *Astronomical Society of the Pacific Conference Series*, page 429, Jan 2013a.
- K. A. Lawrie, M. R. Burleigh, P. Dufour, and S. T. Hodgkin. SDSS J000555.90-100213.5: a hot, magnetic carbon-dominated atmosphere WD rotating with a 2.1 d period. , 433(2):1599–1606, Aug 2013b. doi: 10.1093/mnras/stt832.
- B. C. Lee, I. Han, and M. G. Park. Planetary companions orbiting M giants HD 208527 and HD 220074. , 549:A2, Jan 2013. doi: 10.1051/0004-6361/201220301.
- A. Léger, D. Rouan, J. Schneider, P. Barge, M. Fridlund, B. Samuel, M. Ollivier, E. Guenther, M. Deleuil, H. J. Deeg, et al. Transiting exoplanets from the CoRoT space mission. VIII. CoRoT-7b: the first super-Earth with measured radius. , 506(1):287–302, Oct 2009. doi: 10.1051/0004-6361/200911933.
- C. Leinert, M. Haas, F. Allard, R. Wehrse, D. W. McCarthy, H. Jahreiss, and C. Perrier. The Nearby Binary Gliese 866 A/B: Orbit Masses, Temperature and Composition. , 236:399, Sep 1990.
- P. Lenz and M. Breger. Period04 User Guide. *Communications in Asteroseismology*, 146:53–136, Jun 2005. doi: 10.1553/cia146s53.
- S. P. Littlefair, S. L. Casewell, S. G. Parsons, V. S. Dhillon, T. R. Marsh, B. T. Gänsicke, S. Bloemen, S. Catalan, P. Irawati, L. K. Hardy, M. Mcallister, M. C. P. Bours, A. Richichi, M. R. Burleigh, B. Burningham, E. Breedt, and P. Kerry. The substellar companion in the eclipsing white dwarf binary SDSS J141126.20+200911.1. , 445(2):2106–2115, Dec 2014. doi: 10.1093/mnras/stu1895.

- M. Livio and N. Soker. Star-planet systems as possible progenitors of cataclysmic binaries. , 208:763–781, Jun 1984. doi: 10.1093/mnras/208.4.763.
- K. Lodders. Solar System Abundances and Condensation Temperatures of the Elements. , 591(2):1220–1247, Jul 2003. doi: 10.1086/375492.
- N. R. Lomb. Least-Squares Frequency Analysis of Unequally Spaced Data. , 39(2):447–462, Feb 1976. doi: 10.1007/BF00648343.
- E. S. Longstaff, S. L. Casewell, G. A. Wynn, P. F. L. Maxted, and C. Helling. Emission lines in the atmosphere of the irradiated brown dwarf WD0137-349B. , 471(2):1728–1736, Oct 2017. doi: 10.1093/mnras/stx1786.
- K. Mandel and E. Agol. Analytic Light Curves for Planetary Transit Searches. *The Astrophysical Journal*, 580(2):L171–L175, Dec 2002. doi: 10.1086/345520.
- C. J. Manser, B. T. Gänsicke, S. Eggl, M. Hollands, P. Izquierdo, D. Koester, J. D. Landstreet, W. Lyra, T. R. Marsh, F. Meru, et al. A planetesimal orbiting within the debris disc around a white dwarf star. *Science*, 364(6435):66–69, Apr 2019. doi: 10.1126/science.aat5330.
- D. Maoz, T. Mazeh, and A. McQuillan. Kepler and the seven dwarfs: detection of low-level day-time-scale periodic photometric variations in white dwarfs. , 447(2):1749–1760, Feb 2015. doi: 10.1093/mnras/stu2577.
- P. Martini, J. Elias, S. Points, D. Sprayberry, M. A. Derwent, R. Gonzalez, J. A. Mason, T. P. O’Brien, D. P. Pappalardo, R. W. Pogge, et al. KOSMOS and COSMOS: new facility instruments for the NOAO 4-meter telescopes. In , volume 9147 of *Society of Photo-Optical Instrumentation Engineers (SPIE) Conference Series*, page 91470Z, Jul 2014. doi: 10.1117/12.2056834.
- F. J. Masci, R. R. Laher, B. Rusholme, D. L. Shupe, S. Groom, J. Surace, E. Jackson, S. Monkewitz, R. Beck, D. Flynn, et al. The Zwicky Transient Facility: Data Processing, Products, and Archive. , 131(995):018003, Jan 2019. doi: 10.1088/1538-3873/aae8ac.
- P. Massey. *A Users Guide to CCD reductions with IRAF*. 1997.

- P. Massey, F. Valdes, and J. Barnes. A User's Guide to Reducing Slit Spectra with IRAF. 1992.
- P. F. L. Maxted, T. R. Marsh, and R. C. North. KPD 1930+2752: a candidate Type Ia supernova progenitor. , 317(3):L41–L44, Sep 2000. doi: 10.1046/j.1365-8711.2000.03856.x.
- M. Mayor, D. Queloz, G. Marcy, P. Butler, R. Noyes, S. Korzennik, M. Krockenberger, P. Nisenson, T. Brown, T. Kennelly, C. Rowland, S. Horner, G. Burki, M. Burnet, and M. Kunzli. 51 Pegasi. , 6251:1, Oct 1995.
- M. Mayor, F. Pepe, D. Queloz, F. Bouchy, G. Rupprecht, G. Lo Curto, G. Avila, W. Benz, J. L. Bertaux, X. Bonfils, T. Dall, H. Dekker, B. Delabre, W. Eckert, M. Fleury, A. Gilliotte, D. Gojak, J. C. Guzman, D. Kohler, J. L. Lizon, A. Longinotti, C. Lovis, D. Megevand, L. Pasquini, J. Reyes, J. P. Sivan, D. Sosnowska, R. Soto, S. Udry, A. van Kesteren, L. Weber, and U. Weilenmann. Setting New Standards with HARPS. *The Messenger*, 114:20–24, Dec 2003.
- G. P. McCook and E. M. Sion. A Catalogue of Spectroscopically Identified White Dwarfs. *VizieR Online Data Catalog*, 1:2035, Jan 2016.
- J. McCormac, D. Pollacco, I. Skillen, F. Faedi, I. Todd, and C. A. Watson. DONUTS: A Science Frame Autoguiding Algorithm with Sub-Pixel Precision, Capable of Guiding on Defocused Stars. , 125(927):548, May 2013. doi: 10.1086/670940.
- J. McCormac, I. Skillen, D. Pollacco, F. Faedi, G. Ramsay, V. S. Dhillon, I. Todd, and A. Gonzalez. A search for photometric variability towards M71 with the Near-Infrared Transiting ExoplanetS Telescope. , 438(4):3383–3398, Mar 2014. doi: 10.1093/mnras/stt2449.
- W. McDonough. In *Earthquake Thermodynamics and Phase Transformation in the Earth's Interior*, page 5. Academic Press, San Diego, 2000.
- C. Melis, P. Dufour, J. Farihi, J. Bochanski, A. J. Burgasser, S. G. Parsons, B. T. Gänsicke, D. Koester, and B. J. Swift. Gaseous Material Orbiting the

- Polluted, Dusty White Dwarf HE 1349-2305. , 751(1):L4, May 2012. doi: 10.1088/2041-8205/751/1/L4.
- R. Napiwotzki, P. J. Green, and R. A. Saffer. A Comparative Study of the Mass Distribution of Extreme-Ultraviolet-selected White Dwarfs. , 517:399–415, May 1999. doi: 10.1086/307170.
- A. Nebot Gómez-Morán, B. T. Gänsicke, M. R. Schreiber, A. Rebassa-Mansergas, A. D. Schwope, J. Southworth, A. Aungwerojwit, M. Bothe, P. J. Davis, U. Kolb, et al. Post common envelope binaries from SDSS. XII. The orbital period distribution. *Astronomy and Astrophysics*, 536:A43, Dec 2011. doi: 10.1051/0004-6361/201117514.
- B. Nelson and W. D. Davis. Eclipsing-Binary Solutions by Sequential Optimization of the Parameters. , 174:617, Jun 1972. doi: 10.1086/151524.
- L. R. Nittler, T. J. McCoy, P. E. Clark, M. E. Murphy, J. I. Trombka, and E. Jarosewich. Bulk element compositions of meteorites: A guide for interpreting remote-sensing geochemical measurements of planets and asteroids. *Antarctic Meteorite Research*, 17:231, Jan 2004.
- S. Noll, W. Kausch, M. Barden, A. M. Jones, C. Szyszka, S. Kimeswenger, and J. Vinther. An atmospheric radiation model for Cerro Paranal. I. The optical spectral range. , 543:A92, Jul 2012. doi: 10.1051/0004-6361/201219040.
- J. Nordhaus, D. S. Spiegel, L. Ibgui, J. Goodman, and A. Burrows. Tides and tidal engulfment in post-main-sequence binaries: period gaps for planets and brown dwarfs around white dwarfs. , 408(1):631–641, Oct 2010. doi: 10.1111/j.1365-2966.2010.17155.x.
- D. O’Donoghue. High Speed CCD Photometry. *Baltic Astronomy*, 4:519–526, Jan 1995. doi: 10.1515/astro-1995-0411.
- J. Osborn, D. Föhring, V. S. Dhillon, and R. W. Wilson. Atmospheric scintillation in astronomical photometry. , 452(2):1707–1716, Sep 2015. doi: 10.1093/mnras/stv1400.
- B. Paczyński. Evolutionary Processes in Close Binary Systems. , 9:183, Jan 1971. doi: 10.1146/annurev.aa.09.090171.001151.

- C. Paquette, C. Pelletier, G. Fontaine, and G. Michaud. Diffusion in White Dwarfs: New Results and Comparative Study. , 61:197, May 1986. doi: 10.1086/191112.
- S. G. Parsons, B. T. Gänsicke, T. R. Marsh, P. Bergeron, C. M. Copperwheat, V. S. Dhillon, J. Bento, S. P. Littlefair, and M. R. Schreiber. An accurate mass and radius measurement for an ultracool white dwarf. *Monthly Notices of the Royal Astronomical Society*, 426(3):1950–1958, Nov 2012a. doi: 10.1111/j.1365-2966.2012.21773.x.
- S. G. Parsons, T. R. Marsh, B. T. Gänsicke, V. S. Dhillon, C. M. Copperwheat, S. P. Littlefair, S. Pyrzas, A. J. Drake, D. Koester, M. R. Schreiber, and A. Rebassa-Mansergas. The shortest period detached white dwarf + main-sequence binary. , 419(1):304–313, Jan 2012b. doi: 10.1111/j.1365-2966.2011.19691.x.
- S. G. Parsons, T. R. Marsh, B. T. Gänsicke, A. Rebassa-Mansergas, V. S. Dhillon, S. P. Littlefair, C. M. Copperwheat, R. D. G. Hickman, M. R. Burleigh, P. Kerry, D. Koester, A. Nebot Gómez-Morán, S. Pyrzas, C. D. J. Savoury, M. R. Schreiber, L. Schmidtobreick, A. D. Schwope, P. R. Steele, and C. Tappert. A precision study of two eclipsing white dwarf plus M dwarf binaries. , 420(4):3281–3297, Mar 2012c. doi: 10.1111/j.1365-2966.2011.20251.x.
- S. G. Parsons, B. T. Gänsicke, T. R. Marsh, A. J. Drake, V. S. Dhillon, S. P. Littlefair, S. Pyrzas, A. Rebassa-Mansergas, and M. R. Schreiber. Eclipsing post-common envelope binaries from the Catalina surveys. *Monthly Notices of the Royal Astronomical Society*, 429(1):256–268, Feb 2013. doi: 10.1093/mnras/sts332.
- S. G. Parsons, J. J. Hermes, T. R. Marsh, B. T. Gänsicke, P. E. Tremblay, S. P. Littlefair, D. I. Sahman, R. P. Ashley, M. Green, S. Rattanasoon, et al. Two white dwarfs in ultrashort binaries with detached, eclipsing, likely sub-stellar companions detected by K2. , 471(1):976–986, Oct 2017. doi: 10.1093/mnras/stx1610.
- F. Pepe, P. Molaro, S. Cristiani, R. Rebolo, N. C. Santos, H. Dekker, D. Mégevand, F. M. Zerbi, A. Cabral, P. Di Marcantonio, et al. ESPRESSO:

- The next European exoplanet hunter. *Astronomische Nachrichten*, 335(1):8, Jan 2014. doi: 12.1002/asna.201312004.
- D. Pollacco, I. Skillen, A. Collier Cameron, D. Christian, J. Irwin, T. Lister, R. Street, R. West, W. Clarkson, N. Evans, A. Fitzsimmons, C. Haswell, C. Hellier, S. Hodgkin, K. Horne, B. Jones, S. Kane, F. Keenan, A. Norton, J. Osborne, R. Ryans, and P. Wheatley. The WASP Project and SuperWASP Camera. , 304(1-4):253–255, Aug 2006. doi: 10.1007/s10509-006-9124-x.
- D. M. Popper and P. B. Etzel. Photometric orbits of seven detached eclipsing binaries. , 86:102–120, Jan 1981. doi: 10.1086/112862.
- S. Pyrzas, B. T. Gänsicke, S. Brady, S. G. Parsons, T. R. Marsh, D. Koester, E. Breedt, C. M. Copperwheat, A. Nebot Gómez-Morán, A. Rebassa-Mansergas, et al. Post-common envelope binaries from SDSS - XV. Accurate stellar parameters for a cool 0.4 M white dwarf and a 0.16 M M dwarf in a 3 h eclipsing binary. *Monthly Notices of the Royal Astronomical Society*, 419(1):817–826, Jan 2012. doi: 10.1111/j.1365-2966.2011.19746.x.
- D. Queloz, F. Bouchy, C. Moutou, A. Hatzes, G. Hébrard, R. Alonso, M. Auvergne, A. Baglin, M. Barbieri, P. Barge, et al. The CoRoT-7 planetary system: two orbiting super-Earths. , 506(1):303–319, Oct 2009. doi: 10.1051/0004-6361/200913096.
- S. Rappaport, B. L. Gary, T. Kaye, A. Vanderburg, B. Croll, P. Benni, and J. Foote. Drifting asteroid fragments around WD 1145+017. , 458(4):3904–3917, Jun 2016. doi: 10.1093/mnras/stw612.
- S. Rappaport, A. Vanderburg, L. Nelson, B. L. Gary, T. G. Kaye, B. Kalomeni, S. B. Howell, J. R. Thorstensen, F. R. Lachapelle, M. Lundy, and J. St-Antoine. WD 1202-024: the shortest-period pre-cataclysmic variable. , 471(1):948–961, Oct 2017. doi: 10.1093/mnras/stx1611.
- F. A. Rasio, C. A. Tout, S. H. Lubow, and M. Livio. Tidal Decay of Close Planetary Orbits. , 470:1187, Oct 1996. doi: 10.1086/177941.
- A. Rebassa-Mansergas, B. T. Gänsicke, M. R. Schreiber, D. Koester, and P. Rodríguez-Gil. Post-common envelope binaries from SDSS - VII. A

- catalogue of white dwarf-main sequence binaries. *Monthly Notices of the Royal Astronomical Society*, 402(1):620–640, Feb 2010. doi: 10.1111/j.1365-2966.2009.15915.x.
- I. N. Reid, E. Lewitus, A. J. Burgasser, and K. L. Cruz. 2MASS J22521073-1730134: A Resolved L/T Binary at 14 Parsecs. , 639:1114–1119, Mar. 2006. doi: 10.1086/499484.
- I. Renedo, L. G. Althaus, M. M. Miller Bertolami, A. D. Romero, A. H. Córscico, R. D. Rohrmann, and E. García-Berro. New Cooling Sequences for Old White Dwarfs. , 717:183–195, July 2010. doi: 10.1088/0004-637X/717/1/183.
- G. R. Ricker, J. N. Winn, R. Vanderspek, D. W. Latham, G. Á. Bakos, J. L. Bean, Z. K. Berta-Thompson, T. M. Brown, L. Buchhave, et al. Transiting Exoplanet Survey Satellite (TESS). *Journal of Astronomical Telescopes, Instruments, and Systems*, 1:014003, Jan 2015. doi: 10.1117/1.JATIS.1.1.014003.
- A. C. Robin, C. Reylé, S. Derrière, and S. Picaud. A synthetic view on structure and evolution of the Milky Way. , 409:523–540, Oct 2003. doi: 10.1051/0004-6361:20031117.
- C. Rodrigo, E. Solano, and A. Bayo. SVO Filter Profile Service Version 1.0. Technical report, Oct 2012.
- M. Roelens, S. Blanco-Cuaresma, T. Semaan, L. Palaversa, N. Mowlavi, and L. Eyer. Gaia16ali and Gaia16alj supernovae confirmed by Euler imaging. *The Astronomer’s Telegram*, 8980:1, Apr 2016.
- I. J. Sackmann, A. I. Boothroyd, and K. E. Kraemer. Our Sun. III. Present and Future. , 418:457, Nov 1993. doi: 10.1086/173407.
- J. D. Scargle. Studies in astronomical time series analysis. II. Statistical aspects of spectral analysis of unevenly spaced data. , 263:835–853, Dec 1982. doi: 10.1086/160554.
- V. Schaffenroth, S. Geier, U. Heber, T. Kupfer, E. Ziegerer, C. Heuser, L. Classen, and O. Cordes. Binaries discovered by the MUCHFUSS project. SDSS J162256.66+473051.1: An eclipsing subdwarf B binary with a brown dwarf companion. , 564:A98, Apr 2014. doi: 10.1051/0004-6361/201423377.

- V. Schaffenroth, B. N. Barlow, H. Drechsel, and B. H. Dunlap. An eclipsing post common-envelope system consisting of a pulsating hot subdwarf B star and a brown dwarf companion. , 576:A123, Apr 2015. doi: 10.1051/0004-6361/201525701.
- M. Schönberg and S. Chandrasekhar. On the Evolution of the Main-Sequence Stars. , 96:161, Sep 1942. doi: 10.1086/144444.
- L. Siess and M. Livio. The accretion of brown dwarfs and planets by giant stars - I. Asymptotic giant branch stars. , 304(4):925–937, Apr 1999a. doi: 10.1046/j.1365-8711.1999.02376.x.
- L. Siess and M. Livio. The accretion of brown dwarfs and planets by giant stars - II. Solar-mass stars on the red giant branch. , 308(4):1133–1149, Oct 1999b. doi: 10.1046/j.1365-8711.1999.02784.x.
- N. M. Silvestri, M. P. Lemagie, S. L. Hawley, A. A. West, G. D. Schmidt, J. Liebert, P. Szkody, L. Mannikko, M. A. Wolfe, J. C. Barentine, et al. New Close Binary Systems from the SDSS-I (Data Release Five) and the Search for Magnetic White Dwarfs in Cataclysmic Variable Progenitor Systems. *The Astronomical Journal*, 134(2):741–748, Aug 2007. doi: 10.1086/519242.
- M. F. Skrutskie, R. M. Cutri, R. Stiening, M. D. Weinberg, S. Schneider, J. M. Carpenter, C. Beichman, R. Capps, T. Chester, J. Elias, et al. The Two Micron All Sky Survey (2MASS). *The Astronomical Journal*, 131(2):1163–1183, Feb 2006. doi: 10.1086/498708.
- J. Southworth, P. F. L. Maxted, and B. Smalley. Eclipsing binaries in open clusters - II. V453 Cyg in NGC 6871. , 351(4):1277–1289, Jul 2004. doi: 10.1111/j.1365-2966.2004.07871.x.
- S. P. Souza, B. A. Babcock, J. M. Pasachoff, A. A. S. Gulbis, J. L. Elliot, M. J. Person, and J. W. Gangestad. POETS: Portable Occultation, Eclipse, and Transit System. , 118(849):1550–1557, Nov 2006. doi: 10.1086/509665.
- D. S. Spiegel, A. Burrows, and J. A. Milsom. The Deuterium-burning Mass Limit for Brown Dwarfs and Giant Planets. , 727(1):57, Jan 2011. doi: 10.1088/0004-637X/727/1/57.

- P. R. Steele, M. R. Burleigh, P. D. Dobbie, R. F. Jameson, M. A. Barstow, and R. P. Satterthwaite. White dwarfs in the UKIRT Infrared Deep Sky Survey Large Area Survey: the substellar companion fraction. , 416(4):2768–2791, Oct 2011. doi: 10.1111/j.1365-2966.2011.19225.x.
- P. R. Steele, R. P. Saglia, M. R. Burleigh, T. R. Marsh, B. T. Gänsicke, K. Lawrie, M. Cappetta, J. Girven, and R. Napiwotzki. NLTT 5306: the shortest period detached white dwarf+brown dwarf binary. , 429(4):3492–3500, Mar 2013. doi: 10.1093/mnras/sts620.
- D. Tody. The IRAF Data Reduction and Analysis System. In D. L. Crawford, editor, , volume 627 of *Society of Photo-Optical Instrumentation Engineers (SPIE) Conference Series*, page 733, Jan 1986. doi: 10.1117/12.968154.
- P.-E. Tremblay, P. Bergeron, and A. Gianninas. An Improved Spectroscopic Analysis of DA White Dwarfs from the Sloan Digital Sky Survey Data Release 4. , 730:128, Apr. 2011. doi: 10.1088/0004-637X/730/2/128.
- W. D. Vacca, M. C. Cushing, and J. T. Rayner. A Method of Correcting Near-Infrared Spectra for Telluric Absorption. , 115(805):389–409, Mar 2003. doi: 10.1086/346193.
- J. E. Van Cleve, S. B. Howell, J. C. Smith, B. D. Clarke, S. E. Thompson, S. T. Bryson, M. N. Lund, R. Handberg, and W. J. Chaplin. That’s How We Roll: The NASA K2 Mission Science Products and Their Performance Metrics. , 128(965):075002, Jul 2016. doi: 10.1088/1538-3873/128/965/075002.
- Z. Vanderbosch, J. J. Hermes, E. Dennyhy, B. H. Dunlap, P. Izquierdo, P. E. Tremblay, P. B. Cho, B. T. Gänsicke, K. J. Bell, M. H. Montgomery, and D. E. Winget. A White Dwarf with Transiting Circumstellar Material Far Outside Its Tidal Disruption Radius. *arXiv e-prints*, art. arXiv:1908.09839, Aug 2019.
- A. Vanderburg and J. A. Johnson. A Technique for Extracting Highly Precise Photometry for the Two-Wheeled Kepler Mission. , 126(944):948, Oct 2014. doi: 10.1086/678764.

- A. Vanderburg, J. A. Johnson, S. Rappaport, A. Bieryla, J. Irwin, J. A. Lewis, D. Kipping, W. R. Brown, P. Dufour, D. R. Ciardi, R. Angus, L. Schaefer, D. W. Latham, D. Charbonneau, C. Beichman, J. Eastman, N. McCrady, R. A. Wittenmyer, and J. T. Wright. A disintegrating minor planet transiting a white dwarf. , 526(7574):546–549, Oct 2015. doi: 10.1038/nature15527.
- G. Vauclair, S. Vauclair, and J. L. Greenstein. The chemical evolution of white dwarf atmospheres : diffusion and accretion. , 80:79–96, Nov 1979.
- S. Vennes, R. J. Smith, B. J. Boyle, S. M. Croom, A. Kawka, T. Shanks, L. Miller, and N. Loaring. White dwarfs in the 2dF QSO Redshift Survey - I. Hydrogen-rich (DA) stars. , 335(3):673–686, Sep 2002. doi: 10.1046/j.1365-8711.2002.05658.x.
- S. Vennes, A. Kawka, and P. Németh. The heavily polluted atmosphere of the DAZ white dwarf GALEX J193156.8+011745. , 404(1):L40–L44, May 2010. doi: 10.1111/j.1745-3933.2010.00830.x.
- D. Veras and B. T. Gänsicke. Detectable close-in planets around white dwarfs through late unpacking. , 447(2):1049–1058, Feb 2015. doi: 10.1093/mnras/stu2475.
- D. Veras, J. D. Hadjidemetriou, and C. A. Tout. An exoplanet’s response to anisotropic stellar mass loss during birth and death. , 435(3):2416–2430, Nov 2013. doi: 10.1093/mnras/stt1451.
- D. Veras, Z. M. Leinhardt, A. Bonsor, and B. T. Gänsicke. Formation of planetary debris discs around white dwarfs - I. Tidal disruption of an extremely eccentric asteroid. , 445(3):2244–2255, Dec 2014. doi: 10.1093/mnras/stu1871.
- E. Villaver and M. Livio. Can Planets Survive Stellar Evolution? , 661(2): 1192–1201, Jun 2007. doi: 10.1086/516746.
- R. F. Webbink. Double white dwarfs as progenitors of R Coronae Borealis stars and type I supernovae. *The Astrophysical Journal*, 277:355–360, Feb 1984. doi: 10.1086/161701.
- B. Y. Welsh, N. Craig, P. W. Vedder, and J. V. Vallerga. The Local Distribution of NA i Interstellar Gas. , 437:638, Dec 1994. doi: 10.1086/175028.

- B. Y. Welsh, D. M. Sfeir, M. M. Sirk, and R. Lallement. EUV mapping of the local interstellar medium: the Local Chimney revealed? , 352:308–316, Dec 1999.
- K. Werner and T. Rauch. Hubble Space Telescope ultraviolet spectroscopy of the hottest known helium-rich pre-white dwarf KPD 0005+5106. , 583:A131, Nov 2015. doi: 10.1051/0004-6361/201527212.
- F. Wesemael. Accretion from interstellar clouds and white dwarf spectral evolution. , 72:104–110, Feb 1979.
- A. A. West, S. L. Hawley, J. J. Bochanski, K. R. Covey, I. N. Reid, S. Dhital, E. J. Hilton, and M. Masuda. Constraining the Age-Activity Relation for Cool Stars: The Sloan Digital Sky Survey Data Release 5 Low-Mass Star Spectroscopic Sample. , 135(3):785–795, Mar 2008. doi: 10.1088/0004-6256/135/3/785.
- R. G. West, E. Gillen, D. Bayliss, M. R. Burleigh, L. Delrez, M. N. Günther, S. T. Hodgkin, J. A. G. Jackman, J. S. Jenkins, G. King, et al. NGTS-4b: A sub-Neptune transiting in the desert. , 486(4):5094–5103, Jul 2019. doi: 10.1093/mnras/stz1084.
- P. J. Wheatley, D. L. Pollacco, D. Queloz, H. Rauer, C. A. Watson, R. G. West, B. Chazelas, T. M. Louden, N. Bannister, J. Bento, et al. Next Generation Transit Survey (NGTS). In M. Booth, B. C. Matthews, and J. R. Graham, editors, *Exploring the Formation and Evolution of Planetary Systems*, volume 299 of *IAU Symposium*, pages 311–312, Jan 2014. doi: 10.1017/S1743921313008740.
- P. J. Wheatley, R. G. West, M. R. Goad, J. S. Jenkins, D. L. Pollacco, D. Queloz, H. Rauer, S. Udry, C. A. Watson, B. Chazelas, et al. The Next Generation Transit Survey (NGTS). , 475(4):4476–4493, Apr 2018. doi: 10.1093/mnras/stx2836.
- B. Willems and U. Kolb. Detached white dwarf main-sequence star binaries. *Astronomy and Astrophysics*, 419:1057–1076, Jun 2004. doi: 10.1051/0004-6361:20040085.

- D. J. Wilson, B. T. Gänsicke, D. Koester, R. Raddi, E. Breedt, J. Southworth, and S. G. Parsons. Variable emission from a gaseous disc around a metal-polluted white dwarf. , 445(2):1878–1884, Dec 2014. doi: 10.1093/mnras/stu1876.
- D. J. Wilson, B. T. Gänsicke, D. Koester, J. Holberg, M. R. Burleigh, and C. Be-  
lardi. New Observations of the Mysterious Metal-Polluted White Dwarf GD  
394. In P. E. Tremblay, B. Gänsicke, and T. Marsh, editors, *20th European  
White Dwarf Workshop*, volume 509 of *Astronomical Society of the Pacific  
Conference Series*, page 107, Mar 2017.
- D. E. Winget, H. M. van Horn, and C. J. Hansen. The nature of the ZZ Ceti  
oscillations - Trapped modes in compositionally stratified white dwarfs. , 245:  
L33–L36, Apr 1981. doi: 10.1086/183516.
- C. Wolf, C. A. Onken, L. C. Luvaul, B. P. Schmidt, M. S. Bessell, S.-W. Chang,  
G. S. Da Costa, D. Mackey, T. Martin-Jones, S. J. Murphy, T. Preston, R. A.  
Scalzo, L. Shao, J. Smillie, P. Tisserand, M. C. White, and F. Yuan. SkyMap-  
per Southern Survey: First Data Release (DR1). , 35:e010, Feb 2018. doi:  
10.1017/pasa.2018.5.
- A. Wolszczan and D. A. Frail. A planetary system around the millisecond pulsar  
PSR1257 + 12. , 355:145–147, Jan. 1992. doi: 10.1038/355145a0.
- J. T. Wright. *Radial Velocities as an Exoplanet Discovery Method*, page 4. 2018.  
doi: 10.1007/978-3-319-55333-7<sub>4</sub>.
- D. G. York, J. Adelman, J. Anderson, John E., S. F. Anderson, J. Annis, N. A.  
Bahcall, J. A. Bakken, R. Barkhouser, S. Bastian, E. Berman, et al. The Sloan  
Digital Sky Survey: Technical Summary. *The Astronomical Journal*, 120(3):  
1579–1587, Sep 2000. doi: 10.1086/301513.
- E. M. Zeidler-K. T., V. Weidemann, and D. Koester. Metal abundances in  
helium-rich white dwarf atmospheres. , 155:356–370, Feb 1986.
- B. Zuckerman and E. E. Becklin. Excess infrared radiation from a white  
dwarf—an orbiting brown dwarf? , 330(6144):138–140, Nov 1987. doi:  
10.1038/330138a0.

B. Zuckerman, D. Koester, C. Melis, B. M. Hansen, and M. Jura. The Chemical Composition of an Extrasolar Minor Planet. , 671(1):872–877, Dec 2007. doi: 10.1086/522223.